UNIVERSITY OF OKLAHOMA

GRADUATE COLLEGE

SYNERGISTIC AND COMPETITIVE BEHAVIOR OF ANISOTROPIC PARTICLES AND SURFACTANT MOLECULES AT FLUID INTERFACES

A DISSERTATION

SUBMITTED TO THE GRADUATE FACULTY

in partial fulfillment of the requirements for the

Degree of

DOCTOR OF PHILOSOPHY

By

ELTON LIMA CORREIA
Norman, Oklahoma
2023

SYNERGISTIC AND COMPETITIVE BEHAVIOR OF ANISOTROPIC PARTICLES AND SURFACTANT MOLECULES AT FLUID INTERFACES

A DISSERTATION APPROVED FOR THE

SCHOOL OF SUSTAINABLE CHEMICAL, BIOLOGICAL AND MATERIALS ENGINEERING

BY THE COMMITTEE CONSISTING OF

Dr. Sepideh Razavi, Chair

Dr. Dimitrios V. Papavassiliou, Co-Chair

Dr. Jeffrey Harwell

Dr. Edgar O'Rear

Dr. Deepak Devegowda

I dedicate this work to my parents, Josy and Juarez,

who taught me that there are no limits to what I can achieve.

ACKNOWLEDGEMENTS

First, I'd like to thank my advisor Prof. Sepideh Razavi, who has guided me through this tortuous path during these four years. She taught me so much through this wonderful journey and gave me the freedom to pursue directions that I found to be more interesting. Her belief in my potential and high expectations pushed me to do my best. She was always available to talk and discuss the ideas I came up with. Her insights were always helpful, and I could not have done any of this work without her support. I am really happy that I had the opportunity to work with her. It was a pleasure to be one of the first researchers in Razavi's Lab.

I am also grateful for the members of my committee, Prof Dimitrios Papavassiliou, who has been a wonderful mentor, as well as a great transport and math professor; Prof. Jeffrey Harwell, who taught me the fundamentals of surfactants science; Prof. Edgar O'Rear for the amazing classes of transport phenomena; and Prof. Deepak Devegowda, for his service in my committee and willingness to help with my PhD.

I'd also like to thank Prof. Henning Winter, from the University of Massachusetts Amherst, for all the enthusiastic discussions and for teaching me key concepts of rheology; to Prof. James Gilchrist, from Lehigh University, for sending me the particle monolayers, which saved me so much time on fabricating my Janus Particles; and to Prof. Ilona Kretzschmar, for lending the trough that was used to generate my shear rheology data.

I wish to thank the members of our research group, who shared most of journey with me, for all they have taught me, personally and academically: Aanahita Ervin, Nick Brown, Alec de la Pena, Emma Shields, Siddharth Thakur, Matthew Webb, Eduarda Barros de Oliveira, Blake Bartlett, Deepika Sitaraman, and Ashley Copelin. I also would like to extend this

acknowledgement to members of Prof. Papavassiliou's group, for the fruitful discussions: Thao Nguyen, Vi Nguyen, and Marco Tulio Portella. Additionally, I have to thank Andrew D'Amico, for all the great discussions and for helping with the 3D prints that allowed me to run some of the key experiments in this work.

Of course, I must thank my girlfriend, fiancée, spouse, wife, partner, and friend, Ana Carolina Roncoli Jerdy, who has been on my side for more than 8 years, cheering me up on the hard times, supporting me to overcome any obstacles, hearing me talk about my research almost every day. I cannot thank you enough. There is simply no way I can put to words how grateful I am for sharing my life with you.

Finally, I have to thank my parents, Maria Josileide de Lima and Juarez Gomes Correia, who did everything they could to enable me to follow my path. They raised me to be the person I am today, to follow my dreams and to never give up on anything. I'm really lucky to have both of you to look after me. And Mom, now you can finally call me Dr. Elton!

I'd like to acknowledge the support of the National Association for Surface Finishing (NASF) for the graduate scholarship and the Gallogly College of Engineering Dissertation Excellence Award. I'm grateful for the support from the National Science Foundation through the award CBET-1934513.

TABLE OF CONTENTS

LIST OF TABLES

LIST OF FIGURES

SYNERGISTIC AND COMPETITIVE BEHAVIOR OF ANISOTROPIC PARTICLES AND SURFACTANT MOLECULES AT FLUID INTERFACES

ABSTRACT

Colloidal systems are a common feature in different application domains, from complex underground frameworks such as petroleum recovery and water remediation to industrialized consumer products such as cosmetics and paint. These systems usually consist of multiple components, such as nanoparticles, polymers, surfactants, and ions exhibiting unique properties that are different from those of simple fluids. In addition, in many applications involving the water-energy nexus, these complex fluids come in contact with surfaces and interfaces. For instance, an enhanced oil recovery operation usually consists of flooding a multicomponent fluid (e.g., aqueous solution of surfactants and polymers) through a reservoir rock that has heterogeneous porosity and anisotropic permeability. Another example is the treatment of produced water generated from the oil industry to separate the organic contaminants that are stabilized by surface-active species present in both phases. Given the range of phenomena that take place simultaneously, from the dynamic wetting of complex fluids on a solid surface to interfacial stresses and deformations at a fluid interface, advancing our understanding of the key factors that govern the interactions present in such systems and their resulting properties, will lay the foundation for the engineering of complex interfacial systems with a tailored set of properties.

To decode the behavior of multicomponent fluidic systems, it is crucial to understand the role of components present, both individually and synergistically, in the governing physics. For instance, surfactants, as amphiphilic molecules, populate the interface providing interfacial stability via a reduction in interfacial tension. In contrast, colloidal particles stabilize an interface

by occupying the contact area between the two fluids. Hence, attributes such as particle size and surface chemistry can be used to control their position at the interface and the resulting reduction in the free energy. Moreover, particles encountered in real-world applications, such as those encountered in foam flotation for ore recovery, often diverge from the case of isotropic homogeneous particles; thus, it is crucial to understand the impact of heterogeneities present in such scenarios, on the resulting interactions, by studying model particles. These include particles that are rough and possess anisotropies either in shape or surface chemistry. A classic example of a chemically anisotropic particle is the Janus Particle (JP), named after the two-face Roman God. The Janus motif brings unique functionalities to a multicomponent system, augmenting the number of variables that can be tuned to achieve the desired outcomes. Although there is some literature with respect to the dynamics of particles and surfactants at interfaces, little information is available on mixed systems, especially for heterogenous and anisotropic, yet technologically relevant, particles.

The present work is dedicated to probing the roles different surface-active species (i.e., surfactants and nanoparticles) paly in resulting interfacial phenomena such as surface pressure, mechanical properties when subjected to dilational or shear stresses, and the stability of multicomponent fluidic systems. We investigate various features that can be employed in tuning the competitive vs. synergistic behavior of species that make up the system and determine the role non-idealities play in tuning the properties of the populated interface and stability of the interfacial systems. The knowledge base achieved from this PhD work, will equip us with a fundamental understanding of the key attributes in design and engineering of solutions to address real-life challenges in a broad range of applications from wastewater remediation to increasing the shelf-life of a product.

1. Introduction

Studying the behavior of anisotropic particles at fluid interfaces is a rapidly expanding field, as understanding how the introduced anisotropy affects the resulting properties is essential in the engineering of interfacial systems. Surface anisotropic particles, also known as Janus particles (JPs), offer new possibilities for novel applications due to their dual characteristic and stronger binding to fluid interfaces compared to homogeneous particles. Introducing surface anisotropy creates complexity as the orientation of interfacially bound particles affects the interparticle interactions, a contributing factor to the microstructure formation. Additionally, surface rough particles are often present in various applications involving colloidal systems, and the implications of their deviation from isotropic spherical shape are not completely understood. Another layer of complexity arises when colloidal particles are present in a mixture along with surfactant molecules, as they can either compete for populating the fluid interface or act synergistically. Especially for the case of similarly charged particles and surfactants, the resulting interactions near fluid interfaces are still not well understood.

The work performed in this dissertation aims to address a number of the open questions related to these complex interfacial systems. In Chapter 2, we provide a background on the behavior of colloidal particles at fluid interfaces and review the fundamentals behind the important phenomena taking place in such systems. Chapter 3 details the materials and methods utilized to perform the studies in this thesis including experimentation, modelling, and simulations. In Chapter 4, we examine interfacial monolayers formed by colloidal particles and investigate how surface roughness or anisotropy affects the interparticle interactions. We first discuss the impact of particle roughness on the mechanical properties of a monolayer under compression and interpret

the data in terms of the interactions occurring at the fluid interface. Next, we move on to the case of surface anisotropic particles and review the impact of Janus particle amphiphilicity on the capillary interactions at the air-water interface. We then discuss the implications of JPs amphiphilicity on the monolayer response to shear stress and further analyze a glass-transition-like behavior at a high JP surface coverage. In Chapter 5, we proceed to the mixed systems of SDS surfactant molecules, and the particles studied in Chapter 3. To better understand the synergistic and competitive nature of interactions in mixed systems, especially near fluid interfaces, we start by examining the adsorption of SDS surfactant molecules onto the surface of silica particles, and the conditions that promote or prevent adsorption in this case of like-charged species. In addition, we investigate the hydrolysis of SDS and how the dodecanol contaminant can impact the results of surface measurements. Next, we probe the implications of having a surfactant on the subphase for the mechanical properties of networks formed by spherical colloidal silica and rough fumed silica particles. Finally, we provide a preliminary study on the interfacial shear rheology for the case of mixed SDS molecules and Janus particles in order to illustrate the impacts addition of surfactants could have on the stability and mechanical properties of JP monolayers. In Chapter 6 we summarize the findings of this PhD thesis and propose future research directions on the topic.

2. Background

2.1. Motivation

The behavior of colloidal particles in vicinity of fluid interfaces has intrigued scientists ever since particles were first observed to reside at the surface of droplets and bubbles yielding stabilization in emulsions and foams.[1, 2] There is a vast range of applications in which particles are used in engineering the performance of interfacial systems including pharmaceutics, food industry, oil recovery, and personal care products.[3-10] By binding to fluid interfaces, particles remove the energetically unfavorable contact area between the two fluids and replace it with solid/fluid interfaces, which results in an overall reduction in the free energy of the system. The energy required to desorb an interfacially-trapped particle thus depends on the interfacial tension of the fluids, particle contact angle at the interface, and particle size. A large value of binding energy relative to the thermal energy can therefore lead to irreversibly adsorbed particles at the interface.[11-17] As such, parameters including particle size, wettability, and concentration have been used to alter the stability of emulsions and foams.[18-33] With the recent advancements in synthesis and fabrication techniques, particle anisotropy (both in shape and surface properties) has been introduced as another avenue for manipulating the behavior of particles at fluid interfaces. Not only this is a significant step from the standpoint of fundamental science, but is also essential from the practical point of view where in many real applications the particles possess heterogeneities and non-idealities.[34-40] Therefore, due to these deviations, their behavior cannot be fully described by our understanding of homogeneous particles.

In addition to the presence of heterogeneous particles near interfaces, interfacial systems are frequently populated by surface active molecules (or surfactants). Surfactants are molecules that are central to various industrial and technological applications such as emulsions and foams,

drug delivery, coatings, and detergency.[41-43] When present at interfaces, these molecules are responsible for decreasing the excess free energy of the interface. Changes in the excess free energy of the interface are quantified through surface tension (SFT) measurements.[42]

In mixed systems containing both species, depending on the physicochemical characteristics of the colloidal particles and surfactants, and the resulting interactions, they can either compete for populating the interface or act synergistically to achieve enhanced surface properties. An intuitive way of combining the two species is through charge interactions using opposing-charge particle and surfactant systems.[44-49] Fewer studies address interfacial systems composed of like-charged particles and surfactants.[50-53]

Given the ubiquity of particles in colloidal systems and their importance in technological advancement, it is imperative to understand how particle attributes, such as roughness and chemical heterogeneity (i.e., Janus particles) play a key role in governing the self-assembly and the resulting microstructure at fluids interfaces. Additionally, to uncover the physics of more complex interfacial systems composed of both particles and surfactants, it is critical to assess the impact of the surfactant molecules on the resulting interfacial structure and its response under applied stresses.

2.2. Fundamentals of Particles at Fluid Interfaces

2.2.1. Individual Particles at Interfaces

Particles lower the overall interfacial energy by lowering the contact area between two immiscible phases. The equilibrium contact angle (θ_E) of a particle at a fluid interface can be calculated by the minimization of the free energy of the system.[4, 54] For homogeneous particles, this results in the well-known Young's equation as follows:

$$\cos\theta_E = \frac{\gamma_{po} - \gamma_{pw}}{\gamma_{ow}} \quad (2\text{-}1)$$

The factors that determine the interfacial positioning of the particle are thus the fluid/fluid interfacial tension (γ_{ow}) and the surface tension of the particle with both fluid phases (γ_{po} and γ_{pw}).[55-57] Therefore, from a thermodynamic standpoint, particles spontaneously adsorb on a fluid/fluid interface, provided that the surface energy between the two fluids is greater than the difference between the surface energies of the particle with each fluid phase.[58] However, research carried out by Manoharan et al. and others on dynamics of binding has shown that adsorption of particles to a fluid interface can be characterized by a sudden breach, driven by capillary forces, followed by a slow relaxation to equilibrium that appears logarithmic in time.[59, 60] It is proposed that complete equilibration of a particle to the predicted Young's contact angle may take time due to the presence of nanoscale heterogeneities on the particle surface.[61, 62] Once the particles are trapped at a fluid interface, their desorption back into the bulk requires an energy input that goes as:

$$\Delta E = \pi R^2 \gamma_{ow}(1 \pm \cos\theta_E)^2 \quad (2\text{-}2)$$

where R is the radius of the particle. The value of desorption energy is much larger than the thermal energy, e.g. ~$10^7\ k_B T$ (where k_B is the Boltzmann constant) for a 1 μm neutrally wetting ($\theta_E = 90°$) particle trapped at the air-water interface; thus, in contrast to surfactant molecules, the adsorption of colloidal particles to interfaces can be considered as irreversible. It is important to note that thermal energy can still contribute to particle translation at the interface. For non-spherical particles, equating the volume to a spherical shape can be used for the calculation of the detachment energy as shown by Anjali and Basavaraj.[63]

Similar to the derivation of Young's contact angle, the equilibrium position of a Janus particle at a fluid interface can be predicted from the minimization of the free energy of the system with respect to the immersion angle.[64] Because Janus particles carry a dual chemistry — a polar face with a contact angle θ_P and an apolar compartment with a contact angle θ_A — they possess an amphiphilic nature.[65, 66] The degree of amphiphilicity, $\Delta\theta$, for a Janus particle is defined as $\Delta\theta = (\theta_A - \theta_P)/2$. The surface boundary partitioning the polar and apolar faces is indicated by the angle α; values of $\alpha = 0°$ or $\alpha = 180°$correspond to a homogenous particle, whereas $\alpha = 90°$ refers to a Janus particle with two equal-sized patches of different wettability, as depicted in **Figure 2-1a**.[55]

Altering the particle amphiphilicity, through the wettability of each face (θ_P and θ_A), or the location of the Janus boundary, through the value of angle α, will impact the particle configuration at the interface. By assuming that the Janus boundary will align parallel to the plane of the interface, i.e., disregarding the rotational behavior of the particle, the minimization of the free energy yields three possibilities for the equilibrium contact angle (θ_E) of a Janus particle at the interface, schematically shown in **Figure 2-1a-c**, as follows:[64]

$$\theta_P < \theta_A < \alpha, \qquad \theta_E = \theta_A \tag{2-3}$$

$$\theta_P < \alpha < \theta_A, \qquad \theta_E = \alpha \tag{2-4}$$

$$\alpha < \theta_P < \theta_A, \qquad \theta_E = \theta_P \tag{2-5}$$

Therefore, the wettabilities of the two faces determine the equilibrium contact angle of the particle straddling the interface (θ_E), which in turn impacts the magnitude of the particle detachment energy from the interface (ΔE). Similar to homogenous particles, an increase in size of a Janus particle leads to a larger energy of detachment.[67] In contrast with homogeneous particles

that possess an isotropic surface chemistry, the detachment energy of a Janus particle can be further enhanced by increasing the particle's degree of amphiphilicity ($\Delta\theta$), as shown by Binks and coworkers.[56] Analytical calculations illustrated that by switching from a homogeneous particle of neutral wettability ($R = 10$ nm, $\Delta\theta = 0°$, $\theta_E = 90°$) to a highly amphiphilic Janus particle ($\Delta\theta = 90°$), the desorption energy is increased by approximately three-fold.[56] Inspired by the potential of Janus particles at fluid interfaces and the tunability of their behavior, research has boomed in this area with applications spanning from enhanced oil recovery to bi-phasic catalytic reactions.[6, 68-71] However, the rotational behavior of Janus particles cannot be neglected as the particle stability is also influenced by its orientation at the interface.[55, 72-77] Monte Carlo simulations performed by Bon and Cheung illustrated that neglecting the Janus nanoparticle rotation at the interface significantly overestimates the detachment energy and thus the orientational freedom of the particle must be considered.[78] Further studies done by Lee et al. highlighted the impact of the amphiphilicity on the Janus particle orientation at the interface.[63, 72] Gold coated polystyrene Janus particles assumed random orientations at the interface, due to their low amphiphilicity, yielding small energy differences between the cap-up and sideways orientations. In contrast, for thiol-modified Janus particles, a greater energy difference exists between the cap-up and sideways orientations leading to over 90% of particles residing in a configuration where the Janus boundary was aligned with the interface.

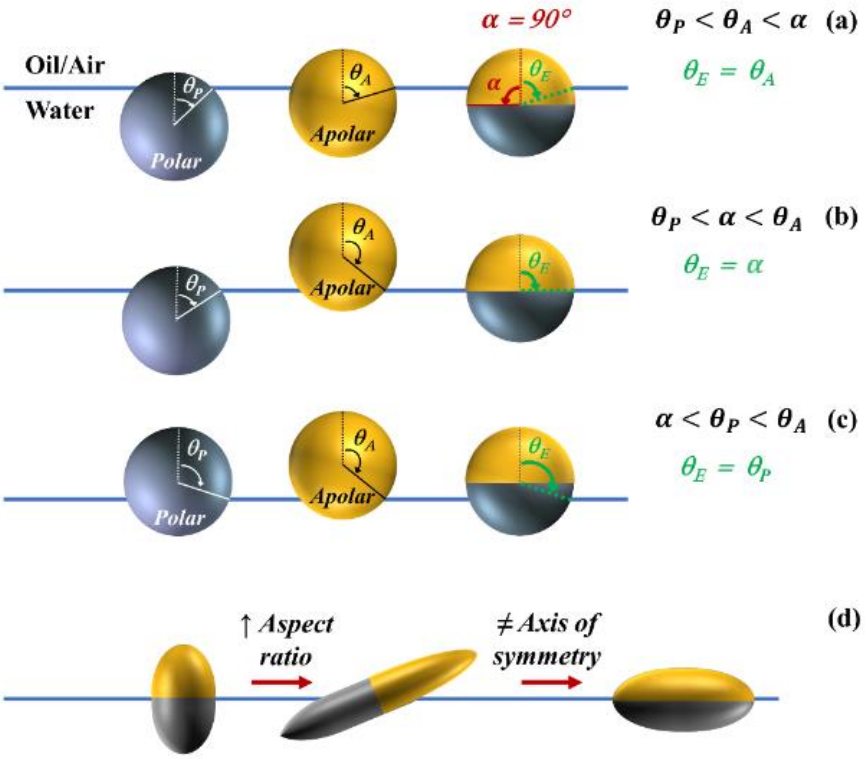

Figure 2-1. Cartoons of equilibrium configurations of a Janus particle residing at a fluid/fluid interface: the equilibrium contact angle (a) equaling the apolar contact angle (Equation (2-3)), (b) coinciding with the Janus boundary (Equation (2-4)), (c) equaling the polar contact angle (Equation (2-5)); (d) the impact of combined shape and surface anisotropy.

2.2.2. Interparticle Interactions at Interfaces

The stability of colloidal particles at fluid interfaces and the microstructure of the resulting interfacial layer is dictated by the type and relative strength of the interparticle interactions that exist in presence of an interface.[79] While the properties of adsorbed particles and fluids making up the interface are the factors determining the interparticle interactions, and consequently the stability of the monolayer, the nature and spectrum of these interactions is an active area of research. Different terms of interparticle interactions considered in the literature can be broadly

classified into attractive and repulsive categories[12], examples of which are illustrated in **Figure 2-2**.

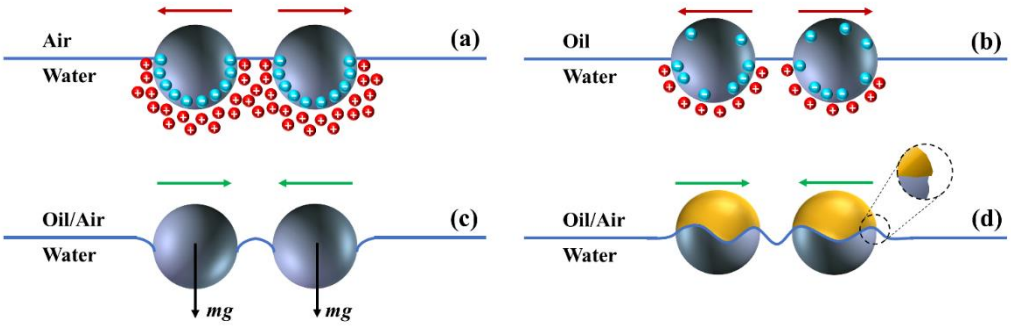

Figure 2-2. Examples of some interparticle interactions that can be present at fluid interfaces. (a) Dissociation of surface groups causing repulsive dipole-dipole interactions; (b) water entrapment on the particle surface in contact with the oil phase causing long-ranged repulsive interactions; (c) gravitational forces deforming the interface generating attractive capillary interactions; (d) interface undulations caused by surface roughness along the Janus boundary resulting in capillary interactions.

The repulsive interaction between charged colloids trapped at a fluid/fluid interface has been attributed to the dissociation of surface charges in the polar medium, which yields an asymmetric screening cloud with respect to the interface plane, shown in **Figure 2-2a.**[80-82] As suggested by Pieranski[57] and validated by experiments[83-85], the effective dipole generated by the particle surface charge and the resulting screening cloud in the polar medium leads to long-range dipole-dipole interaction between particles that scales as $F \sim r^{-4}$ for particle separation distance of r.[80, 86, 87] It has also been suggested that monopoles, originated from the dissociated surface groups in the polar phase and exposed to the non-polar phase, could contribute to the repulsive interparticle interactions as illustrated in **Figure 2-2b**.[85, 88-90]

The attractive dispersion van der Waals (VDW) interactions that originate from the fluctuations of the electron cloud around the atomic nucleus, can be calculated for colloidal particles suspended in a fluid (3D) using the value of the Hamaker constant (A_{131}) for particles interacting through a medium.[91] A similar formalism has been proposed for the calculation of

VDW interactions between interfacially-trapped colloidal particles using the Derjaguin approximation, when the range of interactions is small compared to the particles radius of curvature.[92] It has been assumed that the VDW interactions occur between the immersed parts and the emergent parts of the particle through different fluid media, with different Hamaker constants assigned for interactions through each fluid phase.

The double layer repulsion and the VDW attraction make up the Derjaugin–Landau–Verwey–Overbeek (DLVO) potential, which dominates most aqueous dispersions and accounts for the stability of colloidal particles in bulk (3D). However, the behavior of colloidal particles at an interface (2D) is not fully captured by the DLVO approximation.[93] The retarded VDW forces are short-ranged and typically extend over a range of tens of nanometers for micrometer-sized colloids,[91] while an unexpected long-ranged attraction has been reported for interfacially-trapped particles.[94-97] This strong long-ranged attractive interaction has been attributed to capillary forces, an interfacial phenomena with no analogy in bulk aggregation,[72, 98] which result from the distortions imposed on the interface by the particles,[87, 99-109] as illustrated in **Figure 2-2c**. The interfacial distortions can originate from the weight of particles (gravity-driven capillary attraction for heavier or bigger particles)[110] or electrostatic stresses caused by the particles dipolar field (electrodipping).[107, 111] In addition, surface roughness, chemical inhomogeneity, and shape anisotropy of particles cause the meniscus to take an irregular shape over the particle surface in order to satisfy the correct contact angle at all points along the perimeter, as shown in **Figure 2-2d**.[101, 112-116]

The relative strength of electrostatic repulsions and capillary interactions dictate the assembly behavior of colloidal particles and the resulting microstructure. Hence, by tuning the interactions and switching from a repulsive to attractive potential, clustering and aggregate

formation can be stimulated.[72, 117-119] A plethora of opportunities exists for tuning the colloidal interactions, for instance, through particle wettability, introducing anisotropy, addition of electrolytes, solution pH, and synergism in presence of surfactants.[9, 29, 120, 121] For example, Horozov et al. observed that silica particles of low hydrophobicity ($\theta_E = 65°$ measured through the water phase) form disordered unstable aggregates at the octane/water interface, whereas very hydrophobic particles ($\theta_E = 152°$) result in a highly ordered monolayer. These results were explained in terms of a pair potential composed of contributions from electrostatic repulsion (through both polar and non-polar media) and capillary attraction (due to three-phase contact line undulations) and were attributed to the change in the magnitude of the surface charge density on the particle/octane interface as particle hydrophobicity is increased.[89] Achieving microstructures with a percolated network can then be employed in designing interfaces with a desirable stability.[122] For instance, interfacially-trapped colloidal monolayers of sufficient yield stress are shown to impact gas dissolution from the particle-coated bubbles arresting Ostwald ripening in foams.[24] Similarly, the elastic modulus of a jammed network of colloidal particles at a droplet surface is shown to offset the Laplace stress driving the fusion of droplets resulting in arrested coalescence in emulsions.[123] Recent work on Janus particles as interfacial stabilizers also reports on correlations between dilational viscoelasticity of particle-laden interfaces and foam drainage-half time, where Janus particles exhibited higher elastic modulus and outperformed systems stabilized with homogeneous particles, surfactants, or a foaming agent.[124, 125] As can be seen, rheology plays a key role in performance of interfacial systems; therefore, to unlock the tremendous potential of colloidal particles at interfaces, it is important to gain a fundamental understanding on the link between interparticle interactions, especially in case of heterogeneous particles, and the interfacial rheology of the ensuing microstructure as reviewed in the next section.

2.3. Mixed systems of Particles and Surfactants

In addition to the presence of heterogeneous particles near interfaces, interfacial systems are frequently populated by surface active molecules (or surfactants). Surfactants are molecules that are central to various industrial and technological applications such as emulsion and foam stabilization, drug delivery, coatings, and detergency.[41-43] When present at interfaces, these molecules are responsible for decreasing the excess free energy of the interface. Changes in the excess free energy of the interface are quantified through surface tension (SFT) measurements.[42] The surface activity of surfactant molecules is related to their amphiphilic nature, which is determined by the balance between the hydrophilic head group and the hydrophobic tail contribution, often referred to as the hydrophilic/lipophilic balance (HLB).[42, 126] For example, a head group that possesses a higher polarity is able to compensate for the lack of affinity from a longer hydrocarbon tail when considering water-soluble surfactants.[127]

Colloidal systems combining nanoparticles and surfactants have gained considerable attention in diverse sectors such as consumer care products, drug delivery, paper production, and subsurface energy recovery.[128-131] The use of surfactant/particle mixtures in these applications, with the aim of adjusting the formulation properties, is highly dependent on the interactions occurring between the species present in the system. Interactions between particles can be manipulated by altering a number of factors including the charges on both species, particles surface chemistry, and surfactants HLB.[131-133] For instance, a study by Sharma et al. showed that enhanced oil recovery (EOR) nanofluids exhibit an increased stability and effectiveness when anionic surfactants are added with the negatively-charged hydrophilic silica nanoparticles, which in turn improves recovery by altering the wettability of reservoir rocks, and reducing the interfacial tension and the oil viscosity.[134] Another example is mixed systems with application to the laundry

cycle, where surfactant adsorption to particle surface has been reported to be more toxic to bacteria compared to unmodified silver nanoparticles. The study showed that negatively charged silver nanoparticles display charge reversal when mixed with oppositely charged cationic surfactants. In contrast, an increase in the magnitude of zeta potential was found in the same study when a similarly charged anionic surfactant was added to the negatively charged silver nanoparticles, which was attributed to adsorption of surfactant molecules onto the particles surface.[128] Besides from the performance standpoint in an application of interest, the nature of resulting interactions is of extreme importance from environmental remediation point of view since the nanoparticles can act as surfactant carriers to the environment.[135-137] Hence, it is imperative to gain a comprehensive understanding on the interactions present between species in a mixed surfactant/particle system, considering their widespread usage in technological advancements and their environmental impact.

Fluid interfacial properties can also be impacted by the presence of mixed systems containing both species. Depending on the physicochemical characteristics of the colloidal particles and surfactants, and the resulting interactions, they can compete for populating the interface and/or act synergistically to achieve enhanced surface properties. The majority of studies found in the literature are focused on opposing-charge particle and surfactant systems.[44-49] In these systems, the surfactant adsorption on the particle surface results in a change of the particle wettability, which could potentially improve the particle adsorption. In the work done by Maestro et. al.[45], they show that by using a cationic surfactant (hexadecyltrimethylammonium bromide, or CTAB) to modify their negatively charged silica nanoparticles (hydrodynamic diameter of 15 nm and zeta potential of -30 mV) they could change the amount of particles populating the interface. This led to an order of magnitude increase in the surface shear moduli, from 0.2 N/m (at 8×10^{-5}

M) to 2 N/m (at 5×10^{-4} M). The same trend is shown by Vatanparast et at.,[46] by measuring the dilational dynamics of the CTAB and silica nanoparticles system with a pendant drop geometry. They found that the synergism between CTAB and the negatively charged silica nanoparticles can increase the surface elasticity by a factor of 3 for a CTAB bulk concentration of 0.09 mM upon the addition of 1.5 wt% of nanoparticles.

Fewer studies focused on like-charged species.[50-53] For example, in systems containing both anionic surfactant and negatively charged colloidal silica particles dispersed in the bulk, no particle adsorption to the air-water interface was observed.[51] However, an increase in the surfactant adsorption to the interface was reported in the presence of the particles. This was evidenced by a decrease in the equilibrium interfacial tension of the system upon increase in particle concentration, as well as the decrease on the dynamic surface elasticity in comparison to a pure SDS solution (from 6 mN/m to 2.8 mN/m at 0.01 Hz). The increase in surface activity of anionic surfactants by the presence of negatively charged silica particles was further investigated by Eftekhari et al.[52] The authors conclude that the increase in surface activity is due to a change in ionic strength of the system rather than electrostatic repulsion between the particles and surfactants. Katepalli et al.[138] investigated the response of emulsions stabilized by negatively-charged carbon black particles upon the addition of different kinds of surfactants. They found that even the previously adsorbed particles were expelled from the surface upon addition of the anionic surfactant. They attributed the behavior to the change in the particle wettability caused by the hydrophobic adsorption of the surfactants. On the other hand, a study on negatively charged polystyrene particles directly deposited at the air-water interface showed that the presence of like-charged surfactants in the aqueous sub-phase affects particle interactions at the interface, the resulting microstructure formed by the particles at the interface, and the response of such particle-

laden interface to shear stresses.[53] The authors reported that the presence of SDS in the subphase changes the interfacial structure from a soft glassy state to a transition or hexatic state. In contrast, by adding a non-ionic surfactant (polysorbate 80), the particles arranged in a hexagonal fashion with consequential implications for the complex interfacial shear modulus, which, upon the addition of ~0.8 mM of SDS, decreased close to 2 orders of magnitude compared to the case of surfactant-free system at low salt concentration (40 mM NaCl). Therefore, it is clear that the presence of surfactants on the subphase impacts the surface properties of the particle-laden interface.

2.4. Interfacial Rheology

Interfacial rheology studies the flow behavior of fluid interfaces in order to investigate the response of adsorbed species (e.g. particles, surfactants, polymers, proteins, etc.) subjected to an applied deformation, in form of changing either the area (i.e., dilational rheology) or shape (i.e., shear rheology) of the interface.[139-142] Similar to bulk rheology, the interfacial rheological techniques can be categorized into strain-controlled and stress-controlled instruments.[143] Strain-controlled instruments operate by applying a prescribed strain γ (or strain-rate $\dot{\gamma}$) to the interface and measuring the stress response, σ. The applied strain can be constant in time or change as a function of time. For example, in step-strain measurements used to probe the stress relaxation in the material, a known rapid strain is applied followed by the measurement of the stress response as a function of time. In oscillatory measurements, the interface is subjected to sinusoidal strain of a given frequency and the interfacial stress is monitored.[144-146] The phase shift (δ) between the applied sinusoidal strain and the measured stress (in a strain-controlled rheometer), illustrated in **Figure 2-4a**, can be used to determine the elastic and viscous moduli. Depending on the material, the response may be purely elastic (stress is proportional to the strain, phase angle of $\delta = 0°$), purely viscous (stress is proportional to the strain rate, $\delta = 90°$), or viscoelastic ($0° < \delta < 90°$). The storage modulus provides information on the presence of structure in the sample and describes the energy stored in such structure, whereas the loss modulus characterizes the energy dissipated in the sample and represents the viscous nature of the material.

To measure the response of interfaces to changes in the area, a number of techniques including Langmuir trough (**Figure 2-3a**), pendant drop tensiometer (**Figure 2-3b**), and the capillary wave technique can be used.[139, 147] Langmuir balance is a versatile technique that can be employed to measure the interfacial activity of particles,[147] examine their microstructure at fluid

interfaces,[148, 149] and probe the mechanical response of interfaces subjected to 1D compressions and expansions.[3, 150] This method measures the surface pressure (i.e., the difference between the interfacial tension in presence of surface-active species and that of bare fluid interface) using a Wilhelmy plate attached to a balance and monitors the change in the surface pressure (Π) as the interfacial area (A) is altered. The resulting information is recorded as pressure vs. area isotherms. Analogous to 3D systems, the static compression modulus of the interface (κ_0^s) can be calculated by taking the derivative of surface pressure with respect to interfacial area at a constant temperature as follows:

$$\kappa_0^s = -A\left(\frac{\partial \Pi}{\partial A}\right)_T = -\left(\frac{\partial \Pi}{\partial ln\, A}\right)_T \qquad (2\text{-}6)$$

Pendant drop tensiometry relies on a geometrical fit of the drop shape to the Young-Laplace equation, which balances gravitational forces with surface forces. This instrument is widely used to monitor the interfacial tension as a function of time, which can yield insight on the adsorption and desorption processes of surface-active species onto the interface,[151-154] but can also be adapted to probe the interfacial rheology.[142, 155] The drop (or bubble) is subjected to volume changes, which consequently results in changes of the surface area. The advantage of this technique is that less particles are needed to cover the interface (A ~tens of mm^2 for droplets of ~10 μL) compared to a Langmuir trough (A ~hundreds of cm^2 with volumes ~500 mL).[156] Moreover, instead of uniaxial compression/expansions, the pendant drop technique allows for a more uniform change of the surface area. The capillary wave technique has also been used for dilational interfacial rheology and is discussed in more details elsewhere.[140, 147] For shear interfacial rheology, magnetic needle (**Figure 2-3c**),[157-159] interfacial disk/bicone (**Figure 2-3d**),[160] and double-wall-ring (DWR) (**Figure 2-3e**)[161] geometries can be used to probe the properties of

the interface in response to applied shear deformations.[162] Microrheology is also utilized in sensitive surface shear rheology measurements, where a ferromagnetic micro-probe pinned to a fluid/fluid interface is actively torqued or forced using externally controlled electromagnets (Figure 2-3f).[163, 164] A more detailed discussion on each technique and their limitations can be found elsewhere.[139, 165]

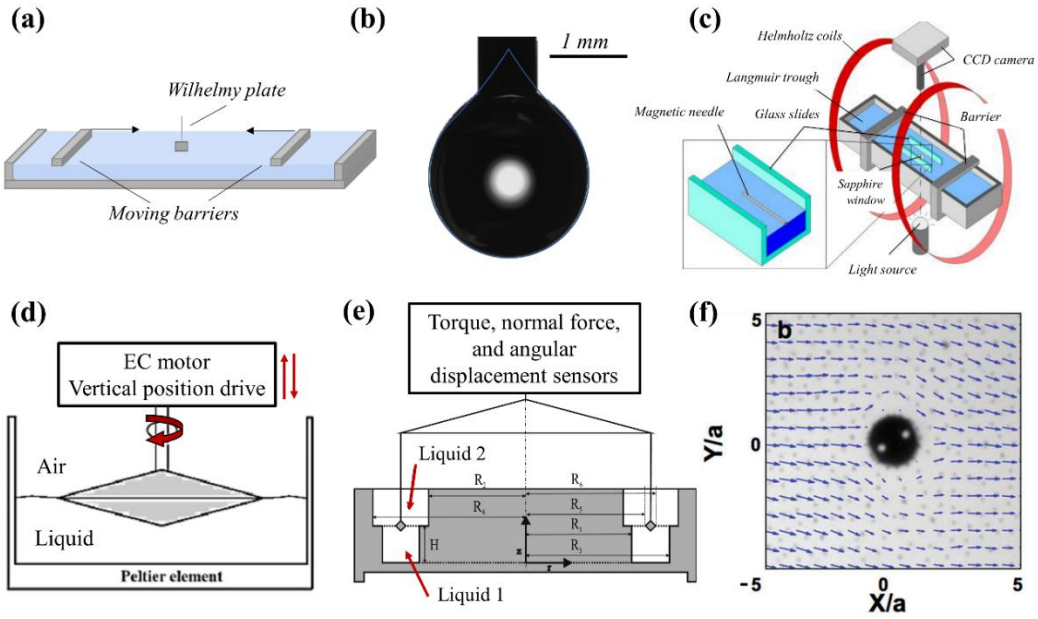

Figure 2-3. Examples of techniques used to perform interfacial rheological measurements. (a) Langmuir Trough – measures the pressure at the interface in response to applied compression and expansion; (b) Pendant Drop – fits the shape of a droplet hanging from a needle in response to expansion and contraction of its volume; (c) Magnetic Needle – measurements of interfacial rheology by shearing the interface with a needle-like probe using an externally applied magnetic field; (d) Bicone – shearing of the interface with a conical shaped probe; (e) Double-walled Ring geometry (R1-R4 define the dimensions of the cup, R5 and R6 indicate the ring dimensions, and H is the distance from the interface to the bottom of the circular channel) – shearing of the interface with a ring; (f) Microrheology – indirect measurements of rheological properties utilizing a microparticle probe pinned at the fluid interface. The radius of the microprobe, a, is 50 μm in this figure. Panel (c) reprinted with permission from ref. [159], copyright 2021 American Chemical Society. Panel (d) reprinted from the open access Ref. [145]. Panel (e) reprinted by permission from [Springer Nature]: [MDPI AG] [Rheologica Acta] Ref. [161] [Copyright 2021]. Panel (f) reprinted with permission from ref. [163], copyright 2021, The Society of Rheology.

In dilational interfacial rheology, the area perturbations can be carried out by either a continuous surface compression at a specified constant rate or oscillatory compression/expansion of the interface. The interfacial area (A) is altered and the resulting change in the surface stress or

surface tension (σ) is measured (as shown in **Figure 2-4a**) and captured in the complex dilational modulus (see Equation (2-7)).[144] The complex dilational modulus (κ^{s*}) can be split into elastic ($\kappa^{s\prime}$) and viscous ($\kappa^{s\prime\prime}$) contributions as follows:

$$\kappa^{s*} = \frac{d\gamma}{dlnA} = \kappa^{s\prime} + i\kappa^{s\prime\prime} \equiv \kappa^{s\prime} + i\omega\eta_d \qquad (2\text{-}7)$$

where ω is the frequency of oscillations and η_d is the surface dilational viscosity.

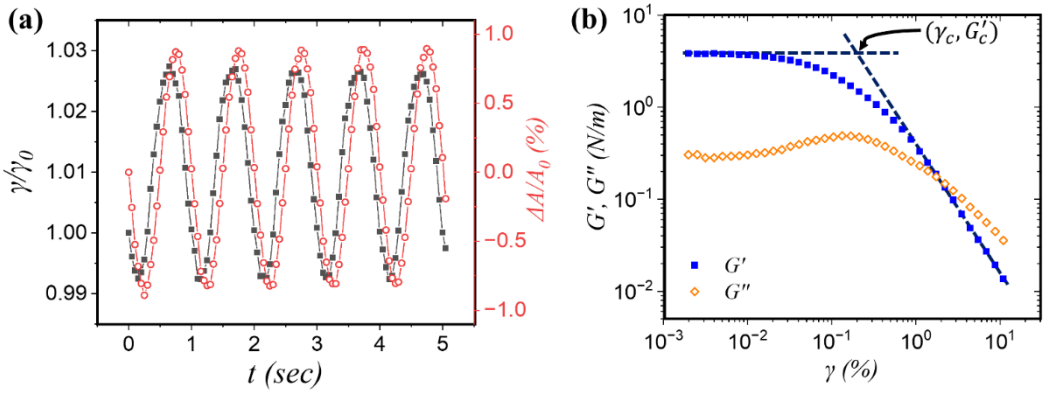

Figure 2-4. Examples of data acquired from interfacial rheology measurements: (a) a bubble suspended in a 2 mM sodium dodecyl sulfate (SDS) surfactant solution and oscillated at 1 Hz. Data depicts the change in surface tension (γ), normalized by the initial surface tension value (γ_0), (solid black symbol) vs. time due to the applied strain (open red symbol) – variations in the surface area (ΔA) normalized by the initial area (A_0). The phase shift (δ) between the two curves is used to calculate the elastic and viscous contributions to the complex modulus (κ^{s*}) as defined in Equation (2-7); (b) data on oscillatory shear rheology measurement performed using a TA Instruments Discovery Hybrid Rheometer-2 (DHR-2) via the DWR geometry (inner cup diameter: 62 mm, inner ring diameter: 69 mm, outer ring diameter: 71 mm, outer cup diameter: 79 mm, ring thickness: 1 mm). Measurements were carried out at 1 Hz on the air-water interface decorated with silica/gold Janus particles. For this dataset, 5 mg of Janus particles were suspended in 200 µL of 70/30 wt% isopropyl alcohol/water mixture that was used as a spreading solvent. After deposition, the interface was left undisturbed for 20 min to allow for the IPA evaporation. The silica/gold Janus particles were fabricated from 1 µm spherical silica particles (Fiber Optic Center, Inc.) half-coated with a 5 nm-thick adhesive layer of titanium followed by a 10 nm gold deposition. The gold face is then modified with dodecanethiol molecules to boost the amphiphilicity of the Janus particle ($\Delta\theta$ ~40°). The solid symbol illustrates the elastic (G') contribution and the open symbol shows the viscous (G'') contribution vs. strain (γ) in a log-log plot. The critical strain (γ_c) and the low-strain plateau elastic modulus (G_c') were obtained using a procedure detailed in Ref.[166] and the yield stress (τ_y) value, calculated using Equation (2-8), was ~0.007 $Pa.m$ for this sample.[167]

Interfacial shear rheology examines the response of interfaces to shear stresses. Similar to the dilational experiments, a complex shear modulus (G^*) can be defined as $G^* = G' + iG''$, where G' and G'' are the storage and loss moduli; respectively, as shown in **Figure 2-4b**.[168] The yield stress, at which viscosity decreases sharply, can be measured and verified by strain amplitude sweep, stress ramp, and creep experiments.[166] In amplitude sweep measurements, as illustrated in **Figure 2-4b**, the critical strain (γ_c) beyond which the interface enters the nonlinear viscoelastic regime is determined by the intersection of the low-strain plateau elastic modulus (G_c') and a power law fit to the data at high strain. From this information, the yield stress (τ_y) can be estimated as:

$$\tau_y = \gamma_c G_c' \tag{2-8}$$

The challenge in designing an interfacial rheometer is the coupling between the flow profile at the interface and that in the surrounding bulk phases.[169] Interfacial rheology experiments are therefore considered more difficult than bulk rheology.[170] To minimize the influence of the bulk phase on the measurements and resulting data, interfacial rheometers rely on the design of geometries that reduce the sub-phase drag contribution relative to that of the surface drag as captured in Boussinesq number (Bo) defined as follows:

$$Bo = \frac{surface\ drag}{subphase\ drag} = \frac{\eta_s}{\eta . a} \tag{2-9}$$

in which η_s is the surface shear viscosity, η is the sub-phase bulk viscosity, and a is a characteristic length scale calculated from the dimensions of the geometry.[169] It should be noted that the Boussinesq number, defined earlier for the interfacial shear rheology, has an analogue for the interfacial dilational stresses relative to the bulk stresses, where the characteristic length is the drop radius in the case of tensiometry.[171, 172] When $Bo \gg 1$, the interfacial stresses dominate, and the surface rheology is captured. This can be accomplished by minimizing the value of a through a

geometry design that maximizes the perimeter of contact between the probe and the interface for a given contact area of the probe with the sub-phase.[169]

Interfacial rheology experiments can be conducted either with particles dispersed in the bulk phase and diffusing to the interface forming a so-called Gibbs monolayer, or deposited directly at the interface, generating a Langmuir monolayer.[173] Factors that need to be considered with the former method are the time required for particles to diffuse to the interface, energetic barriers to adsorption, and the relaxation of the adsorbed particles into their equilibrium configuration.[60, 174] In a diffusion-driven process, it takes ~1 s for a 1 μm colloidal particle suspended in water to diffuse its own radius, whereas for a 10 μm particle the required time increases to 10^3 s. In addition, the stability of particles to sedimentation also needs to be considered. Peclet number (Pe) – the ratio of convective to diffusive transport – is ~ 0.1 for a 1 μm silica particle suspended in water, whereas for a 10 μm particle Pe ~10^3. The diffusion process is followed by the adsorption step, which can be hindered by a repulsion between charges on the particle surface and the interface.[60] There is evidence that even when the charge interaction between the particle and the interface is attractive, adsorption can be hindered by the electrostatic force resulting from an image charge.[12, 174] The image charge effect is not always repulsive, as it has been observed to cause either repulsive or attractive interactions in particle-interface systems depending on the dielectric constant of medium the particle is initially suspended in compared to that of the neighboring phase.[12, 175] Finally, after breaching the interface particles experience a relaxation process towards the equilibrium contact angle, θ_E, which can take up to months, suggesting that experimental time frames may not be capturing the equilibrium state of particles at the interface.[60] The interfacial deposition method relies on the use of a spreading solvent to disperse the colloidal particles at the interface via Marangoni flow. However, the choice of

spreading solvent is shown to impact the contact angle of particles at the interface, thus, different results may be obtained based on the solvent used for this technique.[176, 177] Fernandez et al.[67] studied the role of spreading agent on the interfacial entrapment of particles and concluded that any amount of water in the spreading solvent was not beneficial as the particles would fall through the interface during the deposition process resulting in a reduced entrapment efficacy. The trapping of particles at the interface is therefore an important parameter to consider. It is a common procedure to assume that all particles suspended in the spreading solution will be trapped at the interface upon deposition. This assumption is used to estimate either the area available per particle or the surface concentration of particles in the system under study. However, care must be taken to consider the role of solvent and the particle surface properties on the entrapment efficacy of particles. This is critical when comparing the interfacial behavior for particles of different characteristics. For instance, hydrophilic colloidal silica particles, which are negatively charged at neutral pH due to dissociation of surface silanol groups[178-180], are more likely to fall through the air-water interface upon deposition at the interface given that the interface carries negative charges.[181] The presence of electrolyte in the sub-phase is shown to enhance the entrapment efficacy of particles in this case and the mechanical properties of the resulting interfacial layer.[182, 183] Variation in binding efficacy has also been reported for Janus particles with different degrees of amphiphilicity.[55]

3. Materials and Methods

3.1. Materials

All glassware used in this study was base cleaned by a 1wt% potassium hydroxide solution (KOH, Fischer Scientific) solution in isopropyl alcohol (Fisher Scientific) overnight before its use. DI water (18.2 MΩ.cm) used throughout the study was generated via Milli-Q® IQ 7000 Ultrapure Lab Water System (Millipore Sigma).

3.1.1. Salts, Acid, and Base

For surface measurements with background electrolyte (SDS studies and mixed systems particles with SDS), we utilized 10 mM sodium chloride (NaCl) solutions (Fisher Chemical).

For bulk measurements with background electrolyte (Dynamic Light Scattering and zeta potential studies) potassium nitrate (KNO_3, Fischer Scientific, purity > 95%), nitric acid (HNO_3, Fischer Scientific), and KOH were used as received.

3.1.2. Particles

3.1.2.1. Surface Homogenous Particles

Hydrophilic colloidal silica particles (Fiber Optic Center, nominal diameter of D = 250 nm, calculated specific surface area of 10.5 m^2g^{-1}) were utilized as received or hydrophobically modified with Dimethyldichlorosilane (DMDCS, from Sigma Aldrich). The modification was performed by oven drying 1g of the spherical particles overnight at 60ºC and dispersed in 10mL of cyclohexane. Then 121.7µL of DMDCS was added to the solution (10^{-1} M), which was sonicated in an ultrasonic bath (Fisherbrand™ 11203 Series Advanced Ultrasonic) for 30 minutes. Then, the solution was centrifuged at 7000 rpm for 5 minutes, and the supernatant was removed via vacuum line. Next, an additional 10mL of cyclohexane was added and sonicated again for 30

minutes followed by centrifugation and supernatant removal. This process was then repeated twice with chloroform and anhydrous ethanol, followed by drying the particles in a vacuum desiccator. Hydrophobic Fumed silica particles of low surface area, LSA (125 ± 20 m^2g^{-1}), and medium surface area, MSA (195 ± 20 m^2g^{-1}) from Cabot Corporation were used as received.

Silica nanoparticles with nominal size of 100 nm, 200 nm, and 500 nm (Fiber Optic Center Inc.), were used for bulk measurements of dispersions.

3.1.2.2. Janus Particles

To fabricate the Janus particles (JPs), hydrophilic silica particles (1 μm, Fiber Optic Center) were assembled onto a 2D PVC film by transferring the particles from air-water interface to the air-solid interface using a Langmuir trough.[184] Next, the monolayers were transferred to physical vapor deposition machine (Lesker Nano36 Evaporator, Kurt J Lesker) onto which a thin adhesive layer (5 nm) of titanium was deposited followed by a 10 nm layer of gold. Resulting JPs were labeled as C_0 as no further modification was carried out on the gold cap. To enhance the JP amphiphilicity, gold faces were further modified with butanethiol and octanethiol (Sigma Aldrich) by soaking the slides in 10 mM solution of the thiol in ethanol (Fisher Scientific) overnight. The resulting JPs were labeled as C_4 and C_8, respectively. All particles were removed from the substrate and suspended in ultra-pure Deionized (DI) water via sonication, followed by a filtration using a hydrophilic PC membrane filter (10 μm, Isopore™) to remove large aggregates and gold flakes. After these steps, the dispersions were centrifuged at 3000 rpm for 5 minutes (Legend X1R, Thermo Scientific) followed by the aspiration of the supernatant. The JPs were set to dry under vacuum overnight.

The JP degree of amphiphilicity ($\Delta\theta$) is quantified via the measurement of wettability on each face of the particle. Specifically, the wettability of the silica and gold faces were estimated

by measuring the 3-phase contact angle of water droplets deposited on base-cleaned glass substrates and glass substrates passed through the same gold deposition and surface modification as the particles. The water-drop shape profile obtained in each measurement was fitted and analyzed using a tensiometer, from which the 3-phase contact angle of the polar (θ_P) and apolar (θ_A) faces of the JPs were estimated.

3.1.3. Surfactants

3.1.3.1. Recrystallization

Sodium dodecyl sulfate (SDS) was acquired from Sigma Aldrich (purity >99%). The samples of SDS solutions investigated in this work were used as received (labeled as unpurified throughout the text) or recrystallized to remove the contaminant Lauryl alcohol (LOH). The recrystallization process involves dissolving 25 grams of SDS powder in 100 ml of milliQ ultra-pure water, heating the solution to 30°C, and stirring until SDS molecules are solubilized. The solution is then cooled for 48 h at 5°C. The precipitates are vacuum filtered and resolubilized in 200 ml of ethyl alcohol (Fisher Scientific) with a similar procedure of heating and stirring. The solution is once again refrigerated at 5°C for 24 h and then vacuum filtered and rinsed with ethyl alcohol (Fisher Chemical). The crystals are further dried under vacuum for at least 72 h.

In the absence of electrolyte, the CMC values are measured to be 6.7 mM and 7.5 mM SDS for unpurified and recrystallized SDS solutions, respectively. In 10 mM NaCl solutions, the CMC values are decreased to 3.5 mM and 5.5 mM SDS for unpurified and recrystallized SDS solutions, respectively.

3.1.4. Surfactant/Particle Mixtures

For dynamic light scattering and zeta potential measurements, SDS and KNO_3 solutions were prepared separately and then mixed to achieve the final desired concentrations of SDS (i.e.,

0.01, 0.1, 0.5, 1, 4, 12, 15 mM) and KNO_3 (0.01, 0.1, 1, 10, 100 mM). Thereafter, silica nanoparticles were incorporated to the mixture at a final concentration of 0.005 wt%. The mixture was sonicated for 20 mins prior to any measurements. For the pH titrations, controlled amounts of HNO_3 and KOH solutions, at 1 mM and 100 mM, were added to the dispersion in order to vary the concentration of H^+ and OH^- ions. For pH sweep runs in the range of 2-10, the pH of the prepared dispersion was first increased to ~10, via KOH addition, followed by its gradual decrease to 2 using HNO_3. SDS concentrations of 0, 4, and 12 mM were used in the pH sweep studies.

3.2. Methods

3.2.1. Contact Angle Measurements

As a means of estimating the wettability of particles used in systems of interest in this thesis, we measured the contact angle of a water droplet on glass slides similarly treated to the particles. At least 20 droplets of 5 µL in volume were used to measure the contact angle on each slide using a drop shape tensiometer (Biolin Scientific).

For contact angle measurements on particle coated slides, monolayers were deposited by convective assembly technique, which consists of dispersing the particles (either spherical or fumed particles) in ethanol and spreading the dispersion over a glass slide using a syringe pump. Dispersions of 30wt%, 5wt% and, 3wt% were used for the spherical, LSA and MSA particles respectively.

3.2.2. Scanning Electron Microscopy

3.2.2.1. Homogeneous Particles

The diameter (D_{SEM}, or $2R$) of silica particles were measured via a scanning electron microscope (SEM, Thermo Quattro S field-emission). Fumed silica particles were also imaged.

3.2.2.2. Janus Particles

To evaluate the orientation distribution of the JPs residing the air-water interface, deposition of interfacially trapped particles on a silicon wafer was carried out following an earlier work.[185] Briefly, a silicon wafer was placed at the bottom of the trough at the beginning of the experiment. After the particles were spread at the interface, a 30 min wait period was allowed for the evaporation of the spreading solvent. Next, the monolayer was compressed until a surface pressure of 5 mN/m was reached. The JP network was then transferred from the air-water interface to the silicon wafer substrate by gently aspirating the water from the side of the trough outside the barriers and lowering the interfacial plane until the particle monolayer came in contact with the silicon wafer. The deposited particles were then imaged via the environmental Scanning Electron Microscope (Thermo Quattro S field-emission SEM) equipped with a backscatter detector, which exhibits different brightness for materials of different density.

The distribution of particle orientations was obtained by analyzing ~50,000 particles, for each amphiphilicity studied, using the HEXI software via brightness thresholding of the particles.[186] Particles that showed up brighter in the SEM images (i.e., in contact with the air-phase) were counted as Janus cap up and those dimer were counted as Janus cap down (i.e., facing towards the water subphase). To differentiate the tilted particles, we used the standard deviation of the pixel brightness in each particle as the criterion, since a wider spread in the brightness population is expected for a tilted particle compared to vertically aligned particles. More details on the particle thresholding can be found in the Supplementary Information (**Figure B0-2**). Once the orientation (δ) of all particles is determined, one can calculate a 2D-alignment factor $S = \langle \frac{3cos^2\delta - 1}{2} \rangle$ as a means of quantifying the overall orientation of the JP cap in the particle monolayers formed by different amphiphilicities.[187] To calculate a 2D alignment factor (S), the

value of particle tilt angle (δ) was simply assumed to be 0°, 90°, and 180° for cap up, tilted, and cap down Janus particles, respectively. Therefore, a monolayer populated only by vertically aligned particles (cap up and cap down) corresponds to $S = 1$, whereas for a monolayer comprised of particles in sideways configuration the 2D alignment factor is $S = -0.5$.

3.2.3. Dynamic Light Scattering and Zeta Potential Measurements

3.2.3.1. Particle Dispersions

Hydrodynamic size (D_H) and mobility (μ) measurements were carried out using a dynamic light scattering instrument (DLS, Nanobrook Omni, Brookhaven Instruments). *Pe* number informs about the ratio of diffusive to convective time scales and can be useful in determining the applicability of DLS for characterizing the particle dispersions. It is determined as per the formula: $Pe = \frac{\frac{4}{3}\pi\Delta\rho g R^4}{k_B T}$, where $\Delta\rho$ is the difference in density between the particle and the solvent, g is acceleration due to gravity, R is particle radius, k_B is the Boltzmann's constant and T is the temperature.

3.2.3.2. Analysis of Particle Zeta Potential and Surface Charge Density

The conductance values, measured and reported by the DLS instrument for SDS and silica nanoparticles, were utilized to determine the effective ionic concentration (c_{eff}, mol/L) as follows:

$$c_{eff} = \sum c_i = \sum \frac{\sigma_i}{\Lambda_i^0} \qquad (3\text{-}1)$$

where σ_i is the conductance associated with the ion *i*, and Λ_i^0 is the molar ionic conductivity of the ion *i*, values of which are provided in **Table 3-1** for the species present in the system under study. To calculate the ionic concentration of a sample, it was assumed that the molar ionic conductivities of different ions in the solution were additive.[188, 189] The conductivity of the initial sample (σ_0) was

taken as a reference, with its effective ionic concentration, c_{eff_0}, calculated based on the molar ionic conductivity of salt ions present as follows, $c_{eff_0} = \sigma_0/(\Lambda^0_{K+} + \Lambda^0_{NO3-})$. Then, the analysis was carried out using the conductance reading of the solution before (σ_{before}) the addition of more ions (e.g., those resulting from addition and dissociation of KOH, HNO_3, SDS), comparing it to the new conductance reading (σ_{after}), and attributing the change in the conductance value ($\Delta\sigma = \sigma_{after} - \sigma_{before}$) to the newly added ions, which in turn led to a change in the ionic strength. For instance, in a pH titration with KOH, $\Delta c = \Delta\sigma/(\Lambda^0_{K+} + \Lambda^0_{OH-})$. The resulting concentration can be calculated as $c_{eff,after} = c_{eff,before} + \Delta c$.

The calculated ionic concentration of the solution was then used in the determination of the Debye length (κ^{-1}) as follows:

$$\kappa^2 = \frac{2C_{eff}(ze)^2}{\varepsilon_0 \varepsilon k_B T} \qquad (3\text{-}2)$$

where z is the valence of the ions and is equal to 1 in this study, e is the electron charge, ε_0 is the permittivity of vacuum, ε is the permittivity of water. The magnitude of κR was then calculated to determine the relative thickness of the Debye layer with regards to the particle size, with a diameter $2R$, as estimated from the SEM images. Thereafter, the value of κR was utilized to calculate Henry's function in each case as follows: [190]

$$f(\kappa R) = \frac{16 + 18\kappa R + 3(\kappa R)^2}{16 + 18\kappa R + 2(\kappa R)^2} \qquad (3\text{-}3)$$

Next, the zeta potential (ζ) was calculated from the measured mobility values as follows:

$$\mu = \frac{2\varepsilon_0 \varepsilon \zeta}{3\eta} f(\kappa R) \quad (3\text{-}4)$$

where μ is the mobility [(μ/s)/(V/cm)] and η is the viscosity of water (Pa.s). Thereafter, the particle surface charge density (ρ_s, μC/cm^2) was determined using the following relation, which does not assume any approximations for the Debye-layer thickness:

$$\rho_s = \varepsilon_0 \varepsilon \kappa \Psi_0 [\frac{1 + \kappa R}{\kappa R}] \quad (3\text{-}5)$$

and the surface potential (Ψ_0) was approximated by the value of the measured zeta potential (ζ) to avoid arbitrary assumptions on the thickness of the slip plane.[191-193] It is important to note that to determine the surface potential experimentally, titrating the particle dispersion with a known amount of ions is required.[191]

Table 3-1. Molar ionic conductivity (Λ_i^0) of the ions present in the system under study.[189, 194]

Ion	$\boldsymbol{\Lambda_i^0}$ **(cm^2.s/mol)**
H^+	349
OH^-	198
K^+	73.5
NO_3^-	71.5
DS^-	23.4
Na^+	50.1

3.2.3.3. Model for the Particle Zeta Potential at Various pH Values

The zeta potential of colloidal particles at various pH values can be predicted based on the following implicit equation derived from the Gouy-Chapman formulation:[195]

$$\frac{-eN_A}{1 + 10^{(pKa-pH)} \exp\left(-\frac{e\zeta}{k_B T}\right)} = \frac{2\varepsilon_0 \varepsilon k_B T \kappa}{e} \sinh\left(\frac{e\zeta}{2k_B T}\right) \qquad (3\text{-}6)$$

where N_A is the number density of acid sites, which is determined based on the estimated surface charge density (ρ_s), and pKa is the acid strength. The provided equation assumes that only acid groups are present on the surface. In order to determine the appropriate value for the number charge density, the region where the zeta potential remains nearly constant with pH alterations, (in the current study pH range of 5 to 7), was taken as a reference. Right and left side of the equations were solved independently, and their difference was minimized by varying the guessed value for ζ.

3.2.4. Surface Pressure/Tension Measurements

3.2.4.1. Langmuir Trough

A NIMA Langmuir trough (Biolin Scientific) was filled with 160 mL of DI water and the trough area was set at 150 cm^2, i.e., the open barrier state, in all experiments. To ensure the absence of impurities at the air-water interface, the trough was closed to 25 cm^2 and the change in the surface pressure (Π), defined as the difference between the air-water surface tension (σ_0) and the effective surface tension in presence of particles (σ_{eff}) was monitored. If the surface pressure remained negligible (Π < 0.3 mN/m), the experiment proceeded. The spreading solution was deposited at the interface in a dropwise fashion using a 50 μL syringe (Hamilton) where the particles spread at the interface via the action of Marangoni flows. A 30 min wait period was considered to allow for the solvent evaporation before proceeding with the measurements. The trough area (A) was compressed at 10 mm/min and the surface pressure $\Pi(A)$ was monitored via a Wilhelmy plate. The compression was followed by an expansion of the interfacial area at the same rate to probe the hysteresis of the JP interfacial network. All monolayers were subjected to

3 cycles of compression and expansion. In conjunction with the compression-expansion cycles, an inverted microscope (IX73 Olympus) was utilized to simultaneously capture the microstructure formed by the particles at the air-water interface, using a 20x objective (6.6-7.8 WD, 0.45 NA), and through a custom-designed window machined in the center of the trough (**Figure 3-1a**).

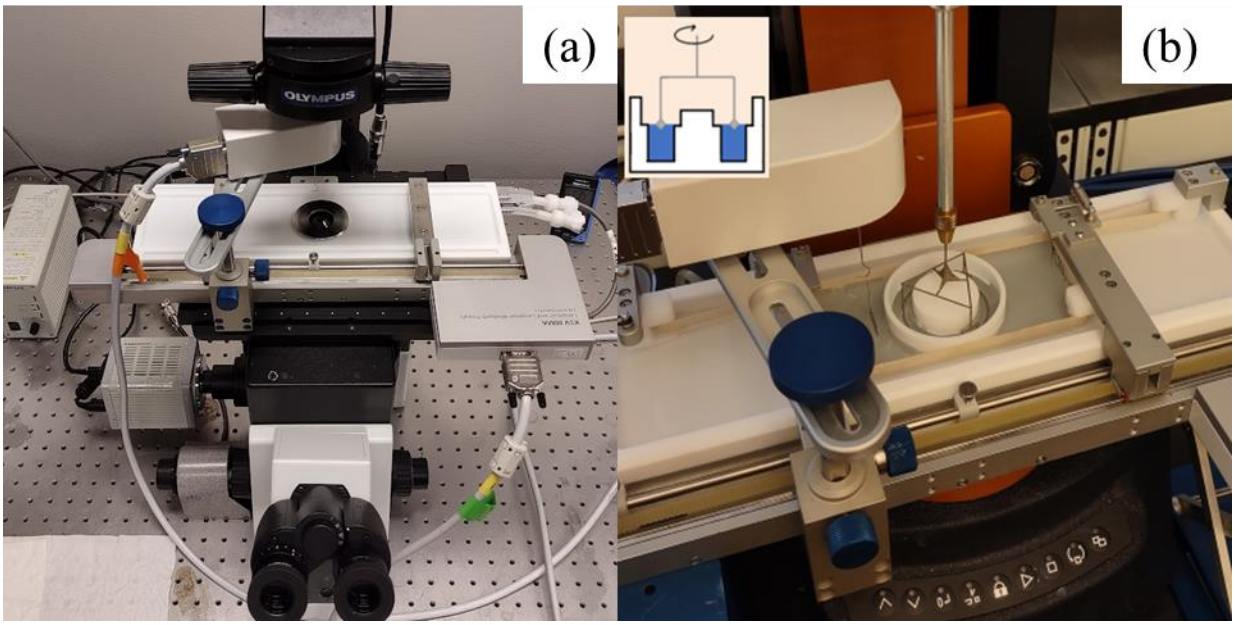

Figure 3-1. Langmuir trough couples with (a) an inverted microscope for microstructure visualization; and (b) a shear rheometer for interfacial shear rheology measurements. Inset on (b) showing the schematics of the system, where the diamond shaped ring sits at the interface.

3.2.4.1.1. Homogeneous Particle Systems

For a quantitative hysteresis analysis, the difference between the areas under the compression and expansion curves were evaluated (Π). This can be understood as calculating the work that is "recovered" from the system after the completion of the cycle. In addition, since after the first cycle the monolayer might lose enough particles to not undergo collapse on the subsequent cycles, we define a normalized hysteresis parameter ($\overline{\Pi}$) as follows:

$$\overline{\Pi} = \frac{\Pi}{\Delta\Pi\Delta A} = \frac{\left(\int_{A_{open}}^{A_{close}} \Pi\, dA\right)_{Compression} - \left(\int_{A_{open}}^{A_{close}} \Pi\, dA\right)_{Expansion}}{\Delta\Pi\Delta A} \quad (3\text{-}7)$$

3.2.4.1.2. Janus Particle Systems

To examine whether the use of a spreading solvent in the deposition of particles at the interface, and the associated Marangoni flows, result in ordered crystalline domains, we applied the procedure provided by Juarez et al. to the captured SEM images to determine the ensemble average of the order parameter C_6. In short, C_6 represents the number of hexagonal close packed neighbors around each particle. By averaging over all particles, we estimate $\langle C_6 \rangle$, which equals 0 for disordered fluid configurations and 6 for an infinite plane of hexagonal close packed particles.[196] The equations associated with $\langle C_6 \rangle$ are described in Appendix B.

3.2.4.2. Drop Shape Tensiometer

The surface tension measurements for contaminated and recrystallized SDS were carried out in the drop shape tensiometer (Biolin Scientific), using a rising air bubble (RB) suspended in the SDS solutions. The Attension® Theta software fits the shape of the bubble to the Young-Laplace equation, which balances surface tension and gravitational forces. As it takes more time for surface tension equilibration,[197] the RB method can be used to probe the dynamic surface tension of a contaminated SDS solution by allowing the bubble age in the solution, while monitoring its shape.

3.2.4.3. Wilhelmy Plate Tensiometer

The surface tension measurements for contaminated and recrystallized SDS solutions were also carried out using Wilhelmy plate (WP) technique. The Wilhelmy plate (DCAT 25 from DataPhysics) was used to measure the surface tension isotherms of solutions with different purity

levels and with no added salt and in 10 mM NaCl solutions. In WP method, a platinum plate hanging from a high precision balance is lowered until it contacts the air/solution surface. The change in the measured force when the plate contacts the water surface is used to calculate the surface tension acting on the plate.

The CMC values for unpurified and recrystallized samples were obtained by carrying out surface tension measurements on solutions at various surfactant concentrations and plotting the SFT readings as a function of the log of surfactant concentration following the procedure described elsewhere[198]. Briefly, it consisted of finding the intersection of the trendlines before and after reaching the CMC.

3.2.5. Thermodynamic Modeling of monolayers

3.2.5.1. Particles-only

To estimate the overall interparticle interactions experienced by the particles within the network, and the resulting surface pressures, a surface equation of state was used to interpret the surface pressure isotherms.[199] As shown by Fainerman et al., the surface pressure of a micron-sized particle monolayer can be related to the particle surface coverage and interparticle interaction parameter via the following equation:

$$-\frac{\Pi\omega_0}{kT} = \ln(1-\theta) + \theta\left(1-\frac{\omega_0}{\omega}\right) + a\theta^2 \qquad (3\text{-}8)$$

where ω_0 is the molecular area of the solvent, ω is the fluid/fluid interfacial area occupied per particle, and θ is the particle surface coverage. Therefore, using the information on the total area occupied by the particles at any time, one can calculate θ. We estimated the total area occupied by particles assuming an arbitrary value for the surface coverage at the inflection point (θ_{IP}) of the isotherm. The Frumkin interaction parameter (a) captures the nonideality (i.e., positive for

attractive and negative for repulsive interactions), and is related to the enthalpic contribution to the interactions.[199] We assumed that the $\frac{\omega_0}{\omega}$ ratio goes to 0 since $\omega \gg \omega_0$, and used both a and θ_{IP} as fitting parameters, to estimate the limiting surface coverage and interaction parameter that best represents the surface pressure data obtained for the studied monolayers. From the maximum surface coverage (i.e., θ_{IP}) that best fits the experimental data, the area occupied by the particles at the inflection point of the isotherm can be estimated. From the total area occupied by particles, we can calculate the number of particles trapped at the surface. Next, the binding efficacy of the particles can be estimated by dividing the total number of particles trapped at the interface by the total number of particles deposited at the interface from the spreading solution.

3.2.5.2. Surfactants

We utilized three thermodynamic models for the fitting of the surfactant adsorption isotherms: the Frumkin model, the van der Waals model, and a model developed by Kralchesvsky et al.[200] The latter builds on the van der Waals adsorption model to include the electrostatic contribution to the free energy of the system. The surface tension isotherms experimentally obtained for the SDS samples, via the WP technique, were used as an input to each adsorption model. For the sake of simplicity, we show the adsorption isotherm equations for a one-component system. The reader can find the equations derived for a two-component system, here applied to mixed interfacial layers of SDS and dodecanol, in the Appendix A.

The Frumkin isotherm model assumes a localized adsorption as follows:[201]

$$Kc = \frac{\omega\Gamma}{1 - \omega\Gamma}\exp\left(-\frac{2\beta\Gamma}{k_B T}\right) \tag{3-9}$$

or

$$Kc = \frac{\theta}{1 - \theta} \exp(-2\alpha\theta) \quad (3\text{-}10)$$

where K is the adsorption constant, k_B is the Boltzmann constant, T is the absolute temperature, c is the bulk surfactant concentration, Γ is the surfactant adsorption at the interface, and ω is the minimum molecular area at the interface. Parameter β is the interaction parameter, usually attributed to the tail-tail van der Waals interactions.[200] Parameter α is the dimensionless interaction parameter, $\alpha = \frac{\beta}{\omega k_B T}$, and $\theta = \omega\Gamma$ is the surface coverage for the surfactant adsorbed to the surface. The equation of state can then be written for one-component systems as follows:

$$\Pi = -\frac{k_B T}{\omega_0} \ln(1 - \omega\Gamma) - \beta\Gamma^2 \quad (3\text{-}11)$$

or

$$\Pi = -\frac{k_B T}{\omega_0} [\ln(1 - \theta) + \alpha\theta^2] \quad (3\text{-}12)$$

where Π is the surface pressure, defined as the air-water surface tension minus the surface tension in presence of the surfactant molecules ($\Pi = \sigma_0 - \sigma$). The excluded molar area has been shown to be dependent on the surface pressure of the system by the following expression:[201-203]

$$\omega = \omega_0 (1 - \epsilon\Pi\theta) \quad (3\text{-}13)$$

where ω_0 is the excluded area at zero surface pressure and ϵ is the intrinsic compressibility coefficient, which can be interpreted as the change in the tilt angle of the molecule tail upon an increase in the surface pressure or surface compression.[202]

The van der Waals adsorption model is similar to the Frumkin model, but assumes a non-localized adsorption.[204] The equations can be written as follows:

$$Kc = \frac{\omega\Gamma}{1 - \omega\Gamma}\exp\left(\frac{\omega\Gamma}{1 - \omega\Gamma} - \frac{2\beta\Gamma}{k_B T}\right) \quad (3\text{-}14)$$

or

$$Kc = \frac{\theta}{1 - \theta}\exp\left(\frac{\theta}{1 - \theta} - 2\alpha\theta\right) \quad (3\text{-}15)$$

$$\Pi = \frac{k_B T\Gamma}{1 - \omega\Gamma} - \beta\Gamma^2 \quad (3\text{-}16)$$

or

$$\Pi = \frac{k_B T}{\omega_0}\left[\frac{\theta}{(1-\theta)} - \alpha\theta^2\right] \quad (3\text{-}17)$$

where the notation used in Eq. (3-9)-(3-13) applies here. To model the experimentally measured isotherms for SDS solutions, the adsorption constant (K), the interaction parameters (α or β), the excluded area at zero surface pressure (ω_0), and the compressibility coefficient (ϵ) of each individual species must be known. For two-component surfactant systems, one must also consider the intermolecular parameters (ω_{12} and α_{12}). By varying the initial guess on the amount of contaminant in the bulk, one can find the LOH concentration that gives the best fit to the measured surface tension isotherm. For both unpurified and recrystallized isotherms, one can vary the initial guess for the molar fraction of dodecanol (a.k.a. LOH) and solve the two-component equations (provided in the Appendix A) by changing the surface coverages (θ_1 and θ_2) until the sum of squared differences between each experimental point and the value calculated by the adsorption model is minimized.

The Kralchesvsky model utilizes Eq. (3-14)-(3-17) and solves for the free energy of the surface accounting for electrostatic interactions present in the system with the Gouy equation.[205,

[206] By taking advantage of the pre-determined values for α and ω for each surfactant, Kralchesvsky et al. were able to develop an algorithm with only the molar fraction of LOH as an adjustable parameter.[200] Briefly, the intermolecular parameters (α_{12} and ω_{12}) were first calculated (see Appendix A). Next, a guess was made for the molar fraction value of LOH, followed by guesses on the surface adsorption concentrations Γ_1 and Γ_2. The adsorption isotherm was solved for the LOH adsorption to determine the optimum values of Γ_2 for the given values of Γ_1. Next, the dimensionless surface potential was calculated based on the Gouy equation to implicitly solve for Γ_1. Finally, the surface tension was calculated from the obtained variables and compared to the experimental data. By changing the molar fraction of LOH one can find the best fit for the measured surface tension isotherm. After its determination, the molar fraction of dodecanol can be used to quantify important parameters of the surface, such as adsorption quantities, surface potential, and the Gibbs elasticity. The authors used previous data from Reference [207] to validate their model.

3.2.5.2.1. Estimation of Depletion Effects on Surfactant Mixtures

The depletion effects were calculated based on the work done by Alvarez et al.,[197] which describes how the depleted bulk concentration is a function of the area available for adsorption (A), the volume of the solution (V), the bulk concentration of surfactants (c_i), their surface adsorption at the maximum packing arrangement (Γ_∞), and their adsorption constant (K). By applying Eq. (3-18), one can calculate the effective depleted concentration of a surfactant species (c_{eff}) as follows:

$$\frac{c_{eff}}{c_i} = \frac{1}{2}\left(1 - \vartheta - \frac{\vartheta}{f}\right) + \frac{1}{2}\sqrt{\left(1 - \vartheta - \frac{\vartheta}{f}\right)^2 + 4\frac{\vartheta}{f}} \qquad (3\text{-}18)$$

where $f = \frac{\Gamma_\infty A}{KV}$ is the ratio of the minimum bulk concentration needed to populate the interface at maximum packing to the adsorption constant K, and $\vartheta = \frac{\Gamma_\infty A}{c_i V}$ is the maximum fractional potential mass lost to the interface.

The time necessary for equilibration is dependent mostly on the depletion depth (h_p) associated with the adsorption. For a planar surface adjacent to a semi-infinite surfactant solution, h_p can be defined as follows:

$$h_p = \frac{\Gamma}{C_\infty} \qquad (3\text{-}19)$$

The timescale for diffusion in this system is then given by $\tau_D = \frac{h^2}{D}$, where D is the bulk diffusion constant of a surfactant molecule in the solvent, and $h = h_p$ for the planar case. This is a good approximation for methods like the Wilhelmy plate. However, for surfaces with an associated curvature, h must be corrected to account for the deviation from a planar geometry (see Appendix A). A more in depth discussion can be found in elsewhere.[197] The beforementioned equations (Eq. (3-18) and (3-19)) were used to estimate time scales and appropriate geometries for our experiments in order to maximize the impact from LOH molecules.

3.2.5.3. Particles and Surfactants

Analogous to the previous model, to include surfactant contributions to the surface pressure isotherm we can use an equation of state,[208] as follows:

$$\Pi = -\frac{kT}{\omega_0}[\ln(1-\theta_P-\theta_S)+\theta_P+\theta_S(1-\ \omega_0/\omega_S)+a_S\theta_S^2 + a_P\theta_P^2] \quad (3\text{-}20)$$

where θ_P (θ_S) is the particle (surfactant) surface coverage, ω_S is the surfactant molecular area, a_P (a_S) is the particle (surfactant) interaction parameter. Note that Eq. (3-20) is the combination of equations (3-12) and (3-8). Since the parameters related to the surfactants can be determined from their surface tension isotherms at a given concentration, the only fitting parameters are the $\theta_P(A_{IP})$ and a_P, similar to the previous scenario.

3.2.6. Surface Rheology Measurements

3.2.6.1. Dilational Rheology for SDS Solutions

The interfacial rheology of rising air bubbles suspended in SDS solutions (unpurified, recrystallized, and aged recrystallized) were measured using the Attension® Theta optical tensiometer (Biolin Scientific). For unpurified and recrystallized samples, the rheology measurements were performed in a concentration range of 1 to 10 mM SDS, with both no NaCl and 10 mM NaCl. For the aged, recrystallized samples, measurements were done only at 5 mM SDS concentration. The surface rheology was probed using rising bubbles (~6 µL) generated on an inverted needle (Biolin Scientific, outer diameter of 2 mm). The concentration of SDS was varied by incrementally increasing the bulk surfactant concentration for the same bubble under study. The amount of solution required to increase the concentration of the solution by 1 mM was added using an automatic pipette (Eppendorf, 20 µl) in 10-step increments, separated by 2-min intervals, to avoid large perturbations to the system. Once the desired bulk concentration was reached, the bubble was aged until the surface tension reading was stable. The bubble volume was then oscillated at a small amplitude, corresponding to small oscillations in the surface area within

the linear viscoelastic regime (area variation of less than 3%), and at a frequency of 1 Hz, which is within the reliable frequency limit for the oscillating bubble tensiometry.[209]

3.2.6.2. Shear Rheology for Particle-only and Mixed Particles and Surfactants Monolayers

A stress-controlled rheometer (DHR2) equipped with the Double Wall Ring (DWR) geometry, mounted inside a Langmuir ribbon trough (L×W = 364×75 mm^2), was used to generate the particle-laden interfaces and examine their response to shear at different states of compression (see **Figure 3-1b**). The surface pressure was measured by a platinum Wilhelmy plate placed parallel to the barriers. The custom design of the jig for the rheometer, to accommodate the integrated trough/DWR setup, and the 3D printed DWR geometry followed the pioneering work of Vermant and coworkers.[161] The DWR used in this study is a two-dimensional double-Couette fixture (cup) with 39 mm inner diameter, 60 mm outer diameter, and the dimensions of the ring are 47 mm inside diameter and 49 mm outside diameter. The instrument was calibrated in precision mode 4 times to reach a higher sensitivity. The Boussinesq number (*Bq*) is commonly used to evaluate the balance between surface and subsurface drag.[210, 211] To ensure that the subsurface drag is not impacting the generated data, one has to use a geometry that maximizes the contact with the surface minimizing the effect on bulk flow ($Bq > 1$). The DWR geometry used in the current study along with the measured surface viscosities yielded $Bq > 10$ in all cases. Experimental results were analyzed and plotted with the "Interactive Rheology Information System" (IRIS) as outlined in a recent review.[212]

After preparing the particle monolayer at the air-water interface on the trough in the open-state (i.e., total surface area of 150 cm^2), the double wall ring (DWR) was slowly lowered to contact the interface via capillary action. The axial load on the ring was carefully monitored while lowering it towards the interface; a sudden increase in the measured force indicated the onset of

contact between DWR and interface. Once the initial contact was made, the ring (1 mm thick) was lowered for an additional 500 μm so that the DWR was centered at the interface. The integrated trough/DWR setup enabled us to achieve specific surface pressure values and carry out rheological measurements on particle networks at different surface coverages. The monolayer was compressed at a rate of 25 cm^2/min until reaching a desired surface pressure. The particles were then allowed to relax and reorganize until the surface pressure stabilized (~10 mins) prior to carrying out the rheological experiments. Strain amplitude sweep and small amplitude oscillatory shear (SAOS) measurements were carried out using this integrated setup to characterize the JP monolayer. The operating windows for the oscillatory measurements that lead to valid reproducible results are calculated following the work of Ewoldt and coworkers.[165] These ranges are color coded in the reported figures. In brief, the data falling in the green range represents an acceptable data set, the data falling in the yellow region represents probably acceptable data, and the rest, falling in the orange region needs to be handled with care.

3.2.7. Rheological Modeling

3.2.7.1. Dilational Rheology of Contaminated SDS solutions

To model the surface dilational rheology, we based our calculations on the work done by Aksenenko et al.[213] The dilational surface viscoelastic modulus (κ^{s*}) can be defined as follows:[214]

$$\kappa^{s*}(i\Omega) = \frac{d\gamma}{d(ln\ A)} e^{i\delta} \qquad (3\text{-}21)$$

where γ is the surface tension, A is the available interfacial area, Ω is the angular frequency of oscillations, and δ is the phase shift of the surface tension oscillations in response to the applied oscillations in the available surface area. The surface complex viscoelastic modulus can be further divided into real ($\kappa^{s\prime}$) and imaginary ($\kappa^{s\prime\prime}$) parts, which correspond to the elastic and viscous

contributions, respectively. Assuming that a diffusion-controlled exchange of surfactant molecules between the adsorption layer and adjacent bulk solution is the governing relaxation process in the system, the resulting surface rheology of a one-component solution is as follows:[215, 216]

$$\kappa^{s*}(i\Omega) = \frac{\kappa_0^s\left(\frac{d\Gamma}{dc}\sqrt{\frac{i\Omega}{D}}\right)}{\left(1+\frac{d\Gamma}{dc}\sqrt{\frac{i\Omega}{D}}\right)} = \kappa_0^s\,\frac{1+\zeta+i\zeta}{1+2\zeta+2\zeta^2} \tag{3-22}$$

$$\kappa_0^s = \frac{d\Pi}{d(\ln\Gamma)} = -\frac{d\gamma_{eq}}{d(\ln\Gamma)} \tag{3-23}$$

$$\zeta = \left(\frac{\Omega_D}{\Omega}\right)^{1/2} \tag{3-24}$$

$$\Omega_D = \frac{D}{2}\left(\frac{dc}{d\Gamma}\right)^2 \tag{3-25}$$

where E_0 is the Gibbs elasticity (i.e., the limiting elasticity at low frequencies), γ_{eq} is the equilibrium surface tension as a function of the surfactant adsorption (Γ), ζ is the dimensionless ratio between the time scale of the experiment and that of the diffusion process, Ω_D is the characteristic diffusion frequency, and D is the surfactant's bulk diffusivity. A description of the equations used for the two-component mixture is provided in the Appendix A. A more in-depth discussion on the surface rheology of surfactant systems can be found elsewhere.[217]

Using the relationship between Γ and c, obtained from the fitting of SFT isotherms to thermodynamic adsorption models, one can apply the surface rheology equations to estimate the complex modulus Eq. (3-21) of a surface populated with one type of surfactant or a binary mixture

of surfactant species. From the resulting information, the real and imaginary contributions to the complex dilational modulus can be calculated.

3.2.7.2. Shear Rheology of Particle Monolayers

Modelling the two-dimensional viscoelasticity of a particle monolayer under shear stresses can be useful to predict interfacial material properties. In analogy to linear viscoelasticity in three dimensions[218, 219], two dimensional linear viscoelasticity can be expressed with a stress $\sigma^s(t)$:

$$\sigma^s(t) = \int_{-\infty}^{t} dt'\, G^s(t-t')\dot{\gamma}^s(t') \qquad (3\text{-}26)$$

where $\dot{\gamma}^s(t')$ is the rate of deformation in the interfacial layer at past times $-\infty < t' < t$, and

$$G^s(t) = {G_0}^s + \int_0^{\tau_{max}} \frac{d\tau}{\tau} H^s(\tau) e^{-t/\tau} \qquad (3\text{-}27)$$

is the interfacial relaxation modulus. The interfacial relaxation time spectrum $H^s(\tau)$ quantifies the distribution of relaxation modes that contribute to $G^s(t)$. The largest relaxation time, τ_{max}, belongs to the slowest relaxation mode at long-time stress relaxation.

For practical purposes, the interfacial relaxation modulus may be described by a discrete spectrum with the relaxation strength of, g_i, corresponding to the relaxation time (τ_i) as follows:

$$G^s(t) = {G_0}^s + \sum_{i=1}^{N} g_i\, e^{-t/\tau_i} \qquad (3\text{-}28)$$

Small angle oscillatory shear (SAOS) results in dynamic moduli:

$$G^{s\prime}(\omega) = {G_0}^s + \int_0^{\tau_{max}} \frac{d\tau}{\tau} H^s(\tau) \frac{\omega^2\tau^2}{1+\omega^2\tau^2} \quad (3\text{-}29)$$

$$G^{s\prime\prime}(\omega) = \int_0^{\tau_{max}} \frac{d\tau}{\tau} H^s(\tau) \frac{\omega\tau}{1+\omega^2\tau^2} \quad (3\text{-}30)$$

These modeling equations will be applied to interfacial rheology experiments in the following manner. The particulate monolayer has no permanent connectivity and rheologically will be treated as a liquid where the equilibrium modulus is zero, ${G_0}^s = 0$. Just like in 3D rheology of viscoelastic liquids, the relaxation time spectrum, $H^s(\tau)$, is the only material property needed for a quantitative description of the two-dimensional linear viscoelasticity of a complex liquid.

3.2.8. Surface Evolver

JPs possess chemical anisotropy, which generates deformations on the air-water interface due to the entrapment of particles in a tilted orientation. Vertically aligned particles will likely generate deformations associated with the surface roughness present at the Janus boundary (commonly described via quadrupolar and hexapolar modes), whereas tilted particles introduce dipolar deformations. Following the work of Rezvantalab et al.,[118] the Surface Evolver software[220] was employed to model a system of a single Janus particle straddling a fluid interface at an arbitrary orientation angle δ. The software can be used to model interfacial deformations that are induced by various forces and constraints present in the system. In our system, the surface energies, which are dependent on the wettability of the particle hemispheres, were considered the governing force. Once the geometry is created, one can refine the mesh and minimize the surface energy until convergence is achieved. The software considers the surface tension between the fluids as 1, which was converted afterwards to the surface tension of water ($\sigma_0 = 72.8$ mN/m). To model the JPs of various amphiphilicities, we set the contact angles of the hemispheres to the experimentally

measured values, held the particle position constant, and incrementally increased the tilt angle. Once the mesh is converged, the contact area between each hemisphere and the subphase was exported and Eq. (4-1) was applied to calculate the desorption energy (ΔE_d) associated with each orientation angle (δ).

4. Mechanical Properties of Particle-Laden Interfaces

In this chapter, we focus on the mechanical properties of particle monolayers at the air-water interface to examine the implications of particle features, such as surface roughness or surface anisotropy for the response of the network to the applied dilational or shear stresses.

4.1. Impact of Particle Roughness on the Mechanical Properties of a Particle-Laden Fluid Interface

4.1.1. Introduction

Particles stabilize fluid interfaces by removing the energetically costly contact area between the two fluid phases. Thus, parameters such as particles size and surface chemistry can be used to tune the resulting reduction in the excess free energy of the system. Furthermore, particle geometry can also be exploited as another design parameter in tuning the stability of Pickering emulsions and foams. Examples of anisotropic particle shapes performance of which have been studied at fluid interfaces are ellipsoids, nanotubes, and fractal-like particles (e.g., fumed silica). Such systems of non-spherical particles are usually dominated by capillary interactions due to the irregular shape of the contact line surrounding the particle surface.

In this section, we have investigated the consequences of introducing surface roughness to a particle monolayer at the air-water interface. We studied the intrinsic differences between the mechanical properties of the resulting interfacial networks when spherical particles (250 nm of diameter) are compared to monolayers formed by fumed silica particles of a similar hydrodynamic diameter. In order to systematically investigate the impact of particle texture, two types of fumed silica particles were used in these studies; i.e., a low specific surface area (LSA) and a medium

specific surface area (MSA). All particles were hydrophobically modified with Dimethyldichlorosilane (DMDCS). We review the surface pressure isotherm results obtained from successive compressions and expansions of the monolayers and discuss the hysteresis associated with each particle system.

4.1.2. Results and Discussions

4.1.2.1. Monolayer formation

SEM pictures of the particles used in this section are shown in **Figure 4-1**. It is evident that the spherical colloidal particles shown in **Figure 4-1a** are remarkably different from the two fumed silica samples (**Figure 4-1b** and **c**). This comes from the fact that while the first is a monodispersed spherical particle with ~250 nm of diameter, fumed silica particles are made from smaller nanoparticles (20 nm each) that are fused together and form a fractal like structure. **Figure 4-1c** shows a magnified image of the particles, where the individual entities that compose the big aggregate of particles are visible. **Figure 4-1b** shows a less magnified point of view for the LSA particles, illustrating that fumed silica particles are far from the ideal spherical shape, and the consequences associated with that will be discussed further on.

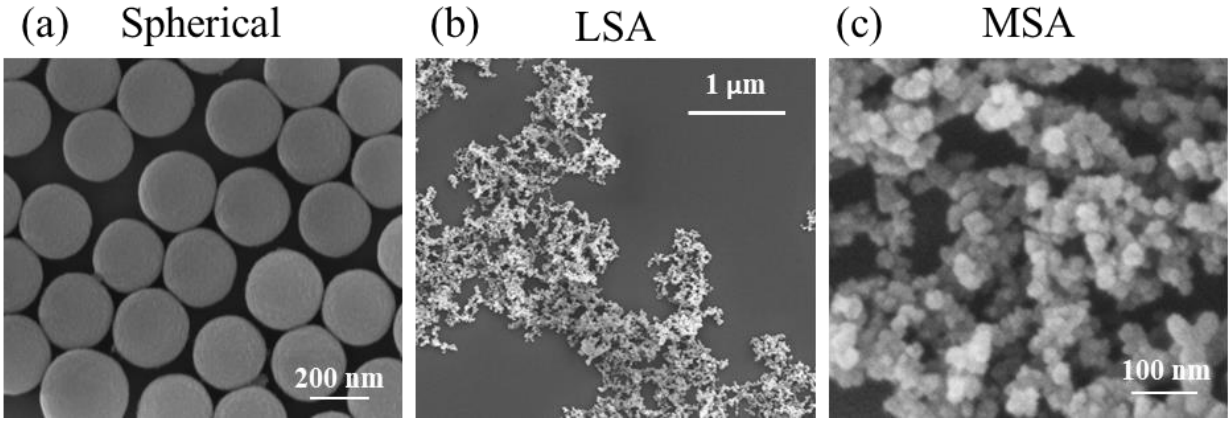

Figure 4-1. SEM pictures of (a) 250 nm spherical colloidal particles; (b) LSA fumed silica particles; (c) MSA fumed silica particles.

To measure the response of particle monolayers formed by each sample to the applied stress, concentrated particle dispersions were deposited to the air-water interface using a spreading solvent. A total amount of 2.5 (0.5) mg of spherical (fumed) silica particles was used to generate the surface pressure isotherms shown in **Figure 4-2a**. The reason for the different deposited mass of particles is so that the monolayers would experience the entire phase space upon compression, from a gaseous state where the surface pressure is ~0 up to the collapse of the monolayer upon compression and beyond, as indicated by the kink present in all of the curves at high surface pressures.

It is interesting to note that even though the same mass of particles was added for both fumed silica particles, MSA shows a surface pressure that was mostly higher than LSA at similar trough areas. This indicates that either the amount of MSA particles trapped was higher or that they were able to form a network at a lower surface coverage (i.e., at a larger trough area). **Figure 4-2b** depicts the same isotherms normalized with their area at the inflection point. The inflection point can be associated with the maximum packing that the monolayer experiences before collapsing. It is possible to determine the percentage of trapped particles for the spherical sample, since its cross-sectional area is known (**Table 4-1**). However, this is not a trivial task for the case of fumed silica particles due to their irregular shape.

From this perspective it is possible to state that there is indeed an earlier network formation for both fumed silica particles when compared to the spherical sample. However, both LSA and MSA curves are overlapping throughout the normalized area span (**Figure 4-2b**), which indicates that the generated monolayers have similar structural properties. This is further shown in **Figure 4-2c** where their isothermal compressibility modulus is plotted with the normalized area. It is possible to see that the 250 nm spherical particles reach a higher κ_0^s than both fumed silica, which

is indicative of a network that is harder to compress (**Table 4-1**). From these points of view, it is clear that MSA particles have indeed a better trapping efficiency than LSA particles.

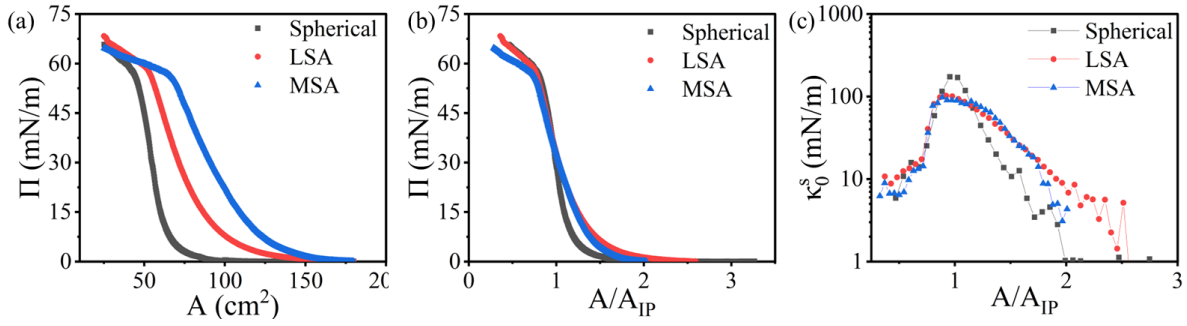

Figure 4-2. (a) Surface pressure isotherm of spherical 250 nm particles, and low surface area (LSA) and medium surface area (MSA) fumed silica particles as a function of trough area; (b) Isotherm normalized with the area at the inflection point; (c) Isothermal compressibility of the monolayers as a function of the area normalized with the inflection point. Black squares, red circles and blue triangles represent spherical 250 nm particles, LSA and MSA fumed silica particles, respectively.

By utilizing an equation of state, one can estimate some physical parameters of relevance for the particle monolayers. **Figure 4-3** depicts the best fit results for Eq. (3-8) generated surface pressure isotherms as a function of the estimated particle surface coverage (θ), and **Table 4-1** shows the fitting parameters from the best fit. It is possible to notice that for the case of spherical 250 nm particles, there is a good agreement between the model and the experimental curve, which is expected. However, when comparing both LSA and MSA modeled curves to the experimentally measured, there is a discrepancy between them. This clearly illustrates that this equation of state lacks the important features to represent monolayers of fumed silica particles. Nevertheless, it is interesting how both monolayers show similar results as well, only with a different maximum packing fraction. Comparing the interaction parameters associated with the best fit for all curves shows that for the case of spherical particles, the network is overall more attractive. However, it is important to note that comparisons between the systems should be taken with care since the model is not proper to represent fumed silica particles.

Table 4-1. Colloidal spherical and fumed silica particles under study and their characterization as follows: binding efficacy at the air-water interface, shift of the inflection point area due to either monolayer compaction and/or particle lost to the subphase comparing compressions 1 and 3 on the Langmuir Trough, the parameters obtained from the fitting of the surface pressure isotherms to the Frumkin equation of state, the surface coverage at the inflection point (θ_{IP}), and the overall interparticle interaction parameter (a).

Particle	Binding Efficacy	% IP shift after 2nd cycle	Maximum κ_0^s (mN/m)	Coverage at IP	a
Spherical	71.7%	5.9%	160 ± 12	89.7%	0.69
LSA Fumed	-	54.2%	105 ± 5	88.3%	0.42
MSA Fumed	-	66.4%	105 ± 5	89.8%	0.42

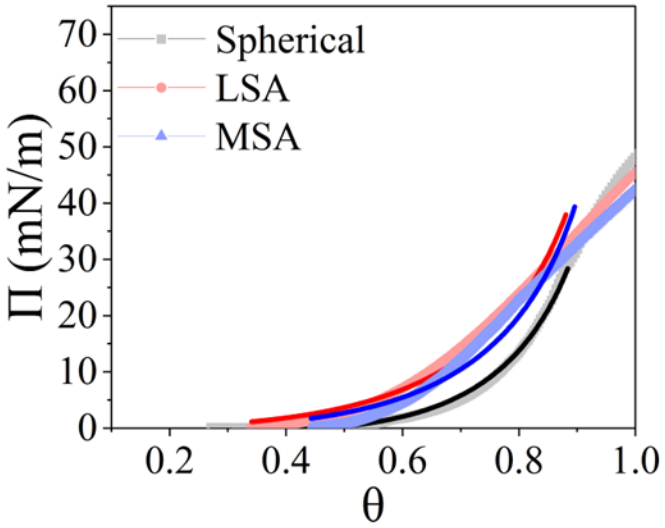

Figure 4-3. Surface pressure (Π) isotherms as a function of surface coverage of particle (θ) obtained for different particles monolayers. Spherical particles are shown in black squares, LSA fumed silica particles in red circles, and MSA fumed silica particles in blue triangles. The experimental data are shown in lighter tones and the best fit from the Frumkin equation of state (Eq. (3-8)) are shown in a darker tone. The function only fits the data for $\theta \leq \theta_{IP}$ since at higher surface coverages the layer of particles is not a 2D structure.

4.1.2.2. Collapse and Hysteresis

When subjected to consecutive compressions and expansions, the monolayers might experience hysteresis, since during compressions part of the applied work might be lost which leads to expansions taking a different path. This is illustrated in **Figure 4-4**, which shows the first and third cycle of compression and expansion for all systems under study. For the spherical

particles, it is possible to note in **Figure 4-4a** that there is hysteresis between the first compression and expansion. However, for the third cycle the difference between the compression and expansion curves is minimized, indicating that the monolayer was compacted after the first cycle. **Figure 4-4b** shows the same curves for LSA samples, where it is possible to notice two major differences in comparison to the spherical sample. The first major contrast is that there is a much larger difference between the first compression and the first expansion curves in the case of fumed silica particles. A similar behavior was captured for MSA monolayers. The second difference between the behavior of spherical and fumed particles is that for the latter case, the maximum surface pressure achieved at the third cycle is smaller than the one achieved at the first cycle. One can also quantify the amount of shift on the inflection point from one compression to another, which is associated with either particle desorption or monolayer compaction. As shown in **Table 4-1**, there is a 10-fold increase in the shift when comparing spherical to fumed silica particles.

The bigger hysteresis experienced by both fumed silica monolayers indicates that they are undergoing a much bigger irreversible change than the one experienced by the spherical particles. To further investigate the processes that are taking place within the monolayer, in response to the applied compressions and expansions, direct visualization via an optical microscope was carried out in tandem with the experiments on the Langmuir trough. By analyzing the images of the monolayer beyond the collapse point, we can see that the monolayer made by spherical particles yields through buckling, generating large folds that maintain the surface area constant (**Figure 4-4d**). However, both fumed silica monolayers show smaller wrinkles upon compression (**Figure 4-4e**), accompanied by some discontinuities on the monolayer, where the particles are pushed out of the interface, generating multilayers of particles ((**Figure 4-4f**). It is likely that fumed silica particles are able to interlock with themselves, forming denser aggregates that do not separate

during the expansion leg of the cycle. Both of these factors contribute to the irreversible character of the monolayers.

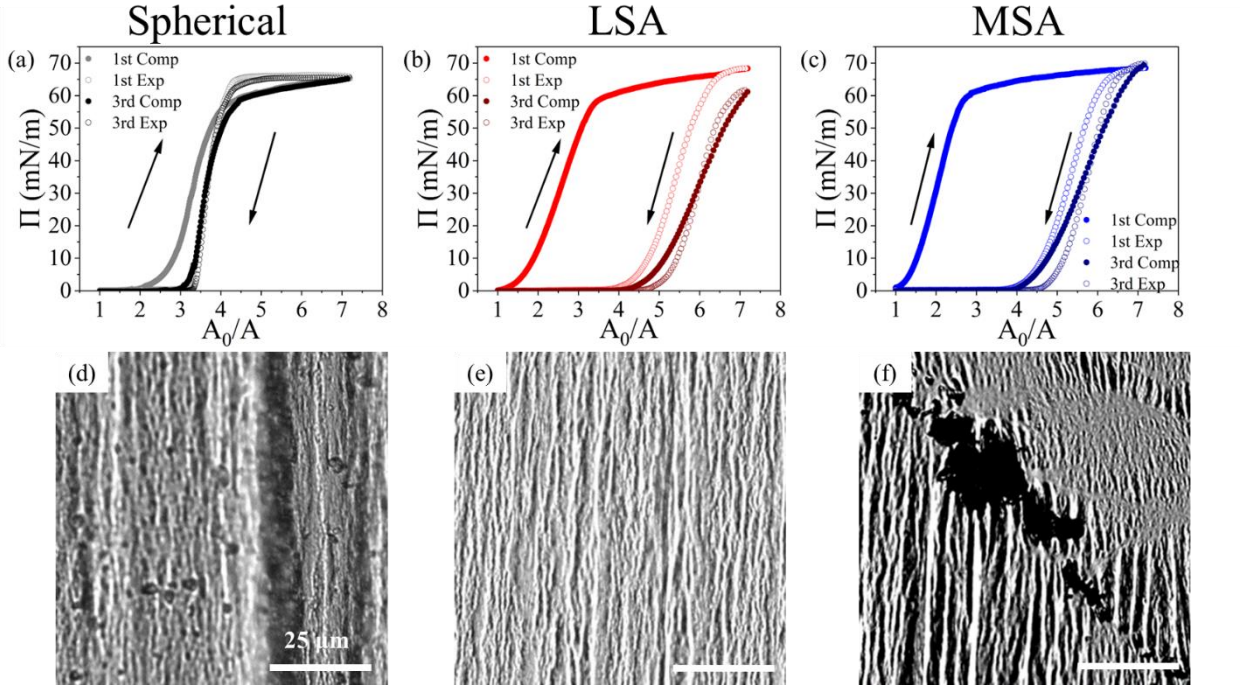

Figure 4-4. Surface pressure (Π) isotherm plotted as a function of the compression ratio (A_0/A) for compression (square closed symbols) and expansion (diamond open symbols) legs of cycles 1 and 3 carried out on monolayers formed by (a) spherical, (b) LSA, and (c) MSA silica particles. Microstructure pictures of the monolayer beyond the collapse point for (d) spherical, (e) LSA, and (f) MSA silica particles.

One way of quantifying the experienced hysteresis is by calculating the work that is added to the system upon compression and "retrieved" from the expansion (Eq. (3-7)). This is analogous to a piston cell in 3D, where the work applied to compress a gas can be calculated based on the pressure and volume differences from the start to finish. However, it is important to highlight that unlike the 3D parallel, the monolayer is not doing work to expand the barriers. **Figure 4-5** shows examples of how the hysteresis coefficient was calculated for monolayers formed with the spherical particles (**Figure 4-5a**) and MSA particles (**Figure 4-5b**). **Figure 4-5c** shows the results for the normalized hysteresis coefficient ($\overline{\Pi}$), as a function of the specific surface areas for each

sample at different cycles of the isotherm. It is possible to notice that for all cycles, there is a direct dependency between $\overline{\Pi}$ and the specific surface area, where MSA particles show 1 order of magnitude larger hysteresis. After the first cycle, cycle 2 shows a decrease in the areas between compression and expansion curves for all particles. From these results we can infer that once the monolayer of spherical particles undergoes the first round of compression and expansion, it achieves an equilibrium state, where the monolayer does not change upon further compressions. However, fumed silica particles show a persistent decrease in $\overline{\Pi}$ as the cycles of compression and expansion are performed. This indicates that some changes in the microstructure are taking place continuously, which are of irreversible character (**Figure 4-4f**). It is important to note that the specific surface area is likely not the determining factor for higher hysteric behavior, but the fact that MSA particles show a higher $\overline{\Pi}$ than LSA particles hints that the surface area, which is related to the porosity of the particles, is somewhat proportional to roughness.

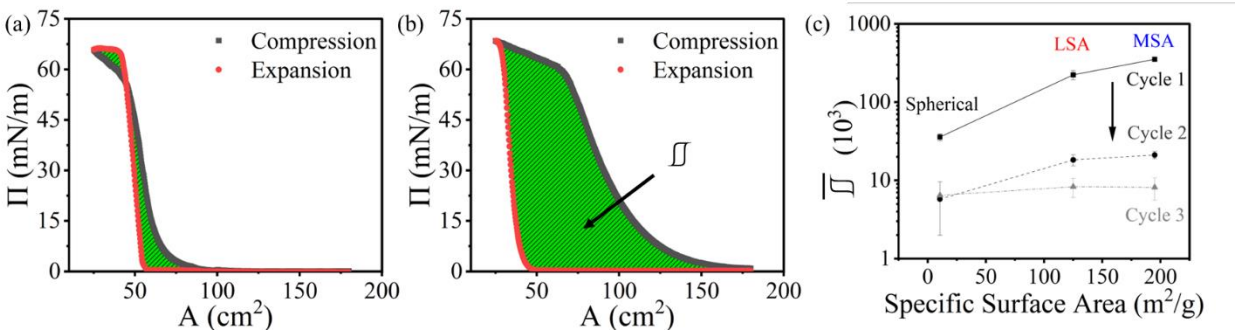

Figure 4-5. Illustration of hysteresis coefficient ($\overline{\Pi}$) calculation for (a) spherical and (b) MSA compression and expansion; (c) Normalized hysteresis coefficient ($\overline{\Pi}$) results for different cycles of compression and expansions as a function of different specific surface areas. Black squares, dark grey circles and grey triangles represent the 1st, 2nd and 3rd cycle respectively.

4.1.3. Summary of Findings

In this section, we discussed the consequences of introducing surface roughness to a particle monolayer at the air-water interface. We showed that there are differences between the

mechanical properties of the monolayer when comparing spherical particles with 250 nm of diameter to two types of fumed silica particles (LSA and MSA). It was found that MSA particles are more surface active than LSA particles, however both of them generate a monolayer that is mechanically similar. When compared to the monolayer formed by the spherical particles, fumed silica particles possess a softer but more open network, likely from the complex capillary interactions taking place. We conclude that the used equation of state is proper for modeling spherical particles but cannot capture the physics of important phenomena taking place within monolayers of fumed silica particles. Nevertheless, it is still useful to make qualitative comparisons with caution. We show that the measured surface pressure isotherm from successive compression and expansion cycles depicts that the spherical monolayer collapses reversibly and is able to regenerate its network in between cycles, whereas both fumed silica monolayers possess a much more drastic hysteric behavior. Finally, we show that there is a relationship between the specific surface area of the particle and the hysteresis experienced by the successive compressions and expansions.

4.2. Janus Particles, Amphiphilicity, and Capillary Interactions

4.2.1. Introduction

Janus particles bring together two different means of stabilizing interfaces. As a colloidal particle, presence of JPs at a fluid interface lowers the overall free energy of the system. Furthermore, the surface amphiphilicity of JPs can be tuned in order to enhance the desorption energy of the particles from the interface by having both hydrophilic and hydrophobic surfaces in contact with the aqueous and non-aqueous phases, respectively. Nevertheless, JPs might not always be in an upright configuration (i.e., Janus boundary aligned with the interface) when their orientational freedom is considered.[221] To better understand the implications of the JP orientation at interfaces, one can estimate the energy required to move an interfacially bound Janus particle to the bulk using the following expression:[118, 222]

$$\Delta E_d = \sigma(A_{a2}\cos\theta_A + A_{p2}\cos\theta_P - A_i) \qquad (4\text{-}1)$$

where A_i is the fluid-fluid interfacial area removed in presence of the particle, A_{p2} and A_{a2} are the areas of the polar and apolar regions on the JP, respectively, that are in contact with the apolar phase (e.g., air or oil). Therefore, assuming a tilted configuration will impact the values of A_{p2} and A_{a2}. Tilted particles not only are associated with changing the desorption energy of the JP, but may generate asymmetric deformations of the contact line depending on their tilt angle at the interface (δ).[118] This is due to the fact that a tilted Janus particle exposes both of its two different wetting surfaces to the subphase. The resulting asymmetric deformations of the fluid interface can thus drastically modify the dominant interparticle interactions as will be discussed in detail next.

From the various interparticle interactions taking place at the fluid surface, Janus particles are often dominated by capillary interactions. A mathematical approach has been developed to

model these capillary interactions, where the deformation of the contact line around the particle surface is captured as a summation of multipoles.[105] These deformations give rise to capillary interparticle interactions that can be estimated by Eq. (4-2) as follows:[223]

$$\frac{\Delta U_{cap}}{\pi\sigma} = H_A^2 S_A + H_B^2 S_B - H_A H_B G \cos(m_B\varphi_B - m_A\varphi_A) - \frac{1}{2}(m_A H_A^2 + m_B H_B^2) \tag{4-2}$$

Where $\Delta U_{cap} = U_{cap}(r) - U_{cap}(\infty)$ is the energy of capillary interaction and r is the center-to-center distance between interacting particles A and B. Considering Y as the index for particles A and B, m_Y is the mode of deformation (m_Y = 1, 2, 3, …) corresponding to dipole, quadrupole, hexapole, etc., H_Y is the undulation amplitude for particle Y, and φ_Y is the azimuthal angle of particle Y, or the rotation angle in the interfacial plane referring to the orientation of the surface deformation. S_Y is related to the mode of deformation and approaches $m_Y/2$ at long distances, and G is the pre-factor that accounts for the multipole interactions, descriptions of both are as follows.

$$S_Y = \sum_{n=1}^{\infty} \frac{n}{2} \coth[n(\tau_A + \tau_B)]\, A^2(n, m_Y, \tau_Y) \tag{4-3}$$

$$G \equiv \sum_{n=1}^{\infty} \frac{nA(n, m_A, \tau_A)A(n, m_B, \tau_B)}{\sinh[n(\tau_A + \tau_B)]} \tag{4-4}$$

$$A(n, m_Y, \tau_Y) = \sum_{k=0}^{min\,(m,n)} \frac{(-1)^{m-k}(m+n-k-1)!}{(m-k)!\,(n-k)!\,k!} \beta^{m+n-2k} \tag{4-5}$$

$$\beta = \exp(-\tau_Y) \tag{4-6}$$

$$\tau_Y = \operatorname{arccosh}\left(\frac{r^2 + r_A^2 - r_B^2}{2rr_Y}\right) \quad (4\text{-}7)$$

Where $A(n, m_Y, \tau_Y)$ is a constant independent of the approach angle, τ_Y is one of the bipolar coordinates related to the interparticle distance and their size, and β comes from the differentiation of the integral form of $A(n, m_Y, \tau_Y)$ bringing the dependence on τ_Y to the summation. For monopole-multipole interactions, another relation must be used.[223]

Introducing the Janus character is shown to drastically change the microstructure generated by particles straddling the interface,[72] due to stronger capillary interactions.[224, 225] Moreover, there is evidence that interfacially trapped JPs can interact through different polar orders (quadrupolar and hexapolar) at the same time.[226] Furthermore, the Janus character brings additional complexity when describing the resulting capillary interactions as the orientation of the JPs axis with regards to the plane of the fluid-fluid interface (δ) will affect the deformation of the contact line around the particle, and thus the terms that remain dominant in the description of the capillary interactions (i.e., m = 1 may not be ignored for JPs). As previously reported, JPs may assume different orientations at the air-water surface.[72, 227] The distribution of tilt angles, captured for interfacially bound Janus particles, brings a unique character to JP monolayers, because in tandem with the higher order interactions such as quadrupolar ($U \sim r^{-4}$) and hexapolar ($U \sim r^{-6}$), dipolar capillary interactions ($U \sim r^{-2}$) can also be present.[118] The mixed modes of interactions may even generate strong repulsion if the interfacial undulations around interacting particles are not matching as they approach each other,[228] phenomenon previously reported for particle rafts at fluid-fluid interfaces.[229] Therefore, understanding the network of interactions with the many modes of capillary interactions present in JP monolayers is not trivial. Even more interesting is the concept that by manipulating the JPs characteristics, such as the degree of amphiphilicity, one can tune the

strength of these interactions.[72, 118] Thus, a JP present in a populated monolayer might experience a complex network of interactions, involving distinct modes of interaction, at different distances from its neighbors. Nevertheless, not much is known about the relation between the complex arrangement of JPs monolayers at a fluid-fluid interface and the modes of capillary interactions at play, which is the focus of this chapter.

4.2.2. Results and Discussions

4.2.2.1. Janus Particles Degree of Amphiphilicity

The degree of amphiphilicity ($\Delta\theta$) is a measure of the particles Janus character. In the system under study, the hydrophobicity of the gold cap was tuned by attaching thiol molecules to the surface. Therefore, by introducing thiols with longer carbon chains onto the gold cap, JP amphiphilicity can be gradually increased, while retaining the wettability on the hydrophilic silica side. Examples of water droplets formed on the unmodified glass substrate, gold coated substrate and thiol modified gold substrates, and the resulting contact angles measured in each case are provided in **Figure 4-6**. Based on this information, the degree of amphiphilicity was estimated for C_0, C_4 and C_8 particles, as provided in **Table 4-2**.

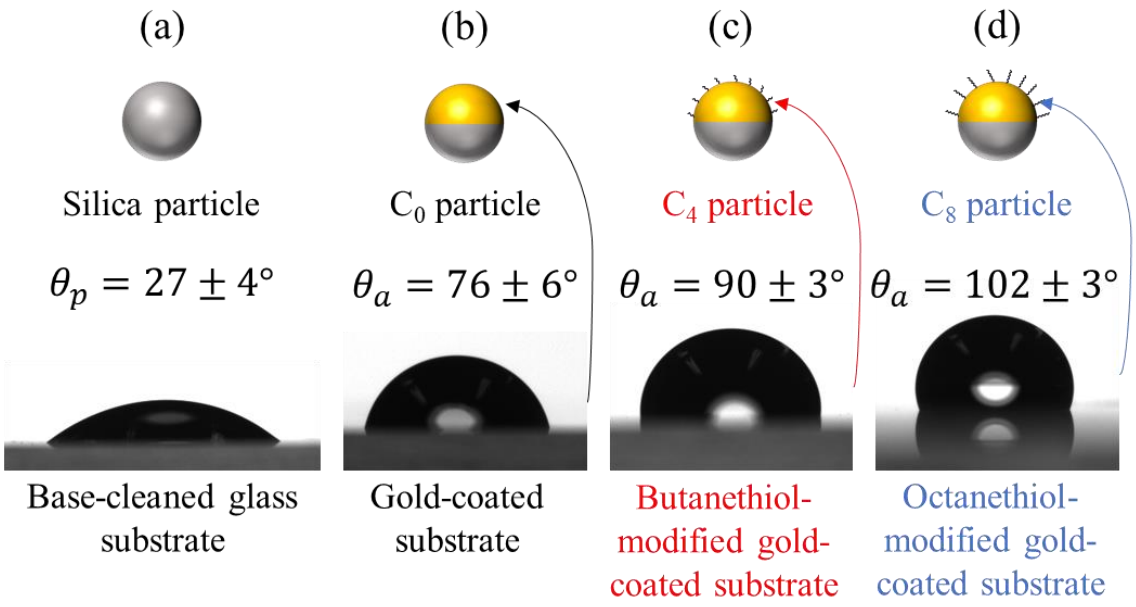

Figure 4-6. Wettability of glass substrates, modified in an analogous fashion to the particles, and measured via the contact angle of water droplets deposited on the substrate. The representative particle surfaces are also provided above each panel. From left to right, (a) the untreated base-cleaned substrate, (b) unmodified gold coated substrate, (c) gold-coated substrate modified with butane thiol, and (d) gold-coated substrate modified with octanethiol. Janus particles are composed of a hydrophilic silica surface mimicked by the glass substrate shown on panel (a) and a gold cap, unmodified or thiol-modified, as shown in panels (b)-(d).

4.2.2.2. Surface Pressure Isotherms

The surface pressure (Π) – area (A) isotherm for the three systems under study are provided in **Figure 4-7a**. It can be noted that each curve goes through an inflection point which is associated with an area (A_{IP}) that is smaller for C_0, intermediary for C_4, and larger for C_8. This can be attributed to each amphiphilicity having a different binding efficacy (**Table 4-2**). The binding efficacy is estimated based on the numbers of particles trapped at the interface, which was calculated based on the particle surface coverage at the inflection point obtained from the fitting of the isotherm to a thermodynamic model, divided by the number of particles deposited onto the fluid interface.[185] The area at the inflection point (A_{IP}) was then used to normalize the surface area along each isotherm, results of which are displayed in **Figure 4-7b**. The inflection point of the isotherm has been associated with the point at which the monolayer has reached its maximum

packing in two dimensions. Compressing the monolayer past the inflection point of the isotherm is shown to result in the collapse of the interfacial network either by expelling the particles from the interface or buckling of the particulate layer.[182]

Table 4-2. Janus particles under study and their characterization as follows: degree of amphiphilicity ($\Delta\theta$), binding efficacy at the interface, shift of the inflection point area, from compression 1 to 3 on the Langmuir Trough, due to hysteresis which can stem from either monolayer compaction and/or particle loss to the subphase, the parameters obtained from the fitting of the surface pressure isotherms to the Frumkin equation of state are the surface coverage at the inflection point (θ_{IP}) and the overall interparticle interaction parameter (a).

Particle	$\boldsymbol{\Delta\theta}$	**Binding Efficacy**	**Maximum κ_0^s (mN/m)**	**% Lost between cycles 1 and 3**	$\boldsymbol{\theta_{IP}}$	$\boldsymbol{a}$
C_0	25 ± 5°	79.2%	170 ± 9	10.4%	80.0%	-0.04
C_4	32 ± 4°	85.5%	228 ± 43	9.9%	88.4%	0.59
C_8	38 ± 4°	88.3%	308 ± 47	4.7%	91.0%	1.09

Comparing the three isotherms, it can be observed that by compressing the interfacial monolayers, the surface pressure picks up for C_0 Janus particles at larger normalized areas, which indicates an early network formation due to the anisotropic nature of interparticle interacitons.[230] There is a clear progression from C_0 to C_4 and then to C_8 where C_8 does not resist compression up to areas close to the inflection point, which indicates a dominance of short-ranged interactions. Plotting the isothermal 2D compressibility modulus (κ_0^s) with the normalized area in **Figure 4-7c**, further illustrates that resistance to the applied compression initiates at larger normalized areas for the particle monolayer formed by the C_0 JPs, followed by the networks of C_4 and C_8 particles, respectively. It should be noted that κ_0^s reaches a maximum at the inflection point of the isotherm as expected, from which one can obtain the maximum resistance to compression exhibited by the monolayers. Surface compressibility values show a direct relationship with the degree of amphiphilicity, as shown in **Table 4-2**. This indicates that JP of higher amphiphilicity yield

monolayers that exhibit a larger resistance to the applied compression when compared at the maximum particle surface coverage obtained in 2D.

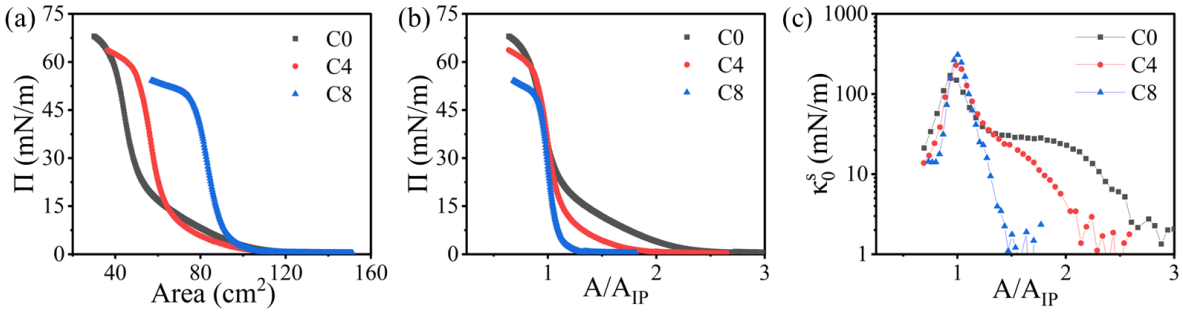

Figure 4-7. Surface pressure (Π) isotherm for Janus particles monolayers of different amphiphilicity as a function of (a) trough area (A) and (b) area normalized by the inflection point area (A_{IP}). (c) Surface compressibility modulus (κ_0^s) of the monolayers for JPs of different amphiphilicity. Data belonging to C_0, C_4, and C_8 particles are illustrated using black squares, red circles, and blue triangles, respectively.

After reaching their maximum resistance to compression at the inflection point, the monolayers yield to the applied stress and undergo a collapse process, which is evidenced by the "shoulder" recorded on the surface pressure isotherm. Imaging of the monolayer during the compression illustrates that the monolayer formed by C_0 JPs possess particle clusters that, upon compression, do not combine to form larger aggregates resulting in areas devoid of particles that persist. In contrast, C_8 monolayer is more uniform and shows wrinkles once compressed beyond the collapse point. It should be noted that monolayer formed by C_4 exhibits an intermediary behavior, with both characteristics, where local wrinkles are observed before the holes between clusters get filled up by particles and disappear completely.

To gain an understanding on how the strength of interparticle interactions is altered by the JP amphiphilicity, we applied an equation of state, proposed by Fainerman et al.,[199] to the measured surface pressure isotherms using both the surface coverage at the inflection point (θ_{IP}) and the interparticle interaction parameter (a) as fitting parameters. The results are provided in **Table 4-2** and are shown in **Figure 4-8**, where the comparison between the experimental data and the

resulting fit are plotted for all amphiphilicities as a function of the particle surface coverage (θ), which was estimated based on the area occupied by particles at the inflection point, calculated from θ_{IP}. In agreement with the results shown in **Figure 4-7**, the surface pressure obtained for the C_0 monolayer is always higher than the other two JP amphiphilicities when compared at a similar surface coverage. In other words, obtaining similar surface pressures requires the lowest surface coverage in the case of C_0 particles. This may be due to the slightly repulsive interaction parameter ($a = -0.04$) in case of C_0 particles, which indicates that the network is overall resisting the applied compression. In contrast, C_8 particles show the lowest surface pressure at the same surface coverage, resulting from the overall attractive interactions (a = 1.09). Moreover, the limiting packing fraction (θ_{IP}) associated with C_0 is the lowest value ($\theta_{IP} = 80\%$), indicating a more open network, devoid of particles, which corroborates with the idea that particle rafts are not attracted to each other. On the other hand, the maximum packing obtained in monolayers formed by C_8 particles corresponds to a hexagonal-close-pack arrangement in 2D and is equivalent to 91%.

It is worth noting that the fitting on C_0 is not optimal. This could be attributed to the complexity of interactions that are occurring at different length scales, i.e., interactions of different magnitude, strength, and sign may be taking place at different interparticle distances as will be discussed later.

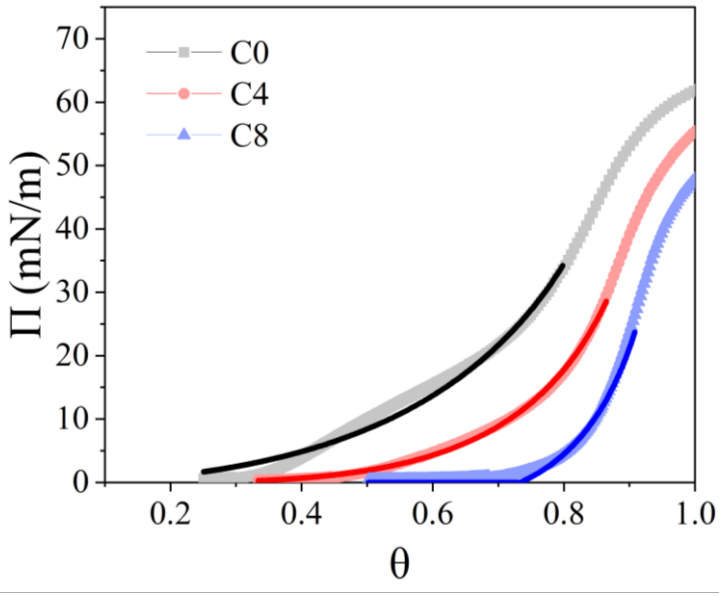

Figure 4-8. Surface pressure (Π) isotherms as a function of surface coverage of particle (θ) obtained for JP monolayers of different amphiphilicities at the air-water interface. C_0 particles are shown in black squares, C_4 particles in red circles, and C_8 particles in blue triangles. The experimental data are shown in lighter tones and the best fit from the Frumkin equation of state (Eq. (3-8)) are shown in a darker tone. The function only fits the data for $\theta \leq \theta_{IP}$ since at higher surface coverages the monolayer is not a 2D structure.

4.2.2.3. Isotherm Hysteresis

Since interfaces are often subjected to repeated external stresses, further analysis was carried on cycles of compression and expansion undergone by the particle monolayers, as the resulting surface pressure isotherms can offer valuable information regarding the hysteresis involved in these systems. **Figure 4-9** shows the comparison between the isotherms obtained on cycle 1 and cycle 3 for interfacial layers formed by the JPs of different amphiphilicity. The data is illustrated as a function of the compression ratio (A_0/A), defined as the ratio between the initial area at the open-barrier state (A_0) and the area at any point (A) during the experiment, which can be useful with regards to hysteresis analysis.[231] From these curves we can learn information regarding the induced monolayer compaction (comparing different compressions), and overall interparticle interactions (from the differences between compression and expansion isotherms). As shown in **Figure 4-9a**, for interfacial layers formed by C_0 JPs, there is a minor shift in the isotherm towards smaller normalized trough areas from cycle 1 to 3, which could be attributed to either

particle loss from the interface or the compaction of the monolayer upon compression. The former scenario is excluded in this case as the maximum pressure reached at the closed-barrier state remains the same across all three cycles.[182] For C_4 and C_8 monolayers, there is a similar shift to the right comparing the compressions in cycle 1 to cycle 3, as illustrated in **Figure 4-9b** and **Figure 4-9c**. Using the inflection point from compressions 1 and 3, one can calculate how many particles were lost between the cycles $Lost\%^{3rd} = (A_{IP}^{3rd} - A_{IP}^{1st})/A_{IP}^{1st}$, results of which are provided in **Table 4-2**.

When comparing the compression to the expansion for each cycle, C_0 monolayers behave similarly, depicted by similar shapes, regardless of the cycle number, with the expansion curve always exhibiting smaller surface pressures than the compression. Interestingly, the expansion surface pressure does not drop to 0 mN/m immediately after the area has reached values larger than the collapse area, indicating that the network is opening and exhibiting a solid-like behavior.[232] In contrast, C_4 and C_8 monolayers exhibit hysteresis at the first cycle. However, in the third cycle, the compression and expansion legs of the isotherms overlap each other indicating that larger aggregates are being formed and are not breaking apart after the expansion, which could be resulting from the lack of repulsion between the particles. C_4 monolayers experience a similar but less drastic version of the phenomena taking place in C_0 in which the surface pressure does not drop vertically to 0, indicating some repulsion. In contrast, C_8 monolayer reaches 0 mN/m of surface pressure as soon as the area is larger than the collapse area, which is evidence of short-range interactions of the particle clusters.

When analyzing κ_0^s, for the monolayer formed by C_0, shown in **Figure 4-9d**, there are clearly two regions, corresponding to a plateau on the lower surface concentrations (on the left) and the peak at the inflection point. The fact that κ_0^s for both compression and expansion cycles have a

comparable shape and similar values indicates that the particles within this monolayer are interacting repulsively, and once the expansion is taking place the same particle clusters that were resisting the compression push each other away. In contrast, for the monolayer formed by the C_8 particles, the compressibility modulus from the first compression shifts to smaller areas and remains relatively the same from the first expansion onwards as depicted in **Figure 4-9f**. This can be attributed to a large degree of compaction taking place within the monolayer, where the particles that were pushed together remain in the form of compact aggregates, due to the attractive nature of their interactions. This is also evidenced in the maximum compressional modulus where the 3rd cycle reaches a higher value (~476 mN/m) than the 1st (~308 mN/m), as the monolayer is compacted upon compression, and thus is harder to compress. Finally, the monolayer formed by C_4 particles exhibits an intermediary behavior; analogous to the C_8 system, the interfacial layer compacts to some degree in response to the applied compression in the first cycle, as shown in **Figure 4-9b**, whereas the shape of the compressional modulus is sustained indicating some repulsiveness in the interparticle interactions, as can be seen in **Figure 4-9e**.

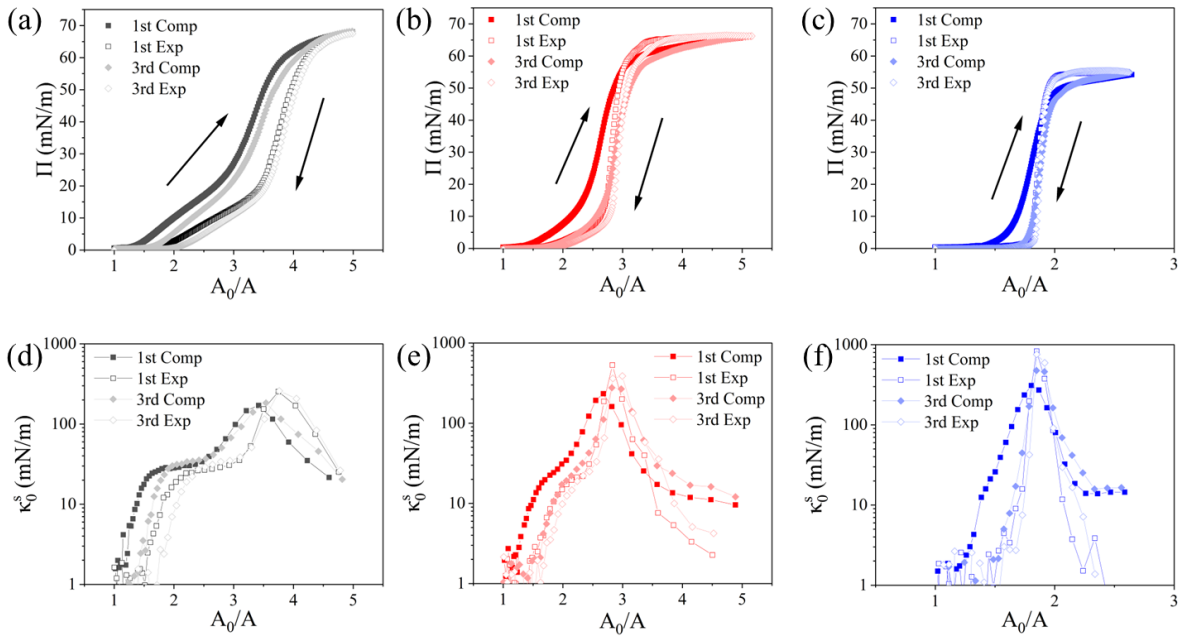

Figure 4-9. Surface pressure (Π) isotherm plotted as a function of the compression ratio (A_0/A) for compression (square closed symbols) and expansion (diamond open symbols) legs of cycles 1 and 3 for the monolayers formed by (a) C_0, (b) C_4, and (c) C_8 Janus particles; the compressional surface modulus (κ_0^s) for each particle monolayer are presented below the isotherms corresponding to (d) C_0, (e) C_4, and (f) C_8 Janus particles. Data belonging to C_0, C_4, and C_8 particles are shown in black, red, and blue color respectively.

4.2.2.4. Microstructure Analysis

To better understand the impact of JP amphiphilicity on the microstructure of the monolayers formed at the interface, imaging of the interface was conducted in tandem with the compression of the layer. The acquired data allows us to simultaneously track the surface pressure and visually inspect the resulting microstructure. Comparing the monolayers formed by JPs of with different degrees of amphiphilicity (at 5 mN/m), different microstructures were observed at the interface as depicted in **Figure 4-10**. The least amphiphilic C_0 JP system appears to consist of mostly open air-water areas devoid of the particles, with some smaller dendritic particle chains and some larger aggregates of more densely packed particles (**Figure 4-10a**). As the particle degree of amphiphilicity is increased, by moving from C_0 JPs to C_4 JPs (**Figure 4-10b**), a decrease in the number of particle chains is observed, whereas the aggregate size and the connectivity of

particle rafts increased. The packing in C_4 particles appears to be more compact in comparison with C_0 particles. For the largest amphiphilicity studied, the surface network of C_8 particles is predominantly covered by large, interconnected aggregates and the bare air-water surface area was the least in this case (**Figure 4-10c**). These results agree qualitatively with **Figure 4-8**, where the surface coverage is inversely proportional to the degree of amphiphilicity when compared at similar surface pressures. The different degree of amphiphilicity present in the particles could impact their orientation at the interface as further analyzed in the next section, which in turn alters the sign and magnitude of the resulting interparticle interactions that govern the assembly of the interfacial network yielding the captured microstructures.

The SEM images of the monolayers are used to further investigate the role of particle amphiphilicity on the orientation distribution of particles and its connection to the microstructure formation at the interface (**Figure 4-10d-f**). The SEM pictures were used since the gold caps, which appear brighter, can be distinguished from the silica cores. From these images, we observe that not all particles are oriented with their caps pointing upwards, towards the air phase, which is predicted to be the preferred orientation for a single Janus particle residing an interface when the rotational freedom of the particle is not cosidered.[56] It is possible to observe that there is a difference in the number of particles residing at various orientations depending on the degree of amphiphilicity.

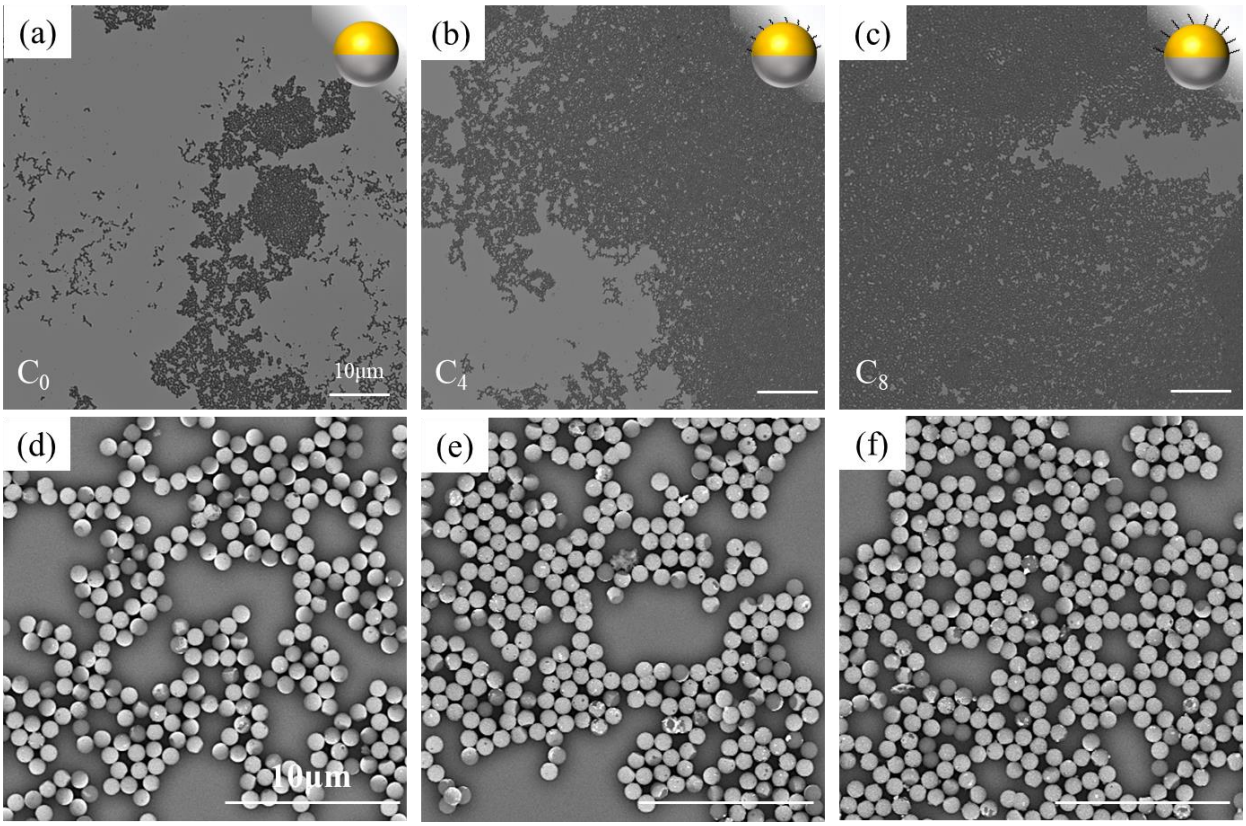

Figure 4-10. Representative optical micrographs of interfacial monolayers formed by (a) C_0, (b) C_4, and (c) C_8 Janus particles of different amphiphilicity. Images are taken at 5 mN/m. Scale bars are 10 μm. Representative SEM pictures of the clusters formed by the Janus particles of different amphiphilicity (d) C_0, (e) C_4, (f) C_8.

The particle orientation distribution for the three systems was quantified and the results are shown in **Figure 4-11**. The percentage of cap up-particles with increasing the JP amphiphilicity improved from 66 ± 2% for C_0 samples to 80 ± 2% for C_8 while the number of tilted particles reduced in half. In addition, the 2D alignment factor, calculated for the different amphiphilicities, illustrated that the presence of more tilted particles was associated with a less ordered monolayer as there is a direct correlation between S and $\Delta\theta$ (see **Table 4-3**). Since the particle orientation distribution is governed by the surface energies between the particle surfaces and the two phases present, the calculations of surface energies were carried out as a function of JP amphiphilicity, and its orientation at the interface, as discussed in the next section.

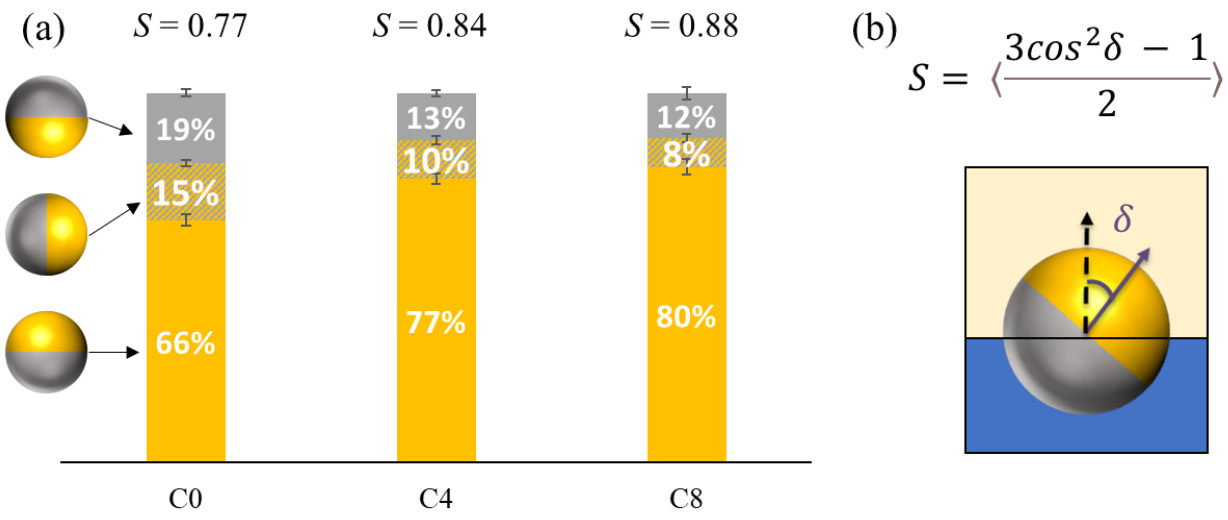

Figure 4-11. (a) Particles orientation distribution for different amphiphilicities. Gold color represents particles residing with their Janus cap aligned with the interface and pointing up towards the air phase, grey pertains to particles sitting with their Janus cap aligned with the interface and pointing down towards the water phase, and the diagonal stripes of gold and grey belong to the particle population with a tilted Janus cap. (b) Schematic showing the orientation angle (δ) and the 2D alignment factor (S).

4.2.2.5. Desorption energy calculations for individual particles at different angles

The role of amphiphilicity in the particle orientation can be assessed by applying the thermodynamics derivation of desorption energy (Eq. (4-1)) to particles at different tilt angles and amphiphilicity. One can calculate the desorption energy assuming that the fluid interface remains flat irrespective of JP tilt angle at the interface (**Figure 4-12a**, full lines). However, because of the anisotropy in chemistry present on the surface of Janus particles, one needs to account for the induced deformations of the air-water interface generated by JPs entrapment in a tilted orientation, which affects the resulting wetted areas on each face of the particle. Deformation of fluid interface ensued from JP tilt angle at the interface can be investigated using the Surface Evolver software. **Figure 4-12b** illustrates the deformation of the air-water interface in response to a Janus particle trapped at the interface with various tilt angles (δ) for a C_8 particle with $\theta_a = 30°$ and $\theta_p = 100°$. The orientation angle varied from the cap-up orientation (i.e., Janus boundary aligned with the

plane of the interface, $\delta = 0°$) to sideways orientation ($\delta = 90°$). These calculations were carried out for all three JPs trapped at different tilt angles at the interface. The change in the desorption energy of the JP, considering the interfacial deformation, is plotted in **Figure 4-12a** as a function of JP tilt angle at the interface.

When comparing the calculated desorption energies associated with a scenario where the surface is flat to a surface that deforms in response to the particle, it should be noted that the deformations of the interface are more thermodynamically favorable since they are associated with more negative desorption energies. Furthermore, for each JP amphiphilicity, the desorption energy becomes less negative as we move from a vertically aligned particle ($\delta = 0°$) to a tilted particle ($\delta = 90°$) indicating that the tilted state is less favorable. Finally, a higher degree of amphiphilicity yields a higher desorption energy for any tilting angle, as expected.

By analyzing the results obtained from the Surface Evolver (**Figure 4-12a**, discrete points), it can be noted that the desorption energy is nearly constant for all particles as we move from $\delta = 0°$ up to a critical angle (δ_c). C_0 exhibits a higher δ_c, followed by C_4 and C_8, which indicates that C_0 is more likely to assume higher tilt angle at the interface compared to the higher amphiphilicity particles. Moreover, the difference between the desorption energy associated with a particle residing at the interface with a cap-up orientation compared to sideways configuration, with a 90° tilt angle, is directly proportional to the particles amphiphilicity. This attribute can be the driving force for the observed particle orientation distributions (i.e., **Figure 4-11**) and how they change with JP amphiphilicity. Under these conditions, we can expect a higher population of particles straddling the interface with their caps oriented upwards for the more amphiphilic system (C_8), as observed from the SEM pictures of **Figure 4-10d-f**. Nonetheless, the high count of cap-down particles cannot be explained from thermodynamics point of view, as this configuration is the most

energetically unfavorable orientation. We offer two possible explanations for this observation. The first is based on the non-ideal manufacturing process, where the presence of multilayers in some locations on the substrate could block the particles residing on the lower planes from getting exposed to the metal coating and therefore leave those particles unmodified. The second possibility is that even though these particles are Janus, they might get trapped in a metastable orientation, due to the energetic Marangoni flows associated with their deposition, at the air-water surface. We believe that both possibilities could be taking place in our system.

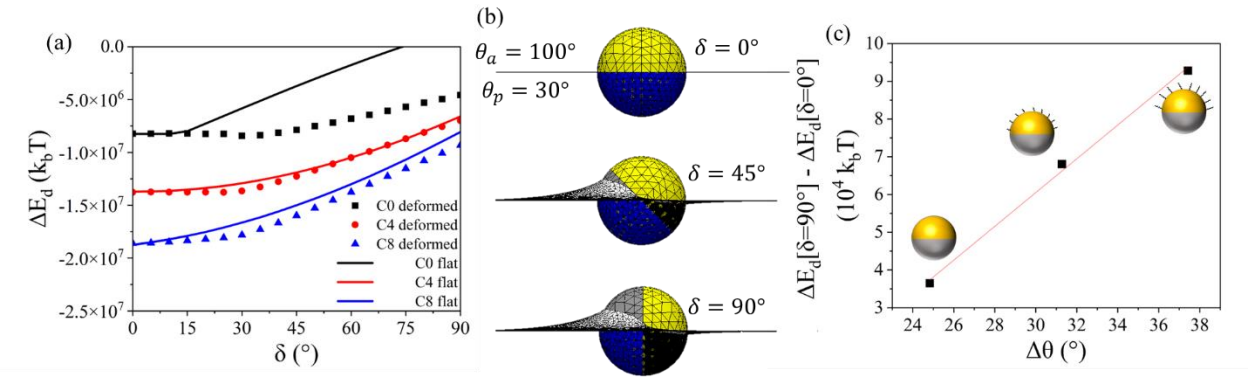

Figure 4-12. (a) Desorption energy (ΔE_d) of an interfacially bound particle calculated for different tilt angles (δ). Full lines represent cases where the surface remains flat regardless of the JP orientation. Discrete points represent results where the deformation of the interface was considered in the calculation of the desorption energy. Results for C_0, C_4, and C_8 particles are shown in black squares, red circles, and blue triangles, respectively. (b) Surface Evolver snapshots and the resulting interfacial deformation induced by the JP tilt angle at the interface displaying a particle with surface characteristics of a C_8 JP on the polar and apolar faces. (c) The difference in the energy required to desorb a tilted JP $\Delta E_d[\delta = 90°]$ and a cap-up oriented JP $\Delta E_d[\delta = 0°]$, from the interface, as a function of the degree of amphiphilicity ($\Delta\theta$) of the JPs.

4.2.2.6. Pairwise Capillary Interactions

In addition to the impact of amphiphilicity on assumed tilted orientations at the interface, which could result in the deformation of the interface, one must also consider the role of particle roughness on interfacial deformation. Since the Janus fabrication method is not seamless (i.e., the Janus boundary introduces surface roughness around the particle), vertically aligned particles (cap up or down) will introduce a contact line deformation that is likely correspondent to the shape of the Janus boundary.[233] These deformations yield capillary interactions between the interfacially

bound particles. Previous studies have associated the interactions between these particles to be quadrupolar ($U \sim r^{-4}$) and/or hexapolar ($U \sim r^{-6}$).[72, 226] While those higher-order capillary interactions are associated with vertically aligned particles, tilted JPs can also be present on the monolayer, which adds the dipolar mode of interaction ($U \sim r^{-2}$) to the system. For instance, even though they are not in the most favorable thermodynamic state, tilted particles are present on the monolayers analyzed in this study (**Figure 4-10d-f).** All of the beforementioned factors contribute to a unique and complex monolayer at the interface and need to be taken into consideration.

As mentioned earlier, interactions between non-tilted JPs can be estimated with quadrupolar and hexapolar interaction modes. These interactions result in different packing arrangements, where quadrupolar dominated systems will form square ordered clusters, whereas hexapolar dominated monolayers will assemble in a hexagonal arrangement.[223, 226] For our system, we observe amorphous clusters, with occurrences of both arrangements locally (see **Figure B0-3a**). The presence of tilted particles also impacts the overall packing which makes it non-trivial to determine a dominant mode of capillary interaction. One way of approaching this problem is to analyze the bond angles between neighboring particles to investigate whether either squared or hexagonal arrangements are more frequent.[234] From the analysis carried out in **Figure B0-3c**, it can be seen that for all the systems under study in this work, there is a higher tendency of finding pairs with bond angles of 60° and 120°, which originate from a hexagonal arrangement even though the microstructure is overall amorphous, as seen in **Figure 4-10d-f**. Therefore, for the sake of simplicity, further analysis of these JP systems was carried out with the assumption that the vertically aligned particles ($\delta = 0°$) deform the contact line predominantly by a hexapolar mode.

As shown in Eq. (4-2), capillary interactions depend on the approach angle between the particles. When looking into a pair of similarly oriented particles, we can estimate the pair-

interaction potential dependence on the azimuthal angle (or approach angle, $\Delta\varphi$). For a pair of particles deforming the interface in a hexapolar fashion, the radial interaction map calculated using Eq. 3 for different center to center distances (r) and approach angles ($\Delta\varphi$), is shown in **Figure 4-13a**. The values shown in the figure represent the total interaction energy (ΔU_{cap}) normalized by the surface tension (σ_0) and the squared deformation amplitude (H^2) assuming $\sigma_0 = 72.8$ mN/m and $H = 32$ nm. For our system, H was estimated based on the roughness of the core particle and the roughness introduced by the metal deposition, following the work of Qiao et al.[225] It is possible to notice that there are three attractive and three repulsive domains, as expected. Therefore, in a dilute regime (i.e., low particle surface coverage), when two particles approach each other in a favorable configuration (i.e., deformation modes are matching), attraction will be ensued. If the particles approach each other in a unfavorable configuration, assuming they are free to rotate in plane (radial movement on the graph), they can align their deformations and switch to the attraction region of the capillary interaction map.[118, 235] For instance, in a system composed of two particles interacting via hexapolar capillary interactions, the maximum in-plane rotation needed for a single particle to switch the interaction signs and move from maximum repulsion to maximum attraction is 60°. **Figure 4-13b** shows a similar scenario for two tilted particles deforming the interface in a dipolar fashion. In comparison to the previous case, two tilted particles approaching each other in the most unfavorable orientation may need to rotate up to (180°) to move from a repulsive domain towards an attractive range. For a dilute system (i.e., low particle surface coverage) this is not an issue. However, when considering populated surfaces, a complicated network of interactions arises from the many-body interactions, which could constrain the in-plane rotations.

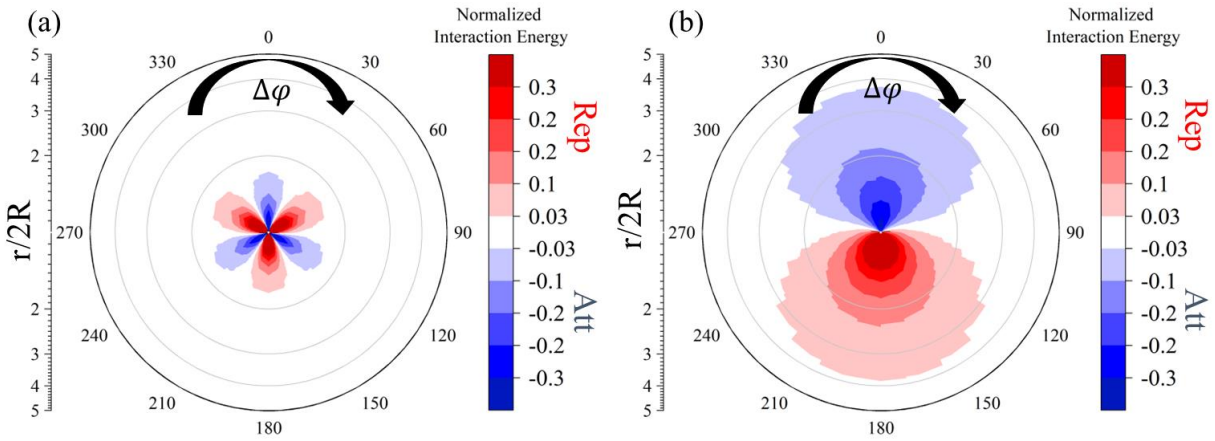

Figure 4-13. Radial map of normalized pairwise capillary interaction for two particles as a function of center-to-center separation distance (r) normalized by particle diameter (2R) distances and their in-plane approach angle ($\Delta\varphi$). (a) Two particles interacting through (a) hexapolar and (b) dipolar capillary interactions. Regions shown in red (blue) represent repulsive (attractive) capillary interactions. Eq. (4-2) Was used to calculate the interactions.

From **Figure 4-13**, we can determine two possible scenarios for each particle pair: the most attractive and the most repulsive paths, which depend on the alignment of the surface deformations that are caused by these particles. These scenarios are illustrated in **Figure 4-14a** and **Figure 4-14b** for particles interacting solely via hexapolar or dipolar modes, respectively. For cap up particles interacting via hexapolar mode (**Figure 4-14a**), they may experience an attraction (particles Ia-IIa) or a repulsion (particles Ia-IIIa) depending on how they approach each other. For tilted particles interacting via dipolar mode (**Figure 4-14b**), we have a similar scenario where matching deformations are attractive (particles Ib-IIb) and opposing deformations are repulsive (particles Ib-IIIb). It is also possible to observe that at smaller distances, vertically aligned particles interact strongly, while the capillary interaction between tilted particles is longer ranged.

The interaction potential between a vertically-aligned particle and a tilted particle is not trivial, as shown previously by Rezvantalab et al. under the simplifying assumption that upright particles do not deform the interface (i.e., smooth Janus boundary), which is not realistic.[118] When considering that vertically-aligned particles deform the surface in a hexapolar fashion, we arrive

at a scenario with interaction profile depicted in **Figure 4-14c**. For the attractive pair (Ic-IIc), at large distances, the particles are attracted to each other, however their interaction energy reaches a minimum before reaching close contact. Upon further reduction in separation distance, particles start repelling each other. This can be explained by acknowledging that when moving a hexapolar particle closer to a dipolar particle, there is a distance at which opposing deformations will overlap because the dipolar deformations are wider than the hexapolar ones. This is exemplified by the pair Ic-IIc in **Figure 4-14c,** where the downwards interfacial deformation around the dipolar particle matches the downwards deformation on the hexapolar particle. Nevertheless, if the particles keep approaching each other, the downwards deformation of the dipolar particle will overlap with the upwards deformations on the hexapolar particle, which is not an energetically favorable state, as it increases the interfacial contact area between the two fluids.

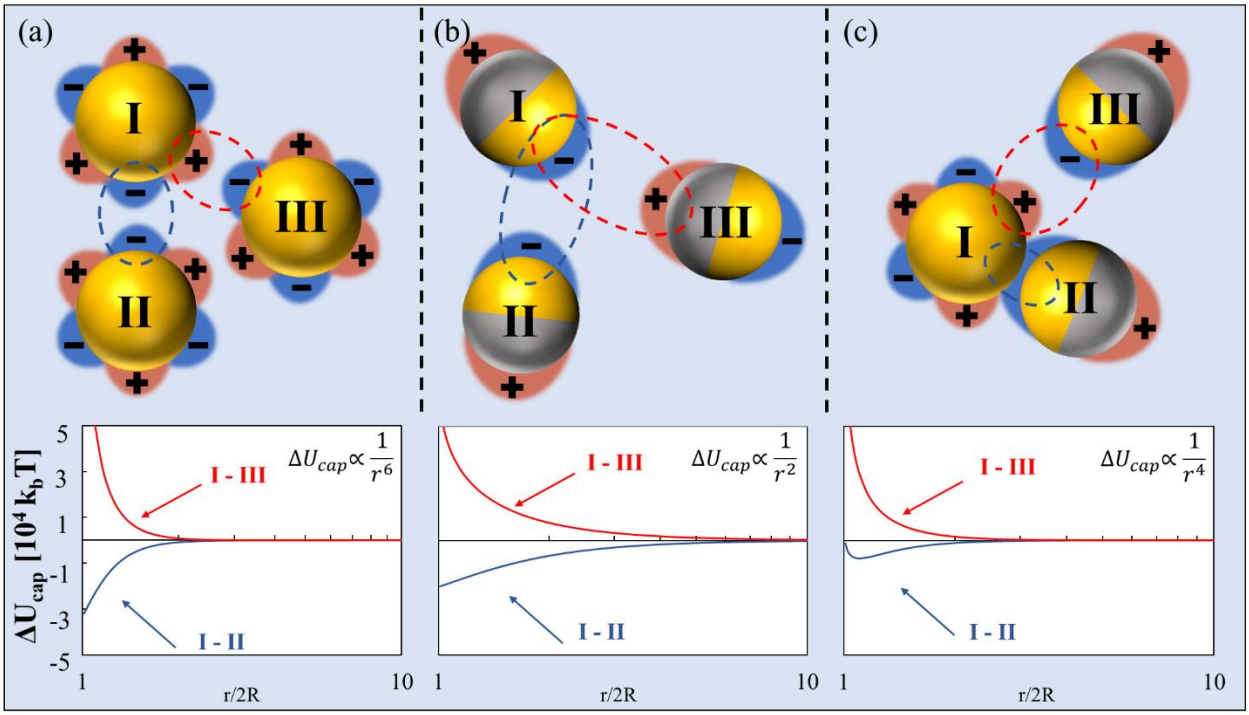

Figure 4-14. Cartoons showing the top-view of three particles trapped at the air-water interface, where upward (downward) surface deformations are represented as a plus (minus) sign and in red (blue) color. Capillary interactions resulting between two pairs are provided in the bottom panel for particles interacting either attractively (particles I and II) or repulsively (particles I and III) and are as follows: (a) Hexapolar-Hexapolar, (b) Dipolar-Dipolar, (c)

Hexapolar-Dipolar. Scaling of capillary interactions with separation distance for each scenario is provided on the plots. Interaction curves were calculated based on the numerical solution provided by Kralchesvky et. al. for multipolar capillary interactions.[223]

We have further analyzed the SEM pictures to examine pairwise interactions present in monolayers formed by each particle amphiphilicity and for the different particle orientations. This can be conducted by setting a threshold distance that characterizes the first shell of neighbors (analysis can be found in the Appendix B, **Figure B0-4**), followed by counting each detected pair and comparing their assigned orientations to get the number of interactions between each case (up-up, up-tilted, etc). As shown in **Figure 4-15**, the majority of interactions are between particles possessing cap up configuration, as expected. When considering C_0 JPs, ~21.0% of the interparticle interactions are between the cap-up and tilted particles, in contrast to only ~12.5% for C_8 JPs. This indicates that within C_0 monolayer, there is a higher recurrence rate of the complex scenario shown in **Figure 4-14c**. This is indeed expected as the higher number of tilted particles are present in the interfacial network formed by C_0 particles, as displayed in **Figure 4-11a**, which in turn results in a higher chance of interactions involving them.

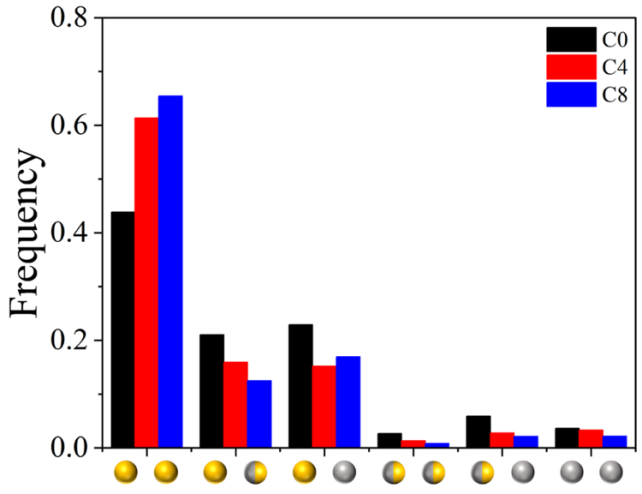

Figure 4-15. Frequency of pairwise interactions for pairs of different orientations as a function of JP amphiphilicity. From left to right, up-up, up-tilted, up-down, tilted-tilted, tilted-down, down-down. Data belonging to C_0, C_4, and C_8 particles are shown in black, red, and blue color respectively.

Once the interacting pairs are identified, the pairwise interaction experienced by each particle can be calculated in order to determine the network of interactions present in each system. An assumption that was made in these calculations was that the amplitude of deformation is constant regardless of the particle orientation in the monolayer. Since upwards and downwards surface deformations around vertically aligned particles cannot be distinguished from an SEM image, we also assume that these particles are always in the most attractive configuration with respect to their pairs. Therefore, pairs containing at least one vertical particle will follow the attractive capillary interaction scenarios (blue curves) shown in **Figure 4-14a** and **Figure 4-14b**. For a pair of tilted particles, the sign of interfacial deformation can be determined based on the cap direction and used in calculating the magnitude and sign of the pairwise capillary interaction.

Table 4-3. The 2D alignment factor (*S*), the normalized stored energy per particle ($\frac{\Delta U_{cap}}{\pi\sigma H^2}$), and the corresponding energy in k_bT for monolayers obtained with each particle system.

Particle	S	$\frac{\Delta U_{cap}}{\pi\sigma H^2}$	ΔU_{cap} $\times 10^4$ (k_bT)
C_0	0.77	-0.62	-3.5
C_4	0.84	-0.81	-4.6
C_8	0.88	-0.89	-5.1

Figure 4-16 shows the normalized particle interaction energy as a Voronoi diagram, where area surrounding each particle is colored with respect to the amount of capillary interaction energy corresponding to that particle resulting from its neighbors. The corresponding SEM images used in the analysis of **Figure 4-16** can be found in the Supplementary Information **(Figure B0-5)**. It is worth noting that the cluster formed by C_0 particles depicts a higher occurrence of repulsive interactions (colored in red) when compared to the C_8 cluster, which is dominated by attractive interactions (blue).

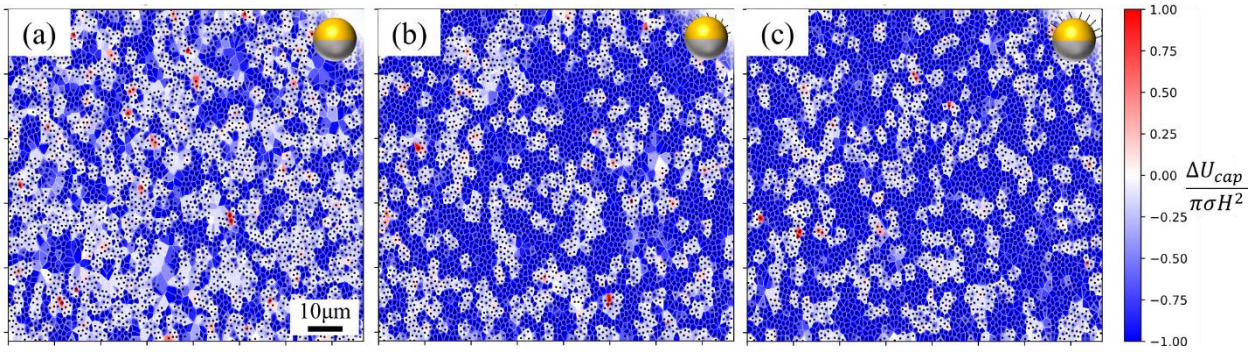

Figure 4-16. Voronoi diagram of a particle cluster from a (a) C_0 and (b) C_4 (c) C_8 monolayer. The particles center is shown as a black circle, and the area surrounding the particle is colored with respect to the energy resulting from the interactions with its neighbors summed up.

From the capillary interaction energy values calculated for each particle in the cluster, we can estimate an average energy stored per particle (ΔU_{cap}), results of which are provided in **Table 4-3**. There is a direct correlation of interaction energy (ΔU_{cap}) with the JP amphiphilicity ($\Delta\theta$). All

amphiphilicities yielded attractive interaction energies, which is expected for a cluster that was self-assembled at the air-water interface. These results are in agreement with the physics obtained from the fitting of the isotherms, where C_8 particles were found to exhibit stronger attractive interactions ($a = 1.09$) compared to the other two amphiphilicities.

It should be noted that a number of assumptions were made in the beforementioned calculations, as follows: (1) cap-down particles are equivalent to cap-up particles in the calculation of pairwise interaction, which might not be true if those particles are indeed homogeneous untreated particles and not cap-down Janus particles; (2) all amphiphilicities considered in this study will result in the deformation of the surface with the same amplitude, whereas the deformation should be dependent on the degree of amphiphilicity;[118] (3) tilted particles are deforming the surface with the same amplitude as the vertical ones; and (4) depression and rise of the fluid interface is the same for tilted particles, which is not necessarily the case since these are not symmetric Janus particles. The impact of these factors on the resulting capillary interactions needs to be carefully investigated.

4.2.3. Summary of Findings

To shed light on the role JP amphiphilicity plays in the formation of an interfacial microstructure and its mechanical properties, JP monolayers of different amphiphilicity were subjected to compression and expansion stresses and their response was examined. The analysis was carried out via the measurement of surface pressure isotherms followed by their characterization with an equation of state to highlight the impact of JP amphiphilicity on the resulting interparticle interactions. The role of JP amphiphilicity on the microstructure formation was further investigated by determining the orientation distribution of JPs at the interface from the images of the particle networks at the air-water interface. Surface Evolver software was used to

estimate the desorption energy associated with such interfacially bound JPs, trapped at different orientation angles with regards to the interface, to underscore the importance of particle amphiphilicity. It was found that for higher amphiphilicity JPs, there is a larger energy penalty for particles to assume a tilted orientation at the interface in comparison to those vertically aligned. It is postulated that the different orientation distribution captured for various degrees of JP amphiphilicity, dictates the modes of capillary interactions that are present within the monolayer. When comparing JPs of different amphiphilicities, it can be concluded that the capillary interactions induced by the tilted JPs at the interface and the resulting interfacial deformations are the main contributing factor to such different self-assembly behavior at the air-water surface and the accompanying response to the applied compression, which is of significance for designing interfacial systems for industrial applications.

Tuning the rheological properties of interfacial networks by engineering the particle attributes that form the monolayer has been envisioned in the field. For example, the rheological properties of interfacial monolayers formed by ellipsoidal particles, such as their yield point, was reported to be higher at similar surface coverages when compared to spherical particles, which in turn has been shown to arrest bubble dissolution, a useful attribute in designing stable Pickering foams.[166] Moreover, the surface pressure of JPs monolayers have also been shown to impact their resulting interfacial rheology.[236] Consequentially, this illustrates the opportunity to use the capillary interactions as a tool to tune the properties of interfacial systems.[53, 237] Understanding these concepts is key in designing interfacial systems, by engineering the surface attributes of particles, and is essential for numerous applications of soft-matter, as listed in the New Directions for Chemical Engineering.[238]

4.3. Janus Particles, Amphiphilicity, and Interfacial Shear Rheology

4.3.1. Introduction

The study of JP-laden interfaces is an active area of research to discern the impact of JP attributes such as amphiphilicity and roughness on the microstructure of the resulting network and its interfacial rheology, which can be utilized in engineering the performance of resulting interfacial systems.[239-245] Using a multicomponent Lattice-Boltzmann method, simulations have shown that not only the Janus character and amphiphilicity of the particle affect the rheological properties of the interfacially-trapped particle monolayer, but an applied shear flow itself has an impact on the configuration of particles and their assembly. The authors observed the directed assembly of a cluster of randomly oriented spherical JPs into ordered structures at a sheared interface between two immiscible fluids.[246] Irrespective of the particle size and for intermediate surface coverages (32 – 65%), the capillary-induced interactions – resulting from the overlap of the deformed fluid interface under shear flow – yielded particle chain formation normal to the shear direction. Despite the computational studies available on JP-laden interfaces, which indicate their unique rheological properties, experimental studies are still lagging behind. A recent investigation has shown that introducing JPs, at very low concentrations, to a monolayer populated by homogeneous particles (1:40 Janus-homogeneous ratio) can increase the surface elastic response by one order of magnitude. The change in surface behavior was attributed to the augmented capillary interactions introduced by the JPs presence in the monolayer.[225] A few studies have assessed the response of JP monolayers to dilational stresses.[247, 248] For instance, the behavior of poly(methyl methacrylate)/poly-tert-butylmethacrylate (PMMA/PtBMA) Janus particles (diameter of 172 nm) at both air-water and decane-water interfaces was studied in comparison with those obtained from PMMA and PtBMA homogeneous particles. Comparing the surface

compression isotherms for the Janus system with their homogeneous counterparts revealed that besides having the highest surface pressure at the entire range of area, Janus particles exhibited a higher static compressional modulus (κ_0^S), indicating the presence of a stronger network.[247] While the shear rheology of particle rafts composed of homogeneous particles has been examined in the literature and the role of particle shape anisotropy on the resulting shear rheology has been highlighted, to the best of our knowledge, experimental studies on the shear rheology of interfaces populated by JPs, which are dominated by capillary interactions, have not yet been reported.

As complex interfacial systems are often subjected to applied stresses in various industrial and technological applications, it is important to study the dynamics and resulting stability of interfacial microstructures. In this regard, we examined the behavior of JP-laden fluid interfaces under large surface compressions (or high surface pressures) and interfacial shear in order to highlight the impact of JP amphiphilicity on the resulting mechanics. To better understand how the interfacial networks of various particle packing behave under shear flow, interfacial shear rheology was carried out using the DWR geometry coupled with a Langmuir trough. As stated in the previous section, the amphiphilicity of JPs affect the resulting interparticle interactions and leads to variations in the microstructure of the particle networks even when compared at the same surface coverage. We propose a comparison between different particles at similar surface pressures, or similar surface energies. As we have determined the relationship between surface pressure and surface coverage, we are able to compare the amphiphilicities under both perspectives. We performed amplitude sweep experiments to identify the linear viscoelastic (LVE) regions and subsequentially performed small amplitude oscillatory shear (SAOS) measurements to characterize the impact of JP amphiphilicity on the surface viscoelasticity of the layer at various frequencies of oscillation.

4.3.2. Results and Discussion

To probe the viscoelastic response of the different JPs monolayers, the LVE regime needs to be determined for each sample at different surface pressures. **Figure 4-17** depicts the shear amplitude sweeps performed for each of the JPs at various surface pressures. For all cases, as the surface pressure increases, the surface elastic modulus ($G^{s\prime}$) also increases, which is expected as higher surface pressures are associated with denser networks. The amplitude sweeps for C_0 JPs (**Figure 4-17a**) show that there is a minimum surface pressure (~10 mN/m) necessary to get a good signal to ratio response in these measurements. This behavior has a direct correlation to the microstructure shown in **Figure 4-10**, where at 5 mN/m the network consists mostly of open spaces and smaller aggregates. Compressing the monolayer increases the surface pressure (and the surface coverage), which then results in a more cohesive and responsive network, that presents the characteristic LVE region and deviates from it at larger amplitudes of oscillations. **Figure 4-17b** shows the same curves for C_4; however, at 5 mN/m the network possesses a more responsive character (compared to C_0). Once again, this can be explained by the fact that to achieve 5 mN/m of surface pressure, C_4 particles require a higher particle surface coverage with less voided space in between particle clusters. The same holds true for C_8 as shown in **Figure 4-17c**. Additionally, when comparing the plateau value of elastic modulus at the LVE plateau ($G_c^{s\prime}$) for each surface pressure, C_0 monolayers presented the largest enhancement in $G_c^{s\prime}$ as the surface pressure was increased, followed by C_4 and C_8 (**Figure 4-18a**) This is directly correlated with the range of surface coverage changes experienced by these monolayers upon compression of the layer and increase in the surface pressure (**Figure 4-10**).

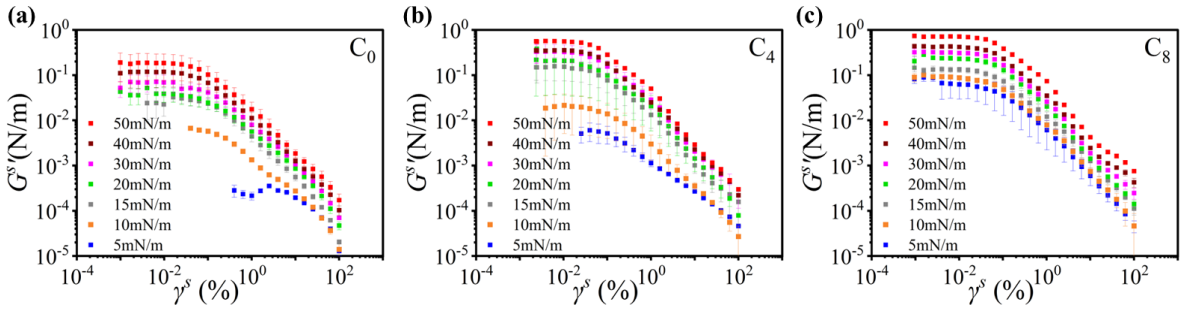

Figure 4-17. Elastic shear moduli of JP monolayers measured at ω = 1 rad/s, with increasing shear strain amplitude γ^s, as a function of surface pressure. The monolayers were formed by particles of different amphiphilicity as follows (a) C_0, (b) C_4, and (c) C_8.

From the shear amplitude sweeps, one can estimate the yield stress (τ_y) associated with each monolayer at a given surface pressure as described before (**Figure 2-4b**). **Figure 4-18** shows the results for all $\Delta\theta$. **Figure 4-18a** depicts the critical elastic modulus ($G_c^{s\prime}$) for each JP at different surface pressure. As discussed before, there is an increase in $G_c^{s\prime}$ as the surface pressure is increased. Interestingly, C_0 monolayers always show a smaller $G_c^{s\prime}$ when compared to C_4 and C_8. However, C_4 shows a transition from 10 to 15 mN/m where it shifts from an elastic modulus of the same order of magnitude as C_0 to $G_c^{s\prime}$ values comparable to C_8. This could be attributed to the changes in the microstructure where a transition from a more open network to a more densely packed is taking place upon the compression of the monolayer.

Figure 4-18b shows the critical shear strain (γ_c^s) for each sample at various surface pressures. The value of γ_c^s is closely related to the range at which interactions take place,[249] where longer-range interactions are associated with higher critical strains. It is possible to note that over the lower surface pressures studied (i.e., $\Pi < 30$ mN/m), C_0 monolayers show the higher γ_c^s, which can be associated with the dominance of the long-range dipolar interactions present at the monolayer from the higher concentration of tilted particles (**Figure 4-11**). Once the monolayer is

further compressed, the short-range hexapolar interactions take place and dominate the network, represented by a convergence of all samples at $\Pi \geq 30$ mN/m.

As shown by Eq. (2-8), the product of γ_c^s and $G_c^{s\prime}$ can be understood as the yield stress of the monolayer (τ_y). **Figure 4-18c** shows τ_y for each sample as a function of surface pressure and **Figure 4-18d** illustrates the same data as a function of surface coverage (estimated from the equation of state calculations, **Figure 4-8**). The shape of the curves is dictated by $G_c^{s\prime}$, especially at higher surface pressures, where γ_c^s values are similar for all samples. Nevertheless, τ_y of C_0 monolayers are slightly closer to C_4 and C_8 due to its higher γ_c^s. When shifting perspectives and looking into τ_y as a function of surface coverage (θ) in **Figure 4-18d**, C_0 monolayers show a higher yield stress at first, since it needs a lower surface coverage to form a network that resists the shear stresses. However, at high surface coverages, τ_y is comparable for all samples under study, which indicates that surface yielding at close to jamming surface coverages is weakly related to the monolayer amphiphilicity.

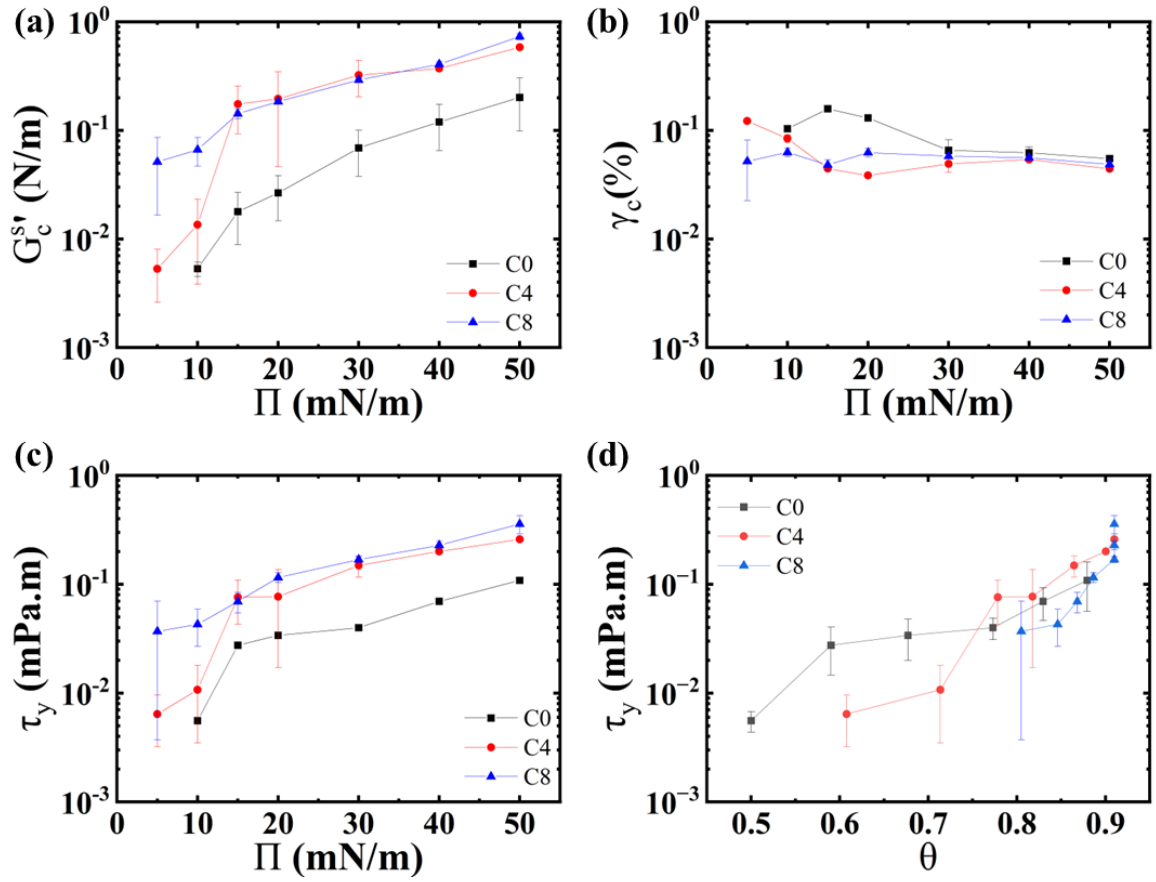

Figure 4-18. (a) Critical dynamic moduli, (b) critical shear strain γ_c^s, (c) yield stress τ_y of the JP monolayer with different amphiphilicities at various surface pressures and (d) surface coverages calculated from **Figure 4-8**, measured at ω = 1 rad/s.

Similar to the analysis done in **Figure 4-18**, one can also determine the properties of the surface related to yielding based on the crossover point, or the point at which $G^{s\prime} = G^{s\prime\prime}$, and the surface transitions from solid-like to fluid-like. **Figure 4-19** shows the results associated with the crossover for all amphiphilicities under study. It is possible to note that the crossover dynamic moduli (**Figure 4-19a**) has similar features to the one shown before (**Figure 4-18a**). However, from this perspective one can determine the crossover $G^{s\prime}$, for C_0 at the lowest surface pressure (5 mN/m), which was not captured in the previous analysis. **Figure 4-19b** shows the crossover strain (γ_{xo}^s), which is associated with the range of interactions taking place. It is clear that both C_0 and

C_4 are dominated by long range interactions at the lower surface pressures, whereas C_8 has a constant crossover strain amplitude throughout the surface pressures probed.

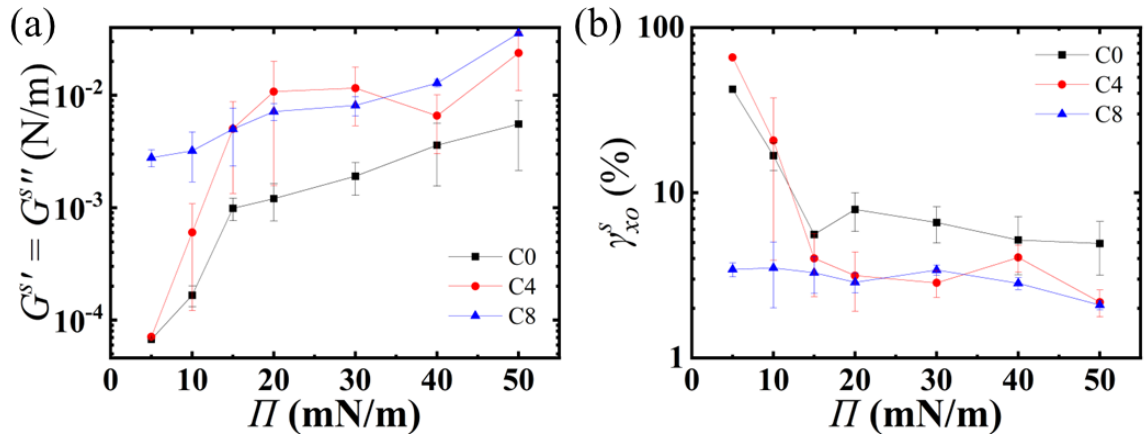

Figure 4-19. (a) Crossover dynamic moduli, or the point at which $G^{s\prime} = G^{s\prime\prime}$; (b) crossover shear strain γ^s_{xo}, or the amount of strain necessary to shift the monolayer from solid to liquid state.

Figure 4-20 shows the frequency sweep results within the linear LVE region for the different JPs at various surface pressures. It should be noted that the experiments were performed at a frequency range that encompasses a region dominated by instrument inertia (highlighted in red). Therefore, no data analysis was performed on the data within the highlighted range. In line with the results obtained for compression, the larger differences are observed between monolayers formed by the C_0 particles (**Figure 4-20a**) and those created by the C_8 particles (**Figure 4-20c**). The network formed by C_0 particles shows a frequency dependent response, with $G^{s\prime}$ increasing as the oscillating frequency increases. In contrast, the interfacial network of C_8 particles appears to be less sensitive to the time scale of the applied stress within the experimental window of frequency. Interfacial layer formed by the C_4 particles (**Figure 4-20b**) behaved in an intermediary fashion. This highlights that more amphiphilic particles tend to behave more solid-like when compared to less amphiphilic C_0 JPs, likely due to the more packed state of the interface.

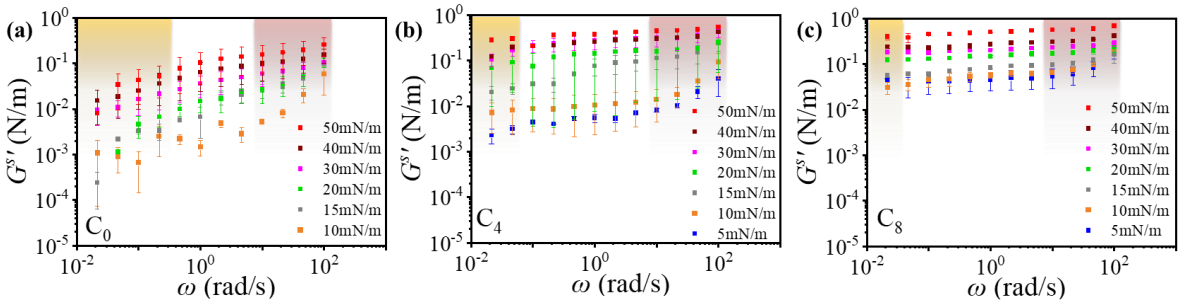

Figure 4-20. Dynamic moduli of the JP monolayer with different amphiphilicities at various surface pressures, measured at ω = 1 rad/s, with increasing shear frequency (ω). (a) C_0, (b) C_4 and, (c) C_8. For any data interpretation, high frequencies (highlighted in red) should be avoided since they are dominated by geometry inertia. Data highlighted in yellow should be taken with care.

The viscoelastic nature of the monolayer can be evaluated by analyzing the loss tangent, $\tan(\delta) = {G^{s\prime\prime}}/{G^{s\prime}}$, in which the value of $\tan(\delta)$ is lower than 1 for solid-like surfaces and smaller than 1 for fluid-like surfaces. **Figure 4-21** shows the evolution of the loss tangent over the frequency sweeps (in the range of 0.02 – 10 rad/s), at 15 and 40 mN/m. There is a clear tendency of a monolayer being more elastically dominated with higher amphiphilicities. Additionally, it is possible to notice that throughout the frequency range probed at the lower surface pressure (**Figure 4-21a**), C_0 monolayers transition from a fluid-like behavior at low frequencies to a solid-like response at frequencies higher than 2 rad/s. Such transition is present only for C_4 particles, which approach $\tan(\delta) = 1$ at frequencies close to 0.2 rad/s. C_8 monolayers behave solid-like throughout the whole range. It is important to note that at low surface pressures and frequencies, the measured torque approaches the limits of the rheometer[165], which explains the scatter data for C_0. For the higher surface pressure (**Figure 4-21b**), all curves are shifted down, towards a more solid-like scenario, as expected. At these conditions of pressure and frequency, the monolayer formed by C_0 particles is the only to cross $\tan(\delta) = 1$. Once more, this is likely due to the different microstructures present at these monolayers, in which C_0 possesses a lower surface coverage in comparison to the other samples.

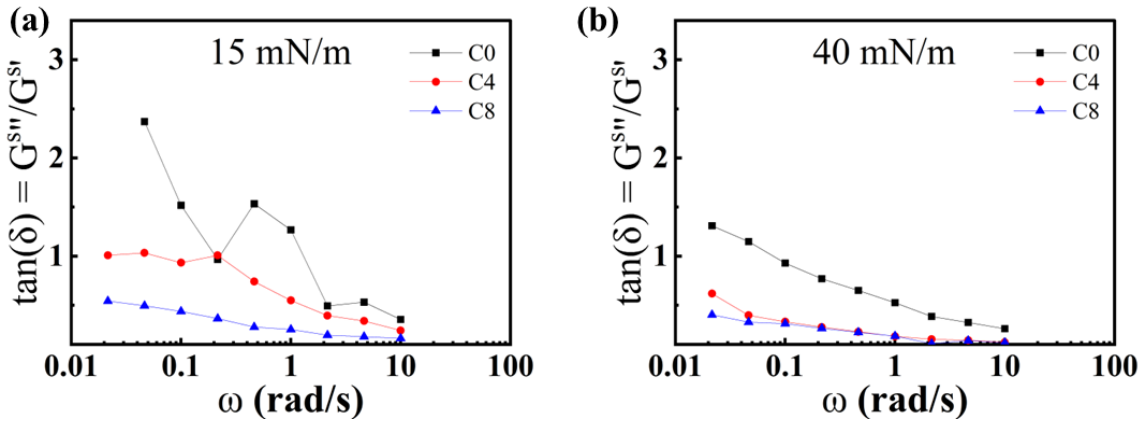

Figure 4-21. Loss tangent, $\tan(\delta)$, for monolayers formed by each JP sample at (a) 15 mN/m and (b) 40 mN/m. Data belonging to C_0, C_4, and C_8 particles are illustrated using black squares, red circles, and blue triangles, respectively.

It is possible to model the elastic response by a power law relation as $G^{s\prime} \propto \omega^{\beta}$ where the exponent $\beta = x - 1$; x is the effective noise temperature and is related to the energy barriers the particles need to overcome in order to jump into a new configuration of lower energy.[45] As x approaches 1 ($\beta \rightarrow 0$), the system approaches a glassy state. We fitted the experimental points within the frequencies of 0.1 and 10 rad/s as this is the most reliable range of measurements.[165] **Figure 4-22** shows the exponent β as a function of both the surface pressure and surface coverage of the monolayer. It is clear that there is an inverted correlation between β and $\Delta\theta$, as at all surface pressures, C_8 particles possess the smaller exponents, followed by C_4 and C_0. Even when changing perspectives and visualizing the data as a function of surface coverage the trend is similar (**Figure 4-22b**). Therefore, this is an indication that at those conditions of surface pressure and frequency of oscillations, C_8 particles are approaching a glassy state. A more in-depth discussion on this topic will be presented in the next section.

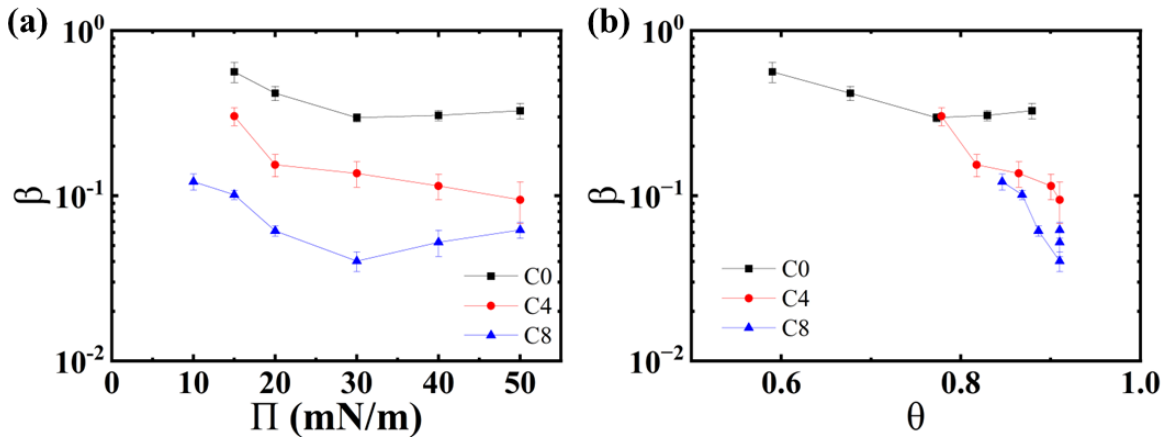

Figure 4-22. Exponent β as a function of (a) surface pressure and (b) surface coverage. Data belonging to C_0, C_4, and C_8 particles are illustrated using black squares, red circles, and blue triangles, respectively.

4.3.3. Summary of Findings

We studied the interfacial shear rheology of Janus particle monolayers formed by particles of different amphiphilicities. Amplitude sweep experiments were initially performed to determine the LVE regime and the conditions at which the surface layer yields. From the perspective of surface pressure, C_0 was associated with the smaller yield stress in comparison to C_4 and C_8. However, when shifting the perspective to surface coverage, it is possible to notice that C_0 forms a network strong enough to present a yield stress at lower surface coverages. Based on the amplitude necessary to yield and/or to reach the crossover, C_8 particles showed the shorter range of interactions, followed by C_4 and C_0, which is in agreement with the study done in the previous chapter. From the frequency sweeps, it is possible to conclude that C_0 monolayer exhibits a more viscoelastic character, followed by C_4 and C_8, which are more elastically dominated. From the exponential dependence present in the elastic modulus with frequency, we were able to infer that the C_8 monolayer is approaching a phenomenon analogous to a glass transition, which is the topic discussed in further detail in the next chapter.

4.4. Two-dimensional glass-transition-like behavior of Janus particle-laden interface

4.4.1. Introduction

In many applications, interfacial materials become subjected to shear flows and the interface does not remain static; therefore, the response of particle-laden interfaces under applied stresses is of critical importance for the stability of interfacial systems. Bulk rheological studies have been used to understand the properties of colloidal systems. For example, Katepalli et al. (2017) investigated the rheological behavior of Pickering emulsions stabilized by either spherical or fractal-like particles. It was demonstrated that by tuning the interparticle interactions of fractal-like particles from repulsive to attractive, the emulsion viscosity increased by one order of magnitude, whereas for spherical particles no appreciable difference was found.[117]

The two-dimensional rheology of interfaces has been used to corroborate stability mechanisms impacting the resulting performance of multi-component systems. Cicuta et al. (2003) showed that the elastic modulus of highly concentrated protein monolayers (β-lactoglobulin) at an air-water interface scales linearly with surface concentration. The authors relate this result to a parallel in 3D, where compressed emulsions at concentrations above the random close packing exhibit a similar behavior.[250] Soft-glassy behavior, reported to occur for asphaltene populated hexadecane-water surfaces (~2 molecules/nm^2), is shown to be responsible for the prevention of drop coalescence.[251] Similarly, unique rheological features have also been reported for particle-laden interfaces by altering the interparticle interactions via particle size, wettability, roughness, and shape, and the fluid properties such as pH and electrolytic strength.[155, 252] For instance, Van Hooghten et al. (2013) reported that rough carbon black particles (33 and 62 nm) present at an octane-water interface formed a monolayer that exhibited an attractive glassy behavior, which aged with time yielding a more elastic interface.[34] Maestro et al. (2015) demonstrated that hydrophobic

modification of silica nanoparticles (diameter of 30 nm) with surfactants increased their surface coverage and switched the surface behavior from fluid-like to solid-like, with 2D glass properties.[45] Shear-thinning behavior has been reported for percolating particle-laden interfaces at surface coverages below jamming.[253] Polystyrene particles (diameter 3.1 ± 0.2 μm) were studied at the air-water interface (3-phase contact angle of $\theta_E = 117°$), where the presence of a monovalent salt in the sub-phase (0.4 M NaCl) screened the repulsive interparticle interactions and allowed for the formation of dense particle aggregates strongly bound to the interface. Shear-thinning behavior at low surface coverage (Γ = 0.6) was attributed to the breakup of initially densely packed aggregates into smaller disordered clusters upon increasing the shear rate. At higher surface coverages (Γ > 0.7), some degree of shear induced ordering of particles into hexagonal packing was observed. The existence of a slip plane separating high and low shear rate zones was an indicator that the shear thinning behavior stems from yielding of the particle layer at the interface.[253] Shape anisotropic particles have also been studied at air-water interfaces.[166, 254, 255] Beltramo et al. (2017) demonstrated a significant yield stress in interfacial networks of shape anisotropic particles (polystyrene ellipsoids 2.48 μm long and 0.45 μm wide), much higher than for spherical particles at the same interfacial coverage.[166] This was sufficient to halt bubble dissolution and can be utilized in the design of Pickering foams with excellent stability to reduce bubble Ostwald ripening. A more comprehensive review on the rheology of particle-laden interfaces can be found elsewhere.[147, 256-258]

The rheological properties of JP monolayers formed by particles of different amphiphilicities were discussed in the previous section. In this section, we focus on interfacial monolayers formed by JPs of high amphiphilicity (i.e., C_8) to demonstrate how existing knowledge on 3D bulk rheology can help to gain understanding of the dynamics of particle-laden interfaces

and provide predictive capabilities for other linear viscoelastic material functions. Our data on frequency dependent interfacial rheology demonstrates that the 2D networks of JP-laden air-water interface undergoes a transition that resembles a glass at increased surface pressures.

4.4.2. Results and Discussions

4.4.2.1. Surface Pressure and Microstructure of Janus Particles at the Air-Water Interface

The surface pressure isotherm and the accompanying microstructure formed by the C_8 Janus particles at various surface pressures are provided in **Figure 4-23a**. As the surface area available for the particles was reduced by closing the barriers, from 150 to 60 cm^2, the surface pressure increased. The microstructure present at lower surface pressures (1 mN/m and 5 mN/m) illustrates large particle clusters with an area spanning open network. Additional pictures of the microstructure at 1 mN/m are provided in the Appendix B, **Figure B0-6**. The formation of area-spanning dendritic structures by JPs at a fluid interface has been reported by Park et al.,[259] and is attributed to the presence of capillary interactions between Janus particles. Compressing the monolayer further to surface pressure of 10 mN/m and above resulted in the disappearance of the open spaces and yielded a dense surface monolayer that is highly populated by the particles. The surface pressure isotherms obtained from these experiments were in good agreement with measurements carried out on the ribbon trough. The analysis of JPs orientation distribution with regards to the plane of the interface, performed on the SEM images, examples of which are provided in **Figure 4-23b** and **Figure B0-7**, shows that 78% of the particles resided at the interface with their gold cap orienting upwards (i.e., the Janus boundary was aligned with the air-water interface). It should be noted that the ensemble averaged value of the crystallinity order parameter (C_6), obtained over all particles in the monolayer captured within the SEM images, is calculated to be ~2.0 ± 0.1, indicating an amorphous structure (Appendix B).

Janus particles at fluid interfaces tend to present microstructures dominated by capillary interactions.[259, 260] These capillary interactions are usually of high order multipoles (either quadrupoles or hexapoles) as monopolar interactions are negligible for micron-sized particles (~10^{-7} k_BT) and dipolar interactions are neglected for homogeneous particles.[223] However, as shown in the SEM pictures of the microstructure and their analysis (cf. **Figure 4-23b**), not all the particles have their Janus boundary aligned with the surface. The presence of tilted particles introduces dipolar capillary interactions,[118] which in addition to the higher order capillary interactions dictate the overall microstructure. Moreover, while the capillary interactions between particles separated at large distances are attractive because the particles are able to reorient themselves with the generated torque, at smaller distances, and with the many-body interactions present in a dense monolayer, particles might not be able to reorient; thus, the lateral capillary interactions in the near field can even be repulsive. This is also evidenced in **Figure 4-29**, whereby increasing the surface pressure the maximum relaxation time increases, indicating larger structures that take longer to relax. Therefore, a complex network arises from these capillary interactions, which yields the interfacial rheological behavior reported in this work. The role of the particle orientation distribution on the resulting microstructure and its consequence for interfacial rheology of the JP monolayer have been discussed in chapters 5 and 6, respectively.

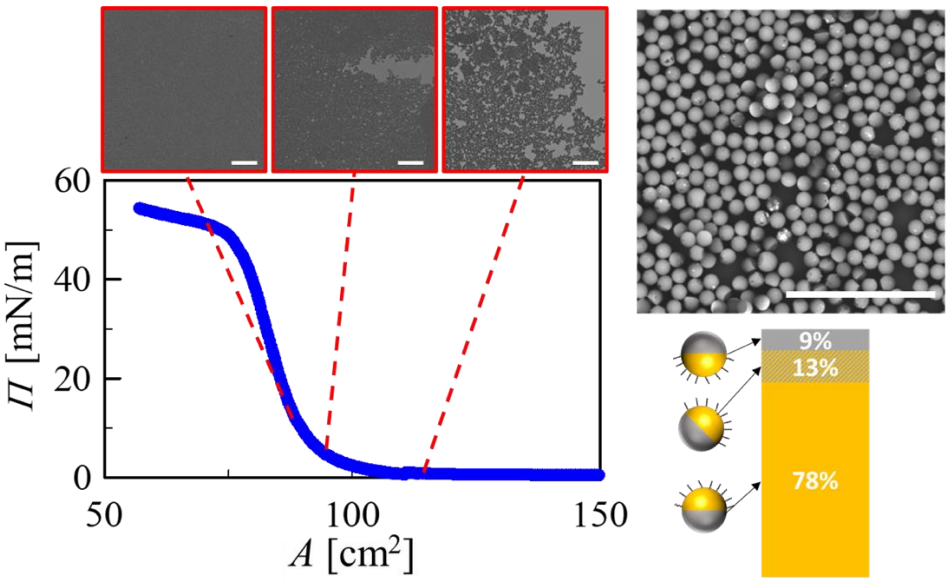

Figure 4-23. Surface pressure isotherm for the Janus particle monolayer at the air-water interface; examples of the microstructure formed at different surface pressures and captured by an inverted optical microscope are provided along the isotherm; from right to left the micrographs belong to the surface pressures in increasing order as follows: 1 mN/m, 5 mN/m, and 10 mN/m, respectively. Scale bar is 11 μm. (b) Illustrative SEM picture of Janus particle monolayer at 5 mN/m along with the distribution of the Janus cap orientation with regards to the plane of the interface (i.e., cap up, sideways, and cap down). Scale bar is 10 μm.

4.4.2.2. Surface Shear Rheology of Janus Particles at the Air-Water Interface

To identify the linear viscoelastic regime (LVE) for 2D interfacial networks, images of which are provided in **Figure 4-23**, strain amplitude sweeps were performed at 1 rad/s, and in the oscillation shear strain range of 0.001-100%, results of which are provided in **Figure 4-24**. It was found that the connectivity of the JP surface layer is strong enough to support shearing up to a shear strain amplitude of about 0.04%. With the knowledge obtained on the LVE region, the JP monolayer was subjected to a shear frequency sweep and its dynamic response was calculated from the instrument torque. The measured dynamic moduli are shown in Figure 4 at various surface pressures, which are related to the surface packing of JPs. Small amplitude oscillatory shear (SAOS) experiments provided reliable modulus data, $G^{s\prime}(\omega)$ and $G^{s\prime\prime}(\omega)$, by choosing a shear strain amplitude of 0.03%, which is in the LVE regime as determined earlier (see **Figure 4-24**).

The dynamic modulus increases in value as the surface pressure is increased as displayed in **Figure 4-25**.

As shown in **Figure 4-23**, the particle surface coverage is increased by compressing the surface area, as expected. From the Langmuir trough measurements, it is possible to note that most of the surface is occupied by particles at 10 mN/m, indicating that the surface coverage does not change considerably upon further compression. However, from the rheological measurements, there is an increase in $G^{s\prime}$ as the surface pressure is increased, which has been related to an increase in surface coverage.[166] We attribute this difference in behavior to the high interfacial shear viscosity of the monolayer, which can lead to a heterogeneous pressure distribution along the interface, specifically through the side openings of the geometry cup. Therefore, differences could exist between the surface pressure inside the cup and the value obtained from the Wilhelmy plate residing outside the cup.

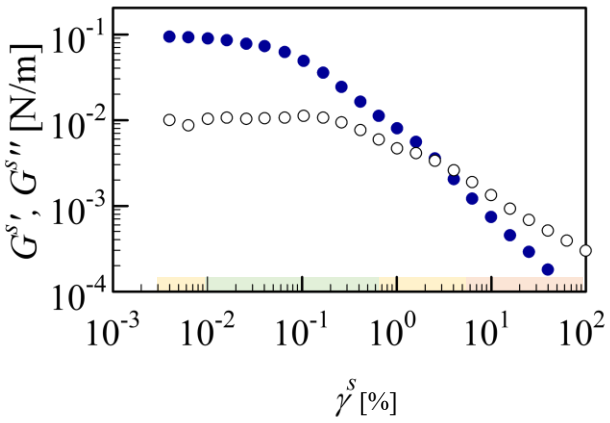

Figure 4-24. Dynamic moduli of the JP monolayer at Π = 30 mN/m, measured at ω = 1 rad/s, with increasing shear strain amplitude γ^{s}. Colored bars on the horizontal axis depict the operating windows as follows: measured stress/inertia stress is (orange) < 5, (yellow) > 5, and (green) > 10.

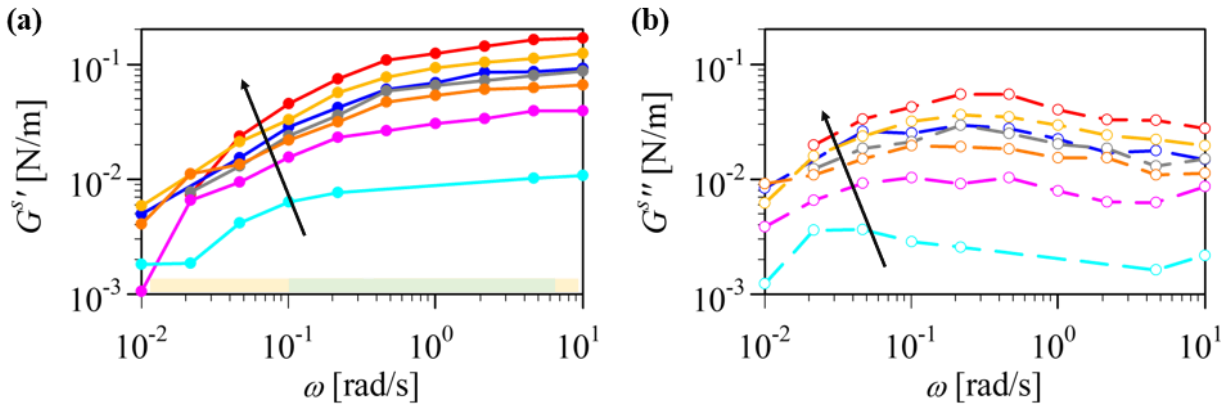

Figure 4-25. Dynamic moduli at increasing surface pressure (shown by the arrow) of Π = 5, 10, 15, 20, 30, 40, and 50 mN/m; (a) Storage modulus, (b) Loss modulus. Colored bars on horizontal axis depict the operating windows as follows: measured stress/inertia stress is (orange) < 5, (yellow) > 5, and (green) > 10.

With the exception of the lowest surface pressure (5 mN/m), which showed particle-void domains within the microstructure (cf. **Figure 4-23**), all $G^{s\prime}$ and $G^{s\prime\prime}$ data assume the same shape, for all surface pressures studied, and can be merged into a single set of master curves via a time-pressure superposition (tΠs). The tΠs process follows the classical pattern of 3D time-temperature superposition. Data at surface pressure of Π = 30 mN/m were chosen as reference state for generating the master curves. This required the time shift (horizontal shift factor, a_Π) and the modulus shift (vertical shift factor, b_Π) values of which are provided in **Figure 4-26**. The resulting master curves belonging to the various surface pressures are illustrated in **Figure 6a** and expressed as complex viscosity in **Figure 4-27b**. Both shift factors are about equally involved. In this way, the time-pressure superposition (tΠs) of JP monolayer dynamics varies from traditional time-temperature shifting where the vertical shift factor for $G^{s\prime}$ and $G^{s\prime\prime}$ is close to unity for many viscoelastic materials (3D).

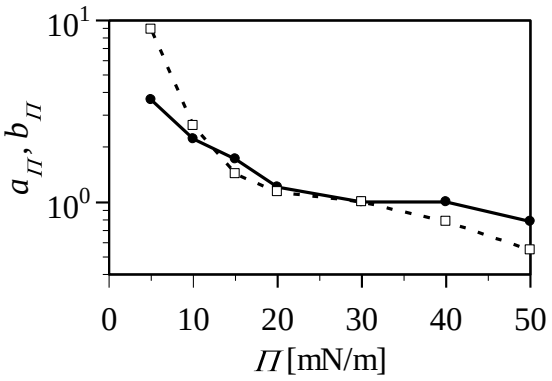

Figure 4-26. Horizontal shift factors a_Π (closed symbol) and vertical shift factor b_Π (open symbol). The reference state is Π = 30 mN/m.

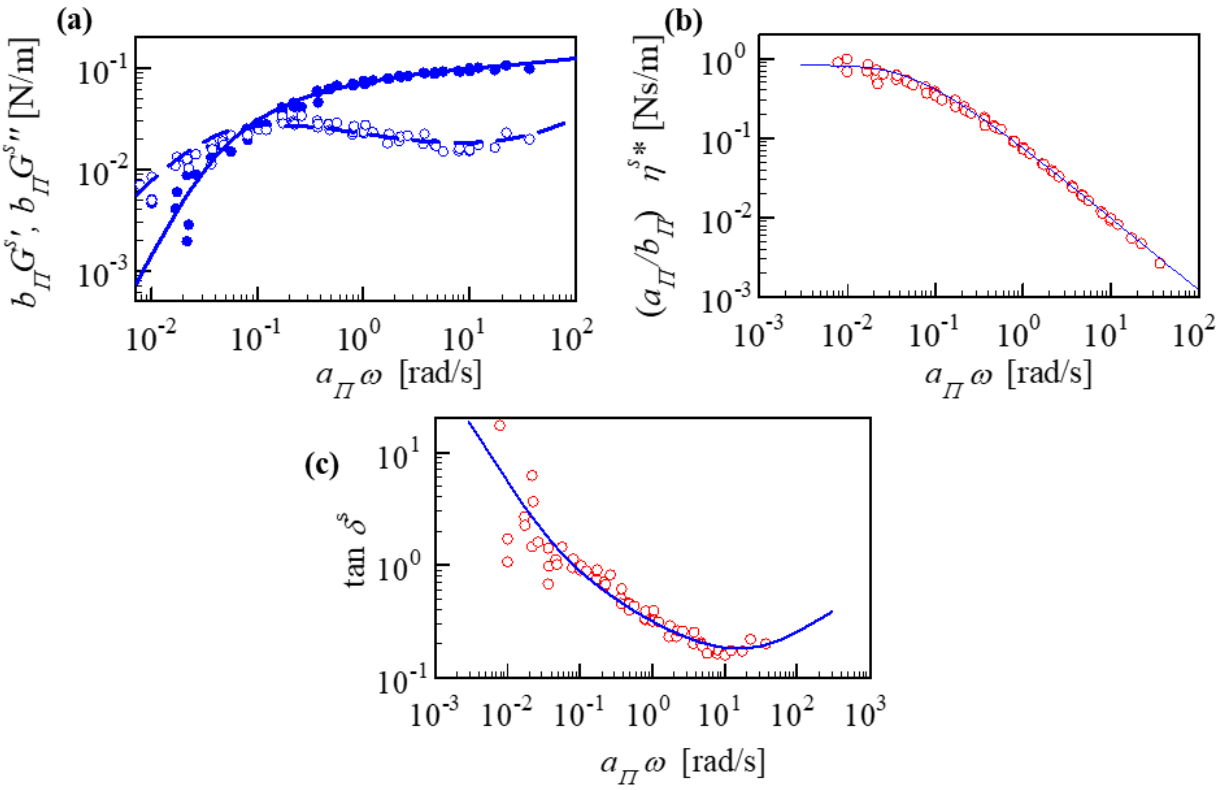

Figure 4-27. (a) Dynamic modulus data merged onto Π = 30 mN/m; $b_\Pi G^{s\prime}(\omega)$ closed symbols, $b_\Pi G^{s\prime\prime}(\omega)$ open symbols. (b) Complex shear viscosity from master curve at Π = 30 mN/m. (c) $tan\,\delta^s$ for master curve with experimental data as red open circles. The lines belong to the power law relaxation time spectrum, Eq. (4-8), as discussed in the text, with parameters listed with **Figure 4-28**.

The same data are presented in three different ways, always in conjunction with the respective spectrum predictions (Eq. (4-8), below). The loss tangent, displayed in **Figure 4-27c**, has the typical format as expected for a liquid. The choice of surface pressure Π = 30 mN/m as reference state is purely arbitrary. The data can now be shifted to other surface pressures, even to Π values in between, where no experiment has been executed. This free use of the data is possible because of the known tΠs shift functions, values of which are provided in **Figure 4-26**.

The validity of the $G^{s\prime}$, $G^{s\prime\prime}$ data was confirmed using the Kramers-Kronig check,[261] which involves the calculation of the relaxation time spectrum. At first, the data of **Figure 4-27** were modeled with the parsimonious model of Baumgärtel et al.,[262, 263] which seeks a discrete relaxation time spectrum, Eq. (4-8), with the least number of discrete modes for optimal fit (avoiding over-fitting) and converts this spectrum into an approximate continuous form. The pattern of the parsimonious spectrum for the JP monolayer suggests a power law format. Inserted into equations (3-29) and (3-30), the continuous relaxation time spectrum of the parsimonious model[262, 263] was able to fit the experimental $G^{s\prime}$and $G^{s\prime\prime}$ of **Figure 4-24** and **Figure 4-27a**. The shape of the parsimonious relaxation time spectrum (**Figure 4-28**), having a dominant positive slope and a fairly abrupt cutoff, indicates the possibility of a power-law spectrum very much like the BSW spectrum of a colloid near its glass transition.[264, 265] This is expressed as a linear superposition of two power laws. The long-time relaxation behavior (α-mode) belongs to large scale rearrangements in the surface layer, while localized particle rearrangements and their short time characteristics give rise to the faster β-mode:

$$H^s(\tau) = {H_\alpha}^s \left(\frac{\tau}{\tau_{max}}\right)^{n_\alpha} + {H_\beta}^s \left(\frac{\tau}{\tau_\beta}\right)^{-n_\beta} \qquad (4\text{-}8)$$

Valid for $\tau \leq \tau_{max}$. Beyond that upper time limit, $\tau_\alpha = \tau_{max}$, the spectrum does not exist, $H^s(\tau) = 0$, for $\tau > \tau_{max}$. τ_β denotes the minimum in the spectrum where the two power laws meet. This spectrum was found to closely reproduce the experimental data as shown in **Figure 4-27** for the Π = 30 mN/m interface. An overlay of the parsimonious spectrum and the BSW spectrum compares the two in **Figure 4-28**.

As previously discussed by Winter (2013), the relaxation time spectrum for glass transition and gelation phenomena of bulk materials broadens and assumes a power law format. However, the power law exponent is positive for glass transitions and negative for gelation near the transition. This distinguishing difference originates from the fact that gel rheology is dominated by fast modes of relaxation, whereas glass transitions are dominated by slow modes of larger patches.[265] Therefore, the fact that H^s obtained for the Janus particle monolayer at 30 mN/m has a positive slope, corroborates the idea that a transition analogous to a glass is taking place.

The re-appearance of the BSW spectrum is really striking. There seems a common rheological pattern in viscoelastic liquids when caging dominates their dynamics. The BSW spectrum has occurred in polymeric liquids with long linear flexible molecules of uniform length.[266] There, polymer molecules are envisioned to be caged by neighboring molecules in a tube-like constraint.[267] In this study, 2D dynamics of the Janus particles at the interface involves constraining by neighboring particles, which can be envisioned as two-dimensional caging. To go even further, the glass transition of colloids can also be envisioned as a caging process, which will occur in three dimensions and also is governed by BSW dynamics. Caging is the common feature that might connect all three. However, as the capillary interactions governing the monolayer of JPs of this work are dependent on the orientation of the Janus patches as the particles approach each other, and because densification of the particles at higher surface pressures constrains their

reorientation at the interface, both attractive and repulsive capillary interactions may be present between the particles throughout the interfacial monolayer. Therefore, the 2D cages present in our experiments are more complex and harder to define as further elaborated below.

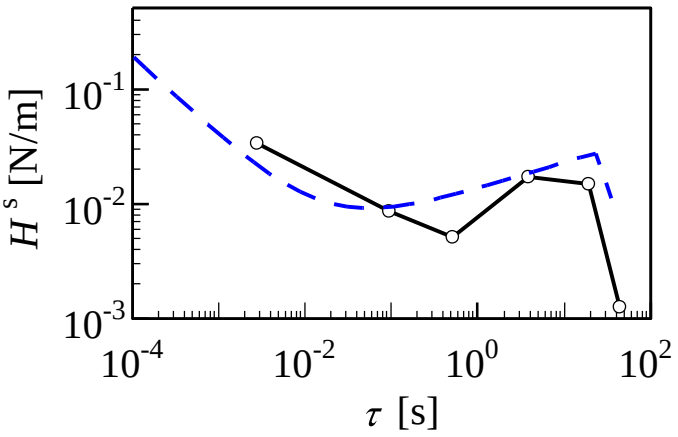

Figure 4-28. Continuous relaxation time spectrum $H^s(\tau)$ as determined by parsimonious method[262, 263], shown with discrete points, and approximated as continuous function, Eq. (4-8), shown in dashed line. Π = 30 mN/m data were approximated with ${H_\alpha}^s = 0.03$ N/m; $\tau_\alpha = 34.7$s; $n_\alpha = 0.2$; $\tau_\beta = 1.35 \times 10^{-3}$s; $n_\beta = 0.7$, using a simplified ${H_\beta}^s = {H_\alpha}^s$.

The pair of master curves of dynamic moduli for all surface pressures (see **Figure 4-27**a), shifted to 30 mN/m, includes the crossover between $G^{s\prime}$ and $G^{s\prime\prime}$, which characterizes the frequency at which the surface behavior is switched from viscous-dominant to elastic-dominant, all while remaining in the liquid state. It has become common practice to define a nominal longest relaxation time based on the frequency of the $G^{s\prime} = G^{s\prime\prime}$ crossover.

$$\tau_{G^{s\prime}=G^{s\prime\prime}} = \frac{2\pi}{\omega_{G^{s\prime}=G^{s\prime\prime}}} \qquad (4\text{-}9)$$

For the JP monolayer of this study, the longest relaxation time is close to $\tau_{G^{s\prime}=G^{s\prime\prime}}$ only slightly smaller:

$$\frac{\tau_{max}}{\tau_{G^{s\prime}=G^{s\prime\prime}}} = 0.42 \qquad (4\text{-}10)$$

The value of this ratio depends on material specifics but is the same for all compositions of this study satisfying tΠs. That includes the Janus dynamics, see **Figure 4-27**. The BSW model, Eq. (4-8) with data of **Figure 4-28**, provides the values of $\tau_{G^{s\prime}=G^{s\prime\prime}}$ and of τ_{max} as appropriate for the experimental data. The values of τ_{max} obtained for different surface pressures are provided in **Figure 4-29**. The relation between τ_{max} and Π was generated by taking the τ_{max} value at the reference state, τ_{max} = 34 s at Π = 30 mN/m, and shifting it in the same way as $G^{s\prime}$ and $G^{s\prime\prime}$ were shifted to generate the Π = 30 mN/m master curve.

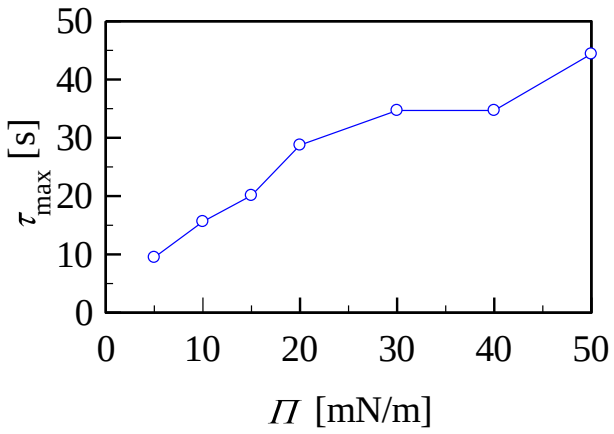

Figure 4-29. Dependency of the maximum relaxation time on the surface pressure of the JP monolayer.

The relaxation time spectrum of interfacial layers formed by Janus particles, Eq. (4-8), is new for 2D viscoelasticity, but it is exactly the same as was found earlier in 3D viscoelasticity. There, it defines the dynamics of the colloidal glass transition in three dimensions.[264] Macroscopically, the colloidal dynamics of the 3D glass transition is re-occurring in the two-dimensional viscoelasticity of the Janus particle monolayer. From these findings, and due to the

similarity to the 3D phenomenon, we infer that the interfacial assembly of Janus particles undergoes a transition analogous to a 2D glass.

4.4.2.3.Linear viscoelastic properties of Janus particle-laden interfaces

The known relaxation time spectrum can now provide predictive capabilities to be used to evaluate linear viscoelastic material functions such as the relaxation modulus $G^s(t)$, as defined in Eq. (3-27), and the creep compliance $J^s(t)$. For this, we use the relaxation time spectrum as calculated with the parsimonious model in comparison to BSW. The time-dependent relaxation modulus and creep compliance, **Figure 4-30**, are very similar for the two models of the relaxation time spectrum presented in **Figure 4-28**.

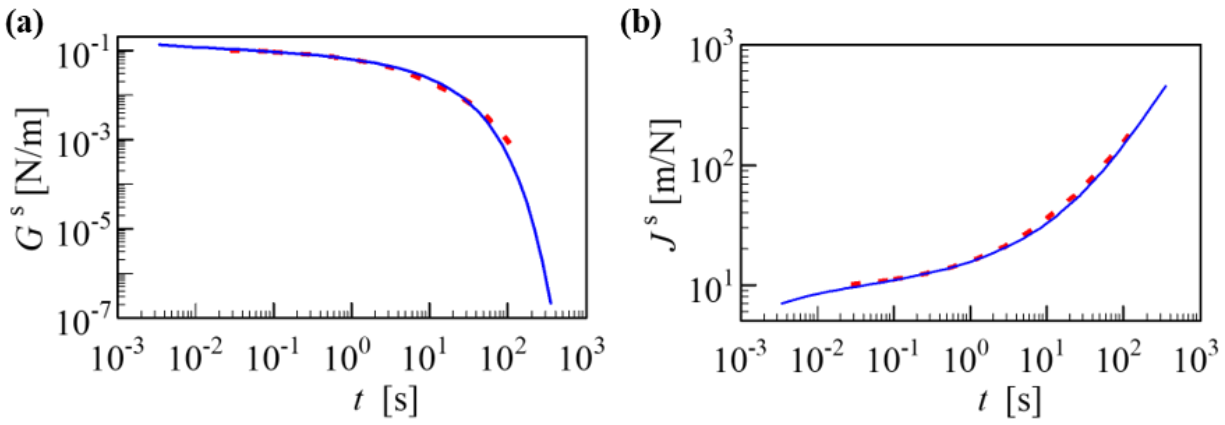

Figure 4-30. The known relaxation time spectra allow predictions of other linear viscoelastic functions for Π = 30 mN/m dynamics: (a) Relaxation modulus, (b) Creep compliance; dotted lines for parsimonious spectrum and continuous lines for BSW power law relaxation time spectrum, Eq. (4-8), and parameter values as listed with **Figure 4-28**.

The SAOS experiments did not allow us to increase the frequency to a level where more of the β-dynamics would govern as the geometry inertia takes place. It is outside our SAOS range, while barely showing the onset of β-dynamics as the upper end of the ω-window. Dedicated high frequency methods would be needed to learn more about the β-dynamics, which is outside the focus of the current study. In consideration of this limitation, little information is available here

about the β-modes since $G^{s\prime}$ and $G^{s\prime\prime}$ data were taken in a frequency range were the α-modes dominate. Without accounting for the β-modes, the zero-shear surface viscosity reduces to:

$$\eta_0{}^s = \frac{H_\alpha{}^s \tau_{max}}{1 + n_\alpha} \tag{4-11}$$

The corresponding zero-shear compliance calculates as:

$$J_0{}^s = \frac{n_\alpha}{H_\alpha{}^s}\left(1 + \frac{1}{2n + n^2}\right) \tag{4-12}$$

These are a few examples. The choice of Π = 30 mN/m is arbitrary. With the given spectrum we can equally predict properties at the other surface pressures, or in between, as long as they satisfy the tΠs. Material functions as shown here are useful for advancing application examples which were provided in the introduction.

The shear response of monolayers at interfaces is frequently weaker when compared to that of bulk materials. For that reason, measurements are usually taken close to the lower torque limits of rheometers. In addition, the subphase drag contribution might introduce noise into the system if one is operating at low values of *Bq* number.[165] To account for the subphase corrections, flow field calculations were developed by Vandebril et al. to correct the apparent shear rate taking into account the coupling of bulk and interface.[161] In short, the algorithm consists of solving the velocity profile at the interface and in the subphase numerically, and estimating the drag contribution from the subsurface, which allows for its removal from the raw data. As stated in Vandebril et al., *Bq* >> 100 is desired when conducting interfacial rheology measurements to ensure negligible contributions from subphase drag.[161] Therefore, we applied the subphase correction to decouple the interfacial contribution from the bulk generated drag and examine the significance of the bulk contribution in the generated data. The comparison between the raw data

and the sub-phase corrected data is provided in **Figure 4-31**, which illustrates that the master curve obtained from both data sets are in good agreement.

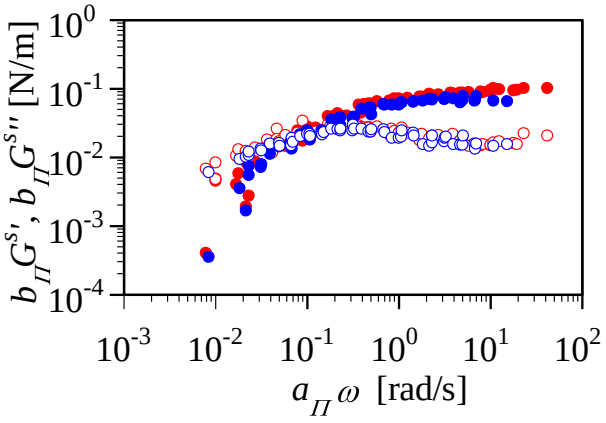

Figure 4-31. Comparison of the master curves generated by the raw data and the subphase-corrected data obtained using the algorithm by Vandebril et al. Red is the raw data and blue the corrected data.

4.4.3. Summary of Findings

In this chapter, we demonstrated how classical rheology analysis can be applied to the generated small amplitude oscillatory shear data obtained in 2D such as the Janus particle monolayers, which are the subject study in this thesis. The data obtained at various surface pressures were collapsed into a master curve via a time-pressure superposition (tΠs). By analyzing the time relaxation spectrum, we have found that a transition that resembles that of a glass transition is occurring in the interfacial network of Janus particles. The time-relaxation spectrum further provides us with predictive capabilities and allows us to describe additional linear viscoelastic material functions for two-dimensional materials that can be useful in the rational design of formulations tailored to different applications.

5. Mixed Systems of Negatively Charged Particles and Sodium Dodecyl Sulfate

In this chapter, we focused on studying the mixed systems of particles and surfactants at interfaces to understand their synergistic/competitive behavior near interfaces. However, since we are investigating a system with similarly charged particles and surfactants, we first need to address two subjects carefully: (1) Is there adsorption of SDS onto the surface of silica? If so, what are the conditions that promote or prevent such adsorption? (2) What is the importance of SDS hydrolysis on interfacial properties relevant to the system? At which point does the contaminant concentration become relevant? We will first investigate these two questions and then proceed to the interfacial measurements of the mixed system.

5.1. Adsorption of SDS onto hydrophilic silica particles: Studies in Buk

5.1.1. Introduction

The interactions of oppositely charged species are well documented, especially for mixed systems including silica particles, due to their ubiquitous industrial and technological applications.[131, 268] When negatively charged silica particles are mixed in solution with a cationic surfactant such as Dodecyltrimethylammonium Bromide (DTAB), the strong attractive interaction between the two species leads to the adsorption of surfactant molecules onto the surface of nanoparticles.[268-270] This phenomenon has been reported for multiple sizes of silica nanoparticles[268, 269] and has been employed in tuning the particles wettability. Adsorption of cationic surfactants onto the surface of silica particles, – that are hydrophilic due to the dissociation of their surface silanol groups in water – promotes the hydrophobicity of silica particles, which in

turn makes the mixture of silica particles and cationic surfactant an effective stabilizer for foams and emulsions.[271, 272] While at low surfactant concentrations, the attraction of the cationic surfactants polar head onto the surface of the negatively charged particle leads to an adsorbed surfactant layer, increasing the surfactant concentration can result in the formation of a bilayer on the surface of the particles, with the surfactant head groups exposed to the bulk solution.[271-273] Since the adsorption of surfactants, in form of a single layer or a bilayer, onto the surface of an oppositely charged particle can alter the particles wettability and surface charge differently, tuning the surfactant concentration is of interest in many industrial applications.[270, 273]

When comparing like-charged species, such as silica nanoparticles and anionic surfactants, a distinct scenario can arise in contrast to oppositely charged species. One observation is that the addition of anionic surfactant to a dispersion of silica nanoparticles can induce a more negative zeta potential in the system; this behavior has been attributed to the surfactants adsorption onto the surface of the particle, in a tail down configuration, since the polar head is repelled from the surface.[274] This type of interaction could decrease particle agglomeration and enhance the dispersion stability as the presence of anionic surfactant molecules on the particles surface leads to a pronounced repulsive interparticle interaction.[274] In contrast, it has also been reported in the literature that silica nanoparticle dispersions can be slightly destabilized by the addition of anionic surfactant, a behavior which has been attributed to an increased negative background potential that facilitates particle collisions.[275] A number of factors are reported to affect surfactant adsorption onto silica particles including the particle size, surfactant concentration, and solution properties such as its ionic strength and pH.[276-279] Even for the case of widely used anionic surfactant, sodium dodecyl sulfate (SDS), previous studies[276, 277, 280-286] have been inconclusive with regards to the solution conditions at which SDS adsorption onto silica particles occurs, if at all, specifically

regarding the impacts salt addition and pH alterations will have on the resulting behavior, as illustrated in **Figure 5-1**.

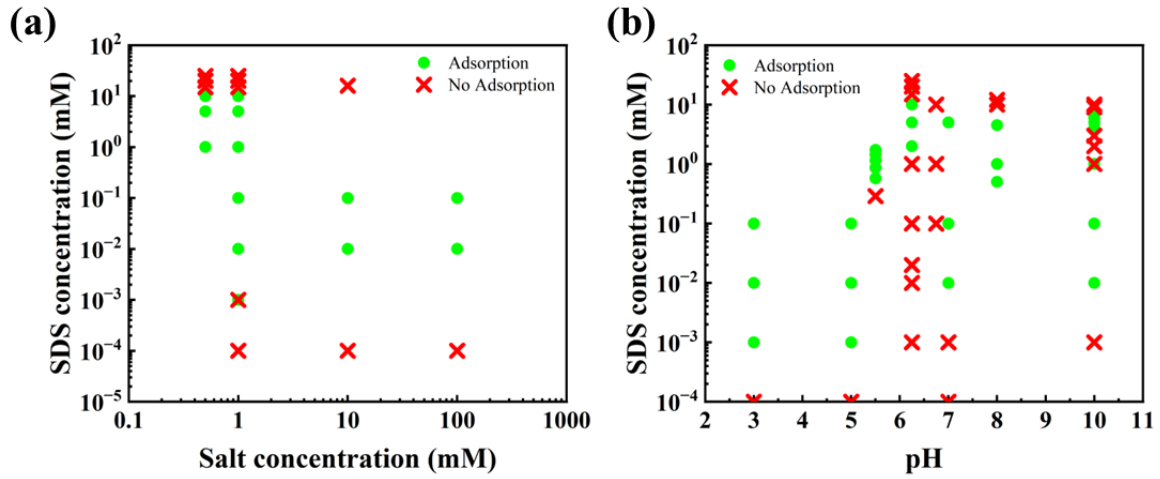

Figure 5-1. Studies available in the literature on mixed SDS surfactant/silica particle systems reporting on adsorption, or lack thereof, SDS molecules onto the surface of silica particles. Available data on studies carried out at various SDS concentrations are presented as a function of (a) salt concentration, and (b) pH. Green circles (red crosses) indicate conditions at which adsorption (no adsorption) was reported. Data is reproduced from the following references *276, 277, 280-286*.

In presence of salt, in a mixed solution of silica nanoparticles and SDS molecules, adsorption of the surfactant onto the particle surface has been reported under certain conditions. For instance, significant adsorption has been reported at electrolyte concentrations above 10 mM and surfactant concentrations above 0.01 mM.[276] Adsorption has also been observed to increase as surfactant concentration increases under varying salt conditions until the critical micelle concentration (i.e., CMC) is reached, at which point adsorption is reported to decrease as micelles form in the solution.[285] In contrast, a complete lack of adsorption of SDS on the surface of silica particles has also been reported even in the presence of electrolyte.[287] As can be seen in **Figure 5-1a**, with the reports available on the effects of salt addition on the adsorption, or lack thereof, in a mixed system of SDS and like-charged silica particles, it remains unclear what electrolyte conditions induce adsorption.

The effect of pH on adsorption is similarly inconclusive. At a slightly basic pH of 8, low quantities of SDS were found to adsorb onto the silica particle surface.[286] Adsorption is also reported at the more basic pH of 10 where the occurrence of adsorption was confirmed by both increased hydrodynamic size of silica particles and their supercharging.[282] In some cases, it has been suggested that SDS does not adsorb onto silica particles, specifically near neutral pH conditions.[280, 283, 288] In contrast, occurrence of adsorption has also been reported at a neutral pH, for SDS surfactant concentrations in the range of 3.5 mM to above CMC (~8 mM).[281, 289] A study on pH effects reported adsorption at various pH values tested (i.e., 3, 5, and 7); where a decrease in the amount of adsorbed surfactant was found upon increasing the pH, increasing the SDS surfactant concentration was reported to promote adsorption at all pH values.[276] As can be seen in **Figure 5-1b,** while reports are available on mixed system of silica particles and SDS, the findings are inconclusive about the pH range and surfactant concentration at which adsorption between the two species occurs. Furthermore, in mixed SDS/silica systems, without any background electrolytes, conflicting results have been reported regarding the SDS adsorption. Some authors suggest the occurrence of adsorption, while others argue its absence.[28, 284, 290, 291]

In order to tune the adsorption of surfactants onto the surface of similarly charged particles, it is first necessary to determine the conditions that induce adsorption. Through systematic variation of the surfactant concentration, ionic strength of the solution (i.e., by the addition of background salt and/or SDS), and the particle's surface charge, conditions needed for adsorption could be examined. For instance, pH variations affect the dissociation of the surface groups on the particles surface, altering the strength of electrostatic interactions between similarly charged species.[52] Additionally, changes in the ionic strength could affect the interactions between the surfactant molecules and the corresponding CMC value.[292] Therefore, one needs to carefully

examine the impact of each contributing factor on the resulting behavior in order to specify the regions within the parametric space over which adsorption occurs between similarly charged silica particles and SDS surfactant. The focus of the present work is to investigate the significance of factors that, in the available literature, are reported to play a role in the observed behavior in the mixed SDS/silica system and decouple the convoluted impacts of solution pH, electrolyte concentration, and surfactant concentration. We utilize light scattering experiments to measure the mobility of particles in mixed SDS surfactant/silica particle systems. From this information, we estimate the particles surface charge density and examine the impact of different variables such as the electrolyte concentration, pH, and surfactant concentration on the adsorption behavior. Our findings provide insight on the significance of these attributes with respect to adsorption behavior and highlight the range of solution properties that promote like-charge adsorption.

5.1.2. Results and Discussions

5.1.2.1. Characterization of Particle Dispersions

Results of SEM imaging of particles and the characterization of particle dispersions at low background salt concentration of 0.1 mM KNO_3 are provided in **Table 5-1**. The pH value, averaged over all the dispersions used in these studies, was 5.4 ± 0.2. It should be noted that silica particles of size larger than 500 nm, for which $Pe \geq 1$, were not deemed suitable for this study as particle sedimentation impacts the DLS measurements.

Table 5-1. Properties of silica nanoparticles used in this study: particle diameter estimated from SEM analysis (D_{SEM}), hydrodynamic diameter (D_H) obtained from the DLS measurements carried out in 0.1 mM background KNO_3 electrolyte solution, value of particle's zeta potential (ζ) measured at the same conditions, and the charge densities estimated using κR determined based on the measured D_{SEM}. The pH for all dispersions was 5.4 ± 0.2.

Silica particle nominal size (nm)	$\boldsymbol{D_{SEM}}$ **(nm)**	$\boldsymbol{D_H}$ **(nm)**	$\boldsymbol{\zeta}$ **(mV)**	$\boldsymbol{\rho_s}$ **(μC/cm^2)**

100	100 ± 30	129 ± 1	-57 ± 1	0.31 ± 0.01
200	210 ± 40	253 ± 4	-58 ± 6	0.26 ± 0.03
500	500 ± 60	529 ± 7	-72 ± 2	0.31 0.02

5.1.2.1.1. Effect of Electrolyte

Variation in the electrolyte concentration was carried out in particle dispersions of different sizes in order to examine the severity of the resulting aggregation. Initial experiments were carried out in the absence of SDS to determine the salt concentrations that can be used in the study of mixed surfactant/particle systems to generate reliable data from the DLS measurements. The experiments were performed at a number of KNO_3 electrolytic concentrations (0.1, 1, 10, and 1000 mM), without adding any acid or base to the dispersion. The effect of salt concentration on the measured hydrodynamic diameter (D_H) of the particles is presented in **Figure 5-2a**. As expected, with increasing the salt concentration, the average particle size also increased. As the salt concentration increased in the range of 1 to 100 mM, the rate of increase in the measured hydrodynamic size was larger for the 500 nm particle sample, which could be interpreted as aggregate formation even at low salt concentrations (1 mM) in this case and faster sedimentation for aggregates forming by the larger 500 nm particles. As the salt loading was further increased to 100 mM KNO_3, the 100 nm particles formed aggregates of larger size (1578 ± 296 nm) compared to those resulted from 200 nm (298 ± 10 nm) and 500 nm particles (850 ± 61 nm), which can be explained by their higher surface to volume ratio and the reduced surface electric potential at the high salt concertation used. **Figure 5-2b** depicts the variation in the measured zeta potential of the particle dispersions as a function of electrolyte concentration. It can be observed that zeta potential exhibited a logarithmic dependence on the ionic strength, where increasing the electrolyte concentration led to a reduced magnitude of the zeta potential. Moreover, with increasing the electrolyte concentration, the magnitude of zeta potential reduced for all particle dispersions. This

trend is expected due to screening of particle surface charges by increasing the ionic strength in the bulk, which results in a shorter Debye length. The value of κ^{-1} estimated from the calculated effective concentrations reduced from 17.8 ± 0.7 nm at 0.1 mM KNO_3, to 1.0 ± 0.1 nm at 100 mM KNO_3.

It is important to highlight that the hydrodynamic size measurements could be used as an indication for colloidal stability vs. aggregate formation. Therefore, these experiments were run as screening tests in order to determine whether such effects (e.g., aggregation) are present in particle dispersions, at various solution conditions of interest, because they could impact the results and interpretation of the mobility measurements, which are then used to infer about SDS adsorption. Since the 500 nm particle samples exhibited an increase in measured particle size at all electrolyte concentrations, we limited the study of mixed surfactant/particle systems in bulk to the 100 nm and 200 nm particle sizes only. In the latter two cases, we also restricted the interpretation of the data obtained via hydrodynamic size measurements to electrolyte concentration below 10 mM in order to avoid aggregation effects impacting the results of the measurements.

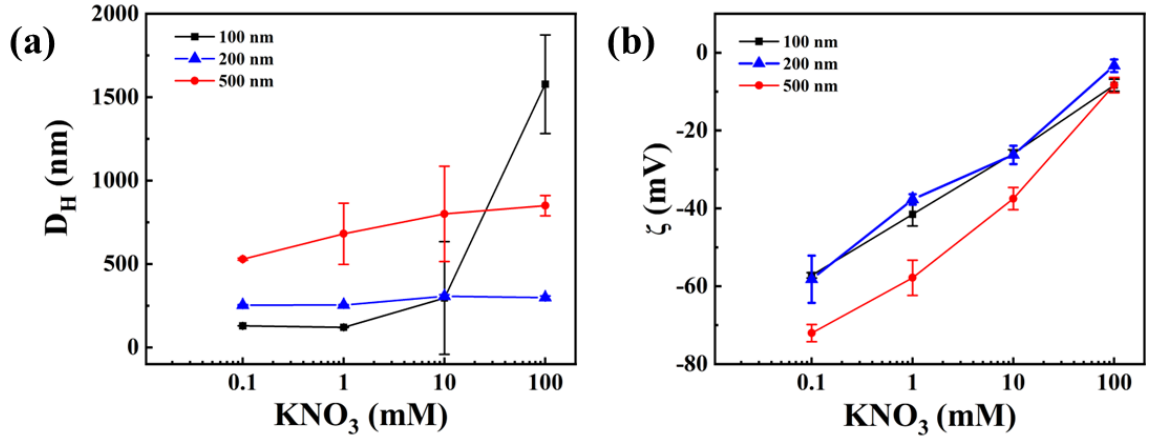

Figure 5-2. Effect of KNO_3 electrolyte concentration on (a) hydrodynamic size (D_H) and (b) zeta potential of particle dispersions with particles of size 100 nm (black square), 200 nm (blue triangle), and 500 nm (red circle).

5.1.2.1.2. Effect of pH

In order to examine the response of particle-only dispersions to alterations in pH and the differences between the characteristics of the two particle sizes under study (i.e., 100 nm vs. 200 nm), zeta potential measurements were carried out at different pH values (at 1 mM KNO_3) results of which are displayed in **Figure 5-3**. It is worth noting that no pronounced aggregation was observed for the systems analyzed here. For the case of 100 nm particle dispersions (**Figure 5-3a**), at a neutral to high pH range (6-9), the value of measured zeta potential remained nearly constant with pH alterations. This behavior could be attributed to the complete dissociation of the surface silanol groups present on the silica particles, which may possess several pKa values depending on their characteristics.[178-180] At low pH values (pH <5), due to the presence of excess hydronium H_3O^+ ions in the bulk, there was a reduced tendency for ionization of the surface silanol groups, which consequently resulted in a decrease in the magnitude of the measured zeta potential. Applying the model described in Eq. (3-6), it was found that the pKa value associated with the best fit is ~2.1, which is aligned with the pKa value attributed to vicinal silanol groups.[180]

For the 200 nm dispersion (**Figure 5-3b**), a similar response to pH alterations was captured. Modeling the zeta potential values obtained from the pH sweep in case of 200 nm particle dispersions yielded a pKa value of ~2.9, which agrees with the pKa values for external geminal silanol groups.[180] This corroborates the higher surface charge density found for 100 nm particles when compared to the 200 nm (**Table 5-1**), since vicinal groups are associated with silanol that are in proximity to each other. In addition, at the high pH region, there was a further increase in the magnitude of the zeta potential, which might be associated with isolated silanol groups (pKa ~8.9) present in the 200 nm particle surface.[179, 180] To incorporate this factor when fitting the data

with the model, the left-hand side of the Eq. 6 was calculated with both pKa values (2.9 and 8.9) and summed.

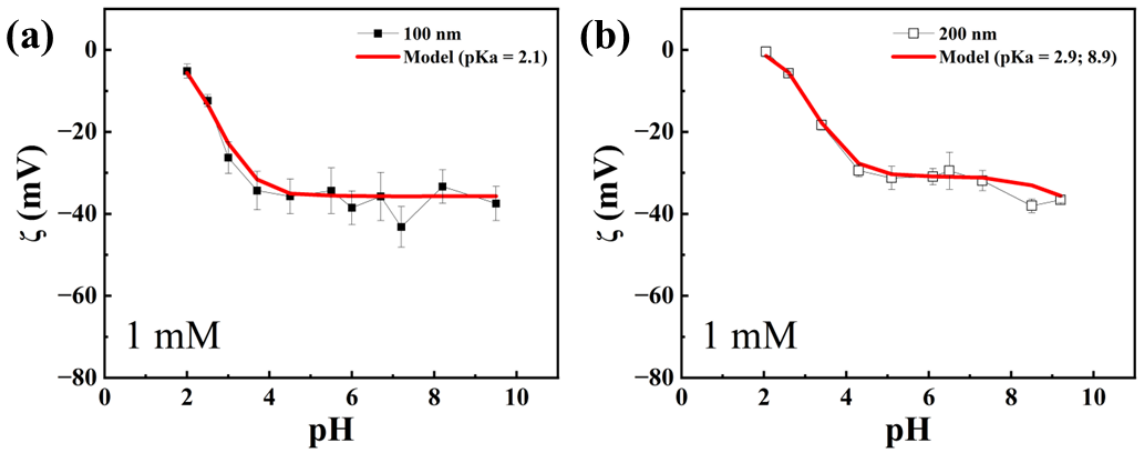

Figure 5-3. Effect of pH on the zeta potential of (a) 100 nm (b) 200 nm particles. The model was calculated based on Eq. (3-6) and a pKa input value of 2.1 was used to fit the zeta potential data obtained for 100 nm particles, while a combination of pKa values of 2.9 and 8.9 were used for the case of 200 nm particles.

5.1.2.2. Characterization of Mixed Surfactant/Particle Systems in Bulk

5.1.2.2.1. Effect of SDS at Various pH

The behavior of the mixed surfactant/particle system was analyzed as a function of the solution pH, for the salt (KNO_3) concertation of 1 mM. It should be noted that for the mixed surfactant/particle systems, no pronounced increase in the measured particle size was observed as the pH was lowered. **Figure 5-4a** illustrates the change in the measured zeta potential for mixtures prepared with 100 nm particle dispersions. The presence of surfactant affects the particle surface characteristics, as manifested in the increased zeta potential magnitude across pH values smaller than 5. Measuring a more negative zeta potential value, in presence of the surfactant within the mixture, can be attributed to the adsorption of surfactant molecules onto the particles surface. At a neutral to high pH range (6-9), the effect of surfactant addition on the zeta potential was less

pronounced compared to its impact at low pH range (2-5). This trend is expected since at the high pH range, there is a higher extent of dissociation for the silanol groups present on the particle surface, which may have curtailed the interaction between the silica particle surface and surfactants due to charge-charge repulsion.

Figure 5-4b presents the calculated charge density on the particle surface, for the case of 100 nm particles, and its variation as a function of pH and SDS concentration. It is noteworthy that the charge density on the silica surface remained higher for all cases involving SDS, at all pH ranges under study, compared to the values calculated for the particle-only dispersions in the absence of SDS. In addition, the particle's surface charge density was higher in samples containing 12 mM SDS compared to those prepared at 4 mM SDS. This result contradicts another study mentioned beforehand, where SDS adsorption was found to decrease at concentrations higher than CMC (~8 mM for SDS at these salt conditions).[285] However, as stated elsewhere, surfactant adsorption reaches a plateau at CMC, and the additional surfactant molecules are responsible for populating the micelles,[293] which is in line with our findings that the maximum adsorption is at concentrations equal or above the CMC. Therefore, the higher magnitude of zeta potential observed for cases involving SDS, can be attributed to the presence of charged species on the silica particle surface.

Figure 5-4c illustrates the change in zeta potential at various SDS concentrations for 200 nm particles. When comparing the particle-only to SDS/silica mixtures, there is a clear increase in the magnitude of the zeta potential when SDS is present for almost all pH values. Interestingly, at the higher pH values ($pH \geq 8$) there is a decrease in the magnitude of the zeta potential for both samples containing SDS, whilst the particle-only dispersion showed an increase in the magnitude of the zeta potential, as discussed previously. This corroborates the earlier finding that isolated

silanol groups (pKa ~8.9) are present in the 200 nm particles. While the dissociation of these isolated silanol groups, at high levels of pH, generates an increase in the charge density for the particle-only systems, it deters SDS adsorption and therefore leads to a decrease in the particle surface charge density for the samples with SDS (**Figure 5-4d**). Therefore, adsorption of SDS is considered to be at its maximum at lower and intermediary pH values, in the range of 5 to 8, and decreases upon the increasing the pH to highly basic conditions (pH ≥ 8).

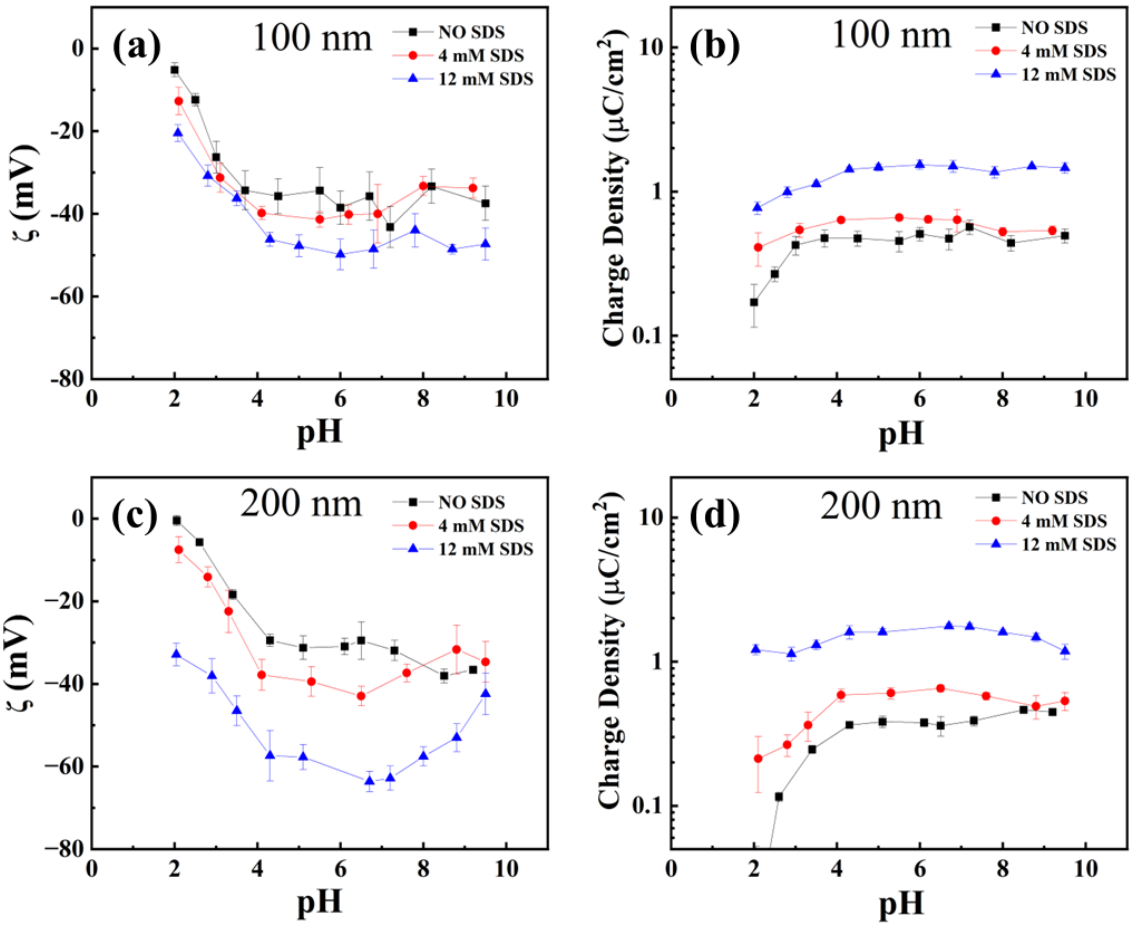

Figure 5-4. Effect of surfactant concentration on (a, c) zeta potential, and (b, d) surface charge density of 100 nm and 200 nm silica particle dispersions measured as a function of solution pH at salt concentration of 1 mM.

5.1.2.2.2. Effect of SDS at Various Electrolyte Concentrations

In order to isolate the effect of added electrolyte on the overall ionic strength of the solution and the resulting impact on the surfactant/particle interactions, variation in the salt and surfactant concentration was carried out at a fixed solution pH. This was done by considering not only the background salt concentration but also the effect of any added electrolyte to the overall ionic strength (i.e., $I = I_{KNO_3} + I_{KOH} + I_{HNO_3} + I_{SDS}$) of the mixture. **Figure 5-5a** depicts the measured change in the zeta potential resulting from varying the overall ionic strength in the solution at pH values between 5 and 6. As expected, for the particle-only dispersions (i.e., no SDS systems), a decrease in the magnitude of the measured zeta potential was observed with an increase in the ionic strength. This trend is expected and is attributed to the screening of particle surface charges by the ionic cloud and shortening of the Debye length. In the presence of surfactants, however, a deviation from this trend was observed depending on the SDS concentration. At low surfactant concentrations ($c_{SDS} \leq 0.01$ mM), the trend was similar to that observed for no SDS systems. For intermediate SDS concentrations ($0.1 \leq c_{SDS} \leq 0.5$ mM), results of some measurements showed deviations from the trend observed for the no SDS condition. Furthermore, as the surfactant loading was increased ($c_{SDS} \geq 1$ mM), the zeta potential became more negative, which could be caused by the presence of surfactants on the particle surface. The excess negative charges were probably caused by the added SDS head groups. This was further evidenced when comparing charge densities, depicted in **Figure 5-5b**. At high surfactant concentrations ($c_{SDS} \geq 1$ mM) in mixed surfactant/particle systems, presence of surfactant molecules enhanced the magnitude of the particle surface charge density. This finding further confirmed that the reported deviation stems from the surfactant adsorption onto the particle surface. However, at low ionic concentrations, originating from the presence of either salt or surfactant in the dispersion, the density of surface charges on the particle were lower. This results from the calculation of the

charge density (Eq. (3-5)), where the Debye length is the dominating variable at low ionic strengths, overcoming the increased zeta potential measured. In contrast, at high ionic strengths, ionic effects are minimized as electric fields are dissipated at shorter distances due to the high solution conductivity. Therefore, there is a tradeoff for increasing the overall ionic strength, which changes both the Debye length and the measured zeta potential. This can be visualized in **Figure 5-5b**, where there is a maximum supercharging at total ionic concentrations between 1 and 10 mM. In other words, increasing the overall ionic strength leads to screening of charge effects, which neutralizes the charges around the particle surface. Therefore, there are signs of adsorption at moderate pH conditions (between 5-6). Nevertheless, from the charge density perspective, the results are scattered since there is a convoluted effect of SDS and KNO_3 on the ionic strength (I).

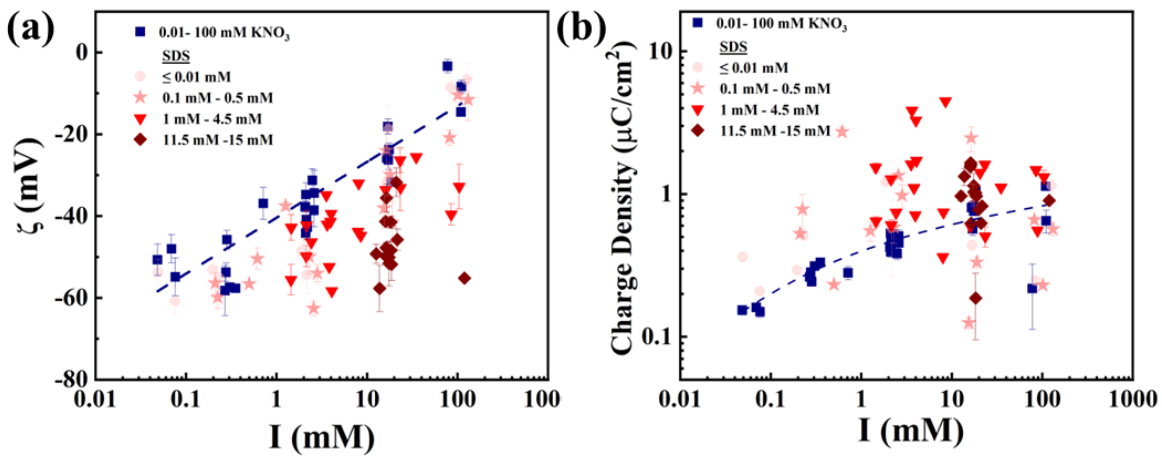

Figure 5-5. Effect of variation in the added salt (KNO_3) and surfactant (SDS) concentration, reflected in an increase in the total ionic concentration (I) of the dispersion, on (a) zeta potential and (b) charge density of the particles. Data includes measurement on both 100 nm and 200 nm particle samples with pH values in the range of 5 to 6. Data belonging to particle-only dispersions, prepared at different KNO_3 concentrations, are shown using blue symbols, whereas measurements obtained for mixed SDS/silica samples, obtained at different KNO_3 and SDS concentrations are shown using red symbols. Darker tones of red represent higher SDS concentrations.

5.1.2.2.3. Effect of SDS from the Perspective of Mean Ionic Product

To decouple the effects of SDS on the ionic strength of the solution, from that of the added KNO_3 salt, and examine the origin of the observed supercharging on the particle surface, we used

the mean ionic product (c^*), which accounts for the impact of ions, other than those resulting from SDS, present in the system to normalize the concentration of surfactant solutions at various background salt concentrations. In this approach, the mean ionic product is defined as follows:[294]

$$c^* = \gamma_{\pm}(c_{SDS+\ other\ ions} \times c_{SDS})^{1/2} \qquad (5\text{-}1)$$

where c_{SDS} is the concentration of SDS, $c_{SDS+other\ ions}$ is the concentration of all species, $\gamma_{\pm}$ is the average activity coefficient of the system, calculated from the Debye-Hückel equation as follows:

$$\log \gamma_{\pm} = -\frac{0.5115 \times \sqrt{I}}{1 + 1.316 \times \sqrt{I}} + 0.055 \times I \qquad (5\text{-}2)$$

Using the mean ionic product to analyze the measured data allows for the comparison of the results in mixed SDS/silica systems to those obtained from particle-only dispersions with a similar ionic strength. Data on the particle's zeta potential and surface charge density as a function of the effective ionic concentration (c^*), for samples containing SDS, is shown in **Figure 5-6**. For comparison, the corresponding values for samples without SDS, i.e., particle-only dispersions, are also provided in the figure as a function of the total ionic strength (I). In addition, data available in the literature on the mixed SDS/silica system, obtained from various references, [28, 281, 282, 285, 286] are also displayed on the same plot. It is worth noting that inferring about the SDS adsorption, or lack thereof, onto the particle surface, solely based on the zeta potential results shown in **Figure 5-6**, is not trivial since there are multiple factors at play in case of mixed systems. There is a large scatter in the data, both from this work and those reported elsewhere.[28, 281, 282, 285, 286] To illustrate the clear distinction between the data obtained for mixed surfactant/particle systems with SDS (full symbols) and those for particle-only dispersions without SDS (open symbols), the particle surface

charge density was calculated from the measured zeta potential in each case, as shown in **Figure 5-6b**. As can be seen, at the same effective ionic concentration, particle dispersions containing SDS exhibit a higher charge density when compared to a sample without SDS. This effect appears to be enhanced at larger SDS concentrations, which is expected since there is a higher activity of SDS molecules in the bulk. It is important to note that some of the data taken from the literature pertain to particles that are not spherical in shape (fumed silica). For those cases, the reported D_H was used in the charge density calculations and therefore the results exhibit greater variability. Compared to **Figure 5-1a** where a definitive region indicating SDS adsorption was not clearly delineated, **Figure 5-6b** offers a more distinct differentiation between the characteristics of samples with SDS and those of particle-only dispersions.

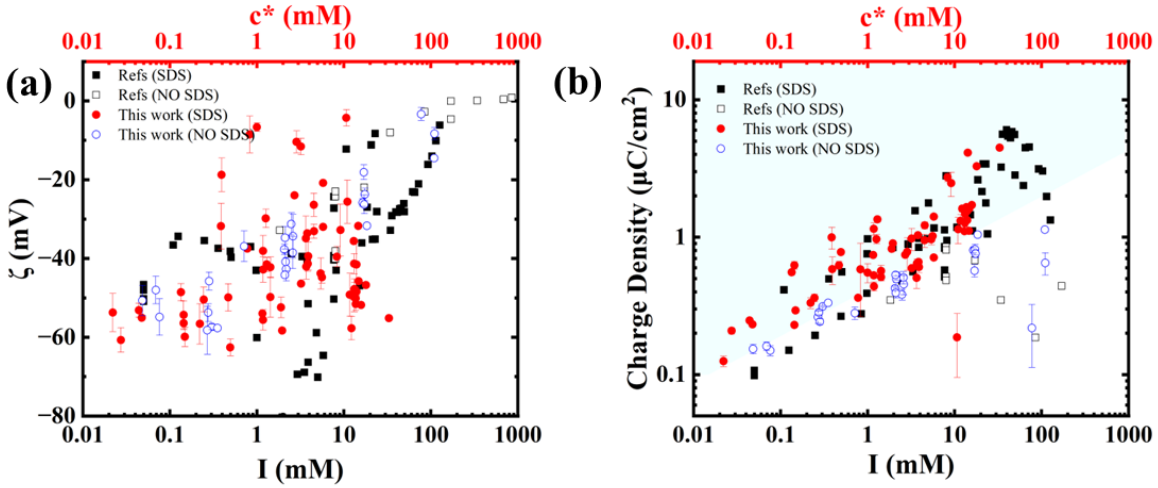

Figure 5-6. Effect of variation in the salt and surfactant concentration, at pH values between 5 and 6, in 100 nm and 200 nm particle dispersions: (a) zeta potential and (b) surface charge density. Data is plotted as a function of the ionic strength (I) for samples without SDS and mean ionic product (c^*) for samples with SDS. Our data is shown along with data taken from several references.[28, 281, 282, 285, 286] Full symbols correspond to mixed surfactant/particle samples and open symbols belong to particle-only dispersions (black squares for reference data, red and blue circles for data from this work). Area shaded in teal color corresponds to data for mixed surfactant/particle systems falling in the region for which the resulting particle surface charge density is higher than that obtained for salt only particle dispersions (no SDS), which is attributed to the adsorption of SDS onto the particle surface in the former case.

5.1.2.2.4. Effect of SDS at Various pH and Electrolyte Concentrations

To determine the extent of SDS adsorption onto the silica particle surface for a mixed system that is not at neutral pH, an analogous analysis to the one conducted in the previous section was performed on data acquired at various pH values. The data was generated at two pH ranges that were considered "low" (i.e., pH $\leq$ 5) and "high" (i.e., pH $\geq$ 6). These values were selected based on the response of the particle-only dispersions to pH alterations, where at low pH range, reducing the pH resulted in a decrease in the magnitude of the zeta potential, and over the high pH range, increasing the solution pH did not have a pronounced impact on the measured zeta potential, as depicted in **Figure 5-3**.

Figure 5-7 illustrates the measured zeta potential and calculated charge density corresponding to measurements carried out at low and high pH ranges for SDS/silica mixtures using data from both 100 nm and 200 nm systems. **Figure 5-7a** shows that the measured values of zeta potential in the mixed surfactant/particle samples have a higher magnitude compared to those obtained for the particle-only dispersions in presence of KNO_3. The same trend is observed in **Figure 5-7c,** where the charge density for samples containing SDS is overall higher than those without SDS. It is worth noting that the results at low pH show a more pronounced difference when comparing the particle surface charge density for samples containing surfactant with those of dispersions without SDS. This can be explained by the fact that at these lower pH values, the system is closer to the isoelectric point of silica particles (see **Figure 5-3**), indicating a lower density of surface charges on the particle, which could promote the SDS adsorption onto the particle surface. It is important to note that the variation in ionic strengths for particle-only systems are not only due to different KNO_3 concentrations but also acid addition. Therefore, there is a downward trend of surface charge density with ionic strength as the acid concentration is higher.

Such downward trend is not present in systems with SDS even though the particles were exposed to the same pH conditions.

Figure 5-7b presents systems at high pH range, which do not exhibit a clear distinction depending upon the presence of SDS. This is also evidenced in **Figure 5-7d** where the calculated charge density for some of the mixed surfactant/particle samples falls in the region that belongs to particle-only data in presence of KNO_3 salt, even at high effective concentrations of SDS. Higher pH values are associated with a higher surface charge on the silica surface, as shown in **Figure 5-4b** and **d,** which may hinder adsorption. Nevertheless, at high pH and high SDS concentration, there is indeed an elevated charge density observed, suggesting that even under these conditions, some level of adsorption occurs.

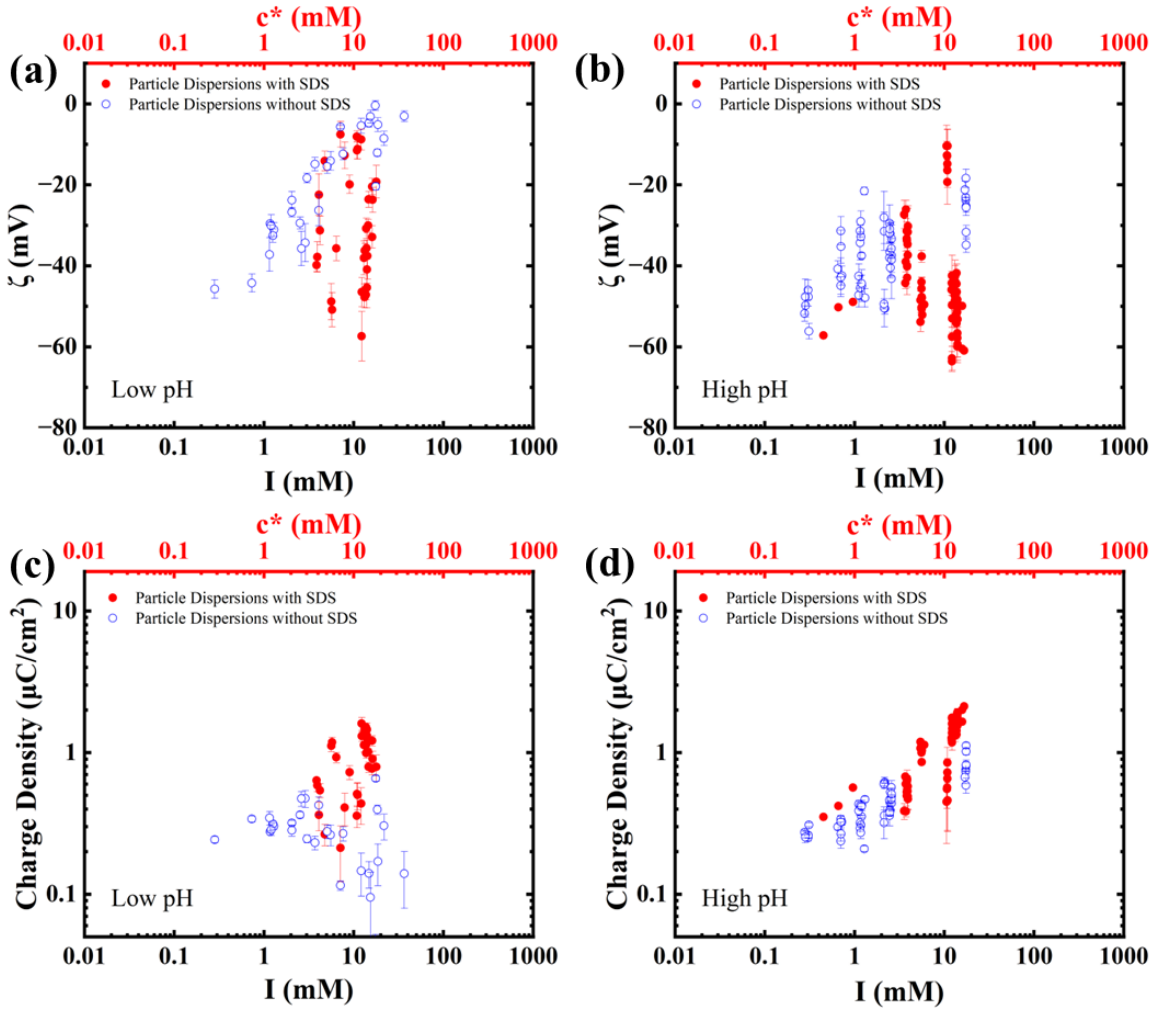

Figure 5-7. Effect of variation in the salt and surfactant concentration at fixed pH on (a, b) zeta potential, (c, d) charge density, as a function of total ionic concentration (I) for samples without SDS, and effective concentration (c^*) for samples with SDS. Top charts (a, c) show data obtained at "low pH" values (pH $\leq$ 5), while the bottom charts belong to those measured at "high pH" range (pH $\geq$ 6). Data obtained from both 100 nm and 200 nm particle samples were used in generating these plots.

5.1.3. Summary of Findings

In this section, we investigated mixed systems of silica particle and SDS surfactant, and examined changes in particle surface properties in response to alterations in solution pH and electrolyte concentration in order to shed light on factors that promote or prevent surfactant adsorption onto the particle surface in case of like-charged SDS/silica system. We applied dynamic light scattering to measure the particles zeta potential, under various dispersion conditions, and

estimated the surface charge density from the conductivity and mobility measurements. We decoupled the contribution of SDS to the ionic strength of the solution and alteration of zeta potential for negatively charged silica nanoparticles. These studies aided in identifying variable domains in which SDS adsorption onto silica particles is more or less likely to occur, and the conditions at which it may affect the zeta potential readings, which are usually used as a direct indication of surfactant adsorption. We showed that charge density is a more fit parameter for identifying adsorption of SDS onto silica particles. Our findings show that SDS adsorption onto the silica surface occurs, likely through entropically-driven interactions, under certain conditions as follows.

i. At moderate pH conditions (between 5 and 6), SDS adsorption takes place over the range of the ionic strengths studied in this work (0.1 to 100 mM). However, it might not decrease the particles zeta potential (i.e., supercharging of the particle surface may not be detected);

ii. An acidic environment improves surfactant adsorption and "supercharging" effect;

iii. Basic environments could hinder adsorption and supercharging in the presence of isolated silanol groups on the silica surface; however, high SDS concentrations ($c^* \geq 10$ mM) might overcome the pH effect.

iv. There is a tradeoff between the ionic strength decreasing the particle's zeta potential and dispersion's Debye length, which leads to a maximum of increase in the magnitude of charge density on the surface of particles to take place in the range of 1-10 mM of total ionic strength.

v. The supercharging effect is less pronounced if the particle's zeta potential is high (-60 mV) prior to the addition of the SDS surfactant and becomes more pronounced as the zeta potential is reduced, which can be achieved by increasing the ionic strength of the solution.

5.2. Contamination in Sodium Dodecyl Sulfate Solutions

5.2.1. Introduction

One of the most commonly used surfactants is sodium dodecyl sulfate (SDS), which is an anionic surfactant with a critical micelle concentration (CMC) of 8.2 mM at 25°C in the absence of electrolytes.[295] Its HLB is estimated to be 40, which characterizes it as a highly water-soluble surfactant.[126] SDS is synthesized by sulfating the long-chain alcohol, n-dodecanol, also known as lauryl alcohol (LOH), which is considered a contaminant in SDS samples.[296] As stated by Mysels,[297] impurities that have similar surface activity to SDS (by weight percent) do not impact the SFT readings. However, LOH exhibits a higher surface activity compared to SDS due to its lower solubility in water, which is attributed to the relatively lower polarity of its head group. As LOH does not form micelles by itself, it is not considered a surfactant species and does not have an HLB value attributed to it. However, for means of comparison, utilizing the method developed by Davies,[298] one can estimate the HLB of a dodecanol molecule to be ~3. Therefore, even trace amounts of LOH present in the solution can affect the behavior of the solution and resulting experimental measurements.[294] For instance, in a 6 mM SDS solution (99.98 mol%) contaminated with 0.02 mol% LOH, the dodecanol molecules occupy more than 80% of the total surface coverage, which yields an additional 20 mN/m reduction in SFT.[200] The isotherm is therefore shifted to lower values compared to that obtained for a purified SDS sample. The amplified reduction in SFT, contributed by LOH molecules, will continue to persist as the SDS concentration is increased. This effect can be attributed to an increase in the bulk concentration of LOH molecules present in the sample until the CMC of the SDS solution is reached.[297] Once SDS micelles are formed, contaminant LOH molecules can be solubilized in the micelles.[299] As a result, increasing the SDS concentration past the CMC results in SFT readings that are closer to the values

for pure SDS samples.[299] A characteristic dip in SFT isotherm around CMC value is thus an indicator for the presence of LOH in the sample.[300] It is important to mention that the presence of LOH molecules at the interface is not as consequential if the non-polar phase is oil. As LOH is highly soluble in organic phases, it does not accumulate at the interface.[301]

Adsorption of SDS molecules onto the interface is strongly impacted by the presence of electrolyte in the solution. The air-water interface carries a negative electrostatic potential compared to the bulk due to the ordered water molecules at the interface and/or preferential adsorption of anions (e.g., hydroxyl group from the dissociation of water).[302] The net surface charge at the air-water surface becomes less negative in presence of electrolyte, promoting SDS adsorption.[303, 304] Additionally, the presence of ions in solution increases the surface activity of SDS molecules by decreasing the electrostatic repulsion between the anionic head groups.[305] Reduced electrostatic repulsion between the SDS head groups at higher electrolyte concentrations facilitates micelle formation and leads to lower CMC values and higher aggregation number in SDS micelles.[306, 307]

To remove LOH from SDS solutions, several purification methods have been developed. Among these methods, foaming the sub-micellar solution,[297, 308, 309] passing the solution through an adsorption column,[310] successive compression and aspiration of the surface,[311] and repeated recrystallization of the solution with alcohol (e.g. reagent alcohol or ethanol) and water[297, 308, 312, 313] have been utilized, individually or in series, to achieve a higher degree of purity. However, even after laborious work of purifying the sample, contamination could still remain a problem as SDS molecules hydrolyze back to LOH after the purified solution begins to age with the rate of hydrolysis depending on the concentration of both SDS and LOH molecules, temperature, and pH of the solution.[294, 297, 314]

Few methods have been proposed since the 1980s, mostly relying on the direct measurement of fluid properties, to quantify the amount of LOH present in the solution. To our knowledge, Czichocki and co-workers were the first to determine the amount of LOH in SDS samples based on both high performance liquid chromatography (HPLC) method and later SFT measurements.[315, 316] The HPLC method was shown to be sensitive to the alcohol chain length and could distinguish between different alcohols present in the solution. The HPLC results were complementary to the surface tension readings, which cannot differentiate between varying alcohol chain lengths. A criterion for surface chemical contaminations, under equilibrium and non-equilibrium conditions, and based on surface tension shifts, was derived by Lunkenheimer et al.[317] as a means to check the purity of the system via SFT measurements. Therefore, the criterion is not based on the bulk concentration of the contaminant, but it is based on its impact on the surface. Thus, it relies on the sensitivity and accuracy of the instrument used to measure the SFT values. Vollhardt and Czichocki[318] studied the effect of different isomeric alcohol molecules co-adsorption with SDS. When comparing the reduced SFT in contaminated SDS solutions with that of the purified solutions, it was found that increasing the contaminant concentration leads to an increase in the SFT difference, where 0.1 wt% of contamination yields a 15 mN/m difference from the pure SDS surface tension value. A more rigorous approach based on a thermodynamic adsorption model was developed by Kralchevsky et al.[200] to determine the amount of dodecanol contamination in the sample. Further information on this thermodynamic model will be provided in the materials and methods section.

When considering the use of SFT readings to trace the presence of contamination in SDS solutions, several techniques are available for SFT measurements, such as the Wilhelmy plate, the drop weight, and the bubble shape tensiometry methods. The use of different surface geometries

(e.g., planar in the Wilhemly plate vs. spherical in the bubble shape tensiometry) can impact the adsorption dynamics by potentially hindering the adsorption of less concentrated species to the interface.[319] Not only the geometry, but differences in aging time for surfaces to reach equilibrium with the bulk phase can also be a crucial consideration.[197] If one compares the SFT measurements using a pendant liquid droplet in air with that of a rising air bubble in the solution, besides the higher area per volume ratio (A/V) for the drop geometry, the surfactant adsorption will also be impacted by the concavity of the interface itself.[197] A low concentration of contaminants can also be an issue when comparing two different methods; depending on the method's A/V, the initial bulk concentration could be considerably depleted, influencing the equilibrium state of the system.[197] This effect has been illustrated by Addison and Hutchinson[312], where the drop weight method (performed at different rates) and the Wilhelmy plate method were used to measure the surface tension of SDS solutions. The slower the rate of formation of the drop on the drop-weight method, the more time was allowed for the adsorption of contaminant molecules, and the closer the surface tension was to the SFT readings obtained from the stationary (planar) surface of the Wilhelmy plate method. All these factors impact readings of both thermodynamic (surface tension) and dynamic (surface dilational rheology) measurements using the drop geometry.

Dynamics of interfaces can be examined in two modes: shear rheology (i.e., interfacial response to shear deformation at a constant area) and dilational rheology (i.e., interfacial response to variations in the interfacial area while conserving the shape). A number of methods have been developed for probing the response of interfaces to shear such as the magnetic needle,[157-159] interfacial disk/bicone,[160] double-wall-ring,[161] and microrheology.[139, 163, 164] For example, Poskanzer et al.[320] studied the effect of adding dodecanol to the surface viscosity of SDS solutions and found that a synergism between the two molecules greatly increase the surface viscosity (up

to a factor of 5). Surface dilational rheology can be probed using techniques such as capillary waves, a Langmuir trough with oscillating barriers, and oscillating drop/bubble,[147, 217, 321, 322] the latter two are the focus of studies carried out in this section.

The surface dilational rheology of LOH-contaminated SDS solutions was studied by Wantke et al., using the oscillating bubble method with frequencies ranging from 1-500 Hz.[323] To model their experimental results, the one-component rheology model was used due to the relatively constant concentration of LOH molecules at the surface during oscillations. It was shown that pure LOH surfaces exhibit a completely elastic response, whereas pure SDS samples present a strong viscoelastic behavior, with mixtures showing intermediary properties. It should be pointed out that the sample labeled as "pure-SDS" in these experiments exhibited a small dip in the SFT isotherm, which points to some degree of contamination. These results were later utilized by Aksenenko et al.,[213] as input to their two-component rheology model. However, even with the more robust approach compared to Wantke et al.[323], their model was only able to qualitatively fit the experimental data from the previous work done by the authors.[323]

When considering the effect of background electrolyte, Fainerman et al.[324] measured the dynamic surface tension and the surface rheology of SDS solutions with hardness salts such as $CaCl_2$ and $MgCl_2$ present in the solution. It was found that the presence of hardness salts results in a higher viscoelastic modulus when compared to solutions with NaCl as the electrolyte, which was attributed to the formation of $Ca(DS)_2$ and $Mg(DS)_2$ complexes that are more surface active than SDS. Moreover, the rate of hydrolysis was much higher for the SDS solutions in presence of the divalent salts. The dynamic surface tension results were used to estimate the concentration of dodecanol in these solutions via the generalized Frumkin model.[325]

This section aims to better understand the importance of SDS hydrolysis and how it impacts surface measurements. We compare the results obtained from the interfacial rheological measurements with the values predicted by different thermodynamic adsorption models. In addition, we investigate the effect of electrolyte on the results obtained for both unpurified and recrystallized samples. Findings of these studies provide valuable insights on more complex interfacial systems in which interfacial activity of SDS molecules under dynamic conditions is of interest.

5.2.2. Results and Discussions

5.2.2.1. Surface Tension Isotherms

The surface tension isotherms of the unpurified and recrystallized samples, measured using the WP method, are depicted in **Figure 5-8**. A comparison is provided with the reference data from Tajima and coworkers[326] on pure SDS solution (purified by isotropic mixing with dodecanol in ethanol followed by extraction with ether to remove the dodecanol), also measured using the WP method and with no background electrolyte present. From **Figure 5-8a**, it is noticeable that the SFT measurements obtained for both the unpurified and recrystallized samples are not in agreement with the reference data. This is due to the synergistic effect of SDS and LOH when both present at the surface, which results in a decrease of the SFT to a larger extent compared to a surface solely populated by SDS molecules.[320] The difference between the measured curve for recrystallized sample in this study and the reference curve in[326] hints at the presence of LOH molecules in the solution even after the recrystallization process. Data obtained for the recrystallized sample displays the characteristic contamination dip in the curve before plateauing at concentrations above CMC.

Next, we moved on to SFT measurements in presence of electrolyte using 10 mM NaCl solutions, as shown in **Figure 5-8b**. For comparison with the data available in the literature, in this case we used the reference curve provided by Tajima.[327] In this reference, the SFT was measured with the drop-volume (i.e., drop-weight) method, with a similar pure SDS sample used in the work by Tajima et al.,[326] but using 10 mM NaCl solutions. For the present study, the measured SFT curve for recrystallized samples in 10 mM NaCl solutions overlaps with the reference data from Tajima.[327] The higher ionic strength of the solution promotes the adsorption of SDS, which can be explained by the decreased electrostatic repulsion between the negatively charged dodecyl sulfates and the reduction in net negative charge at the air-water surface,[303] thus, increasing SDS activity. However, as established from the results in **Figure 5-8a**, it should be noted that the recrystallized sample still contains LOH molecules. Therefore, the presence of background electrolyte could mask the presence of dodecanol impurities in the surfactant solution when one is only interpreting the thermodynamic data via the surface tension isotherm.

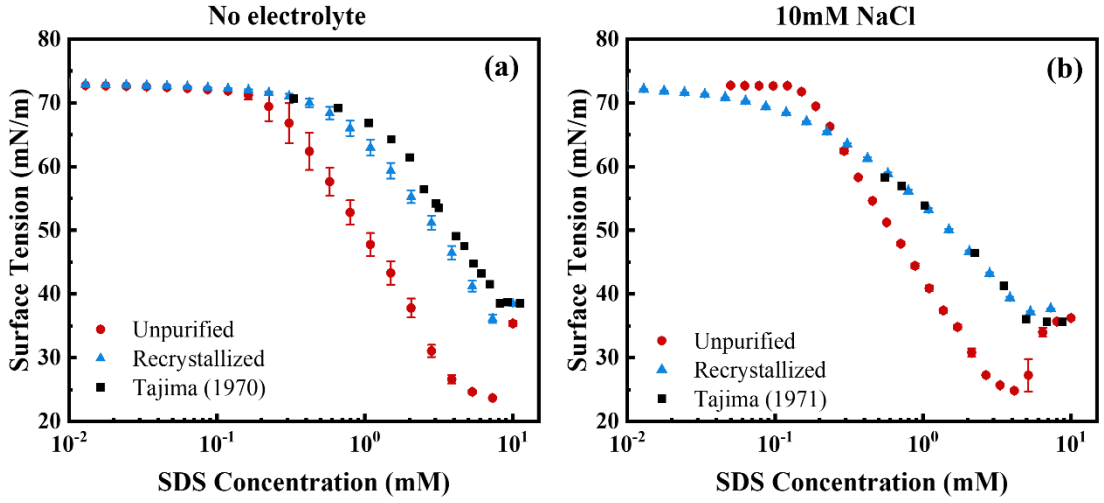

Figure 5-8. Surface tension isotherms of unpurified (red circles) and recrystallized (blue triangles) SDS solutions with (a) no background electrolyte and (b) 10 mM NaCl. Comparison is also provided with reference data (black squares) from Tajima on: (a) pure SDS solutions with no electrolyte [326] and (b) pure SDS solutions with 10 mM electrolyte [327]. Some error bars are not visible because they are smaller than the symbol size. Data adapted from Refs [326] and [327] are provided with permission from the Bulletin of the Chemical Society of Japan.

5.2.2.2. Depletion Effects in Different Techniques

Determining the appropriate technique for measuring the surface tension of dilute SDS solutions is an important factor. The difference in geometry (i.e., the area-to-volume ratio) between varying techniques makes one method more sensitive to contamination than another. This is because a smaller volume used in a method results in fewer total molecules being present in the bulk in one technique compared to another. For instance, the Wilhelmy plate method relies on a large volume with a relatively small area available for adsorption ($A/V \sim 100\ \mathrm{m}^{-1}$), which makes it more sensitive to impurities – usually present in small concentrations – compared to the pendant drop shape tensiometer, which has a larger area-to-volume ratio ($A/V \sim 2000\ \mathrm{m}^{-1}$). This phenomenon is caused by the depletion effect that takes place when highly surface-active molecules, such as LOH, are present in bulk in dilute concentrations and have access to a large area available for adsorption.[197] When the amount of molecules on the surface exceeds the amount of molecules in the bulk ($\Gamma \times A > c \times V$), depletion is considered to be significant [197]. As explained by Semmler et al.[328], when depletion effects cannot be neglected, both dynamic and equilibrium surface tension readings differ from systems with an infinite surfactant reservoir. Therefore, one should take depletion into account when the conditions of the application fall into the beforementioned criterion. **Table 5-2** shows the A/V for the three geometries discussed in this work.

Table 5-2. Values of area to volume ratio (A/V) calculated for different methods used in the measurement of the surface tension.

Method	A/V [m^{-1}]
Pendant Drop	1916
Rising Bubble	110
Wilhelmy Plate	94

In order to compare the impacts of different geometries, the normalized effective concentration ($\frac{c_{eff}}{c_i}$, Eq. (3-18)) of LOH, calculated for the unpurified sample, is provided in **Figure 5-9a**. Pendant drop shape tensiometer results are most affected (notice the high A/V value in Table 1), having less than 100% of the initial LOH bulk concentration (c_i, Eq. (3-18)) over the entire range of SDS concentrations. By analyzing this graph one can infer that both WP and the RB shape tensiometry (overlapping) are less affected by depletion of the contaminant compared to the pendant drop shape tensiometry. This is mostly caused by the higher surfactant reservoir available in both WP and RB methods in contrast to the pendant drop. Therefore, methods with a high A/V value may not be suitable for capturing the impact of contamination's presence in the bulk through surface measurements.

As diffusion to the surface is a key factor in the systems affected by depletion, aging time is also expected to play a role in the results. **Figure 5-9b** compares the isotherms obtained for the unpurified sample using the WP method and the RB shape tensiometry. Two major differences can be noticed between these measurements. First, the surface tension measurements in the RB geometry take a longer time to stabilize due to the slow adsorption process.[197, 319] For comparison, the surface tension readings after 30s and 3h are provided as a function of concentration for the RB measurements. Such slow adsorption is caused both by the A/V of the system and the "quasi-spherical" shape of the bubble, and the fact that the air-water surface is surrounded by the surfactant solution and adsorption is taking place in a convex surface;[197] hence, the time necessary to reach equilibrium is increased as compared to the WP, which has a planar adsorption geometry and a slightly smaller A/V value (see **Table 5-2**). In addition, measurements at low surfactant concentrations (below 1 mM of SDS for our samples) indicate that even after 3h the surface tension

readings from the RB measurements do not match those obtained by the WP (**Figure 5-9b**). This is possibly due to the slightly larger A/V for the RB, which can affect the equilibrium surface tension at a constant bulk concentration.[197, 328]

Finally, by using Eq. (3-19), one can calculate the depletion depth and the diffusion time scale for WP geometry. For the RB geometry, one has to correct h_p to h to account for the curvature.[197] Comparing the two geometries, as shown in Figure 2c, it can be seen that the WP requires less time for equilibration than the RB, for both unpurified and recrystallized samples. At lower concentrations of SDS, the number of LOH molecules present in the bulk is small; therefore, the time required for equilibrium is just a function of the geometry. As SDS concentration increases, the unpurified and recrystallized samples start to behave differently due to the different molar fraction of LOH present. There is a peak in the diffusion time scale for LOH molecules in both unpurified and recrystallized samples, which can be explained by the sharp increase in the equilibrium adsorption (Γ) calculated for LOH (see **Figure A0-2**a in Appendix A). Therefore, there is an increase in demand for LOH molecules from the surface, while the bulk concentration increases at the same rate. The peak shift in LOH diffusion time scale peak observed between the unpurified and recrystallized samples can also be explained by the different molar fraction in both samples, as shown in **Figure A0-2b**, where both adsorption curves for LOH increase sharply at the same bulk LOH concentration. Past this critical point, the diffusion time decreases with the bulk concentration and the surface adsorption does not change drastically.

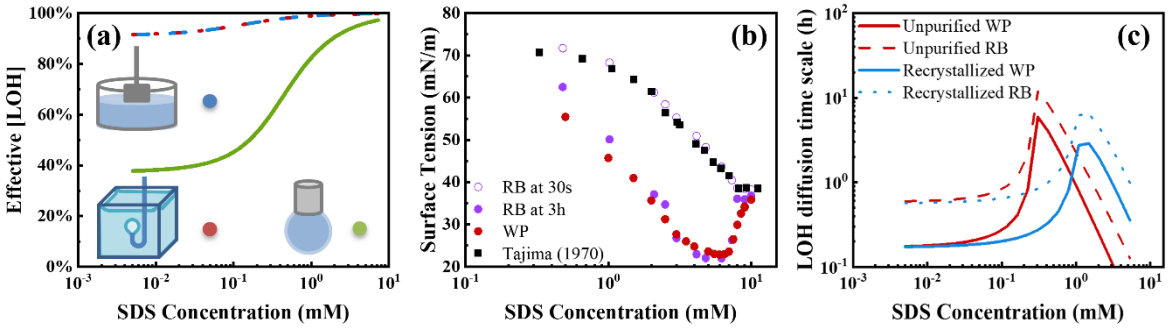

Figure 5-9. (a) LOH normalized effective concentration for different geometries (blue dashed curve for WP; red dotted curve for RB; and green full curve for pendant drop) at different SDS concentrations. (b) Comparison of the surface tension isotherms for unpurified SDS solutions in the absence of electrolyte measured with: (i) the rising bubble shape tensiometer (RB), at two different aging times (open purple circles are 30s, full purple circles are 3h), and (ii) the Wilhelmy plate (WP) method (red circles). The values reported by Tajima for pure SDS solutions (measured by the WP technique) are provided as a reference (black squares)[326]. (c) Calculated diffusion time scales with model given by ref[197] for LOH molecules based on their bulk availability in unpurified (red curves, estimated molar fraction of 0.478 mol%, see next section) and recrystallized (blue curves, molar fraction of 0.104 mol%) for both WP (full) and RB (dashed) geometries.

5.2.2.3. Determination of the Impurity Content via Thermodynamic Models

Isotherms obtained for both unpurified and recrystallized samples were fitted by the three thermodynamic adsorption models in order to estimate the degree of contamination in the samples. Results achieved from each model are shown in **Table 5-3**. The error related to the LOH molar fraction estimation was calculated, based on the method used in the appendix of the work by Kralchesvsky[200], by relating the minimum standard deviation calculated comparing the fit to the experimental data to the estimated error on the molar fraction value. The Kralchesvsky model yielded a higher degree of contamination, which can be attributed to the additional feature of considering the charged air-water surface.

Table 5-3. Molar fraction of dodecanol (xLOH in mol%) obtained from best fit of the experimentally measured isotherms, using WP method, to each thermodynamic model for both unpurified and recrystallized samples.

Adsorption Model	Unpurified (mol%)	Recrystallized (mol%)
Frumkin	0.435 ± 0.009	0.028 ± 0.003

van der Waals	0.338 ± 0.027	0.044 ± 0.007
Kralchesvsky	0.478 ± 0.006	0.104± 0.004

The fit obtained by the Kralchesvsky model for both unpurified and recrystallized samples is shown in **Figure 5-10**. The fits obtained using both Frumkin and van der Waals model are shown in **Figure A0-1**. As previously discussed in **Figure 5-9a**, at lower SDS concentrations the depletion effect is significant, which could possibly result in a higher surface tension reading. To circumvent the effect of depletion phenomenon, data obtained for SDS concentrations above 1 mM SDS were used to fit the model. The best fits to the unpurified and recrystallized samples corresponded to LOH molar fraction of 0.478 mol% and 0.104 mol%, respectively. The order of magnitude of the results agree with those obtained in the original work by Kralchesvsky.[200]

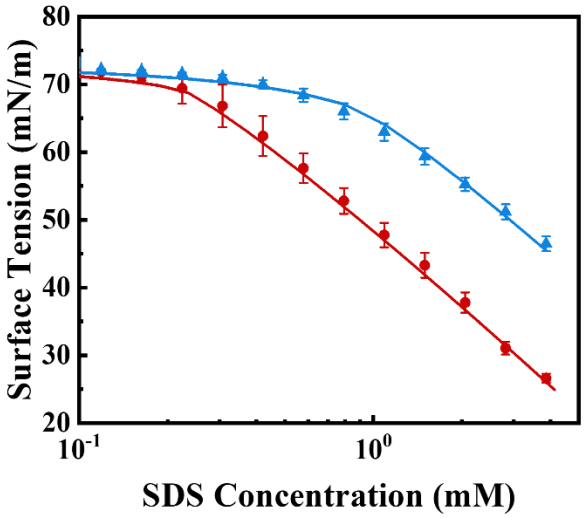

Figure 5-10. Surface tension isotherms for the unpurified (red circles) and recrystallized (blue triangle) samples fitted to the thermodynamic model developed by Kralchevsky et al.[200]

5.2.2.4. Surface Rheology Measurements

In order to obtain the surface rheology of the adsorbed layer, one can impose oscillations to a bubble surface area, as illustrated in **Figure 5-11a**, and track how the surface tension changes with the applied perturbations (Eq. (3-21)). The surface storage modulus ($\kappa^{s\prime}$) obtained from rheological measurements on a rising bubble suspended in unpurified and recrystallized samples is shown in **Figure 5-11b**. Results are provided for solutions in the absence and presence of the electrolyte. The surface viscous modulus ($\kappa^{s\prime\prime}$) of both unpurified and recrystallized samples is not negligible as depicted in **Figure 5-11c**. This implies that the surface layer is populated by a mixture of SDS and LOH molecules since a surface purely covered with LOH molecules would be elastic in nature with a negligible viscous modulus.[213, 323] As expected, due to the higher concentration of LOH molecules in the unpurified solutions, these samples resulted in a higher surface elastic modulus (one order of magnitude larger) compared to those measured for the recrystallized samples.

The impacts of electrolyte's presence in the solution on the resulting surface properties has also been examined for both unpurified and recrystallized samples. As illustrated in **Figure 5-11b**, the $\kappa^{s\prime}$ of the unpurified sample is not greatly affected by the addition of 10 mM NaCl at concentrations below the CMC, other than shifting the entire curve to lower SDS concentrations. This indicates that the composition of the surface layer is not very different between the two cases, possibly due to the high degree of dodecanol contamination present in the unpurified sample. In contrast, addition of electrolyte to the recrystallized solutions resulted in a decrease in E' and an increase in $\kappa^{s\prime\prime}$. This can be attributed to the higher surface-activity of SDS molecules in presence of NaCl in the aqueous phase. While the screening of the electrostatic repulsion between the SDS polar head groups is present in both unpurified and recrystallized samples, the larger contamination present in the former is sufficient to mask this effect. As a result, the addition of salt did not result

in a pronounced impact on the surface rheological response of the unpurified solutions. For all samples, there is a significant drop in $\kappa^{s\prime}$ at concentrations above the CMC. This behavior indicates that the surface is populated by both SDS and LOH molecules at concentrations below the CMC, whereas the solubilization of LOH molecules into SDS micelles at concentrations above CMC dramatically reduces the effective concentration of LOH in the bulk, which drives the adsorbed LOH molecules out of the surface and into the bulk.[294, 299] For the recrystallized samples in 10 mM NaCl, measurements on SDS solutions at concentrations larger than 6 mM SDS (above the CMC of 5.5 mM for this sample) yielded negligible rheological readings.

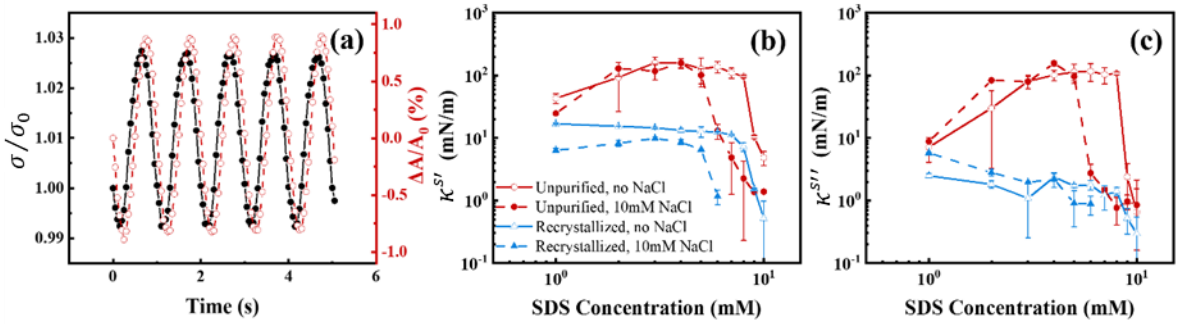

Figure 5-11. (a) The area oscillations (red open circles) and resulting surface tension readings (black full circles) of a 2 mM unpurified SDS solution at 1 Hz. (b) The elastic modulus ($\kappa^{s'}$) and (c) viscous modulus $\kappa^{s''}$ of unpurified (red symbols) and recrystallized (blue symbols) samples. The effect of electrolyte is examined using samples with no added salt (open symbols) and in 10 mM NaCl solutions (full symbols). Some error bars are not visible because they are smaller than the symbol size.

5.2.2.5. Surface Rheological Modeling via Two-Component Model

The composition of the solution (i.e., the amount of LOH and SDS present in the sample), obtained from the fitting of SFT isotherms to thermodynamic models (see **Table 5-3**), is used in calculating the resulting surface rheology via a two-component model. The experimentally measured rheological properties (i.e., **Figure 5-11b** and **c**) are compared to results obtained from the two-component model as illustrated in **Figure 5-12**. For the unpurified SDS sample, there is a qualitative agreement between the experimental data and the predicted values. However, using the

LOH values obtained from the fits of the SFT isotherms to Frumkin and van der Waals models as an input for the rheological modeling yields some features in the rheology predictions (see **Figure 5-12a** and **b**) that are not observed in the experimentally measured data and are not expected, as the surface concentration of both molecules is expected to increase monotonically with bulk concentration. In comparison, these local minima and maxima are not present in predictions derived from Kralchesvsky's model as shown in **Figure 5-12c**. These local maxima and minima present for both Frumkin and van der Waals models are due to the dependence of the adsorption value calculated from the surface tension fits (**Figure A0-2c-d**). In addition, the Kralchesvsky model properly predicts the viscous contribution measured experimentally; however, there is a large difference in the predicted versus experimentally measured elastic modulus. This is likely due to both the bulk depletion affecting LOH adsorption (**Figure 5-9c**) and the high LOH adsorption value predicted from the adsorption isotherm (**Figure A0-2a**).

For the recrystallized sample, a good agreement does not exist between the measured data and the predicted results based on any of the adsorption model inputs, as shown in the Appendix A (**Figure A0-3**). This could be due to depletion effects playing a more prominent role in the recrystallized samples because of the much lower LOH content in these systems. This will affect both the time necessary to achieve the equilibrium surface tension and the magnitude of it, as discussed earlier.

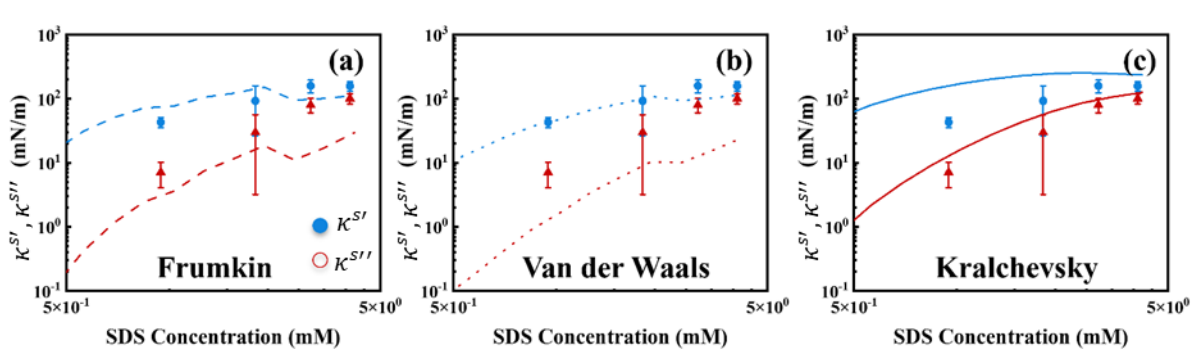

Figure 5-12. Comparison of the experimentally measured surface rheological properties (elastic modulus, $\kappa^{s'}$, in blue circles and viscous modulus, $\kappa^{s''}$, in red open circles) to the predictions obtained from a two-component rheological model. The presented data is for unpurified samples and no electrolyte is added to the solutions. Input to the two-component rheological model is provided from fitting of the surface tension isotherms to (a) Frumkin, (b) van der Waals, and (c) Kralchevsky adsorption models.

5.2.2.6. Aging and Hydrolysis

To examine the aging of the solution, we monitored a recrystallized sample, prepared at 40 mM of SDS and kept at room temperature, for a period of 90 days. This concentration was chosen to increase the rate of hydrolysis based on the work done by Nakagaki and co-workers.[314] Over the 90 days period of aging, surface tension and rheology experiments were performed on a recrystallized SDS solution. The occurrence of hydrolysis process is expected to increase the overall degree of contamination in the sample.[314] Shown in **Figure 5-13a** are the surface tension isotherms measured after 0, 14 and 90 days of aging. The measured surface tension isotherms are also fitted to the Kralchesvky thermodynamic model, results of which are provided in **Figure 5-13a** as well. The sample's dodecanol quantity, obtained from the thermodynamic model, is tracked as a function of aging time as shown in **Figure 5-13b**. As can been seen from this data, there is no appreciable difference between the surface tension measurements from day 0 (xLOH = 0.119 ± 0.004 mol%) to day 14 (xLOH = 0.122 ± 0.003 mol%). However, once 90 days have passed it is possible to notice a downward shift of the surface tension values, corresponding to a larger dodecanol content (xLOH = 0.138 ± 0.003 mol%). By comparing the isotherms at 5 mM

SDS, it can be seen that the surface tension values exhibit a slight decrease due to aging (i.e., 46.5 ± 0.9 mN/m at day 0 and 44.7 ± 0.2 mN/m at 90 days of aging). To capture the effect of aging on the surface rheology, rising bubble shape tensiometry measurements were carried out in parallel on solutions at 5 mM SDS concentration. This concentration was chosen because it is high enough to maximize the adsorption of LOH molecules within a reasonable experimental time necessary (**Figure 5-9c**), ~1h, while remaining below the CMC of the solution to prevent the solubilization of the LOH molecules into the SDS micelles. As shown in Figure 6c, the complex modulus (κ^{s*}) of the surface increases with aging time,[294, 324] while the phase angle (δ) exhibits a reduction in magnitude, indicating a more elastic response. This is expected for surfaces with high coverage of LOH molecules, which behave more elastically than SDS populated surfaces.[213, 323] When comparing the values from day 0 to day 90, E increases by a factor of 3 and δ decreases from 62 ± 29° to 6.1 ± 0.8°. In agreement with the results obtained from fitting of the isotherms to the thermodynamic models, the surface rheology of the system points to a higher degree of contamination of the aged sample. However, it is noticeable that the increase in the complex modulus and the decrease in the phase angle are more pronounced than the increase in the molar fraction given by the best fit to the thermodynamic model. This highlights the higher sensitivity obtained when examining the dynamics of the surface in contrast to its equilibrium condition.

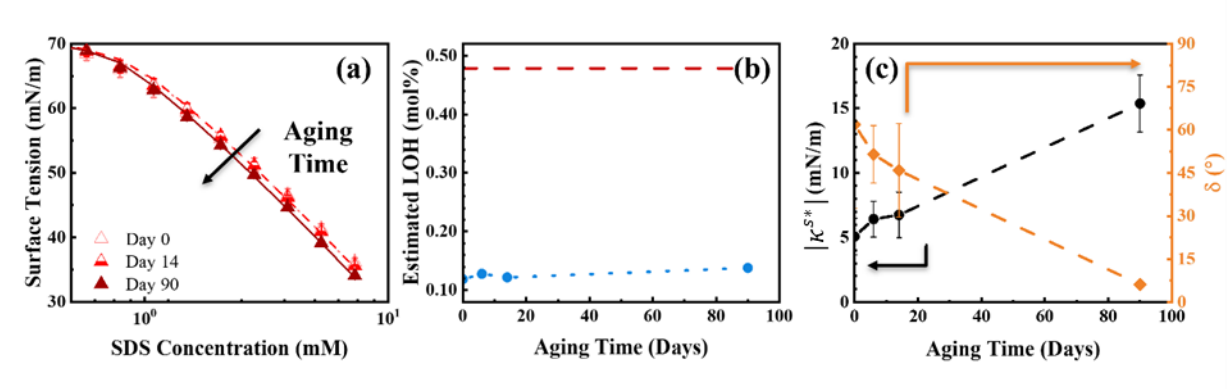

Figure 5-13. (a) Surface tension isotherm of aged samples for day 0 (empty triangles), 14 (half-filled triangles) and 90 (full triangles), and the corresponding fits from the Kralchesvsky adsorption model. (b) Molar fraction of LOH present in a recrystallized SDS sample as a function of the solution aging time (blue circles). The amount of LOH contamination in an unpurified sample is also shown for reference (red dashed line). (c) Surface rheological results obtained for a recrystallized sample at 5 mM SDS as a function of the aging time. The complex modulus is shown in black circles and the phase angle is shown in orange diamonds. Some error bars are not visible because they are smaller than the symbol size.

5.2.3. Summary of Findings

This section discussed the implications of LOH presence in SDS solutions. In mixed SDS and LOH solutions, even small concentrations of LOH (e.g., below 0.5 mol%) have a strong impact on the surface properties, such as surface tension and surface dilational rheology, which is summarized as follows.

(i) In contrast with pure SDS solutions, the surface tension of mixed systems can further decrease by 20 mN/m at concentrations close to the CMC. The adsorption models were used to calculate the degree of contamination present in the solution, where a higher contamination was predicted by the Kralchesvsky model.

(ii) With regards to the surface rheology, the surface becomes more elastic as the surface concentration of LOH increases in the mixed solution. For instance, the complex modulus increases one order of magnitude as the amount of LOH contamination goes up from 0.1 to 0.5 mol% in the bulk. Fitting of the surface tension isotherms to the three thermodynamic models

provided an estimate for the LOH content in the solution; these values were then used as an input to a two-component rheological model. All thermodynamic models yielded surface rheology predictions for the mixed solution that were in fairly good agreement with the experimentally measured data. Nevertheless, the only model able to capture the experimentally measured rheological data, without features that are not physical, was the Kralchevsky model.

(iii) The presence of background electrolyte improves the SDS adsorption and decreases the overall impact of LOH molecules on the readings of surface measurements carried out on the contaminated sample. This was evidenced by the apparent disappearance of the characteristic dip in the surface tension isotherm for the mixed solutions (**Figure 5-8b**) and the lower values of elastic modulus for the recrystallized sample in presence of added electrolyte (**Figure 5-11b**). However, the surface rheology of the 10 mM NaCl system probed at concentrations lower than the CMC indicates that traces of impurity are present in the recrystallized samples. This is further confirmed by the decay in the elastic modulus once the CMC is reached, with the LOH desorbing from the interface and populating the mixed micelles.

(iv) The hydrolysis process that converts SDS molecules back into LOH molecules was examined using a recrystallized sample. Both surface tension and surface dilational rheology were measured during the aging time up to 90 days. The effect of aging on surface tension and surface rheology readings were compared using data at 5 mM SDS. While the surface tension values exhibited a slight decrease due to aging, our results highlight that the surface rheology measurements can capture the increase in LOH content through an increase in the complex modulus and a decrease in the phase angle.

5.3. Mechanical Properties of Mixed Monolayers Composed of SDS and Silica Particles at the Air-Water Interface

5.3.1. Introduction

As stated in the previous section of this chapter, interfacial systems composed of like-charged particles and surfactants are not well understood. Even less is known on the effect of particle attributes such as roughness on their behavior in presence of similarly charged surfactants.

We investigated these scenarios using negatively charged silica particles (spherical and fumed) and the anionic surfactant sodium dodecyl sulfate (SDS). The systems were tested at the air-water interface using a Langmuir trough coupled with a microscope for microstructure observation. We compared the impact of SDS presence on the measured surface pressure isotherms and the related compressibility modulus. Next, we estimated the contact angle of the spherical particles at various SDS concentrations and discussed how the interparticle interactions and packing efficiency of monolayers formed are affected by the presence of SDS on the subphase. Finally, we discussed the hysteresis associated with each of the systems and relate it to the observed mode of collapse.

5.3.2. Results and Discussions

5.3.2.1. Contact Angle and Zeta Potential

As a means of characterizing the particle systems studied in the section, the contact angle of a deposited monolayer of particles was measured with DI water droplets and the zeta potential of the particles was measured at the experimental salt and SDS concentrations under study on this section, shown in **Figure 5-14**. The measured contact angles illustrate a hydrophobic character for all the particles used in this study, which originates from the replacement of the silanol groups on the surface of silica particles via silanization reaction using DMDCS. Since these contact angle

measurements were performed on a particle-coated slide, there is inherently roughness associated with the measured value, which is known to alter the wettability of a surface.[329] Thus, since the surface is far from smooth, the measured contact angle can be represented by the Cassie-Baxter equation, which considers the air that is trapped between the particle surface and the drop and how it enhances the hydrophobic character of the surface.[329] This effect is expected to be more prominent on surfaces with higher roughness, which is the observed trend in **Figure 5-14a;** as the specific surface area increases from spherical to LSA and MSA, the measured contact angle also increases.

Figure 5-14b depicts the measured zeta potential for the particles at different background salt and SDS effective concentrations. As established in the previous sections, the effective concentration of SDS is useful to account for the background electrolyte concentration on the activity of the molecule. It is possible to note that for all systems there is a tendency of supercharging as the SDS effective concentration increases. As established in the first section of this chapter, supercharging can be interpreted as SDS adsorption to the silica surface. In fact, since the silica particles under study in this chapter are hydrophobically modified, it is likely that SDS tail-down adsorption, with the polar head facing the solution, is enhanced due to the favorable interactions between the SDS hydrophobic tail and the dimethyl groups on the particle's surface. Therefore, it is expected that the particle will become more hydrophilic at higher SDS concentrations, which will be discussed further in this section.

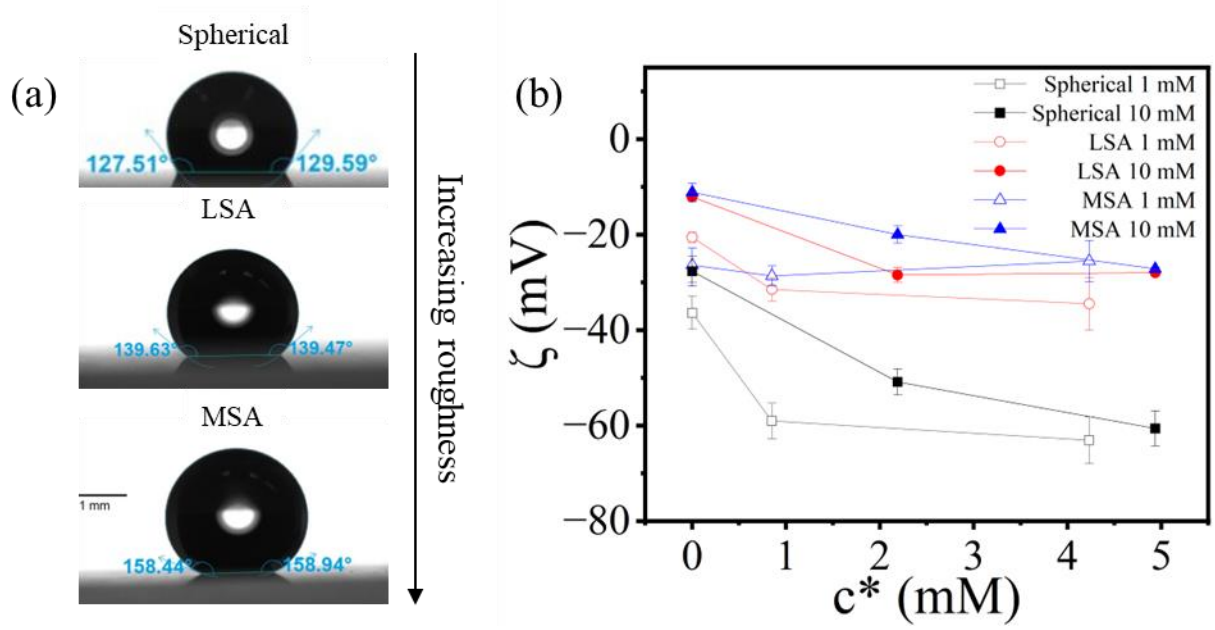

Figure 5-14. (a) Contact angle of DI water droplets on glass slides coated with the particles of interest. From top to bottom, spherical silica particles, and LSA and MSA fumed silica particles; (b) Measured zeta potential of the particle systems in dispersions of 1 and 10 mM of NaCl electrolyte concentration as a function of effective SDS concentration (c^*).

5.3.2.2. Surface Pressure Isotherms

When a mixture of particles and surfactants is present near a fluid interface, both species will impact the surface pressure measured by the Wilhelmy plate. For the case of SDS, which are soluble in water and can readily adsorb to and desorb from the interface, it is assumed that their presence in bulk leads to a constant contribution to the resulting surface tension (or surface pressure), which is set by their bulk concentration. **Figure 5-15a** shows the total surface pressure that result from the spherical silica particles and surfactant mixtures at three different SDS concentrations of 0, 9, and 42% CMC value at that background salt concentration of 10 mM. It should be noted that the surfactant was added to the bulk first followed by the deposition of particles to the air-water interface. As can be seen from the figure, higher SDS concentrations are associated with a higher initial surface pressure, related to their adsorption at the air-water surface. We can assume that their contribution to the overall surface pressure is only a function of their

bulk concentration in order to isolate the impact of particles on the resulting surface pressure by defining a "particle-only" surface pressure ($\Pi_P = \Pi - \Pi_{SDS}(c_{SDS})$). **Figure 5-15b** shows Π_P as a function of trough area for the same systems. It is important to note that, different from **Figure 5-15a**, where all the surface pressures converged at the end of compression, i.e., in the closed-barrier state, **Figure 5-15b** exhibits different surface pressures for each case at the end of the compression, since we excluded the surfactant contribution. Additionally, from **Figure 5-15b** we can infer that the presence of SDS at the air-water surface affects the binding efficacy of the deposited spherical particles, represented by the shift of the inflection point towards lower trough areas. The binding efficiency of the particles will be discussed further on.

Following the procedure that was utilized in previous chapters, we chose the trough area at the inflection point of the isotherm as the reference point and normalized all isotherms with regards to it, as shown in **Figure 5-15c**. Interestingly, there is an overlap at all SDS concentrations, indicating that, aside from the lowered particle trapping efficacy in presence of surfactant molecules, the monolayers formed by the particles are interacting over a similar range. **Figure 5-15d** shows the compressibility modulus for the monolayers as a function of the normalized area. It is possible to note that the compressibility modulus decreased from 160 ± 11 mN/m at 0% CMC to 77 ± 5 mN/m at 42% CMC. Thus, the presence of SDS in the system decreased the amount of force required to compress the monolayer.

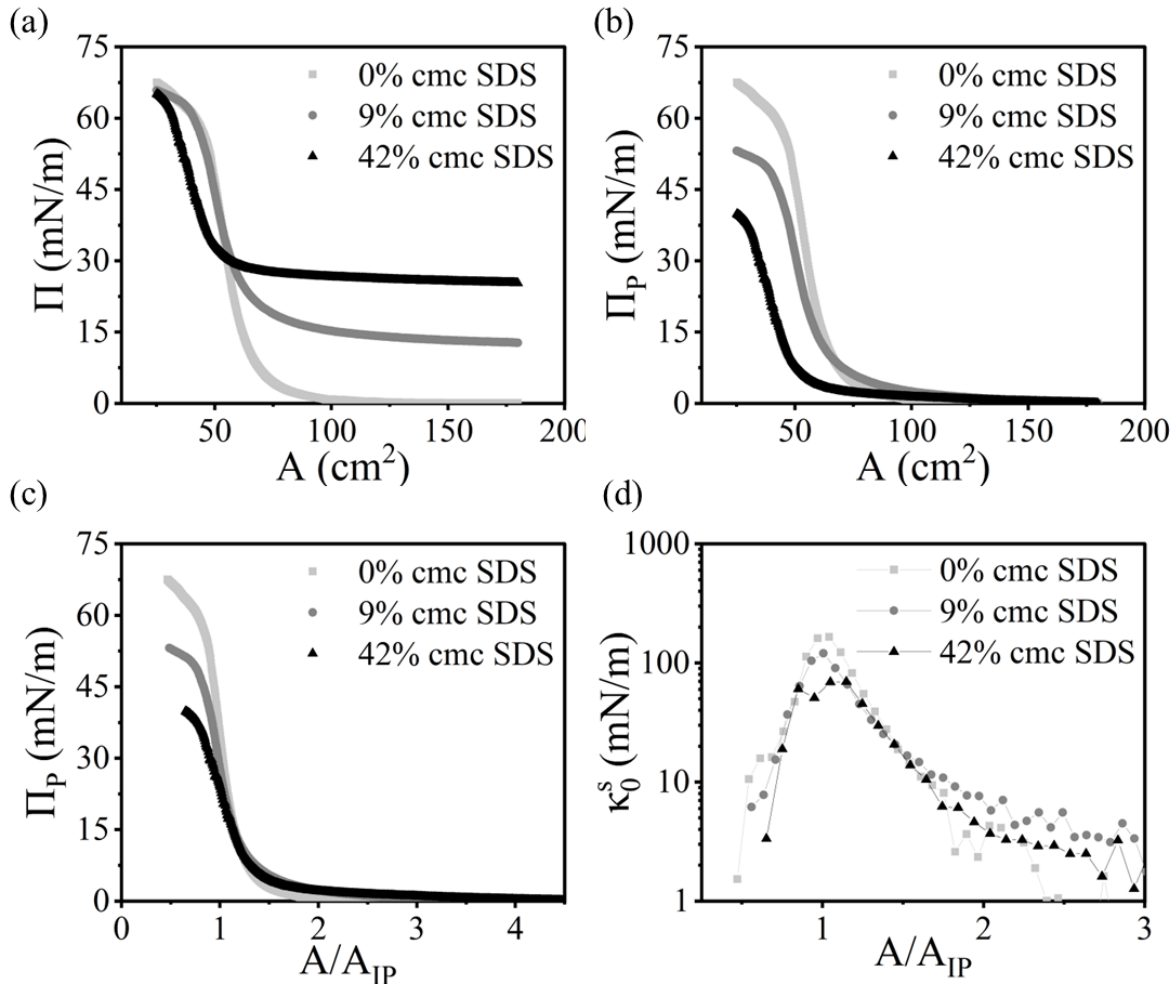

Figure 5-15. Surface pressure isotherms for spherical particles with varying SDS concentrations in bulk at 10 mM NaCl. (a) Total surface pressure (considering particles and surfactants contributions) as a function of trough area; (b) Particle only surface pressure as a function of trough area; (c) Particle only surface pressure as a function of the inflection-point normalized area; (d) Surface isothermal compressibility as a function of the inflection-point normalized area. Different concentrations of SDS are shown in different shades of grey, where darker tones are associated with higher SDS concentrations.

An equation of state can be used to shed light in the differences between mixed and particle-only systems. Eq.(3-20) can be used to fit the experimental data by varying the particle surface coverage at the inflection point (θ_{IP}) and the Frumkin interparticle interaction parameter (a_P). **Figure 5-16a** depicts the surface pressure isotherms and the best fits from Eq.(3-20) as a function of the particle surface coverage (θ_P). It is possible to note that the isotherm modeled for the particle only system is in good agreement with the measured data and possessed the highest θ_{IP} of ~0.89.

For the mixed system of particles and surfactants, as the surfactant concentration was increased, the curves shifted to the left, indicating a more open network is being formed. It is important to note that the agreement between the model and the experimental data worsened at concentrations close to 50% of the CMC. This indicates that some key attributes of the monolayers are not being captured by the used equation of state at high SDS concentrations. The possible sources contributing to the resulting discrepancy could be that the model lacks the contribution from interactions between the surfactants and the particles, and/or that dodecanol molecules (which are not being considered in the model) are affecting the surface pressure.

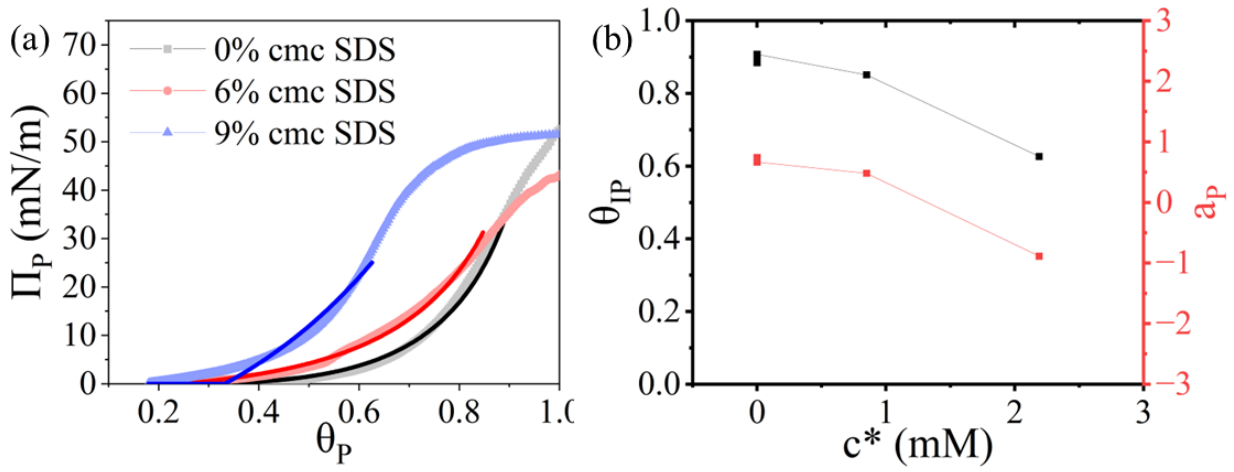

Figure 5-16. (a) Spherical Particle-only surface pressure (Π_P) isotherms as a function of particle surface coverage (θ_P) obtained for different SDS concentrations. Results for the case in the absence of surfactants is shown in black squares, whereas mixed particle/surfactant systems are displayed in red circles and blue triangles for samples with SDS at 6% CMC and 9% CMC, respectively. The experimental data are shown in lighter tones and the best fit from the Frumkin equation of state (Eq.(3-20)) are shown in a darker tone. The function only fits the data for $\theta \leq \theta_{IP}$ since at higher surface coverages the monolayer is not a 2D structure. (b) Fitting parameters for Eq. (3-20) found for systems as a function of the effective SDS concentration (c^*) calculated for various systems. Particle surface coverage at inflection point θ_{IP} is shown in black, and the Frumkin interaction parameter (a_P) is shown in red.

By analyzing all measured isotherms at each effective SDS concentration with the equation of state, we can determine the trend of the fitting parameters taking place as SDS concentration is increased, shown in **Figure 5-16b**. First, a_P shows a downward trend as the SDS concentration

increases, shifting from attractive (positive) to repulsive (negative) at $1 < c^* < 2$ mM. This can be related to the fact that in the presence of surfactant, interparticle interactions shift from attractive through capillary and hydrophobic interactions, to repulsive through electrostatic interactions, as the surfactants adsorb onto the particle surface. This agrees with the supercharging effect experienced for the spherical particles shown in **Figure 5-14b**. Next, θ_{IP} decreased as c^* increased. This is agreement with the results shown earlier on **Figure 5-15d**, where higher SDS concentrations show a lower resistance to compression, indicative of a less populated monolayer. However, the magnitude of decrease is likely overestimated by the model.

Another way to capture the interaction between the hydrophobic spherical particles and SDS is by estimating the contact angle of the particles as the surfactant concentration increases. To avoid spreading effects associated with drop tensiometer contact angle measurements, we chose to use the surface pressure isotherms to indirectly determine the contact angle at which the particles are sitting at the interface. As shown by Aveyard et al.[330] the collapse point can be interpreted as the work necessary to desorb a particle trapped at the surface. This is therefore related to the energy associated with a particle straddling an interface with an equilibrium contact angle (θ_E) as shown in Eq. (2-2). Rearranging and solving for θ_E we obtain:

$$\theta_E = \cos^{-1}\left(\sqrt{\frac{\Pi_C A_C}{A_P \sigma_{SDS}} - 1}\right) \qquad (5\text{-}3)$$

Where Π_C is the particle contribution to the collapse pressure, A_C is the collapse area, A_P is the area occupied by particles at the surface and, σ_{SDS} is the surface tension of the system at a given SDS concentration. A_P can be estimated from the calculated θ_{IP} on **Figure 5-16b**.

Figure 5-17 shows the results for the contact angle as a function of the effective SDS concentration. It is possible to note that as SDS concentration increases, there is a decrease in the contact angle, indicating that the silica particles are becoming more hydrophilic. This is in agreement with the data shown previously, where the zeta potential becomes more negative as the SDS concentration increases (**Figure 5-14b**). It is important to note that Eq. (2-2) is valid only for single particles at interfaces and does not account for interparticle interactions. Therefore, the trend observed in **Figure 5-17** should be taken as qualitative rather than quantitative.

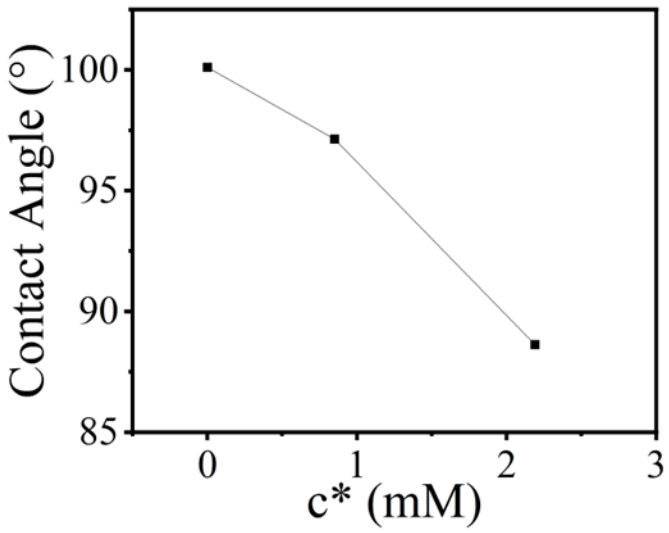

Figure 5-17. Contact Angle calculated from the collapse pressure of spherical particles based on Eq. (5-3) as a function of the effective SDS concentration.

5.3.2.3. Hysteresis

As reported in chapter 4, increasing the surface roughness of particles drastically impacts the resulting hysteresis in response to cyclic compressions and expansions. In this section, we extend the same analysis to the mixed SDS/silica systems under study to examine the impacts of SDS on the resulting hysteresis obtained from different particle systems at the air-water interface. **Figure 5-18** shows the 1st, 2nd, and 3rd compressions for all particles under study at SDS

concentrations of 0 and 42% CMC. The trend observed for particle-only systems in **Figure 5-18a-c** is similar to what was discussed earlier in chapter 4, and is shown here as a baseline for the implications of SDS presence. **Figure 5-18d** illustrates the compressions at 42% CMC, which exhibit no overlap at the higher compression ratios from 2nd to 3rd compression, in contrast with the behavior reported for the particle-only system in **Figure 5-18a**. The hysteric effect is more dramatic for the fumed silica particles (**Figure 5-18e, f**), where after the first compression, the subsequent isotherms do not reach the inflection point, which would indicate that no collapse is taking place. However, this is not the case since from the second compression to the third compression, there is evidence of hysteresis shown by the lower surface pressures measured.

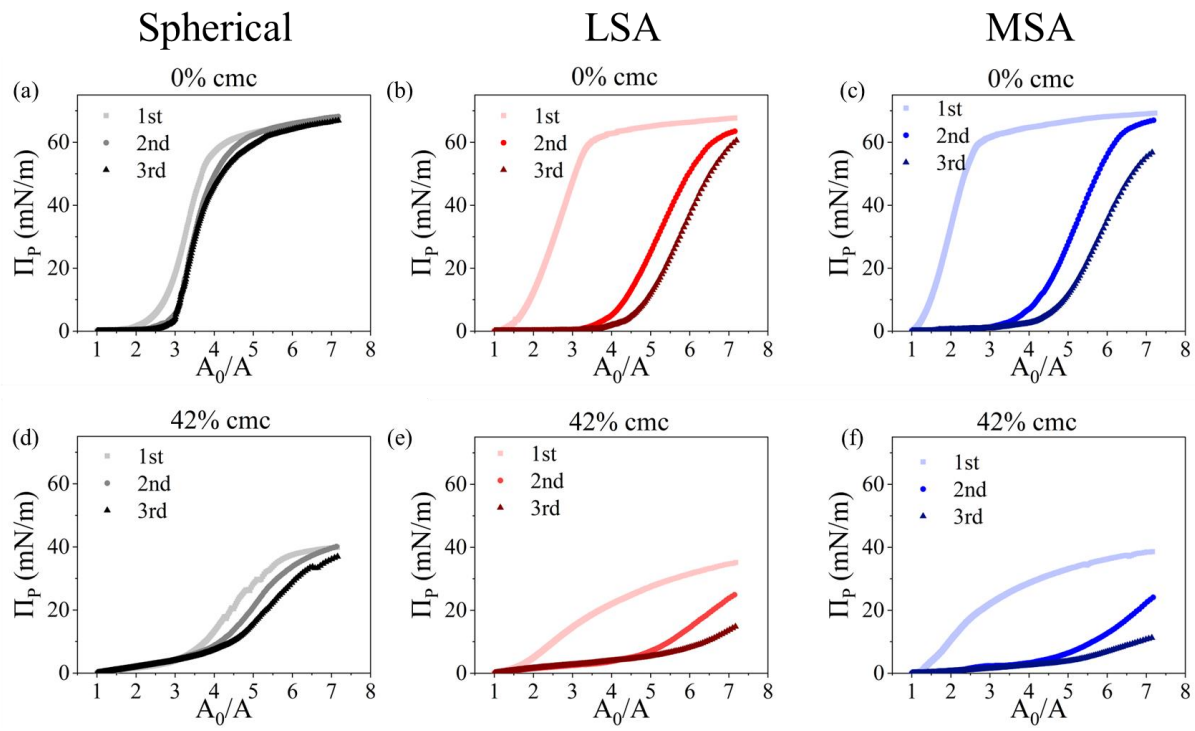

Figure 5-18. Surface pressure isotherms of the successive compressions for (a, d) spherical particles in different shades of grey, (b, e) LSA fumed silica particles in different shades of red and, (c, f) MSA fumed silica particles in different shades of blue. The top row shows the results for 0% CMC, and bottom row shows the results for 42% CMC. Darker tones are associated with higher counts of compressions.

Analogously to procedure carried out in previous chapters, it is possible to quantify the hysteresis experienced by each particle system by applying Eq. (3-7). **Figure 5-19** shows the results for the three cycles measured. It is clear that for the first cycle (**Figure 5-19a**), for all SDS concentrations, $\overline{\Pi}$ is directly proportional to the specific surface area, as found before in chapter 4. However, in the second cycle, at SDS effective concentrations higher than 0, spherical particles show a higher hysteresis when compared to the fumed particles (**Figure 5-19b**). The same is true for the third cycle (**Figure 5-19c**). We attribute this trend to the fact that, even after the first cycle, monolayers made from spherical particles collapsed, which was not observed for the monolayers formed by either fumed silica particles (**Figure 5-18e, f**). Interestingly, for the first cycle, SDS concentration is mainly affecting the spherical particles hysteresis, as increasing SDS concentration resulted in an increase in $\overline{\Pi}$.

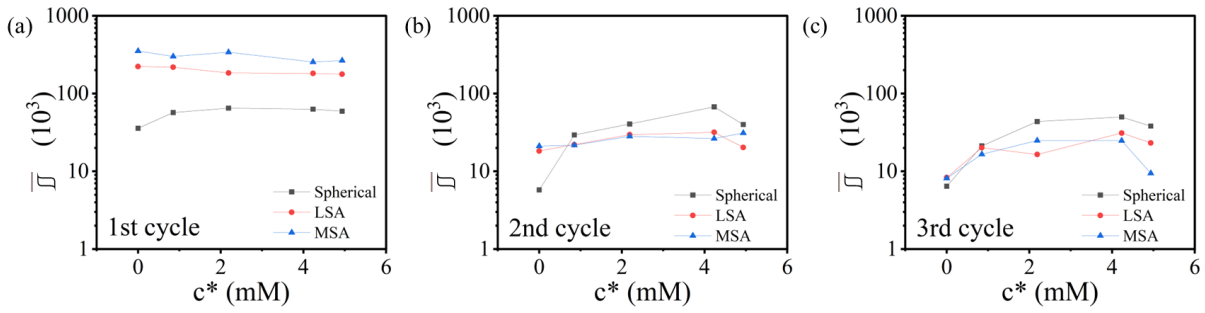

Figure 5-19. Normalized hysteresis coefficient ($\overline{\Pi}$) results for different particles as a function SDS concentration for (a) 1st, (b) 2nd, and (c) 3rd cycle. Black squares, red circles, and blue triangles represent spherical particles, and LSA and MSA fumed silica particles, respectively.

5.3.2.4. Collapse Mode

The inflection point on the surface pressure isotherm can be used as a reference to identify the state at which the particle monolayer achieves its maximum compaction in 2D. Beyond that point, further compressions cause 3D deformations (for example, in form of particle expulsion to the bulk phase or buckling of the particle monolayer).[182] **Figure 5-20** shows the state of the

monolayer at surface areas smaller than the collapse area for the different particles under study at SDS concentrations of 0 and 42% CMC. Monolayers formed by spherical particles exhibited buckling, with large amplitudes and wavelengths for both 0 (**Figure 5-20a**) and 42% (**Figure 5-20d**) CMC SDS concentrations. For LSA monolayers, at 0% CMC, the collapse is characterized by wrinkles with small amplitudes and wavelengths (**Figure 5-20b**). This is attributed to the fact that fumed silica particles have intrinsically smaller features than the round and smooth spherical particles. As SDS concentration increases to 42% CMC (**Figure 5-20e**), the wrinkles disappear, and thicker structures are formed, which are interpreted as subduction of fumed silica particles forming multilayers. A similar trend is seen for MSA particles at 42% CMC (**Figure 5-20f**), where thicker aggregated structures are visible in the micrographs. Additionally, MSA particles at 0% CMC (**Figure 5-20e**) show an irregular point at which particles are forced out of the surface, caused by the irregular edges of the clusters overlapping. This is likely the cause for the high hysteresis observed for all fumed silica particles at 0 SDS concentration, and such phenomena has not been observed for monolayers formed by spherical particles.

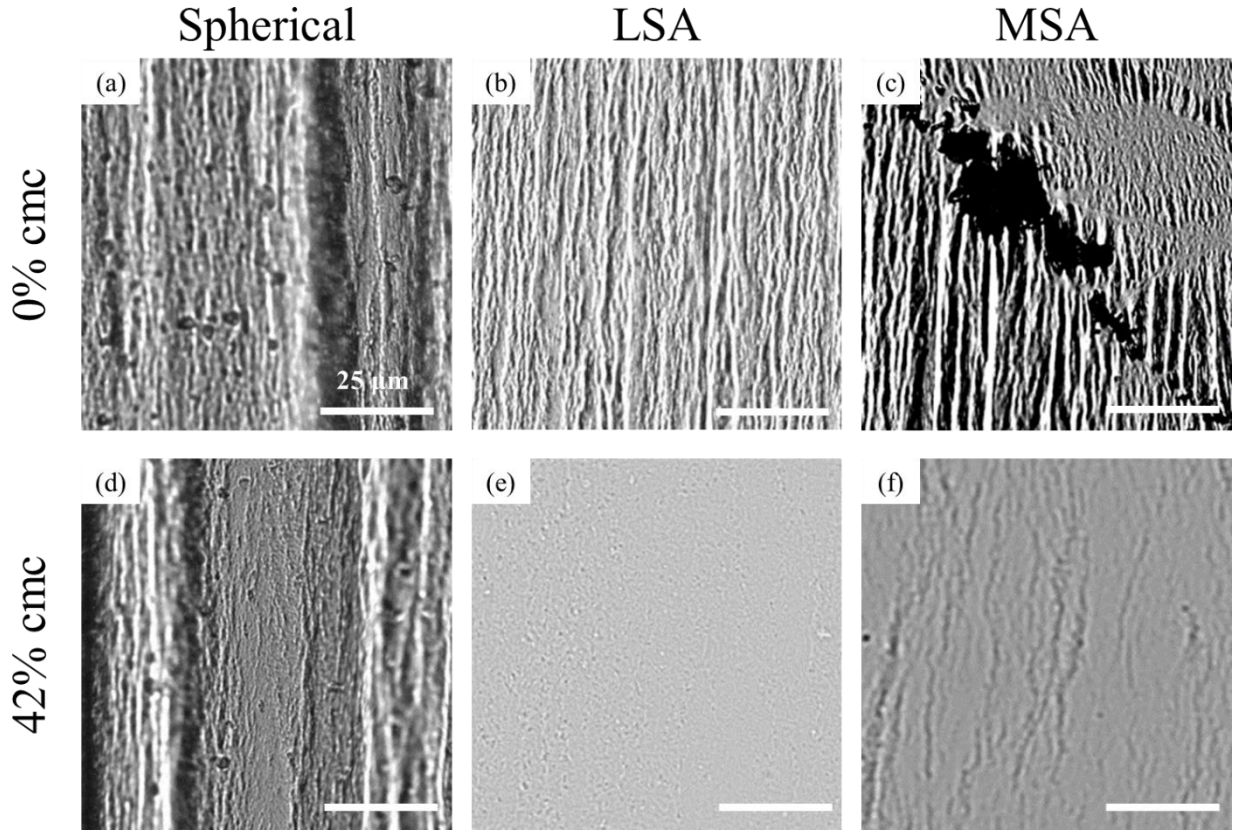

Figure 5-20. Snapshots of the collapse mode for monolayers formed by (a, d) spherical silica particles, and (b, e) LSA and (c, f) MSA fumed silica particles. The top row shows the results for no SDS system, and the bottom row shows the results for mixed systems at SDS concentration of 42% CMC.

5.3.3. Summary of Findings

In this section, we investigated the properties of surface monolayers formed by like-charged particles and surfactants using negatively charged silica particles (spherical and fumed) and the anionic surfactant sodium dodecyl sulfate (SDS). We studied the impact of SDS presence on the measured surface pressure isotherms and the related compressibility modulus. Our results show that SDS decreases the trapping efficiency of spherical particles and their packing at the inflection point, which lowers their maximum compressibility. We inferred the interparticle interactions via the surface equation of state, which indicated that as SDS concentration is increased, the interactions shift from attractive to repulsive. This was attributed to the tail-down

adsorption of SDS onto the silica surface, which yields the particles more hydrophilic, as shown by the supercharging captured in the zeta potential measurements and the decrease in the estimated contact angle of particles at the interface based on the collapse point of the monolayer. Finally, we compared the effects of roughness on the hysteresis at various SDS concentrations. We conclude that for the first compression cycle, the hysteric behavior is directly proportional to the specific surface area. However, on the subsequent cycles, SDS increases the hysteresis experienced by spherical particles. For fumed silica particles, subsequent cycles do not reach an inflection point, indicating that there is an irreversible compaction taking place at every cycle. This is illustrated by the mode of collapse, which is unchanged for spherical particles, but is drastically altered for the monolayers of fumed silica particles upon the presence of SDS.

5.4. Preliminary Studies on Mixed Systems of Janus Particles with SDS

5.4.1. Introduction

In the previous chapters, we learned that the presence of surfactants in the subphase lowers the interfacial tension of the system, which not only impacts the trapping efficacy of the deposited particles but could also decrease the energy required to desorb a particle from the interface. In addition to populating fluid interfaces, surfactants can adsorb onto the surface of particles. Depending on the driving force for the adsorption, surfactants can be present on the particle's surfaces in a head-down or tail-down configuration, which will in turn alter the surface characteristics of the particles. For Janus particles, each hemisphere needs to be considered separately with regards to its interaction with surfactant molecules. In the case of the negatively charged silica cores, an anionic surfactant like SDS will adsorb tail-down onto the surface, promoting the magnitude of the surface charge and rendering the silica surface more hydrophilic. When considering the gold cap (or thiolated gold), a tail-down adsorption is likely, which once again yields the surface more hydrophilic. Therefore, the presence of surfactants not only changes the surface energy of the system but also can alter the amphiphilicity of the particles.

As Janus Particles can be present at the interface with a distribution of cap orientations, as depicted in Section 4.2, different JP faces might be submerged in the aqueous subphase and available for SDS adsorption. As the area of contact between each hemisphere and the aqueous phase is only a function of the JP contact angle and cap orientation at the interface, and because the SDS adsorption can alter the wettability of JP faces, the orientation distribution of particles may be tuned by the addition of surfactants to the subphase. For instance, considering the JPs used in this study, it might be possible to enhance the amphiphilicity of JP particles that are in the cap up configuration via adsorption of SDS on the silica face in contact with the aqueous subphase,

whereas for the case of tilted particles, SDS adsorption would enhance the particle hydrophilicity, as shown schematically in **Figure 5-21**.

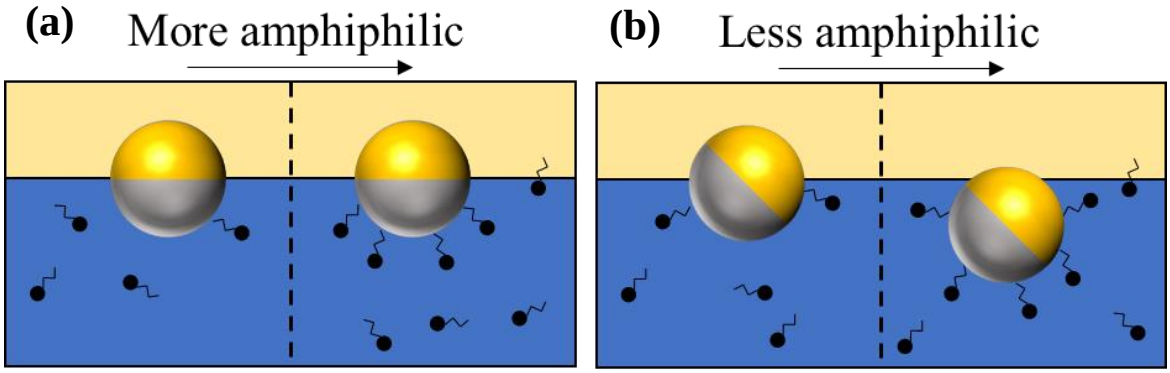

Figure 5-21. Schematics of JPs in a (a) vertically aligned or (b) tilted configuration at the air-water interface. Cartoons illustrate the impact of SDS adsorption onto the faces of the JP particle on the particle's amphiphilicity.

5.4.2. Preliminary Results

As a first approximation, if one considers one particle, assuming no SDS adsorption onto the particle's surface, the overall free energy of the system (E_i) can be considered to arise from independent contributions by each species present as follows:[50]

$$E_i = E_{SDS} + N_P \Delta E_d \qquad (5\text{-}4)$$

Where E_{SDS} is the energy contribution from the surfactant covered interface, N_P is the number of particles trapped at the interface, ΔE_d is the desorption energy of the particles from the interface, as discussed earlier in Chapter 4. Since ΔE_P is a function of JP's amphiphilicity and its orientation, by plugging Eq. (4-1) the expression becomes:

$$E_i = \sigma_{SDS} A_{SDS} + N_P \sigma (A_{a2} \cos\theta_A + A_{p2} \cos\theta_P - A_i) \qquad (5\text{-}5)$$

Where σ_{SDS} is the surface tension at a given SDS concentration, A_{SDS} is the area occupied by the surfactants and, σ is the surface tension in the absence of SDS. Since there is a competition between the JP particle and SDS molecules for populating the fluid interface, we can compare which species

is more likely to occupy the interface by calculating the free energy difference (ΔE_{Ads}) between the two following states; a state associated with a particle being adsorbed to the surface and a state in which surfactants are adsorbed onto the interface, with the same interfacial area occupied:

$$\Delta E_{Ads} = (\sigma_{SDS} - \sigma)A_i - \Delta E_P \qquad (5\text{-}6)$$

From Eq. (5-6), we can calculate ΔE_{Ads} for each amphiphilicity at different SDS concentrations. When $\Delta E_{Ads} > 0$, JPs would be more likely to occupy the interface, whereas if $\Delta E_{Ads} < 0$, adsorption of SDS molecules onto the fluid interface would more energetically favorable. Results of this analysis are shown in **Figure 5-22**, for the JPs of three different amphiphilicity under study in this thesis. It is worth noting that the wettability of each JP faces that were estimated in Chapter 4, Section 4.2, are used in these calculations. The color map shows the sign and magnitude of ΔE_{Ads} normalized by the thermal energy. As expected, there is a higher tendency for SDS adsorption onto the fluid interface with increasing either the SDS concentration or the JP tilt angle. It is interesting to note that C_4 particles are the particles most likely to desorb from the interface at a lower tilt angle. This can be explained by the fact that C_0 particles less area from the interface due to its contact angle of ~76°, whereas C_4 particles sit at a contact angle of 90°, occupying the maximum area, which makes more area available for SDS molecules to adsorb, further reducing the surface free energy.

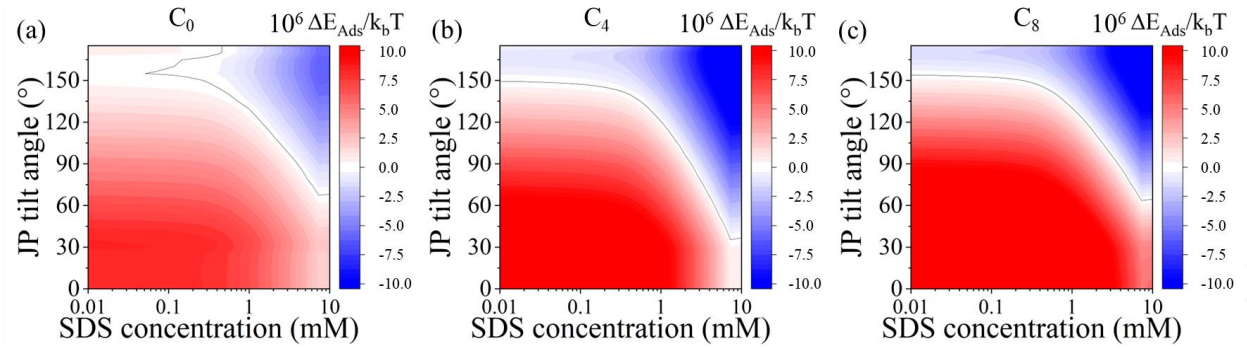

Figure 5-22. Energy of adsorption (ΔE_{Ads}) map calculated with Eq. (5-6) for (a) C_0, (b) C_4 and, (c) C_8. Red regions pertain to phase space in which JP adsorption to the fluid interface is more favorable, whereas blue regions pertain to condition that favor the SDS adsorption onto the interface.

With these results on the competition of Janus particles and SDS molecules for adsorption onto the interface, interfacial shear rheology experiments were conducted at several concentrations of SDS as follows. The particle monolayer was first prepared by depositing JPs at the air-water interface and compressing the particle network to the surface pressure of 50 mN/m. Next, a concentrated solution of SDS was added dropwise to the subphase from the outside of the trough barriers. After the addition of SDS molecules, the system was allowed to equilibrate. To ensure the systems equilibrium, we tracked the time evolution of the dynamic moduli with small amplitude oscillations at a constant frequency of 1 rad/s until they reached a constant value (~40 minutes) prior to the frequency sweep experiments. The results for the elastic and viscous moduli of the interface are shown in **Figure 5-23** as a function of the SDS concentration and compared to the case of particle-only system in the absence of SDS in the subphase. It is possible to note that there is a decrease in both moduli for all amphiphilicities after the addition of SDS, which could be attributed to the desorption of particles from the interface. However, at 0.5 mM SDS, C_0 shows the least variation, which is in agreement with the energy map provided **Figure 5-22**, where at this concentration there is minimum likelihood of desorption for C_0 particles, even at high tilt angles. It is important to note that the energy calculations assume no SDS adsorption to the particle

surface, which might be important. In contrast, both C_4 and C_8 particles show an appreciable difference in the dynamic moduli measured as the SDS concentration was increased. At higher concentrations of SDS, all monolayers are affected by the presence of surfactant.

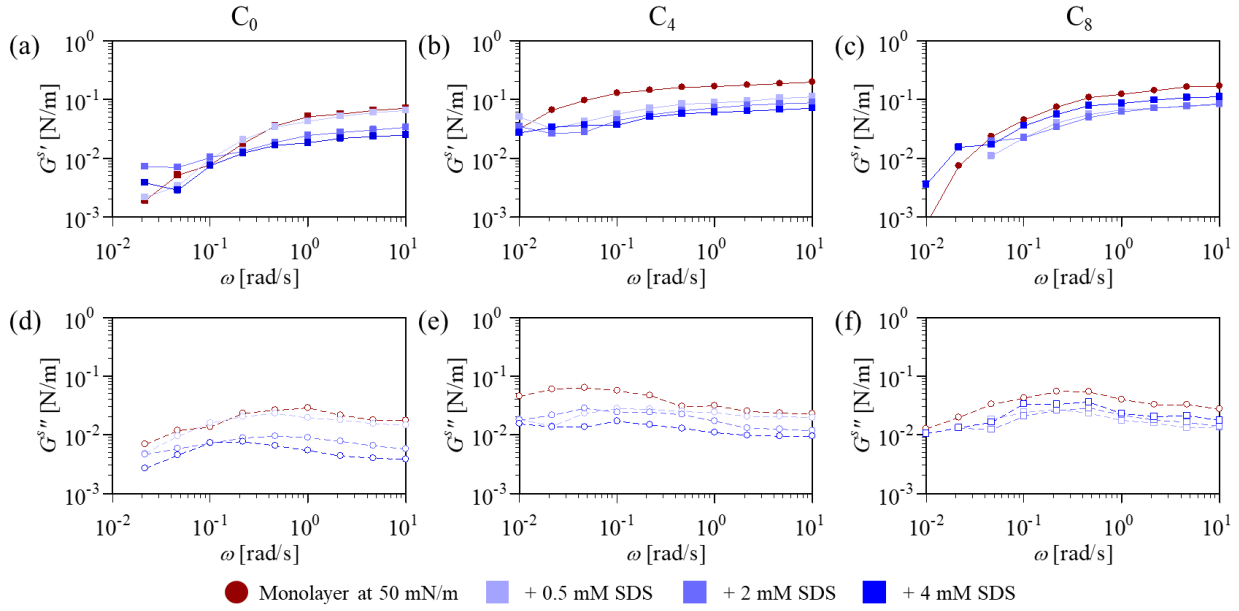

Figure 5-23. Dynamic moduli of JPs monolayers at 50 mN/m in the absence and presence of SDS in the subphase at concentrations of 0.5, 2, and 4 mM. Panels (a, b, and c) show the surface elastic moduli, $G^{s\prime}$, and panels (d, e, and f) display the surface viscous moduli $G^{s\prime\prime}$. Results are obtained for particles of different amphiphilicities, namely, C_0, C_4, and C_8 respectively. Data belonging to particle-only monolayers are shown in red, while measured data on mixed systems are provided in different shades of blue.

When looking at the loss tangent, however, there is a clear difference between all amphiphilicities as shown in **Figure 5-24**. C_0 monolayers shows a decreasing loss tangent with increasing in SDS concentration (**Figure 5-24a**). In contrast, C_4 monolayers show an increase in the loss tangent as SDS is added at 0.5 mM, but upon the increase in concentration, $\tan(\delta)$ tends to overlap with the particle-only scenario (**Figure 5-24b**). C_8 monolayers show a departure from the particle-only curve at the lowest frequencies probed, but at frequencies higher than 0.1 rad/s, the loss tangent is similar for all cases (**Figure 5-24c**).

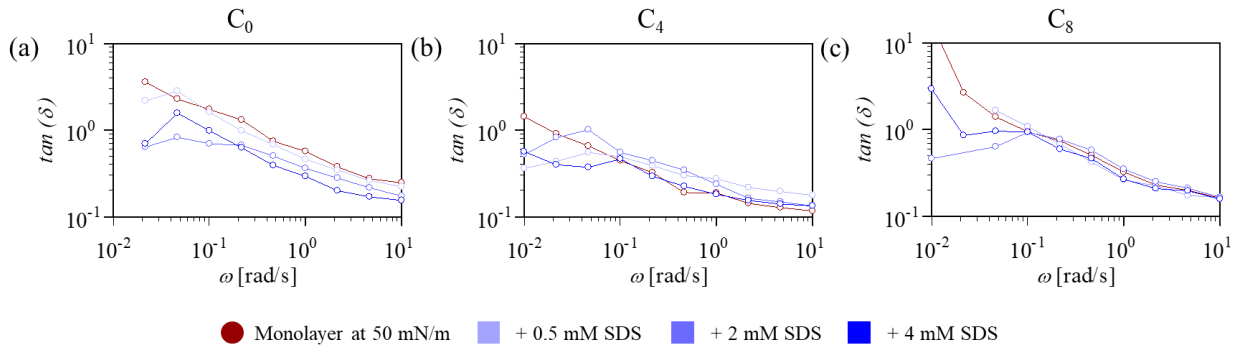

Figure 5-24. Loss tangent results from frequency sweep measurements of JPs monolayers at 50 mN/m upon the addition of different concentrations of SDS to the subphase for (a) C_0, (b) C_4 and, (c) C_8, respectively. Particle-only monolayers are shown in red, and mixed systems with SDS are shown in different shades of blue.

We attribute this difference to the interparticle interactions taking place within the monolayer. For instance, C_0 monolayers have a poor packing efficiency due to the high frequency of occurrence of dipolar capillary interactions, which upon the addition of SDS, become less relevant since a lower surface tension compensates for the surface deformation. Therefore, upon the addition of SDS to the subphase, the particles are able to rearrange and achieve higher packing states, as illustrated by the SEM pictures of a deposited monolayer of C_0 in the absence of SDS and in the presence of SDS at a concentration of 4 mM (**Figure 5-25**) in a procedure similar to the one used in Section 4.2. For C_4 and C_8 particles, since at the higher surface pressures (50 mN/m) they are mainly dominated by short-ranged capillary interactions, the monolayer should remain relatively unchanged upon the addition of SDS.

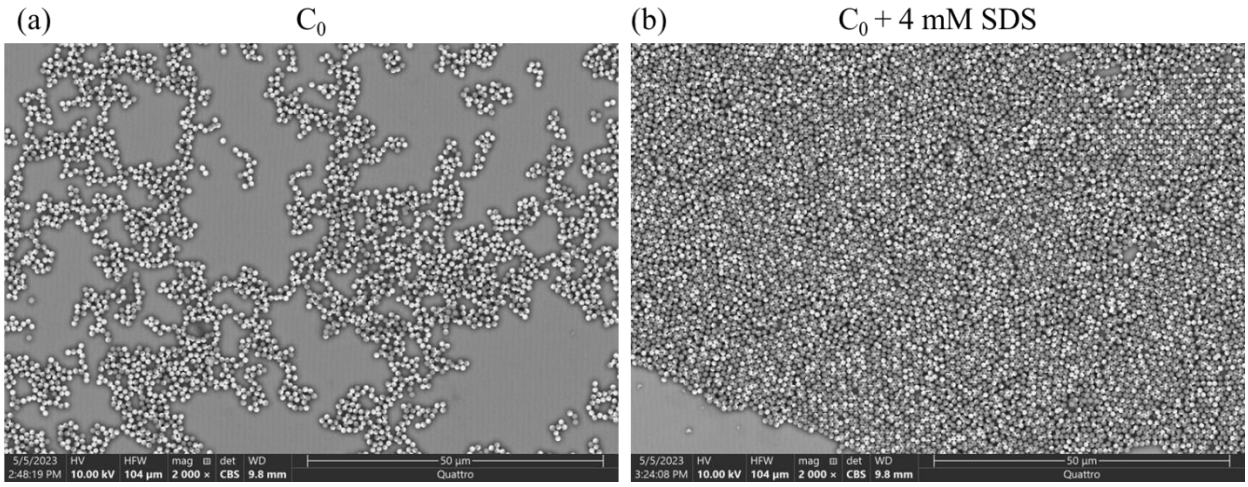

Figure 5-25. SEM micrographs of a deposited monolayer of C_0 at (a) 0 mM SDS and, (b) 4 mM SDS

5.4.3. Summary of Findings

In conclusion, in this section we discussed the effects of surfactants on the thermodynamic and rheological properties of the interface considering the likelihood of adsorption for each JPs along with SDS at different concentrations. We were able to measure the frequency dependence of a monolayer originally populated solely by JPs but altered upon the addition of SDS. It was possible to notice a difference in the behavior for each amphiphilicity, where C_4 was the most affected in the magnitude of the storage modulus, likely due to the desorption of particles from the interface. Next, C_0 monolayers became more solid-like upon the increased concentration of SDS, which was attributed to the attenuation of the repulsive long-ranged dipolar interactions in presence of SDS. Finally, C_8 particles were the least affected since their monolayer is predominantly populated by cap-up particles, which interact with short-ranged interactions and, most likely, will not desorb from the interface in the presence of SDS. Further studies on important properties of the monolayer such as the orientation distribution of JPs in presence of SDS, or their overall interparticle interactions are needed to test the proposed hypothesis of the change in the range of interactions between the particles.

6. Conclusions & Future Work

This work provided a fundamental study on thermodynamic and rheological characteristics of fluid interfaces populated by particles and/or surfactants. We studied two particle attributes, namely roughness and surface anisotropy, to investigate their impact on the mechanical properties of the particle network formed at the air-water interface by examining the resulting changes in the interparticle interactions at play. The interfacially trapped particle monolayer was analyzed on a Langmuir trough in order to investigate the linkage between the particle characteristics and interparticle interactions, resulting microstructure, and the surface pressure exhibited by the network. For monolayers consisting of rough fumed silica particles, we found that the particle roughness gives rise to repulsive capillary interactions between the particles, and their fractal shape allow them to interlock, which has a profound impact on its collapse mode and the observed hysteresis. In addition to the particle surface roughness, we examined the impact of particle surface anisotropy on the properties of the resulting interfacial networks. The study on Janus Particles showed that the orientation distribution of the Janus boundary at the interface will be altered as the JP amphiphilicity changes. It was found that the particle amphiphilicity can be used as a tuning factor to not only increase the energy associated with the particle desorption from the interface but can also affect the range and strength of interparticle capillary interactions occurring within the surface monolayer, which will in turn impact the response of the interfacial network to applied dilation or shear stresses. Highly ordered monolayers formed by Janus particles at a high surface coverage presented characteristics of a two-dimensional glass transition. For mixed systems of silica particles and SDS surfactant molecules, we found that SDS adsorbs onto the silica surface, which promotes the particles hydrophilicity, resulting in a more repulsive interparticle interactions

and a lowered trapping efficacy at the interface. For rough particles, SDS changed the collapse mode from wrinkling to multilayer formation. For JPs, the presence of SDS induces the desorption of some particles, and depending on their amphiphilicity, might change the range at which their interactions are taking place.

The work performed in this dissertation shed light on some of the open questions in the field of particles and surfactants at fluid interfaces. However, there are still opportunities to discover and expand on what has been done. First, this work focuses on the fundamentals of air-water interfaces, and how particle attributes affect the microstructure formed at the fluid interface and its resulting rheological properties. Given the ubiquity of oil-water interfacial systems in technological and industrial applications, it would be useful to expand the studies presented here to incorporate measurements at the oil-water interface, because of the importance of long-ranged dipolar electrostatic interactions through the oil phase. Macroscale measurements of interfacial systems, such as foam and emulsion stability and rheology, can also be helpful to connect the dots between the insights obtained from the fundamental studies carried out in this thesis and the performance in complex multicomponent formulations. Additionally, studies on the mixed systems of JPs and surfactants are still scarce. In particular, there is a gap in our understanding of the dynamics in these complex interfacial systems under various operating conditions such as electrolyte concentration and solution pH, and the nature of the non-aqueous phase (i.e., air vs. oil). For instance, at oil-water interfaces, presence of contaminants resulting from SDS hydrolysis have been shown to impart minimal impact on the measured surface properties. Lastly, examining the behavior of particle systems studied in this thesis; i.e., negatively-charged silica cores and gold caps, in combination with an oppositely-charged cationic surfactant could uncover some unique features, as it opens up the possibility for flipping the wettability of JP faces. For instance, this

task could be achieved by rendering the silica face hydrophobic via the head-down adsorption of surfactant, and turning the the gold side hydrophilic via the tail-down of the surfactant. The resulting amphiphilicity of the JP would then impact its orientation distribution at the interface and the interparticle interactions, therefore, opening up a path for switching the surface properties on demand.

Appendix A

Surfactants

Two-component Frumkin adsorption model

The surface pressure can be written as:[201, 213]

$$-\frac{\Pi\omega_0^*}{k_BT} = \ln(1-\theta_1-\theta_2) + \alpha_1{\theta_1}^2 + \alpha_2{\theta_2}^2 + \alpha_{12}\theta_1\theta_2$$

$$\omega_0^* = \frac{\omega_{10}\theta_1 + \omega_{20}\theta_2}{\theta_1+\theta_2}$$

$$\alpha_{12} = \sqrt{\alpha_1\alpha_2}$$

$$\theta_1 = \Gamma_1\omega_{10}(1 - \epsilon_1\Pi\theta)$$

$$\theta_2 = \Gamma_2\omega_{20}(1 - \epsilon_2\Pi\theta)$$

$$\theta = \theta_1+\theta_2$$

where Π is the surface pressure; ω_0^* is the molar excluded area for both account for both species 1 and 2; k_B is Boltzmann constant; T is temperature; θ_i is the surface coverage of the i^{th} species; α_i is the interaction parameter of i^{th} species; α_{12} is the intermolecular interaction parameter; Γ_i is the surface adsorption of the i^{th} species; ω_{i0} is the molar area of species i at 0 surface pressure; ϵ_i is the surface compressibility constant of the i^{th} species. Therefore, we can write the adsorption isotherm as:[201, 213]

$$K_1c_1 = \frac{\theta_1}{1-\theta_1-\theta_2}\exp(-2\alpha_1\theta_1 - 2\alpha_{12}\theta_2)$$

$$K_2c_2 = \frac{\theta_2}{1-\theta_1-\theta_2}\exp(-2\alpha_2\theta_2 - 2\alpha_{12}\theta_1)$$

where K_i is the adsorption constant and c_i the bulk concentration for the i^{th} species.

Two-component van der Waals (VDW) adsorption model

The surface pressure can be written as:[200, 202]

$$\frac{\Pi\omega_0^*}{k_BT} = \frac{\theta_1 + \theta_2}{(1-\theta_1-\theta_2)} - (\alpha_1{\theta_1}^2 + \alpha_2{\theta_2}^2 + \alpha_{12}\theta_1\theta_2)$$

and the adsorption isotherm is written as follows:

$$K_1c_1 = \frac{\theta_1}{1-\theta_1-\theta_2} exp\left(\frac{\theta_1}{1-\theta_1-\theta_2} - 2\alpha_1\theta_1 - 2\alpha_{12}\theta_2\right)$$

$$K_2c_2 = \frac{\theta_2}{1-\theta_1-\theta_2} exp\left(\frac{\theta_2}{1-\theta_1-\theta_2} - 2\alpha_2\theta_2 - 2\alpha_{12}\theta_1\right)$$

Supplementary equations for the Kralchesvsky adsorption model

The Gouy equation is defined as follows:[200]

$$\Gamma_{DS-} - \Gamma_{Na+} = \frac{4I}{\kappa} sinh\left(\frac{\varphi_s}{2}\right)$$

where Γ_{DS-} is the surface adsorption for dodecyl sulfate ions, Γ_{Na+} is the surface adsorption for sodium counter ions, I is the ionic strength, and κ and φ_s are the Debye parameter and the dimensionless surface potential, defined as follows:

$$\kappa^2 = \frac{8\pi e^2 I}{\epsilon k_B T}$$

$$\varphi_s = \frac{Z_1 e\psi_s}{k_B T}$$

where ϵ is the dieletric constant of water, e is the electronic charge, Z_1 is the ionic valence of the dodecyl sulfate ion, and ψ_s is the surface electric potential.

Two-component surface rheology

The equations for surface rheology are described below:[213]

$$\kappa^{s*} = \frac{1}{B}\left(\frac{\partial \Pi}{\partial ln\Gamma_1}\right)_{\Gamma_2}\left[\sqrt{\frac{i\Omega}{D_1}}a_{11} + \sqrt{\frac{i\Omega}{D_2}}a_{12}\frac{\Gamma_1}{\Gamma_2} + \frac{i\Omega}{\sqrt{D_1 D_2}}\left(a_{11}a_{22} - a_{12}a_{21}\right)\right]$$

$$+ \frac{1}{B}\left(\frac{\partial \Pi}{\partial ln\Gamma_2}\right)_{\Gamma_1}\left[\sqrt{\frac{i\Omega}{D_2}}a_{22} + \sqrt{\frac{i\Omega}{D_1}}a_{21}\frac{\Gamma_1}{\Gamma_2} + \frac{i\Omega}{\sqrt{D_1 D_2}}\left(a_{11}a_{22} - a_{12}a_{21}\right)\right]$$

$$B = 1 + \sqrt{\frac{i\Omega}{D_1}}a_{11} + \sqrt{\frac{i\Omega}{D_2}}a_{22} + \frac{i\Omega}{\sqrt{D_1 D_2}}\left(a_{11}a_{22} - a_{12}a_{21}\right)$$

where Ω is the angular frequency; D_i is the molecular diffusion coefficient, and κ^{s*} is the complex viscoelastic modulus for dilational surface rheology. Then, the real ($\kappa^s{}_r$) and imaginary ($\kappa^s{}_i$) parts can be defined as:

$$\kappa^s{}_r = \frac{(PR + QS)}{(P^2 + Q^2)}$$

$$\kappa^s{}_i = \frac{(PS - QR)}{(P^2 + Q^2)}$$

$$|\kappa^{s*}| = \sqrt{\frac{(R^2 + S^2)}{(P^2 + Q^2)}}$$

$$\delta = arctg\left(\frac{\kappa^s{}_i}{\kappa^s{}_r}\right)$$

with P, Q, R and S as:

$$P = 1 + \frac{\left(\sqrt{\frac{\Omega}{D_1}}a_{11} + \sqrt{\frac{\Omega}{D_2}}a_{22}\right)}{\sqrt{2}}$$

$$Q = \frac{\left(\sqrt{\frac{\Omega}{D_1}}a_{11} + \sqrt{\frac{\Omega}{D_2}}a_{22}\right)}{\sqrt{2}} + \frac{\Omega}{\sqrt{D_1 D_2}}\left(a_{11}a_{22} - a_{12}a_{21}\right)$$

$$P_i = \frac{\left(\sqrt{\frac{\Omega}{D_i}}a_{ii} + \sqrt{\frac{\Omega}{D_j}}a_{ij}\frac{\Gamma_j}{\Gamma_i}\right)}{\sqrt{2}}$$

$$Q_i = P_i + \frac{\Omega}{\sqrt{D_1 D_2}}\left(a_{11}a_{22} - a_{12}a_{21}\right)$$

$$R = P_1\left(\frac{\partial \Pi}{\partial ln\Gamma_1}\right)_{\Gamma_2} + P_2\left(\frac{\partial \Pi}{\partial ln\Gamma_2}\right)_{\Gamma_1}$$

$$R = Q_1\left(\frac{\partial \Pi}{\partial ln\Gamma_1}\right)_{\Gamma_2} + Q_2\left(\frac{\partial \Pi}{\partial ln\Gamma_2}\right)_{\Gamma_1}$$

Finally, a can be written as:

$$a_{11} = \left(\frac{\partial \Gamma_1}{\partial c_1}\right)_{c_2}$$

$$a_{12} = \left(\frac{\partial \Gamma_1}{\partial c_2}\right)_{c_1}$$

$$a_{21} = \left(\frac{\partial \Gamma_2}{\partial c_1}\right)_{c_2}$$

$$a_{22} = \left(\frac{\partial \Gamma_2}{\partial c_2}\right)_{c_1}$$

Calculation of the depletion parameters for non-planar surfaces

For surfactant solutions in a spherical shell, adsorbing from outside to the inner spherical surface:[197]

$$V = \frac{4}{3}\pi(R_f^3 - b^3)$$

$$f = \frac{3\Gamma_\infty b^2}{K(R_f^3 - b^3)}$$

$$\vartheta = \frac{3\Gamma_\infty b^2}{c_i(R_f^3 - b^3)}$$

$$h = b\left[\left(\frac{3h_p}{b} + 1\right)^{1/3} - 1\right]$$

where V is the volume, R_f is the shell radius, b is the inner radius, Γ_∞ is the maximum surface adsorption, K is the adsorption constant, c_i is the initial bulk concentration, h_p is the planar depletion depth, h is the depletion depth corrected for the shell geometry, f is the ratio of the minimum bulk concentration needed to populate the interface at maximum packing to the adsorption constant K, and ϑ is the maximum fractional potential mass lost to the interface.

Surface tension isotherms fitting

Figure A0-1 shows the fits to the surface tension isotherms using the Frumkin and van der Waals adsorption models mentioned in Section 5.2.

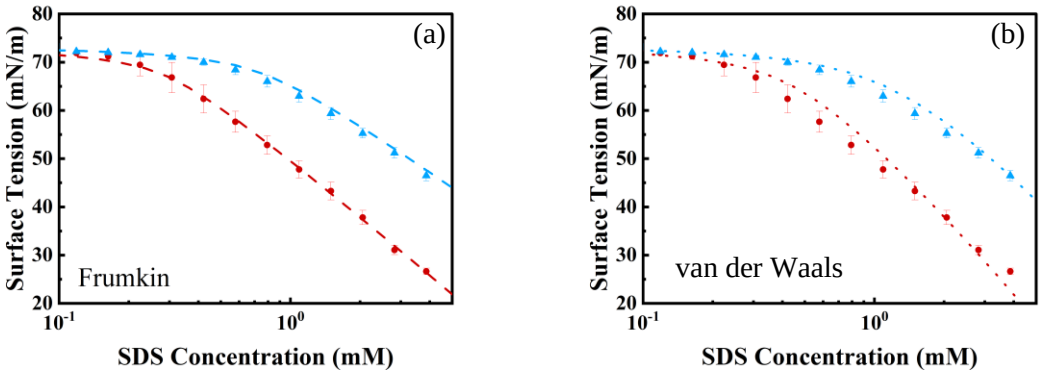

Figure A0-1. Surface tension isotherms of SDS for unpurified (red) and recrystallized (blue) samples as a function of SDS concentration. The isotherms are fitted with (a) Frumkin and (b) van der Waals adsorption models.

Surface adsorption curves

Figure A0-2 shows the surface adsorption isotherms calculated by the Kralchevsky's model.[200] As can be seen, there is a predominant adsorption of LOH molecules in both unpurified and recrystallized samples. However, when comparing both samples, there is a shift in the concentration at which the adsorption increases sharply. This is due to a decrease in LOH concentration present in the bulk for the recrystallized sample. When comparing both adsorption isotherms with respect to LOH concentration in **Figure A0-2b**, there is a critical LOH concentration at which the surface adsorption increases and is located at the same LOH concentration for both samples.

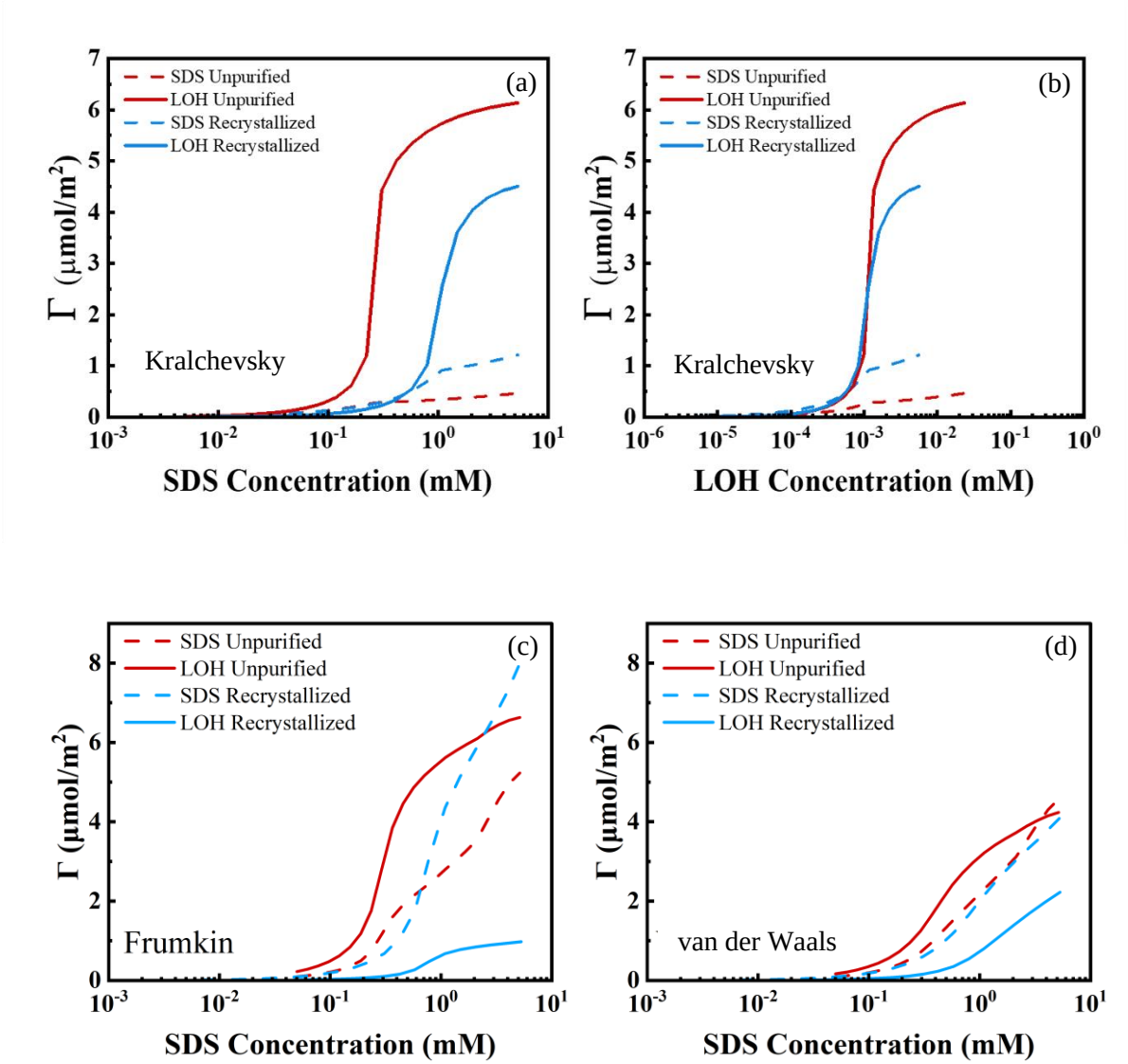

Figure A0-2. Kralchevsky derived surface adsorption of SDS (dashed) and LOH (full) for both unpurified (red) and recrystallized (blue) samples as a function of (a) SDS concentration and (b) LOH concentration. (c) Frumkin derived surface adsorption of SDS (dashed) and LOH (full) for both unpurified (red) and recrystallized (blue) samples with SDS concentration. (d) van der Waals derived surface adsorption of SDS (dashed) and LOH (full) for both unpurified (red) and recrystallized (blue) samples with SDS concentration.

Rheological modeling of recrystallized SDS solutions

Figure A0-3 displays the comparison between the surface dilational rheology for recrystallized SDS samples obtained experimentally and the curves predicted by the rheological model.

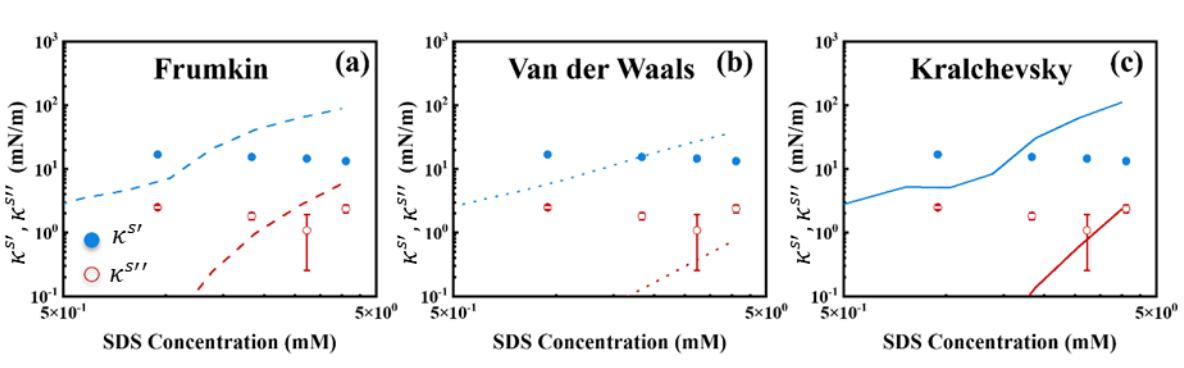

Figure A0-3. Comparison between the experimentally measured and predicted values for the surface rheology of the recrystallized samples estimated using the inputs from thermodynamic models. Experimental values for $\kappa^{s'}$ and $\kappa^{s''}$ are shown in blue circles and red triangles; respectively, and the calculated curves are presented by the lines.

Appendix B

Particles

Monopolar capillary interactions

Capillary interactions resulting from monopolar deformation of a fluid-fluid interface in presence of bound particles can be calculated as described by Danov et al.[223]

$$\Delta U_0 = -2\pi\sigma Q_1 Q_2 K_0(qr)$$

$$Q_i \approx \frac{1}{6} q^2 R_i^3 (2 - 4D_i + 3\cos\theta_i - cos^3\theta_i) \quad (i = 1, 2)$$

$$q^2 = \Delta\rho g/\sigma$$

$$D_i = (\rho_i - \rho_{II})/(\rho_I - \rho_{II})$$

Where ΔU_0 is the monopolar pairwise capillary interaction energy, σ is the interfacial tension between the two fluids, r is the center to center distance between the particles, Q_i is the capillary charge on each particle, K_0 is the modified Bessel function of the second kind and zero order, g is the acceleration due to gravity, ρ_I (ρ_{II}) is the density of the lower (upper) phase, ρ_i is the particle density, R_i is the particle radius, and θ_i is the particle contact angle.

The resulting monopolar capillary interaction energy for two interfacially bound particles separated by a distance of $r = 4R$, calculated for particles of various radii and for particle density of 2.3g/cm^3, is shown in **Figure B0-1a**. It can be noted that the interaction is negligible for particles of size below 10 μm. For instance, **Figure B0-1b** shows the monopolar pairwise capillary interaction as a function of the interparticle separation distance, for a pair of particles with diameter of 1 μm. The resulting capillary interaction energy is considerably smaller than the thermal energy ($k_B T$) in this case, even for small separation distances.

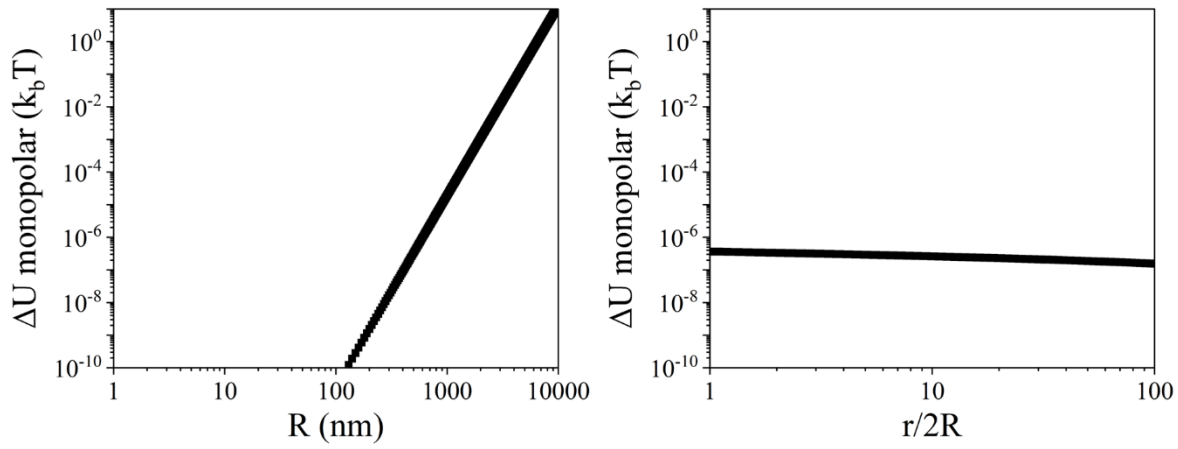

Figure B0-1. (a) Monopolar capillary interactions between two interfacially bound particles of various diameters at a separation distance of $r = 4R$. (b) Resulting interactions between two particles of radius 1 μm at various interparticle separation distance.

Analysis of particle orientation distribution

The particle orientation distribution at the interface was determined by analyzing the average brightness of each particle in the SEM images and is visualized in the histogram shown in **Figure B0-2a**. The particles population can be distributed into three possible orientations. The JP with cap up orientation is expected to have a higher brightness, as shown in the far-right end of the orange peak in **Figure B0-2a**, whereas the cap down particles should have the lower brightness as shown in the far-left peak present in **Figure B0-2a**. We simply took the middle brightness (red dashed line) between the highest and lowest averages on the distribution (shown in blue dashed lines) as a threshold to differentiate between the two orientations. Tilted particles, however, should have intermediary brightness, and were differentiated from the other two (i.e., cap up and cap down) based on their brightness standard deviation (BSD). Each particle was sectioned into 4 quadrants and the average brightness of each slice was taken and used to calculate the brightness standard deviation or BSD, as shown in **Figure B0-2b**. Since the shape of the histogram resembles a skewed distribution, we utilized statistical parameters as a threshold for defining tilted particles.

To be categorized as tilted, the particle had to have a BSD higher than the average BSD of the population plus one standard deviation of the distribution of BSD.

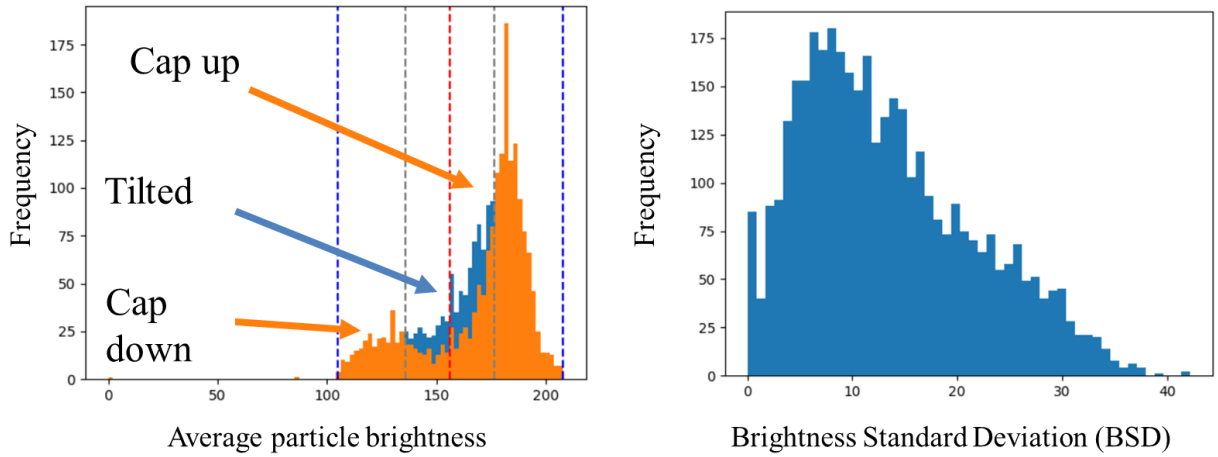

Figure B0-2. (a) Histogram of the average particle brightness intensity (from 0 to 255) showing the peaks represented by cap up particles and cap down particles in orange, with the particles characterized as tilted (with an average brightness in between the grey dashed lines) shown in blue. (b) Histogram of the brightness standard deviation (BSD) of the particles, which was used to differentiate tilted particles from the other two (i.e., cap up and cap down JPs).

Bond angle analysis on JP monolayers of different amphiphilicity

The bond angle was used to characterize the preferred type of packing for the particles studied. For a particle with neighbors, one specific neighbor is selected as the reference, with a bond angle of 0°, while the other neighbors have their bond angle relative to the reference neighbor, as schematically shown in **Figure B0-3a**. The histogram of bond angles for the three JP amphiphilicity used in this study is provided in **Figure B0-3b**. Despite the amorphous nature of the monolayers, particles exhibit a tendency to pack in a hexagonal array based as the bond angles that are found to be more frequent are 60° and 120°.

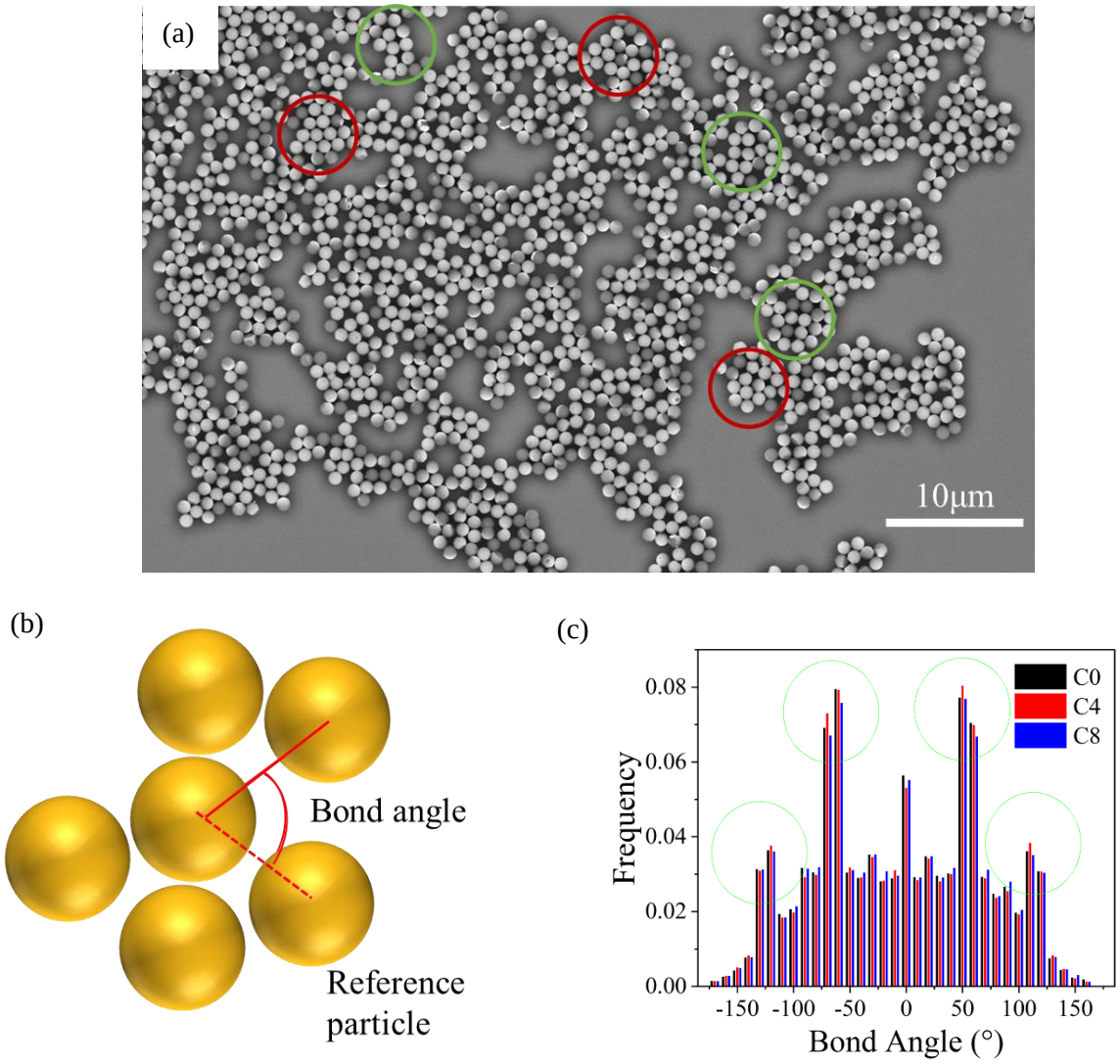

Figure B0-3. (a) an example SEM picture illustrating the occurrence of both types of arrangement, square in green and hexagonal in red. Scale bar is 10 μm; (b) schematics illustrating the bond angle between a particle and its neighbors; (c) Histogram of the bond angles obtained by analysis of SEM images captured for monolayers of JP with different amphiphilicities.

The radial distribution function, g(r), shown in **Figure B0-4**, was used to determine the threshold for the first shell of neighbors. The minimum after the first peak, at $r = 22$ pixels (where 1 μm corresponds to 15 pixels), was taken as the criterion of distance for a particle to be counted as a neighbor. It was found that for all different amphiphilicities in this study the first minimum in g(r) was consistently at around 22 pixels.

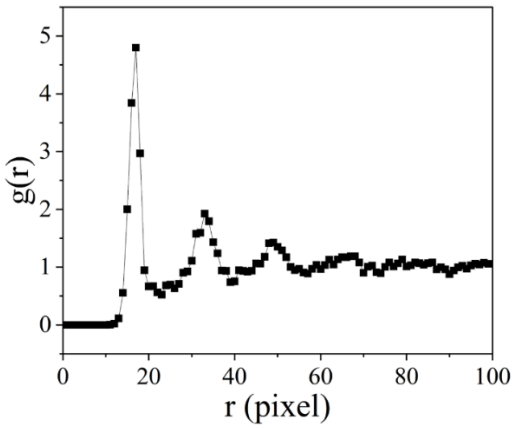

Figure B0-4. Radial distribution function of a C_0 JP monolayer. It should be noted that the first minimum position was found to be similar for all amphiphilicities used in this study.

SEM pictures of JPs monolayers

SEM pictures of the monolayers on which the analysis of **Figure 4-16** was carried out are provided in **Figure B0-5**.

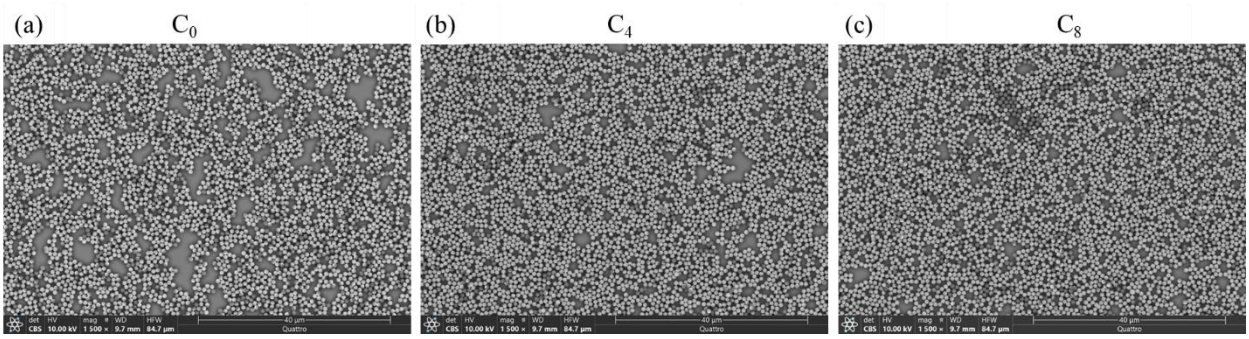

Figure B0-5. SEM graphs corresponding to the Figure 10 of the main text. (a) C0, (b) C4, and (c) C8 monolayers.

Images of the monolayer formed by Janus particles after deposition onto the air-water interface

The following micrographs were generated with A NIMA Langmuir trough (Biolin Scientific) equipped with an imaging window machined in the center mounted on top of an inverted microscope (IX73 Olympus). The imaging of the particle-laden interface was carried out using a 20x objective (6.6-7.8 WD, 0.45 NA). The trough is supported by a moving stage (Applied Scientific Instrumentation) and thus the trough position can be controlled precisely. Therefore, it

is possible to image the microstructure at different locations throughout the monolayer for a better representation of the surface monolayer as shown in **Figure B0-6**.

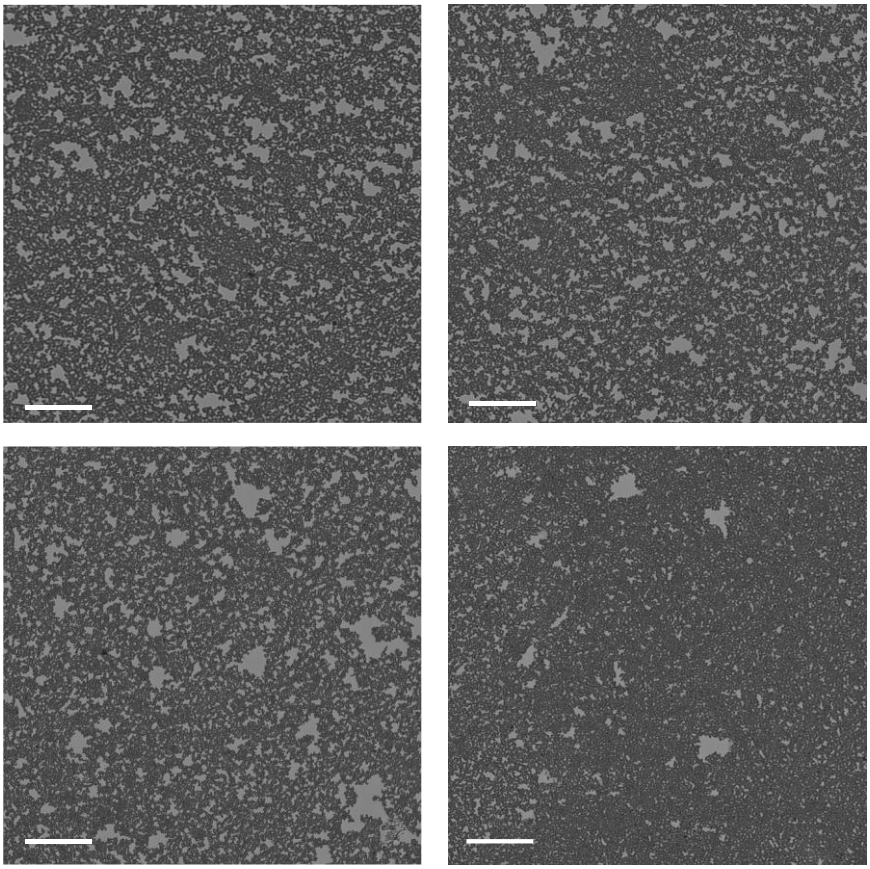

Figure B0-6. Micrographs of the interfacial monolayer formed by Janus particles at the air-water interface sampled at different locations within the interface. Scale bar is 10 μm.

SEM images of Janus particles transferred from the air-water interface onto a silicon wafer

Scanning Electron Microscope (SEM) images were collected for particles deposited on a substrate, examples of which are provided in **Figure B0-7**. The SEM utilized was a Field Emission environmental SEM from Thermo. For the image acquisition, we utilized an accelerating voltage of 10.00 kV and a working distance of 9.7 mm.

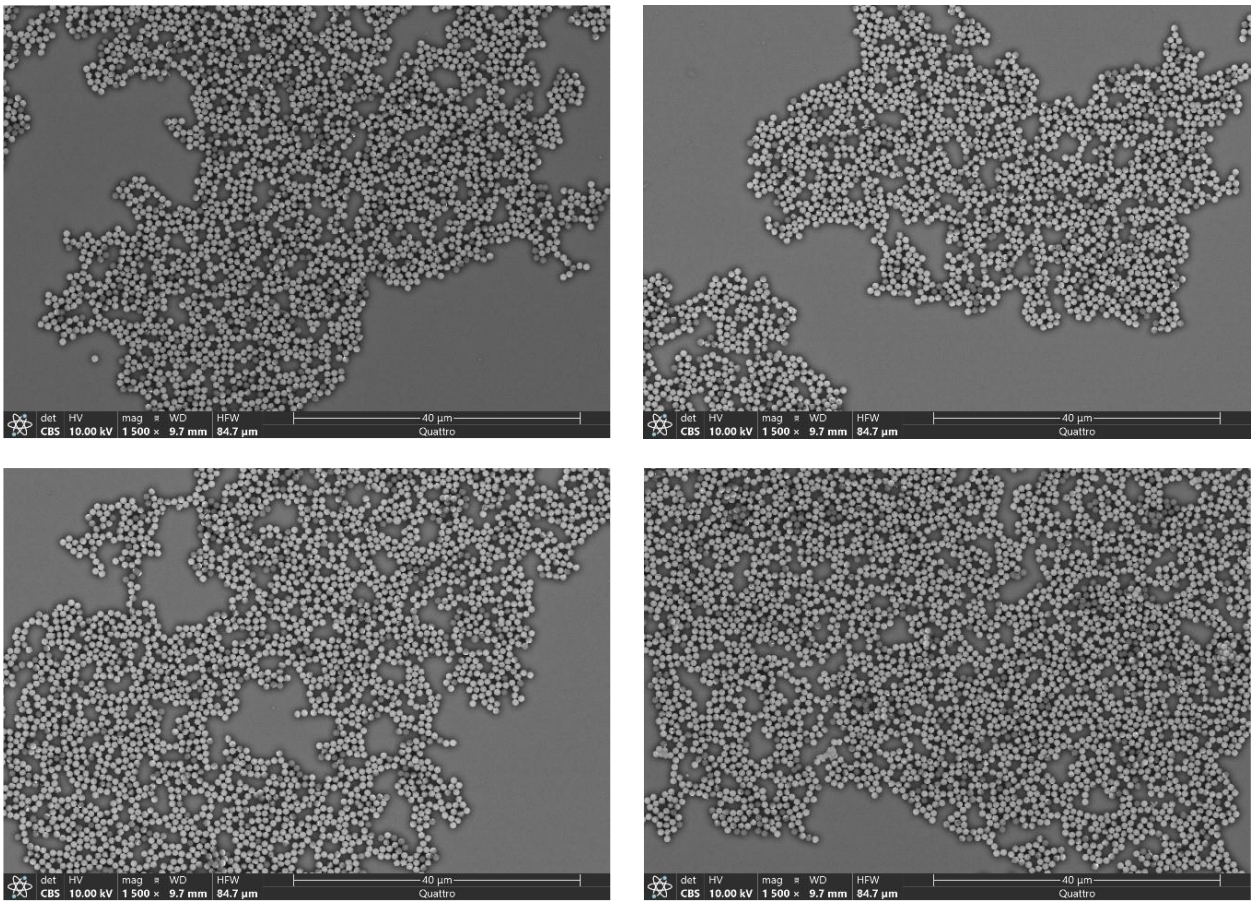

Figure B0-7. SEM pictures of interfacial monolayer of Janus particles formed at the air-water interface imaged after transferring to a silicon wafer from the air-water interface.

From the captured SEM images, examples of which are shown in **Figure B0-7**, we calculated the crystallinity order parameter $C_{6,}$[196] which is defined as the number of hexagonally packed neighbors of a specific particle. The number of neighbors (N_c^k) to the particle *k* are all particles *j* within a coordination radius (r_c). Identification of crystalline neighbors for particle *k* is based on a six-fold orientation order parameter for that particle, (ψ_6^k), which is calculated as follows:

$$\psi_6^k = \frac{1}{N_c^k}\sum_{j=1}^{N_c^k}\left[e^{i6\theta_{kj}} \qquad r_{kj} \le r_c\right]$$

Next, we can calculate the crystalline connectivity (χ_6^{kj}) between particles *k* and *j*.

$$\chi_6^{kj} = \frac{\left|Re\left[\psi_6^k \psi_6^{j*}\right]\right|}{\left|\psi_6^k \psi_6^{j*}\right|}$$

where ψ_6^{j*} is the complex conjugate of ψ_6^j. The number of crystalline near neighbors (C_6^k) for particle *k* is as follows:

$$C_6^k = \sum_{j=1}^{N_c^k} \left[\begin{vmatrix} 1 & \chi_6^{kj} \geq 0.32 \\ 0 & \chi_6^{kj} < 0.32 \end{vmatrix} \right]$$

which is based on a criterion that a connection between particles *k* and *j* only to be crystalline for $\chi_6^{kj} \geq 0.32$. Finally, we can calculate the ensemble average over all particles ($\langle C_6 \rangle$) as:

$$\langle C_6 \rangle = \frac{1}{N} \sum_{k=1}^{N} C_6^k$$

Following this procedure and using ~ 50,000 particles imaged via SEM in this analysis, we estimated the $\langle C_6 \rangle$ of our particle system to be ~ 2.0 ± 0.1. Our data analysis was done on a modified version of the software HEXI.[186] In short, HEXI identifies individual particles and determines their position. With that information one can calculate the beforementioned properties.

References

1. Ramsden, W., Separation of solids in the surface-layers of solutions and 'suspensions'(observations on surface-membranes, bubbles, emulsions, and mechanical coagulation).—Preliminary account. *Proceedings of the royal Society of London* **1904,** *72* (477-486), 156-164.
2. Pickering, S. U., CXCVI.—Emulsions. *Journal of the Chemical Society, Transactions* **1907,** *91* (0), 2001-2021.
3. Mendoza, A. J.; Guzmán, E.; Martínez-Pedrero, F.; Ritacco, H.; Rubio, R. G.; Ortega, F.; Starov, V. M.; Miller, R., Particle laden fluid interfaces: Dynamics and interfacial rheology. *Advances in Colloid and Interface Science* **2014,** *206*, 303-319.
4. Binks, B. P.; Horozov, T. S., *Colloidal Particles at Liquid Interfaces*. Cambridge University Press: 2006.
5. Aveyard, R.; Binks, B. P.; Clint, J. H., Emulsions stabilised solely by colloidal particles. *Advances in Colloid and Interface Science* **2003,** *100-102*, 503-546.
6. Crossley, S.; Faria, J.; Shen, M.; Resasco, D. E., Solid Nanoparticles that Catalyze Biofuel Upgrade Reactions at the Water/Oil Interface. *Science* **2010,** *327* (5961), 68-72.
7. Chen, C. L.; Wang, S. S.; Kadhum, M. J.; Harwell, J. H.; Shiau, B. J., Using carbonaceous nanoparticles as surfactant carrier in enhanced oil recovery: A laboratory study. *Fuel* **2018,** *222*, 561-568.
8. Qian, C.; Telmadarreie, A.; Dong, M.; Bryant, S., Synergistic Effect between Surfactant and Nanoparticles on the Stability of Methane Foam in EOR Processes. In *SPE Western Regional Meeting*, Society of Petroleum Engineers: San Jose, California, USA, 2019; p 16.
9. Binks, B. P., Colloidal Particles at a Range of Fluid–Fluid Interfaces. *Langmuir* **2017,** *33* (28), 6947-6963.
10. Liu, R. C.; Raman, A. K. Y.; Shaik, I.; Aichele, C.; Kim, S. J., Inorganic microfiltration membranes incorporated with hydrophilic silica nanoparticles for oil-in-water emulsion separation. *J. Water Process. Eng.* **2018,** *26*, 124-130.
11. Park, B. J.; Lee, D., Particles at fluid–fluid interfaces: From single-particle behavior to hierarchical assembly of materials. *MRS Bulletin* **2014,** *39* (12), 1089-1098.
12. Kaz, D. M. Colloidal Particles and Liquid Interfaces: A Spectrum of Interactions. PhD Thesis, Harvard University, Manoharan Lab Publications, 2011.
13. Zang, D. Y.; Rio, E.; Langevin, D.; Wei, B.; Binks, B. P., Viscoelastic properties of silica nanoparticle monolayers at the air-water interface. *The European Physical Journal E* **2010,** *31* (2), 125-134.
14. Böker, A.; He, J.; Emrick, T.; Russell, T. P., Self-assembly of nanoparticles at interfaces. *Soft Matter* **2007,** *3* (10), 1231-1248.
15. Furst, E. M., Directing colloidal assembly at fluid interfaces. *Proceedings of the National Academy of Sciences* **2011,** *108* (52), 20853.
16. Komura, S.; Hirose, Y.; Nonomura, Y., Adsorption of colloidal particles to curved interfaces. *The Journal of Chemical Physics* **2006,** *124* (24), 241104.
17. Bresme, F.; Oettel, M., Nanoparticles at fluid interfaces. *Journal of Physics: Condensed Matter* **2007,** *19* (41), 413101.

18. Vishal, B.; Ghosh, P., The effect of silica nanoparticles on the stability of aqueous foams. *Journal of Dispersion Science and Technology* **2019,** *40* (2), 206-218.
19. Hu, N.; Li, Y.; Wu, Z.; Lu, K.; Huang, D.; Liu, W., Foams stabilization by silica nanoparticle with cationic and anionic surfactants in column flotation: Effects of particle size. *Journal of the Taiwan Institute of Chemical Engineers* **2018,** *88*, 62-69.
20. Weston, J. S.; Jentoft, R. E.; Grady, B. P.; Resasco, D. E.; Harwell, J. H., Silica Nanoparticle Wettability: Characterization and Effects on the Emulsion Properties. *Industrial & Engineering Chemistry Research* **2015,** *54* (16), 4274-4284.
21. McGorty, R.; Fung, J.; Kaz, D.; Manoharan, V. N., Colloidal self-assembly at an interface. *Materials Today* **2010,** *13* (6), 34-42.
22. Zhou, J.; Qiao, X.; Binks, B. P.; Sun, K.; Bai, M.; Li, Y.; Liu, Y., Magnetic Pickering emulsions stabilized by Fe3O4 nanoparticles. *Langmuir* **2011,** *27* (7), 3308-16.
23. Owoseni, O.; Nyankson, E.; Zhang, Y.; Adams, D. J.; He, J.; Spinu, L.; McPherson, G. L.; Bose, A.; Gupta, R. B.; John, V. T., Interfacial adsorption and surfactant release characteristics of magnetically functionalized halloysite nanotubes for responsive emulsions. *J Colloid Interface Sci* **2016,** *463*, 288-98.
24. Abkarian, M.; Subramaniam, A. B.; Kim, S.-H.; Larsen, R. J.; Yang, S.-M.; Stone, H. A., Dissolution Arrest and Stability of Particle-Covered Bubbles. *Physical Review Letters* **2007,** *99* (18), 188301.
25. Doroudian Rad, M.; Telmadarreie, A.; Xu, L.; Dong, M.; Bryant, S. L., Insight on Methane Foam Stability and Texture via Adsorption of Surfactants on Oppositely Charged Nanoparticles. *Langmuir : the ACS journal of surfaces and colloids* **2018,** *34* (47), 14274-14285.
26. Xue, Z.; Worthen, A.; Qajar, A.; Robert, I.; Bryant, S. L.; Huh, C.; Prodanović, M.; Johnston, K. P., Viscosity and stability of ultra-high internal phase CO2-in-water foams stabilized with surfactants and nanoparticles with or without polyelectrolytes. *Journal of colloid and interface science* **2016,** *461*, 383-395.
27. Arab, D.; Kantzas, A.; Bryant, S. L., Nanoparticle stabilized oil in water emulsions: A critical review. *Journal of Petroleum Science and Engineering* **2018,** *163*, 217-242.
28. Katepalli, H.; Bose, A., Response of surfactant stabilized oil-in-water emulsions to the addition of particles in an aqueous suspension. *Langmuir* **2014,** *30* (43), 12736-12742.
29. Katepalli, H.; Bose, A.; Hatton, T. A.; Blankschtein, D., Destabilization of Oil-in-Water Emulsions Stabilized by Non-ionic Surfactants: Effect of Particle Hydrophilicity. *Langmuir* **2016,** *32* (41), 10694-10698.
30. Fan, H.; Striolo, A., Mechanistic study of droplets coalescence in Pickering emulsions. *Soft Matter* **2012,** *8* (37), 9533-9538.
31. Hunter, T.; Pugh, R.; Franks, G.; Jameson, G., The role of particles in stabilising foams and emulsions. *Advances in colloid and interface science* **2008,** *137*, 57-81.
32. Lin, Y.; Skaff, H.; Emrick, T.; Dinsmore, A.; Russell, T. P., Nanoparticle assembly and transport at liquid-liquid interfaces. *Science* **2003,** *299* (5604), 226-229.
33. Raman, A. K. Y.; Aichele, C. P., Influence of non-ionic surfactant addition on the stability and rheology of particle-stabilized emulsions. *Colloids and Surfaces A: Physicochemical and Engineering Aspects* **2020,** *585*, 124084.
34. Van Hooghten, R.; Imperiali, L.; Boeckx, V.; Sharma, R.; Vermant, J., Rough nanoparticles at the oil–water interfaces: Their structure, rheology and applications. *Soft Matter* **2013,** *9* (45), 10791-10798.

35. Liu, J.; Li, X.; Jia, W.; Li, Z.; Zhao, Y.; Ren, S., Demulsification of Crude Oil-in-Water Emulsions Driven by Graphene Oxide Nanosheets. *Energy & Fuels* **2015,** *29* (7), 4644-4653.
36. Pawar, A. B.; Caggioni, M.; Hartel, R. W.; Spicer, P. T., Arrested coalescence of viscoelastic droplets with internal microstructure. *Faraday Discussions* **2012,** *158* (0), 341-350.
37. Madivala, B.; Vandebril, S.; Fransaer, J.; Vermant, J., Exploiting particle shape in solid stabilized emulsions. *Soft Matter* **2009,** *5* (8), 1717-1727.
38. Sacanna, S.; Korpics, M.; Rodriguez, K.; Colón-Meléndez, L.; Kim, S.-H.; Pine, D. J.; Yi, G.-R., Shaping colloids for self-assembly. *Nature Communications* **2013,** *4* (1), 1688.
39. Vu, T. V.; Papavassiliou, D. V., Modification of Oil–Water Interfaces by Surfactant-Stabilized Carbon Nanotubes. *The Journal of Physical Chemistry C* **2018,** *122* (48), 27734-27744.
40. Hou, H. B.; Yu, D. M.; Tian, Q.; Hu, G. H., Preparation, Characterization, and Properties of Hollow Janus Particles with Tailored Shapes. *Langmuir* **2014,** *30* (7), 1741-1747.
41. Möbius, D.; Miller, R.; Fainerman, V. B., *Surfactants: chemistry, interfacial properties, applications*. Elsevier: 2001.
42. Rosen, M. J.; Kunjappu, J. T., *Surfactants and interfacial phenomena*. John Wiley & Sons: 2012.
43. Zocchi, G., Foam in consumer products. *Handbook of Detergents. Part A: Properties* **2008**, 419.
44. Binks, B. P.; Rodrigues, J. A.; Frith, W. J., Synergistic interaction in emulsions stabilized by a mixture of silica nanoparticles and cationic surfactant. *Langmuir* **2007,** *23* (7), 3626-3636.
45. Maestro, A.; Deshmukh, O. S.; Mugele, F.; Langevin, D., Interfacial Assembly of Surfactant-Decorated Nanoparticles: On the Rheological Description of a Colloidal 2D Glass. *Langmuir* **2015,** *31* (23), 6289-6297.
46. Vatanparast, H.; Javadi, A.; Bahramian, A., Silica nanoparticles cationic surfactants interaction in water-oil system. *Colloids and Surfaces A: Physicochemical and Engineering Aspects* **2017,** *521*, 221-230.
47. Wang, H.; Gong, Y.; Lu, W.; Chen, B., Influence of nano-SiO2 on dilational viscoelasticity of liquid/air interface of cetyltrimethyl ammonium bromide. *Applied surface science* **2008,** *254* (11), 3380-3384.
48. Liggieri, L.; Santini, E.; Guzmán, E.; Maestro, A.; Ravera, F., Wide-frequency dilational rheology investigation of mixed silica nanoparticle–CTAB interfacial layers. *Soft Matter* **2011,** *7* (17), 7699-7709.
49. Maestro, A.; Guzmán, E.; Santini, E.; Ravera, F.; Liggieri, L.; Ortega, F.; Rubio, R. G., Wettability of silica nanoparticle–surfactant nanocomposite interfacial layers. *Soft Matter* **2012,** *8* (3), 837-843.
50. Smits, J.; Vieira, F.; Bisswurn, B.; Rezwan, K.; Maas, M., Reversible Adsorption of Nanoparticles at Surfactant-Laden Liquid–Liquid Interfaces. *Langmuir* **2019,** *35* (34), 11089-11098.
51. Vatanparast, H.; Shahabi, F.; Bahramian, A.; Javadi, A.; Miller, R., The Role of Electrostatic Repulsion on Increasing Surface Activity of Anionic Surfactants in the Presence of Hydrophilic Silica Nanoparticles. *Scientific Reports* **2018,** *8* (1), 7251.
52. Eftekhari, M.; Schwarzenberger, K.; Javadi, A.; Eckert, K., The influence of negatively charged silica nanoparticles on the surface properties of anionic surfactants: electrostatic repulsion or the effect of ionic strength? *Physical Chemistry Chemical Physics* **2020,** *22* (4), 2238-2248.

53. Rahman, S. E.; Laal-Dehghani, N.; Barman, S.; Christopher, G. F., Modifying interfacial interparticle forces to alter microstructure and viscoelasticity of densely packed particle laden interfaces. *Journal of Colloid and Interface Science* **2019,** *536*, 30-41.
54. Ballard, N.; Law, A. D.; Bon, S. A. F., Colloidal particles at fluid interfaces: behaviour of isolated particles. *Soft Matter* **2019,** *15* (6), 1186-1199.
55. Razavi, S.; Lin, B.; Lee, K. Y. C.; Tu, R. S.; Kretzschmar, I., Impact of surface amphiphilicity on the interfacial behavior of Janus particle layers under compression. *Langmuir : the ACS journal of surfaces and colloids* **2019**, 15813–15824.
56. Binks, B. P.; Fletcher, P. D. I., Particles Adsorbed at the Oil−Water Interface: A Theoretical Comparison between Spheres of Uniform Wettability and "Janus" Particles. *Langmuir* **2001,** *17* (16), 4708-4710.
57. Pieranski, P., Two-Dimensional Interfacial Colloidal Crystals. *Physical Review Letters* **1980,** *45* (7), 569-572.
58. Dinsmore, A. D.; Hsu, M. F.; Nikolaides, M. G.; Marquez, M.; Bausch, A. R.; Weitz, D. A., Colloidosomes: Selectively Permeable Capsules Composed of Colloidal Particles. *Science* **2002,** *298* (5595), 1006.
59. Colosqui, C. E.; Morris, J. F.; Koplik, J., Colloidal Adsorption at Fluid Interfaces: Regime Crossover from Fast Relaxation to Physical Aging. *Physical Review Letters* **2013,** *111* (2), 028302.
60. Kaz, D. M.; McGorty, R.; Mani, M.; Brenner, M. P.; Manoharan, V. N., Physical ageing of the contact line on colloidal particles at liquid interfaces. *Nature Materials* **2012,** *11* (2), 138-142.
61. Rahmani, A. M.; Wang, A.; Manoharan, V. N.; Colosqui, C. E., Colloidal particle adsorption at liquid interfaces: capillary driven dynamics and thermally activated kinetics. *Soft Matter* **2016,** *12* (30), 6365-6372.
62. Razavi, S.; Kretzschmar, I.; Koplik, J.; Colosqui, C. E., Nanoparticles at liquid interfaces: Rotational dynamics and angular locking. *The Journal of Chemical Physics* **2014,** *140* (1), 014904.
63. Anjali, T. G.; Basavaraj, M. G., Contact angle and detachment energy of shape anisotropic particles at fluid-fluid interfaces. *Journal of Colloid and Interface Science* **2016,** *478*, 63-71.
64. Ondarçuhu, T.; Fabre, P.; Raphaël, E.; Veyssié, M., Specific properties of amphiphilic particles at fluid interfaces. *J. Phys. France* **1990,** *51* (14), 1527-1536.
65. Jiang, S.; Granick, S., Janus balance of amphiphilic colloidal particles. *The Journal of Chemical Physics* **2007,** *127* (16), 161102.
66. Gao, Y.; Yu, Y., Macrophage Uptake of Janus Particles Depends upon Janus Balance. *Langmuir* **2015,** *31* (9), 2833-2838.
67. Fernández-Rodríguez, M. A.; Percebom, A. M.; Giner-Casares, J. J.; Rodríguez-Valverde, M. A.; Cabrerizo-Vílchez, M. A.; Liz-Marzán, L. M.; Hidalgo-Álvarez, R., Interfacial Activity of Gold Nanoparticles Coated with a Polymeric Patchy Shell and the Role of Spreading Agents. *ACS Omega* **2016,** *1* (2), 311-317.
68. Yin, T.; Yang, Z.; Dong, Z.; Lin, M.; Zhang, J., Physicochemical properties and potential applications of silica-based amphiphilic Janus nanosheets for enhanced oil recovery. *Fuel* **2019,** *237*, 344-351.
69. Lan, Y.; Choi, J.; Li, H. Y.; Jia, Y. K.; Huang, R. J.; Stebe, K. J.; Lee, D., Janus Particles with Varying Configurations for Emulsion Stabilization. *Industrial & Engineering Chemistry Research* **2019,** *58* (46), 20961-20968.
70. Khanum, R., Effect of Janus particle concentration on water-repellent finish of textile fabric. *J. Text. Inst.* **2017,** *108* (4), 543-546.

71. Fujii, S.; Yokoyama, Y.; Miyanari, Y.; Shiono, T.; Ito, M.; Yusa, S.-i.; Nakamura, Y., Micrometer-Sized Gold–Silica Janus Particles as Particulate Emulsifiers. *Langmuir* **2013,** *29* (18), 5457-5465.
72. Park, B.; Brugarolas, T.; D.H, L., Janus particles at an oil–water interface. *Soft Matter* **2011,** *7*, 6413-6417.
73. Kumar, A.; Park, B. J.; Tu, F.; Lee, D., Amphiphilic Janus particles at fluid interfaces. *Soft Matter* **2013,** *9* (29), 6604-6617.
74. Knapp, E. M.; Dagastine, R. R.; Tu, R. S.; Kretzschmar, I., Effect of Orientation and Wetting Properties on the Behavior of Janus Particles at the Air-Water Interface. *Acs Applied Materials & Interfaces* **2020,** *12* (4), 5128-5135.
75. Wu, D.; Chew, J. W.; Honciuc, A., Polarity Reversal in Homologous Series of Surfactant-Free Janus Nanoparticles: Toward the Next Generation of Amphiphiles. *Langmuir* **2016,** *32* (25), 6376-6386.
76. Gao, H.-M.; Lu, Z.-Y.; Liu, H.; Sun, Z.-Y.; An, L.-J., Orientation and surface activity of Janus particles at fluid-fluid interfaces. *The Journal of Chemical Physics* **2014,** *141* (13), 134907.
77. Koplik, J.; Maldarelli, C., Molecular dynamics study of the translation and rotation of amphiphilic Janus nanoparticles at a vapor-liquid surface. *Phys. Rev. Fluids* **2019,** *4* (4), 23.
78. Cheung, D. L.; Bon, S. A. F., Stability of Janus nanoparticles at fluid interfaces. *Soft Matter* **2009,** *5* (20), 3969-3976.
79. Bleibel, J.; Domínguez, A.; Oettel, M., Colloidal particles at fluid interfaces: Effective interactions, dynamics and a gravitation–like instability. *The European Physical Journal Special Topics* **2013,** *222* (11), 3071-3087.
80. Hurd, A. J., The electrostatic interaction between interfacial colloidal particles. *Journal of Physics A: Mathematical and General* **1985,** *18* (16), L1055-L1060.
81. Hurd, A. J.; Schaefer, D. W., Diffusion-Limited Aggregation in Two Dimensions. *Physical Review Letters* **1985,** *54* (10), 1043-1046.
82. Girotto, M.; dos Santos, A. P.; Levin, Y., Interaction of Charged Colloidal Particles at the Air–Water Interface. *The Journal of Physical Chemistry B* **2016,** *120* (26), 5817-5822.
83. Park, B. J.; Vermant, J.; Furst, E. M., Heterogeneity of the electrostatic repulsion between colloids at the oil–water interface. *Soft Matter* **2010,** *6* (21), 5327-5333.
84. Aveyard, R.; Binks, B. P.; Clint, J. H.; Fletcher, P. D. I.; Horozov, T. S.; Neumann, B.; Paunov, V. N.; Annesley, J.; Botchway, S. W.; Nees, D.; Parker, A. W.; Ward, A. D.; Burgess, A. N., Measurement of Long-Range Repulsive Forces between Charged Particles at an Oil-Water Interface. *Physical Review Letters* **2002,** *88* (24), 246102.
85. Park, B. J.; Pantina, J. P.; Furst, E. M.; Oettel, M.; Reynaert, S.; Vermant, J., Direct Measurements of the Effects of Salt and Surfactant on Interaction Forces between Colloidal Particles at Water−Oil Interfaces. *Langmuir* **2008,** *24* (5), 1686-1694.
86. Oettel, M.; Dietrich, S., Colloidal Interactions at Fluid Interfaces. *Langmuir* **2008,** *24* (4), 1425-1441.
87. Park, B. J.; Furst, E. M., Attractive interactions between colloids at the oil–water interface. *Soft Matter* **2011,** *7* (17), 7676-7682.
88. Quesada-Pérez, M.; Moncho-Jordá, A.; Martínez-López, F.; Hidalgo-Álvarez, R., Probing interaction forces in colloidal monolayers: Inversion of structural data. *The Journal of Chemical Physics* **2001,** *115* (23), 10897-10902.

89. Horozov, T. S.; Aveyard, R.; Binks, B. P.; Clint, J. H., Structure and Stability of Silica Particle Monolayers at Horizontal and Vertical Octane−Water Interfaces. *Langmuir* **2005,** *21* (16), 7405-7412.
90. Xu, H.; Liu, X.; Su, G.; Zhang, B.; Wang, D., Electrostatic Repulsion-Controlled Formation of Polydopamine–Gold Janus Particles. *Langmuir* **2012,** *28* (36), 13060-13065.
91. Israelachvili, J. N., 6 - Van der Waals Forces. In *Intermolecular and Surface Forces (Third Edition)*, Israelachvili, J. N., Ed. Academic Press: San Diego, 2011; pp 107-132.
92. Fernández-Toledano, J. C.; Moncho-Jordá, A.; Martínez-López, F.; Hidalgo-Álvarez, R., Theory for Interactions between Particles in Monolayers. In *Colloidal Particles at Liquid Interfaces*, Binks, B. P.; Horozov, T. S., Eds. Cambridge University Press: Cambridge, 2006; pp 108-151.
93. Ghezzi, F.; Earnshaw, J. C., Formation of meso-structures in colloidal monolayers. *Journal of Physics: Condensed Matter* **1997,** *9* (37), L517-L523.
94. Ghezzi, F.; Earnshaw, J. C.; Finnis, M.; McCluney, M., Pattern Formation in Colloidal Monolayers at the Air–Water Interface. *Journal of Colloid and Interface Science* **2001,** *238* (2), 433-446.
95. Ruiz-Garcia, J.; Gámez-Corrales, R.; Ivlev, B. I., Foam and cluster structure formation by latex particles at the air/water interface. *Physica A: Statistical Mechanics and its Applications* **1997,** *236* (1), 97-104.
96. Ruiz-García, J.; Gámez-Corrales, R.; Ivlev, B. I., Formation of two-dimensional colloidal voids, soap froths, and clusters. *Physical Review E* **1998,** *58* (1), 660-663.
97. Onoda, G. Y., Direct observation of two-dimensional, dynamic clustering and ordering with colloids. *Physical Review Letters* **1985,** *55* (2), 226-229.
98. Vella, D.; Mahadevan, L., The "Cheerios effect". *American Journal of Physics* **2005,** *73* (9), 817-825.
99. Kralchevsky, P. A.; Paunov, V. N.; Ivanov, I. B.; Nagayama, K., Capillary meniscus interaction between colloidal particles attached to a liquid—fluid interface. *Journal of Colloid and Interface Science* **1992,** *151* (1), 79-94.
100. Paunov, V. N.; Kralchevsky, P. A.; Denkov, N. D.; Nagayama, K., Lateral Capillary Forces between Floating Submillimeter Particles. *Journal of Colloid and Interface Science* **1993,** *157* (1), 100-112.
101. Danov, K. D.; Kralchevsky, P. A.; Naydenov, B. N.; Brenn, G., Interactions between particles with an undulated contact line at a fluid interface: capillary multipoles of arbitrary order. *J Colloid Interface Sci* **2005,** *287* (1), 121-34.
102. Kralchevsky, P. A.; Nagayama, K., Capillary interactions between particles bound to interfaces, liquid films and biomembranes. *Advances in Colloid and Interface Science* **2000,** *85* (2), 145-192.
103. Vassileva, N. D.; van den Ende, D.; Mugele, F.; Mellema, J., Capillary Forces between Spherical Particles Floating at a Liquid−Liquid Interface. *Langmuir* **2005,** *21* (24), 11190-11200.
104. Oettel, M.; Domínguez, A.; Dietrich, S., Effective capillary interaction of spherical particles at fluid interfaces. *Physical Review E* **2005,** *71* (5), 051401.
105. Stamou, D.; Duschl, C.; Johannsmann, D., Long-range attraction between colloidal spheres at the air-water interface: The consequence of an irregular meniscus. *Physical Review E* **2000,** *62* (4), 5263-5272.

106. Danov, K. D.; Pouligny, B.; Kralchevsky, P. A., Capillary Forces between Colloidal Particles Confined in a Liquid Film: The Finite-Meniscus Problem. *Langmuir* **2001,** *17* (21), 6599-6609.
107. Nikolaides, M. G.; Bausch, A. R.; Hsu, M. F.; Dinsmore, A. D.; Brenner, M. P.; Gay, C.; Weitz, D. A., Electric-field-induced capillary attraction between like-charged particles at liquid interfaces. *Nature* **2002,** *420* (6913), 299-301.
108. Megens, M.; Aizenberg, J., Like-charged particles at liquid interfaces. *Nature* **2003,** *424* (6952), 1014-1014.
109. Goggin, D. M.; Samaniuk, J. R., Dynamics of Pristine Graphite and Graphene at an Air-Water Interface. *Aiche J.* **2018,** *64* (8), 3177-3187.
110. Kralchevsky, P. A.; Nagayama, K., Capillary forces between colloidal particles. *Langmuir* **1994,** *10* (1), 23-36.
111. Danov, K. D.; Kralchevsky, P. A.; Boneva, M. P., Electrodipping Force Acting on Solid Particles at a Fluid Interface. *Langmuir* **2004,** *20* (15), 6139-6151.
112. Lewandowski, E. P.; Cavallaro, M.; Botto, L.; Bernate, J. C.; Garbin, V.; Stebe, K. J., Orientation and Self-Assembly of Cylindrical Particles by Anisotropic Capillary Interactions. *Langmuir* **2010,** *26* (19), 15142-15154.
113. Kang, D. W.; Choi, K. H.; Lee, S. J.; Park, B. J., Mapping Anisotropic and Heterogeneous Colloidal Interactions via Optical Laser Tweezers. *The Journal of Physical Chemistry Letters* **2019,** *10* (8), 1691-1697.
114. Lee, M.; Xia, M.; Park, B. J., Transition Behaviors of Configurations of Colloidal Particles at a Curved Oil-Water Interface. *Materials (Basel)* **2016,** *9* (3), 138.
115. Ferrar, J. A.; Bedi, D. S.; Zhou, S.; Zhu, P.; Mao, X.; Solomon, M. J., Capillary-driven binding of thin triangular prisms at fluid interfaces. *Soft Matter* **2018,** *14* (19), 3902-3918.
116. Liu, I. B.; Sharifi-Mood, N.; Stebe, K. J., Capillary Assembly of Colloids: Interactions on Planar and Curved Interfaces. *Annual Review of Condensed Matter Physics* **2018,** *9* (1), 283-305.
117. Katepalli, H.; John, V. T.; Tripathi, A.; Bose, A., Microstructure and rheology of particle stabilized emulsions: Effects of particle shape and inter-particle interactions. *Journal of Colloid and Interface Science* **2017,** *485*, 11-17.
118. Rezvantalab, H.; Shojaei-Zadeh, S., Role of Geometry and Amphiphilicity on Capillary-Induced Interactions between Anisotropic Janus Particles. *Langmuir* **2013,** *29* (48), 14962-14970.
119. Hong, L.; Cacciuto, A.; Luijten, E.; Granick, S., Clusters of Charged Janus Spheres. *Nano Letters* **2006,** *6* (11), 2510-2514.
120. Aveyard, R.; Clint, J. H.; Nees, D.; Quirke, N., Structure and Collapse of Particle Monolayers under Lateral Pressure at the Octane/Aqueous Surfactant Solution Interface. *Langmuir* **2000,** *16* (23), 8820-8828.
121. Luo, M.; Olivier, G. K.; Frechette, J., Electrostatic interactions to modulate the reflective assembly of nanoparticles at the oil–water interface. *Soft Matter* **2012,** *8* (47), 11923-11932.
122. Deshmukh, O. S.; van den Ende, D.; Stuart, M. C.; Mugele, F.; Duits, M. H. G., Hard and soft colloids at fluid interfaces: Adsorption, interactions, assembly & rheology. *Advances in Colloid and Interface Science* **2015,** *222*, 215-227.
123. Pawar, A. B.; Caggioni, M.; Ergun, R.; Hartel, R. W.; Spicer, P. T., Arrested coalescence in Pickering emulsions. *Soft Matter* **2011,** *7* (17), 7710-7716.
124. Yao, X.; Zhao, G.; Dai, C.; Wu, Y.; Lyu, Y., Interfacial characteristics and the stability mechanism of a dispersed particle gel (DPG) three-phase foam. *Journal of Molecular Liquids* **2020,** *301*, 112425.

125. Yang, L. L.; Wang, T. D.; Yang, X.; Jiang, G. C.; Luckham, P. F.; Xu, J. P.; Li, X. L.; Ni, X. X., Highly Stabilized Foam by Adding Amphiphilic Janus Particles for Drilling a High-Temperature and High-Calcium Geothermal Well. *Industrial & Engineering Chemistry Research* **2019,** *58* (23), 9795-9805.
126. Davies, J. T., *Interfacial phenomena*. Elsevier: 2012.
127. Graciaa, A.; Lachaise, J.; Marion, G.; Schechter, R. S., A study of the required hydrophile-lipophile balance for emulsification. *Langmuir* **1989,** *5* (6), 1315-1318.
128. Hedberg, J.; Lundin, M.; Lowe, T.; Blomberg, E.; Wold, S.; Wallinder, I. O., Interactions between surfactants and silver nanoparticles of varying charge. *Journal of colloid and interface science* **2012,** *369* (1), 193-201.
129. Landfester, K.; Ramirez, L. P., Encapsulated magnetite particles for biomedical application. *Journal of Physics: Condensed Matter* **2003,** *15* (15), S1345.
130. Barhoum, A.; Rahier, H.; Abou-Zaied, R. E.; Rehan, M.; Dufour, T.; Hill, G.; Dufresne, A., Effect of cationic and anionic surfactants on the application of calcium carbonate nanoparticles in paper coating. *ACS applied materials & interfaces* **2014,** *6* (4), 2734-2744.
131. Almahfood, M.; Bai, B., The synergistic effects of nanoparticle-surfactant nanofluids in EOR applications. *Journal of Petroleum Science and Engineering* **2018,** *171*, 196-210.
132. Correia, E. L.; Brown, N.; Ervin, A.; Papavassiliou, D. V.; Razavi, S., Contamination in Sodium Dodecyl Sulfate Solutions: Insights from the Measurements of Surface Tension and Surface Rheology. *Langmuir* **2022,** *38* (23), 7179-7189.
133. Lele, B. J.; Tilton, R. D., Colloidal depletion and structural force synergism or antagonism in solutions of mutually repelling polyelectrolytes and ionic surfactants. *Langmuir* **2019,** *35* (48), 15937-15947.
134. Sharma, T.; Iglauer, S.; Sangwai, J. S., Silica nanofluids in an oilfield polymer polyacrylamide: interfacial properties, wettability alteration, and applications for chemical enhanced oil recovery. *Industrial & Engineering Chemistry Research* **2016,** *55* (48), 12387-12397.
135. Bae, E.-J.; Park, H.-J.; Park, J.-S.; Yoon, J.-Y.; Kim, Y.-H.; Choi, K.-H.; Yi, J.-H., Effect of chemical stabilizers in silver nanoparticle suspensions on nanotoxicity. *Bulletin of the Korean Chemical Society* **2011,** *32* (2), 613-619.
136. Ju-Nam, Y.; Lead, J. R., Manufactured nanoparticles: an overview of their chemistry, interactions and potential environmental implications. *Science of the total environment* **2008,** *400* (1-3), 396-414.
137. Nourafkan, E.; Hu, Z.; Wen, D., Nanoparticle-enabled delivery of surfactants in porous media. *Journal of colloid and interface science* **2018,** *519*, 44-57.
138. Katepalli, H.; John, V. T.; Bose, A., The response of carbon black stabilized oil-in-water emulsions to the addition of surfactant solutions. *Langmuir* **2013,** *29* (23), 6790-6797.
139. Fuller, G. G.; Vermant, J., Complex Fluid-Fluid Interfaces: Rheology and Structure. *Annual Review of Chemical and Biomolecular Engineering* **2012,** *3* (1), 519-543.
140. Miller, R.; Wüstneck, R.; Krägel, J.; Kretzschmar, G., Dilational and shear rheology of adsorption layers at liquid interfaces. *Colloids and Surfaces A: Physicochemical and Engineering Aspects* **1996,** *111* (1), 75-118.
141. Krägel, J.; Derkatch, S. R., Interfacial shear rheology. *Current Opinion in Colloid & Interface Science* **2010,** *15* (4), 246-255.
142. Ravera, F.; Loglio, G.; Kovalchuk, V. I., Interfacial dilational rheology by oscillating bubble/drop methods. *Current Opinion in Colloid & Interface Science* **2010,** *15* (4), 217-228.

143. Derkach, S. R.; Krägel, J.; Miller, R., Methods of measuring rheological properties of interfacial layers (Experimental methods of 2D rheology). *Colloid Journal* **2009,** *71* (1), 1-17.
144. Maestro, A.; Santini, E.; Zabiegaj, D.; Llamas, S.; Ravera, F.; Liggieri, L.; Ortega, F.; Rubio, R. G.; Guzman, E., Particle and Particle-Surfactant Mixtures at Fluid Interfaces: Assembly, Morphology, and Rheological Description. *Advances in Condensed Matter Physics* **2015,** *2015*, 917516.
145. Miller, R.; Ferri, J. K.; Javadi, A.; Krägel, J.; Mucic, N.; Wüstneck, R., Rheology of interfacial layers. *Colloid and Polymer Science* **2010,** *288* (9), 937-950.
146. Miller, R.; Liggieri, L., *Interfacial rheology*. CRC Press: 2009; Vol. 1.
147. Jaensson, N.; Vermant, J., Tensiometry and rheology of complex interfaces. *Current opinion in colloid & interface science* **2018,** *37*, 136-150.
148. Sashuk, V.; Hołyst, R.; Wojciechowski, T.; Fiałkowski, M., Close-packed monolayers of charged Janus-type nanoparticles at the air–water interface. *Journal of Colloid and Interface Science* **2012,** *375* (1), 180-186.
149. Vora, S. R.; Bognet, B.; Patanwala, H. S.; Chinesta, F.; Ma, A. W. K., Surface Pressure and Microstructure of Carbon Nanotubes at an Air–Water Interface. *Langmuir* **2015,** *31* (16), 4663-4672.
150. Gopal, A.; Lee, K. Y. C., Headgroup Percolation and Collapse of Condensed Langmuir Monolayers. *The Journal of Physical Chemistry B* **2006,** *110* (44), 22079-22087.
151. Fernandez-Rodriguez, M. A.; Ramos, J.; Isa, L.; Rodriguez-Valverde, M. A.; Cabrerizo-Vilchez, M. A.; Hidalgo-Alvarez, R., Interfacial Activity and Contact Angle of Homogeneous, Functionalized, and Janus Nanoparticles at the Water/Decane Interface. *Langmuir* **2015,** *31* (32), 8818-8823.
152. Kwok, D. Y.; Vollhardt, D.; Miller, R.; Li, D.; Neumann, A. W., Axisymmetric drop shape analysis as a film balance. *Colloids and Surfaces A: Physicochemical and Engineering Aspects* **1994,** *88* (1), 51-58.
153. Ferdous, S.; Ioannidis, M. A.; Henneke, D., Adsorption kinetics of alkanethiol-capped gold nanoparticles at the hexane–water interface. *Journal of Nanoparticle Research* **2011,** *13* (12), 6579-6589.
154. Garbin, V.; Crocker, J. C.; Stebe, K. J., Forced Desorption of Nanoparticles from an Oil–Water Interface. *Langmuir* **2012,** *28* (3), 1663-1667.
155. Alvarez, N. J.; Anna, S. L.; Saigal, T.; Tilton, R. D.; Walker, L. M., Interfacial dynamics and rheology of polymer-grafted nanoparticles at air–water and xylene–water interfaces. *Langmuir* **2012,** *28* (21), 8052-8063.
156. Fernandez-Rodriguez, M. A.; Song, Y.; Rodríguez-Valverde, M. Á.; Chen, S.; Cabrerizo-Vilchez, M. A.; Hidalgo-Alvarez, R., Comparison of the Interfacial Activity between Homogeneous and Janus Gold Nanoparticles by Pendant Drop Tensiometry. *Langmuir* **2014,** *30* (7), 1799-1804.
157. Reynaert, S.; Brooks, C. F.; Moldenaers, P.; Vermant, J.; Fuller, G. G., Analysis of the magnetic rod interfacial stress rheometer. *Journal of Rheology* **2008,** *52* (1), 261-285.
158. Fitzgibbon, S.; Shaqfeh, E. S. G.; Fuller, G. G.; Walker, T. W., Scaling analysis and mathematical theory of the interfacial stress rheometer. *Journal of Rheology* **2014,** *58* (4), 999-1038.
159. Tajuelo, J.; Pastor, J.; Martínez-Pedrero, F.; Vázquez, M.; Ortega, F.; Rubio, R.; Rubio, M., Magnetic microwire probes for the magnetic rod interfacial stress rheometer. *Langmuir* **2015,** *31* (4), 1410-1420.

160. Erni, P.; Fischer, P.; Windhab, E. J.; Kusnezov, V.; Stettin, H.; Läuger, J., Stress- and strain-controlled measurements of interfacial shear viscosity and viscoelasticity at liquid/liquid and gas/liquid interfaces. *Review of Scientific Instruments* **2003,** *74* (11), 4916-4924.
161. Vandebril, S.; Franck, A.; Fuller, G. G.; Moldenaers, P.; Vermant, J., A double wall-ring geometry for interfacial shear rheometry. *Rheologica Acta* **2010,** *49* (2), 131-144.
162. Karbaschi, M.; Lotfi, M.; Krägel, J.; Javadi, A.; Bastani, D.; Miller, R., Rheology of interfacial layers. *Current Opinion in Colloid & Interface Science* **2014,** *19* (6), 514-519.
163. Zell, Z. A.; Mansard, V.; Wright, J.; Kim, K.; Choi, S. Q.; Squires, T. M., Linear and nonlinear microrheometry of small samples and interfaces using microfabricated probes. *Journal of Rheology* **2016,** *60* (1), 141-159.
164. Chang, C.-C.; Nowbahar, A.; Mansard, V.; Williams, I.; Mecca, J.; Schmitt, A. K.; Kalantar, T. H.; Kuo, T.-C.; Squires, T. M., Interfacial Rheology and Heterogeneity of Aging Asphaltene Layers at the Water–Oil Interface. *Langmuir* **2018,** *34* (19), 5409-5415.
165. Renggli, D.; Alicke, A.; Ewoldt, R. H.; Vermant, J., Operating windows for oscillatory interfacial shear rheology. *Journal of Rheology* **2020,** *64* (1), 141-160.
166. Beltramo, P. J.; Gupta, M.; Alicke, A.; Liascukiene, I.; Gunes, D. Z.; Baroud, C. N.; Vermant, J., Arresting dissolution by interfacial rheology design. *Proceedings of the National Academy of Sciences* **2017,** *114* (39), 10373-10378.
167. Elton L. Correia, L. E. F., Sepideh Razavi, Unpublished data.
168. Banks, H. T.; Hu, S.; Kenz, Z. R., A Brief Review of Elasticity and Viscoelasticity for Solids. *Advances in Applied Mathematics and Mechanics* **2011,** *3* (1), 1-51.
169. Zasadzinski, J. A.; Ding, J.; Warriner, H. E.; Bringezu, F.; Waring, A. J., The physics and physiology of lung surfactants. *Current Opinion in Colloid & Interface Science* **2001,** *6* (5), 506-513.
170. Franck, A.; Hodder, P., Measuring the Rheological Properties of Ultrathin Films at the Water-Air and Water-Oil Interface by Using a Novel Double Wall Ring (DWR) Geometry. **2009**, 1-4.
171. Pelipenko, J.; Kristl, J.; Rošic, R.; Baumgartner, S.; Kocbek, P., Interfacial rheology: An overview of measuring techniques and its role in dispersions and electrospinning. *Acta pharmaceutica (Zagreb, Croatia)* **2012,** *62*, 123-40.
172. Erk, K. A.; Martin, J. D.; Schwalbe, J. T.; Phelan, F. R.; Hudson, S. D., Shear and dilational interfacial rheology of surfactant-stabilized droplets. *Journal of Colloid and Interface Science* **2012,** *377* (1), 442-449.
173. Garbin, V.; Crocker, J. C.; Stebe, K. J., Nanoparticles at fluid interfaces: Exploiting capping ligands to control adsorption, stability and dynamics. *Journal of Colloid and Interface Science* **2012,** *387* (1), 1-11.
174. Wang, H.; Singh, V.; Behrens, S. H., Image Charge Effects on the Formation of Pickering Emulsions. *J Phys Chem Lett* **2012,** *3* (20), 2986-90.
175. Leunissen, M. E.; van Blaaderen, A.; Hollingsworth, A. D.; Sullivan, M. T.; Chaikin, P. M., Electrostatics at the oil–water interface, stability, and order in emulsions and colloids. *Proceedings of the National Academy of Sciences* **2007,** *104* (8), 2585-2590.
176. Maestro, A.; Bonales, L. J.; Ritacco, H.; Rubio, R. G.; Ortega, F., Effect of the spreading solvent on the three-phase contact angle of microparticles attached at fluid interfaces. *Physical Chemistry Chemical Physics* **2010,** *12* (42), 14115-14120.

177. Fernández-Rodríguez, M. A.; Rodríguez-Valverde, M. A.; Cabrerizo-Vílchez, M.; Hidalgo-Alvarez, R., Surface activity and collective behaviour of colloidally stable Janus-like particles at the air–water interface. *Soft Matter* **2014,** *10* (19), 3471-3476.
178. Sulpizi, M.; Gaigeot, M.-P.; Sprik, M., The silica–water interface: how the silanols determine the surface acidity and modulate the water properties. *Journal of chemical theory and computation* **2012,** *8* (3), 1037-1047.
179. Onizhuk, M.; Panteleimonov, A.; Kholin, Y. V.; Ivanov, V., Dissociation constants of silanol groups of silic acids: quantum chemical estimations. *Journal of Structural Chemistry* **2018,** *59*, 261-271.
180. Pfeiffer-Laplaud, M.; Costa, D.; Tielens, F.; Gaigeot, M.-P.; Sulpizi, M., Bimodal acidity at the amorphous silica/water interface. *The Journal of Physical Chemistry C* **2015,** *119* (49), 27354-27362.
181. Beloqui Redondo, A.; Jordan, I.; Ziazadeh, I.; Kleibert, A.; Giorgi, J. B.; Wörner, H. J.; May, S.; Abbas, Z.; Brown, M. A., Nanoparticle-Induced Charge Redistribution of the Air–Water Interface. *The Journal of Physical Chemistry C* **2015,** *119* (5), 2661-2668.
182. Razavi, S.; Cao, K. D.; Lin, B.; Lee, K. Y. C.; Tu, R. S.; Kretzschmar, I., Collapse of Particle-Laden Interfaces under Compression: Buckling vs Particle Expulsion. *Langmuir* **2015,** *31* (28), 7764-7775.
183. Yu, K.; Zhang, H. G.; Biggs, S.; Xu, Z. H.; Cayre, O. J.; Harbottle, D., The rheology of polyvinylpyrrolidone-coated silica nanoparticles positioned at an air-aqueous interface. *Journal of Colloid and Interface Science* **2018,** *527*, 346-355.
184. Li, X.; Gilchrist, J. F., Large-area nanoparticle films by continuous automated langmuir–blodgett assembly and deposition. *Langmuir* **2016,** *32* (5), 1220-1226.
185. Razavi, S.; Lin, B.; Lee, K. Y. C.; Tu, R. S.; Kretzschmar, I., Impact of Surface Amphiphilicity on the Interfacial Behavior of Janus Particle Layers under Compression. *Langmuir* **2019,** *35* (48), 15813-15824.
186. Domonkos, M.; Jackivová, R.; Pathó, A., Image analysis algorithm for the verification of hexagonal symmetry in spherical nanostructures. *Microelectronic Engineering* **2022,** *251*, 111635.
187. Vu, T. V.; Razavi, S.; Papavassiliou, D. V., Effect of Janus particles and non-ionic surfactants on the collapse of the oil-water interface under compression. *Journal of colloid and interface science* **2022,** *609*, 158-169.
188. Snyder, K. A.; Feng, X.; Keen, B.; Mason, T., Estimating the electrical conductivity of cement paste pore solutions from OH−, K+ and Na+ concentrations. *Cement and Concrete Research* **2003,** *33* (6), 793-798.
189. Domínguez, A.; Fernández, A.; González, N.; Iglesias, E.; Montenegro, L., Determination of critical micelle concentration of some surfactants by three techniques. *Journal of chemical education* **1997,** *74* (10), 1227.
190. Swan, J. W.; Furst, E. M., A simpler expression for Henry's function describing the electrophoretic mobility of spherical colloids. *Journal of colloid and interface science* **2012,** *388* (1), 92-94.
191. Bhattacharjee, S., DLS and zeta potential–what they are and what they are not? *Journal of controlled release* **2016,** *235*, 337-351.
192. Mateos, H.; Valentini, A.; Robles, E.; Brooker, A.; Cioffi, N.; Palazzo, G., Measurement of the zeta-potential of solid surfaces through Laser Doppler Electrophoresis of colloid tracer in a dip-cell: Survey of the effect of ionic strength, pH, tracer chemical nature and size. *Colloids and Surfaces A: Physicochemical and Engineering Aspects* **2019,** *576*, 82-90.

193. Brown, W.; Zhao, J., Adsorption of sodium dodecyl sulfate on polystyrene latex particles using dynamic light scattering and zeta potential measurements. *Macromolecules* **1993,** *26* (11), 2711-2715.
194. CRC handbook of chemistry and physics. **1977**.
195. Shim, S.; Nunes, J. K.; Chen, G.; Stone, H. A., Diffusiophoresis in the presence of a pH gradient. *Physical Review Fluids* **2022,** *7* (11), 110513.
196. Juárez, J. J.; Bevan, M. A., Feedback controlled colloidal self-assembly. *Advanced Functional Materials* **2012,** *22* (18), 3833-3839.
197. Alvarez, N. J.; Walker, L. M.; Anna, S. L., A criterion to assess the impact of confined volumes on surfactant transport to liquid–fluid interfaces. *Soft Matter* **2012,** *8* (34), 8917-8925.
198. Scholz, N.; Behnke, T.; Resch-Genger, U., Determination of the critical micelle concentration of neutral and ionic surfactants with fluorometry, conductometry, and surface tension—a method comparison. *Journal of Fluorescence* **2018,** *28* (1), 465-476.
199. Fainerman, V.; Kovalchuk, V.; Lucassen-Reynders, E.; Grigoriev, D.; Ferri, J.; Leser, M.; Michel, M.; Miller, R.; Möhwald, H., Surface-pressure isotherms of monolayers formed by microsize and nanosize particles. *Langmuir* **2006,** *22* (4), 1701-1705.
200. Kralchevsky, P.; Danov, K.; Kolev, V.; Broze, G.; Mehreteab, A., Effect of nonionic admixtures on the adsorption of ionic surfactants at fluid interfaces. 1. Sodium dodecyl sulfate and dodecanol. *Langmuir* **2003,** *19* (12), 5004-5018.
201. Fainerman, V.; Kovalchuk, V.; Aksenenko, E.; Michel, M.; Leser, M.; Miller, R., Models of two-dimensional solution assuming the internal compressibility of adsorbed molecules: a comparative analysis. *The Journal of Physical Chemistry B* **2004,** *108* (36), 13700-13705.
202. Fainerman, V.; Miller, R.; Kovalchuk, V., Influence of the compressibility of adsorbed layers on the surface dilational elasticity. *Langmuir* **2002,** *18* (20), 7748-7752.
203. Kovalchuk, V.; Loglio, G.; Fainerman, V.; Miller, R., Interpretation of surface dilational elasticity data based on an intrinsic two-dimensional interfacial compressibility model. *Journal of colloid and interface science* **2004,** *270* (2), 475-482.
204. Baret, J., Theoretical model for an interface allowing a kinetic study of adsorption. *Journal of Colloid and Interface Science* **1969,** *30* (1), 1-12.
205. Kralchevsky, P.; Danov, K.; Broze, G.; Mehreteab, A., Thermodynamics of ionic surfactant adsorption with account for the counterion binding: effect of salts of various valency. *Langmuir* **1999,** *15* (7), 2351-2365.
206. Hutchinson, E., Chemistry: Interfacial Phenomena. JT Davies and EK Rideal. Academic Press, New York, ed. 2, 1963. 494 pp. $15. *Science* **1963,** *142* (3595), 1052-1052.
207. Vollhardt, D.; Emrich, G., Coadsorption of sodium dodecyl sulfate and medium-chain alcohols at the air–water interface. *Colloids and Surfaces A: Physicochemical and Engineering Aspects* **2000,** *161* (1), 173-182.
208. Miller, R.; Fainerman, V.; Kovalchuk, V.; Grigoriev, D.; Leser, M.; Michel, M., Composite interfacial layers containing micro-size and nano-size particles. *Advances in colloid and interface science* **2006,** *128*, 17-26.
209. Leser, M.; Acquistapace, S.; Cagna, A.; Makievski, A.; Miller, R., Limits of oscillation frequencies in drop and bubble shape tensiometry. *Colloids and Surfaces A: Physicochemical and Engineering Aspects* **2005,** *261* (1-3), 25-28.
210. Brenner, H., *Interfacial transport processes and rheology*. Elsevier: 2013.

211. Fitzgibbon, S.; Shaqfeh, E. S.; Fuller, G. G.; Walker, T. W., Scaling analysis and mathematical theory of the interfacial stress rheometer. *Journal of Rheology* **2014,** *58* (4), 999-1038.
212. Poh, L.; Narimissa, E.; Wagner, M. H.; Winter, H. H., Interactive Shear and Extensional Rheology—25 years of IRIS Software. *Rheologica Acta* **2022**, 1-11.
213. Aksenenko, E.; Kovalchuk, V.; Fainerman, V.; Miller, R., Surface dilational rheology of mixed surfactants layers at liquid interfaces. *The Journal of Physical Chemistry C* **2007,** *111* (40), 14713-14719.
214. Firouzi, M.; Kovalchuk, V. I.; Loglio, G.; Miller, R., Salt effects on the dilational viscoelasticity of surfactant adsorption layers. *Current Opinion in Colloid & Interface Science* **2022,** *57*, 101538.
215. Lucassen, J.; Van Den Tempel, M., Dynamic measurements of dilational properties of a liquid interface. *Chemical Engineering Science* **1972,** *27* (6), 1283-1291.
216. Lucassen, J.; Van den Tempel, M., Longitudinal waves on visco-elastic surfaces. *Journal of Colloid and Interface Science* **1972,** *41* (3), 491-498.
217. Ravera, F.; Ferrari, M.; Santini, E.; Liggieri, L., Influence of surface processes on the dilational visco-elasticity of surfactant solutions. *Advances in colloid and interface science* **2005,** *117* (1-3), 75-100.
218. Ferry, J. D., *Viscoelastic properties of polymers*. John Wiley & Sons: 1980.
219. Tschoegl, N. W., *The phenomenological theory of linear viscoelastic behavior: an introduction*. Springer Science & Business Media: 2012.
220. Brakke, K. A., The surface evolver. *Experimental mathematics* **1992,** *1* (2), 141-165.
221. Cheung, D. L.; Bon, S. A., Stability of Janus nanoparticles at fluid interfaces. *Soft Matter* **2009,** *5* (20), 3969-3976.
222. Park, B. J.; Lee, D., Equilibrium orientation of nonspherical Janus particles at fluid–fluid interfaces. *Acs Nano* **2012,** *6* (1), 782-790.
223. Danov, K. D.; Kralchevsky, P. A.; Naydenov, B. N.; Brenn, G., Interactions between particles with an undulated contact line at a fluid interface: Capillary multipoles of arbitrary order. *Journal of colloid and interface science* **2005,** *287* (1), 121-134.
224. Brugarolas, T.; Park, B.; Lee, M.; D.H, L., Generation of Amphiphilic Janus Bubbles and Their Behavior at an Air–Water Interface. *Advanced Functional Materials* **2011,** *21*, 3924-3931.
225. Qiao, Y.; Ma, X.; Liu, Z.; Manno, M. A.; Keim, N. C.; Cheng, X., Tuning the rheology and microstructure of particle-laden fluid interfaces with Janus particles. *Journal of Colloid and Interface Science* **2022,** *618*, 241-247.
226. Carrasco-Fadanelli, V.; Castillo, R., Measurement of the capillary interaction force between Janus colloidal particles trapped at a flat air/water interface. *Soft Matter* **2020,** *16* (25), 5910-5914.
227. Adams, D. J.; Adams, S.; Melrose, J.; Weaver, A. C., Influence of particle surface roughness on the behaviour of Janus particles at interfaces. *Colloids and Surfaces A: Physicochemical and Engineering Aspects* **2008,** *317* (1), 360-365.
228. Lucassen, J., Capillary forces between solid particles in fluid interfaces. *Colloids and Surfaces* **1992,** *65* (2), 131-137.
229. Yao, L.; Botto, L.; Cavallaro, J. M.; Bleier, B. J.; Garbin, V.; Stebe, K. J., Near field capillary repulsion. *Soft Matter* **2013,** *9* (3), 779-786.

230. Bykov, A.; Noskov, B.; Loglio, G.; Lyadinskaya, V.; Miller, R., Dilational surface elasticity of spread monolayers of polystyrene microparticles. *Soft Matter* **2014,** *10* (34), 6499-6505.
231. Da, C.; Zhang, X.; Alzobaidi, S.; Hu, D.; Wu, P.; Johnston, K. P., Tuning surface chemistry and ionic strength to control nanoparticle adsorption and elastic dilational modulus at air-brine interface. *Langmuir* **2021,** *37* (19), 5795-5809.
232. Goggin, D. M.; Samaniuk, J. R., Dynamics of pristine graphite and graphene at an air-water interface. *AIChE Journal* **2018,** *64* (8), 3177-3187.
233. Wang, X.; In, M.; Blanc, C.; Malgaretti, P.; Nobili, M.; Stocco, A., Wetting and orientation of catalytic Janus colloids at the surface of water. *Faraday discussions* **2016,** *191*, 305-324.
234. Goggin, D. M.; Samaniuk, J. R., 2D Colloids: Size-and Shape-Controlled 2D Materials at Fluid–Fluid Interfaces. *Langmuir* **2021,** *37* (48), 14157-14166.
235. Jeong, H. W.; Park, J. W.; Lee, H. M.; Choi, K. H.; Lee, S. J.; Kim, J. W.; Park, B. J., Retardation of Capillary Force between Janus Particles at the Oil–Water Interface. *The Journal of Physical Chemistry Letters* **2022,** *13* (42), 10018-10024.
236. Correia, E. L.; Winter, H. H.; Razavi, S., Two-dimensional glass transition–like behavior of Janus particle–laden interface. *Rheologica Acta* **2023**, 1-13.
237. Barman, S.; Christopher, G. F., Role of capillarity and microstructure on interfacial viscoelasticity of particle laden interfaces. *Journal of Rheology* **2016,** *60* (1), 35-45.
238. National Academies of Sciences, E.; Medicine, *New Directions for Chemical Engineering*. 2022.
239. Kobayashi, Y.; Arai, N.; Nikoubashman, A., Structure and dynamics of amphiphilic Janus spheres and spherocylinders under shear. *Soft Matter* **2020,** *16* (2), 476-486.
240. Bianchi, E.; Panagiotopoulos, A. Z.; Nikoubashman, A., Self-assembly of Janus particles under shear. *Soft Matter* **2015,** *11* (19), 3767-3771.
241. DeLaCruz-Araujo, R. A.; Beltran-Villegas, D. J.; Larson, R. G.; Córdova-Figueroa, U. M., Rich Janus colloid phase behavior under steady shear. *Soft Matter* **2016,** *12* (18), 4071-4081.
242. Huang, Z.; Zhu, G.; Chen, P.; Hou, C.; Yan, L.-T., Plastic Crystal-to-Crystal Transition of Janus Particles under Shear. *Physical Review Letters* **2019,** *122* (19), 198002.
243. Kobayashi, Y.; Arai, N., Self-Assembly and Viscosity Behavior of Janus Nanoparticles in Nanotube Flow. *Langmuir* **2017,** *33* (3), 736-743.
244. Paiva, F. L.; Hore, M. J. A.; Secchi, A.; Calado, V.; Maia, J.; Khani, S., Dynamic Interfacial Trapping of Janus Nanorod Aggregates. *Langmuir* **2020,** *36* (15), 4184-4193.
245. Wu, H.; Gao, K.; Lu, Y.; Meng, Z.; Gou, C.; Li, Z.; Yang, M.; Qu, M.; Liu, T.; Hou, J.; Kang, W., Silica-based amphiphilic Janus nanofluid with improved interfacial properties for enhanced oil recovery. *Colloids and Surfaces A: Physicochemical and Engineering Aspects* **2020,** *586*, 124162.
246. Rezvantalab, H.; Connington, K. W.; Shojaei-Zadeh, S., Shear-induced interfacial assembly of Janus particles. *Phys. Rev. Fluids* **2016,** *1* (7), 074205.
247. Fernández-Rodríguez, M. Á.; Rahmani, S.; Yu, C. K. J.; Rodríguez-Valverde, M. Á.; Cabrerizo-Vílchez, M. Á.; Michel, C. A.; Lahann, J.; Hidalgo-Álvarez, R., Synthesis and interfacial activity of PMMA/PtBMA Janus and homogeneous nanoparticles at water/oil interfaces. *Colloids and Surfaces A: Physicochemical and Engineering Aspects* **2018,** *536*, 259-265.

248. Kadam, R.; Zilli, M.; Maas, M.; Rezwan, K., Nanoscale Janus Particles with Dual Protein Functionalization. *Particle & Particle Systems Characterization* **2018,** *35* (3), 1700332.
249. Zhang, H.; Yu, K.; Cayre, O. J.; Harbottle, D., Interfacial particle dynamics: one and two step yielding in colloidal glass. *Langmuir* **2016,** *32* (50), 13472-13481.
250. Cicuta, P.; Stancik, E. J.; Fuller, G. G., Shearing or Compressing a Soft Glass in 2D: Time-Concentration Superposition. *Physical Review Letters* **2003,** *90* (23), 236101.
251. Samaniuk, J. R.; Hermans, E.; Verwijlen, T.; Pauchard, V.; Vermant, J., Soft-glassy rheology of asphaltenes at liquid interfaces. *Journal of Dispersion Science and Technology* **2015,** *36* (10), 1444-1451.
252. Manga, M. S.; Hunter, T. N.; Cayre, O. J.; York, D. W.; Reichert, M. D.; Anna, S. L.; Walker, L. M.; Williams, R. A.; Biggs, S. R., Measurements of submicron particle adsorption and particle film elasticity at oil–water interfaces. *Langmuir* **2016,** *32* (17), 4125-4133.
253. Barman, S.; Christopher, G. F., Simultaneous Interfacial Rheology and Microstructure Measurement of Densely Aggregated Particle Laden Interfaces Using a Modified Double Wall Ring Interfacial Rheometer. *Langmuir* **2014,** *30* (32), 9752-9760.
254. Bertsch, P.; Diener, M.; Adamcik, J.; Scheuble, N.; Geue, T.; Mezzenga, R.; Fischer, P., Adsorption and interfacial layer structure of unmodified nanocrystalline cellulose at air/water interfaces. *Langmuir* **2018,** *34* (50), 15195-15202.
255. Trevenen, S.; Hamilton, H. S.; Ribbe, A. E.; Bradley, L. C.; Beltramo, P. J., Nanoscale porosity in microellipsoids cloaks interparticle capillary attraction at fluid interfaces. **2022**.
256. Derkach, S.; Krägel, J.; Miller, R., Methods of measuring rheological properties of interfacial layers (Experimental methods of 2D rheology). *Colloid journal* **2009,** *71* (1), 1-17.
257. Fuller, G. G.; Vermant, J., Complex fluid-fluid interfaces: rheology and structure. *Annual review of chemical and biomolecular engineering* **2012,** *3*, 519-543.
258. Correia, E. L.; Brown, N.; Razavi, S., Janus particles at fluid interfaces: Stability and interfacial rheology. *Nanomaterials* **2021,** *11* (2), 374.
259. Park, B. J.; Brugarolas, T.; Lee, D., Janus particles at an oil–water interface. *Soft Matter* **2011,** *7* (14), 6413-6417.
260. Guzmán, E.; Ortega, F.; Rubio, R. n. G., Forces Controlling the Assembly of Particles at Fluid Interfaces. *Langmuir* **2022**.
261. Winter, H. H., Analysis of dynamic mechanical data: inversion into a relaxation time spectrum and consistency check. *Journal of Non-Newtonian Fluid Mechanics* **1997,** *68* (2-3), 225-239.
262. Baumgaertel, M.; Winter, H., Determination of discrete relaxation and retardation time spectra from dynamic mechanical data. *Rheologica Acta* **1989,** *28* (6), 511-519.
263. Baumgaertel, M.; Winter, H., Interrelation between continuous and discrete relaxation time spectra. *Journal of Non-Newtonian Fluid Mechanics* **1992,** *44*, 15-36.
264. Siebenbürger, M.; Fuchs, M.; Winter, H.; Ballauff, M., Viscoelasticity and shear flow of concentrated, noncrystallizing colloidal suspensions: Comparison with mode-coupling theory. *Journal of Rheology* **2009,** *53* (3), 707-726.
265. Winter, H. H., Glass transition as the rheological inverse of gelation. *Macromolecules* **2013,** *46* (6), 2425-2432.
266. Baumgaertel, M.; Schausberger, A.; Winter, H., The relaxation of polymers with linear flexible chains of uniform length. *Rheologica Acta* **1990,** *29* (5), 400-408.
267. Doi, M., M. and SF Edwards, Theory of Polymer Dynamics Clarendon Press. *Oxford1988* **1986**.

268. Velegol, S. B.; Fleming, B. D.; Biggs, S.; Wanless, E. J.; Tilton, R. D., Counterion effects on hexadecyltrimethylammonium surfactant adsorption and self-assembly on silica. *Langmuir* **2000,** *16* (6), 2548-2556.
269. Kumar, S.; Aswal, V. K.; Kohlbrecher, J., Size-dependent interaction of silica nanoparticles with different surfactants in aqueous solution. *Langmuir* **2012,** *28* (25), 9288-9297.
270. Tran, T.; Perdomo, M. E. G.; Haghighi, M.; Amrouch, K., Study of the synergistic effects between different surfactant types and silica nanoparticles on the stability of liquid foams at elevated temperature. *Fuel* **2022,** *315*, 122818.
271. Wu, Y.; Fang, S.; Zhang, K.; Zhao, M.; Jiao, B.; Dai, C., Stability mechanism of nitrogen foam in porous media with silica nanoparticles modified by cationic surfactants. *Langmuir* **2018,** *34* (27), 8015-8023.
272. Boakye-Ansah, S.; Khan, M. A.; Haase, M. F., Controlling surfactant adsorption on highly charged nanoparticles to stabilize bijels. *The Journal of Physical Chemistry C* **2020,** *124* (23), 12417-12423.
273. Cui, Z.-G.; Yang, L.-L.; Cui, Y.-Z.; Binks, B., Effects of surfactant structure on the phase inversion of emulsions stabilized by mixtures of silica nanoparticles and cationic surfactant. *Langmuir* **2010,** *26* (7), 4717-4724.
274. Kumar, R. S.; Chaturvedi, K. R.; Iglauer, S.; Sharma, T., Impact of anionic surfactant on stability, viscoelastic moduli, and oil recovery of silica nanofluid in saline environment. *Journal of Petroleum Science and Engineering* **2020,** *195*, 107634.
275. Liu, Z.; Bode, V.; Hadayati, P.; Onay, H.; Sudhölter, E. J., Understanding the stability mechanism of silica nanoparticles: The effect of cations and EOR chemicals. *Fuel* **2020,** *280*, 118650.
276. Li, P.; Ishiguro, M., Adsorption of anionic surfactant (sodium dodecyl sulfate) on silica. *Soil science and plant nutrition* **2016,** *62* (3), 223-229.
277. Flood, C.; Cosgrove, T.; Espidel, Y.; Howell, I.; Revell, P., Effects of surfactants and electrolytes on adsorbed layers and particle stability. *Langmuir* **2008,** *24* (14), 7323-7328.
278. Kumar, S.; Aswal, V., Tuning of nanoparticle–surfactant interactions in aqueous system. *Journal of Physics: Condensed Matter* **2010,** *23* (3), 035101.
279. Li, P.; Li, T.; Ishiguro, M.; Su, Y., Comparison of same carbon chain length cationic and anionic surfactant adsorption on silica. *Colloids and Interfaces* **2020,** *4* (3), 34.
280. Maltesh, C.; Somasundaran, P., Binding of sodium dodecyl sulfate to polyethylene oxide at the silica—water interface. *Journal of colloid and interface science* **1992,** *153* (1), 298-301.
281. Iglesias, G. R.; Wachter, W.; Ahualli, S.; Glatter, O., Interactions between large colloids and surfactants. *Soft Matter* **2011,** *7* (10), 4619-4622.
282. Ahualli, S.; Iglesias, G.; Wachter, W.; Dulle, M.; Minami, D.; Glatter, O., Adsorption of anionic and cationic surfactants on anionic colloids: supercharging and destabilization. *Langmuir* **2011,** *27* (15), 9182-9192.
283. Biswal, N. R.; Rangera, N.; Singh, J. K., Effect of different surfactants on the interfacial behavior of the n-hexane–water system in the presence of silica nanoparticles. *The Journal of Physical Chemistry B* **2016,** *120* (29), 7265-7274.
284. Ma, H.; Luo, M.; Dai, L. L., Influences of surfactant and nanoparticle assembly on effective interfacial tensions. *Physical Chemistry Chemical Physics* **2008,** *10* (16), 2207-2213.
285. Al-Anssari, S.; Arif, M.; Wang, S.; Barifcani, A.; Iglauer, S., Stabilising nanofluids in saline environments. *Journal of colloid and interface science* **2017,** *508*, 222-229.

286. Trzaskus, K. W.; Lee, S. L.; de Vos, W. M.; Kemperman, A.; Nijmeijer, K., Fouling behavior of silica nanoparticle-surfactant mixtures during constant flux dead-end ultrafiltration. *Journal of colloid and interface science* **2017,** *506*, 308-318.
287. Khalilinezhad, S. S.; Mobaraki, S.; Zakavi, M.; Omidvar Sorkhabadi, M.; Cheraghian, G.; Jarrahian, K., Mechanistic modeling of nanoparticles-assisted surfactant flood. *Arabian Journal for Science and Engineering* **2018,** *43*, 6609-6625.
288. Huang, Z.; Yan, Z.; Gu, T., Mixed adsorption of cationic and anionic surfactants from aqueous solution on silica gel. *Colloids and surfaces* **1989,** *36* (3), 353-358.
289. Sun, Q.; Li, Z.; Wang, J.; Li, S.; Li, B.; Jiang, L.; Wang, H.; Lü, Q.; Zhang, C.; Liu, W., Aqueous foam stabilized by partially hydrophobic nanoparticles in the presence of surfactant. *Colloids and Surfaces A: Physicochemical and Engineering Aspects* **2015,** *471*, 54-64.
290. Li, S.; Li, Z.; Wang, P., Experimental study of the stabilization of CO2 foam by sodium dodecyl sulfate and hydrophobic nanoparticles. *Industrial & Engineering Chemistry Research* **2016,** *55* (5), 1243-1253.
291. Thibaut, A.; Misselyn-Bauduin, A.-M.; Grandjean, J.; Broze, G.; Jérôme, R., Adsorption of an aqueous mixture of surfactants on silica. *Langmuir* **2000,** *16* (24), 9192-9198.
292. Wan, L. S.; Poon, P. K., Effect of salts on the surface/interfacial tension and critical micelle concentration of surfactants. *Journal of pharmaceutical sciences* **1969,** *58* (12), 1562-1567.
293. Matarredona, O.; Rhoads, H.; Li, Z.; Harwell, J. H.; Balzano, L.; Resasco, D. E., Dispersion of single-walled carbon nanotubes in aqueous solutions of the anionic surfactant NaDDBS. *The Journal of Physical Chemistry B* **2003,** *107* (48), 13357-13367.
294. Fainerman, V.; Lylyk, S.; Aksenenko, E.; Petkov, J.; Yorke, J.; Miller, R., Surface tension isotherms, adsorption dynamics and dilational visco-elasticity of sodium dodecyl sulphate solutions. *Colloids and Surfaces A: Physicochemical and Engineering Aspects* **2010,** *354* (1-3), 8-15.
295. Mukerjee, P.; Mysels, K. J. *Critical micelle concentrations of aqueous surfactant systems*; National Standard reference data system: 1971.
296. Takei, K.; Tsuto, K.; Miyamoto, S.; Wakatsuki, J., Anionic surfactants: lauric products. *Journal of the American Oil Chemists' Society* **1985,** *62* (2), 341-347.
297. Mysels, K. J., Surface tension of solutions of pure sodium dodecyl sulfate. *Langmuir* **1986,** *2* (4), 423-428.
298. Davies, J. In *A quantitative kinetic theory of emulsion type, I. Physical chemistry of the emulsifying agent*, Gas/Liquid and Liquid/Liquid Interface. Proceedings of the International Congress of Surface Activity, Citeseer: 1957; pp 6-438.
299. Mysels, K. J., C&SC Folklore. 6. The Surface Tension Minimum and Gilbert D. Miles. *Langmuir* **1996,** *12* (9), 2325-2326.
300. Miles, G. D.; Shedlovsky, L., Minima in Surface Tension–Concentration Curves of Solutions of Sodium Alcohol Sulfates. *The journal of physical chemistry* **1944,** *48* (1), 57-62.
301. Javadi, A.; Mucic, N.; Vollhardt, D.; Fainerman, V.; Miller, R., Effects of dodecanol on the adsorption kinetics of SDS at the water–hexane interface. *Journal of colloid and interface science* **2010,** *351* (2), 537-541.
302. Saykally, R. J., Two sides of the acid–base story. *Nature chemistry* **2013,** *5* (2), 82-84.
303. Beloqui Redondo, A.; Jordan, I.; Ziazadeh, I.; Kleibert, A.; Giorgi, J. B.; Wörner, H. J.; May, S.; Abbas, Z.; Brown, M. A., Nanoparticle-induced charge redistribution of the air–water interface. *The Journal of Physical Chemistry C* **2015,** *119* (5), 2661-2668.

304. Karraker, K.; Radke, C., Disjoining pressures, zeta potentials and surface tensions of aqueous non-ionic surfactant/electrolyte solutions: theory and comparison to experiment. *Advances in colloid and interface science* **2002,** *96* (1-3), 231-264.
305. Vatanparast, H.; Shahabi, F.; Bahramian, A.; Javadi, A.; Miller, R., The role of electrostatic repulsion on increasing surface activity of anionic surfactants in the presence of hydrophilic silica nanoparticles. *Scientific reports* **2018,** *8* (1), 1-11.
306. Israelachvili, J. N.; Mitchell, D. J.; Ninham, B. W., Theory of self-assembly of hydrocarbon amphiphiles into micelles and bilayers. *Journal of the Chemical Society, Faraday Transactions 2: Molecular and Chemical Physics* **1976,** *72*, 1525-1568.
307. Quina, F. H.; Nassar, P. M.; Bonilha, J. B.; Bales, B. L., Growth of sodium dodecyl sulfate micelles with detergent concentration. *The Journal of Physical Chemistry* **1995,** *99* (46), 17028-17031.
308. Gildnyi, T.; Stergiopoulos, C.; Wolfram, E., Equilibrium surface tension of aqueous surfactant solutions. *Colloid and Polymer Science* **1976,** *254* (11), 1018-1023.
309. Hines, J. D., The preparation of surface chemically pure sodiumn-dodecyl sulfate by foam fractionation. *Journal of colloid and interface science* **1996,** *180* (2), 488-492.
310. Rosen, M. J.; Hua, X. Y., Surface concentrations and molecular interactions in binary mixtures of surfactants. *Journal of Colloid and Interface Science* **1982,** *86* (1), 164-172.
311. Lunkenheimer, K.; Czichocki, G.; Hirte, R.; Barzyk, W., Novel results on the adsorption of ionic surfactants at the air/water interface—sodium-n-alkyl sulphates. *Colloids and Surfaces A: Physicochemical and Engineering Aspects* **1995,** *101* (2-3), 187-197.
312. Addison, C.; Hutchinson, S., 180. The properties of freshly-formed surfaces. Part IX. Expansion of soluble films of sodium dodecyl sulphate at air–water and toluene–water interfaces. *Journal of the Chemical Society (Resumed)* **1948**, 943-948.
313. López-Díaz, D.; García-Mateos, I.; Velázquez, M. M., Surface properties of mixed monolayers of sulfobetaines and ionic surfactants. *Journal of colloid and interface science* **2006,** *299* (2), 858-866.
314. Nakagaki, M.; Yokoyama, S., Acid-catalyzed hydrolysis of sodium dodecyl sulfate. *Journal of pharmaceutical sciences* **1985,** *74* (10), 1047-1052.
315. Czichocki, G.; Much, H.; Vollhardt, D., Quantitative determination of dodecanol in sodium dodecyl sulphate in the nanogram range by high-performance liquid chromatography with UV detection. *Journal of Chromatography a* **1983,** *280*, 109-118.
316. Czichocki, G.; Müller, P.; Vollhardt, D.; Krüger, M., Determination of trace amounts of alcohols in sodium alkyl sulphate mixtures using high-performance liquid chromatography and surface tension measurements. *Journal of Chromatography A* **1992,** *604* (2), 213-218.
317. Lunkenheimer, K.; Miller, R., A criterion for judging the purity of adsorbed surfactant layers. *Journal of colloid and interface science* **1987,** *120* (1), 176-183.
318. Vollhardt, D.; Czichocki, G., Effect of isomeric alcohols as a minor component on the adsorption properties of aqueous sodium alkyl sulfate solutions. *Langmuir* **1990,** *6* (2), 317-322.
319. Alvarez, N. J.; Walker, L. M.; Anna, S. L., A microtensiometer to probe the effect of radius of curvature on surfactant transport to a spherical interface. *Langmuir* **2010,** *26* (16), 13310-13319.
320. Poskanzer, A. M.; Goodrich, F., Surface viscosity of sodium dodecyl sulfate solutions with and without added dodecanol. *The Journal of Physical Chemistry* **1975,** *79* (20), 2122-2126.
321. Berry, J. D.; Neeson, M. J.; Dagastine, R. R.; Chan, D. Y.; Tabor, R. F., Measurement of surface and interfacial tension using pendant drop tensiometry. *Journal of colloid and interface science* **2015,** *454*, 226-237.

322. Alzobaidi, S.; Da, C.; Wu, P.; Zhang, X.; Rabat-Torki, N. J.; Harris, J. M.; Hackbarth, J. E.; Lu, C.; Hu, D.; Johnston, K. P., Tuning Nanoparticle Surface Chemistry and Interfacial Properties for Highly Stable Nitrogen-In-Brine Foams. *Langmuir* **2021,** *37* (17), 5408-5423.
323. Wantke, K.-D.; Fruhner, H.; Örtegren, J., Surface dilatational properties of mixed sodium dodecyl sulfate/dodecanol solutions. *Colloids and Surfaces A: Physicochemical and Engineering Aspects* **2003,** *221* (1-3), 185-195.
324. Fainerman, V.; Lylyk, S.; Aksenenko, E.; Kovalchuk, N.; Kovalchuk, V.; Petkov, J.; Miller, R., Effect of water hardness on surface tension and dilational visco-elasticity of sodium dodecyl sulphate solutions. *Journal of colloid and interface science* **2012,** *377* (1), 1-6.
325. Fainerman, V.; Aksenenko, E.; Lylyk, S.; Petkov, J.; Yorke, J.; Miller, R., Adsorption Layer Characteristics of Mixed Sodium Dodecyl Sulfate/C n EO m Solutions 1. Dynamic and Equilibrium Surface Tension. *Langmuir* **2010,** *26* (1), 284-292.
326. Tajima, K.; Muramatsu, M.; Sasaki, T., Radiotracer Studies on Adsorption of Surface Active Substance at Aqueous Surface. I. Accurate Measurement of Adsorption of Tritiated Sodium Dodecylsulfate. *Bulletin of the Chemical Society of Japan* **1970,** *43* (7), 1991-1998.
327. Tajima, K., Radiotracer studies on adsorption of surface active substance at aqueous surface. III. The effects of salt on the adsorption of sodium dodecylsulfate. *Bulletin of the Chemical Society of Japan* **1971,** *44* (7), 1767-1771.
328. Semmler, A.; Kohler, H.-H., Surface properties of alkylpyridinium chlorides and the applicability of the pendant drop technique. *Journal of colloid and interface science* **1999,** *218* (1), 137-144.
329. Cassie, A.; Baxter, S., Wettability of porous surfaces. *Transactions of the Faraday society* **1944,** *40*, 546-551.
330. Aveyard, R.; Binks, B.; Fletcher, P.; Rutherford, C., Measurement of contact angles of spherical monodisperse particles with surfactant solutions. *Colloids and Surfaces A: Physicochemical and Engineering Aspects* **1994,** *83* (1), 89-98.